

MATERIALS FOR ADAPTIVE STRUCTURAL ACOUSTIC CONTROL

Period February 1, 1996 to January 31, 1997

Final Report

VOLUME IV

OFFICE OF NAVAL RESEARCH
Contract No.: N00014-92-J-1510

APPROVED FOR PUBLIC RELEASE — DISTRIBUTION UNLIMITED

Reproduction in whole or in part is permitted
for any purpose of the United States Government

L. Eric Cross

DTIC QUALITY INSPECTED⁴

PENNSTATE



19970520 049

**THE MATERIALS RESEARCH LABORATORY
UNIVERSITY PARK, PA**

REPORT DOCUMENTATION PAGE

Form Approved
OMB No. 0704-0188

Public reporting burden for this collection of information is estimated to average 1 hour per response, including the time for reviewing instructions, searching existing data sources, gathering and maintaining the data needed, and completing and reviewing the collection of information. Send comments regarding this burden estimate or any other aspect of this collection of information, including suggestions for reducing this burden, to Washington Headquarters Services, Directorate for Information Operations and Reports, 1215 Jefferson Davis Highway, Suite 1204, Arlington, VA 22202-4302, and to the Office of Management and Budget, Paperwork Reduction Project (0704-0188), Washington, DC 20503.

1. AGENCY USE ONLY (Leave blank)	2. REPORT DATE	3. REPORT TYPE AND DATES COVERED	
	4/14/97	FINAL REPORT 2/1/96-1/31/97	
4. TITLE AND SUBTITLE		5. FUNDING NUMBERS	
MATERIALS FOR ADAPTIVE STRUCTURAL ACOUSTIC CONTROL		ONR CONTRACT NO: N00014-92-J-1510	
6. AUTHOR(S)			
L. ERIC CROSS			
7. PERFORMING ORGANIZATION NAME(S) AND ADDRESS(ES)		8. PERFORMING ORGANIZATION REPORT NUMBER	
MATERIALS RESEARCH LABORATORY THE PENNSYLVANIA STATE UNIVERSITY UNIVERSITY PARK, PA 16802-4800			
9. SPONSORING/MONITORING AGENCY NAME(S) AND ADDRESS(ES)		10. SPONSORING/MONITORING AGENCY REPORT NUMBER	
OFFICE OF NAVAL RESEARCH CODE 1513:NRJ 800 NORTH QUINCY STREET ARLINGTON, VA 22217-5660		GERALD T. SMITH OFFICE OF NAVAL RESEARCH RES. 536 SOUTH CLARK STREET, RM 286 CHICAGO, ILLINOIS 60606-1588 REP.	
11. SUPPLEMENTARY NOTES			
12a. DISTRIBUTION / AVAILABILITY STATEMENT		12b. DISTRIBUTION CODE	
13. ABSTRACT (Maximum 200 words)			
SEE FOLLOWING TWO PAGES.			
14. SUBJECT TERMS		15. NUMBER OF PAGES	
		16. PRICE CODE	
17. SECURITY CLASSIFICATION OF REPORT	18. SECURITY CLASSIFICATION OF THIS PAGE	19. SECURITY CLASSIFICATION OF ABSTRACT	20. LIMITATION OF ABSTRACT

GENERAL INSTRUCTIONS FOR COMPLETING SF 298

The Report Documentation Page (RDP) is used in announcing and cataloging reports. It is important that this information be consistent with the rest of the report, particularly the cover and title page. Instructions for filling in each block of the form follow. It is important to stay *within the lines* to meet optical scanning requirements.

Block 1. Agency Use Only (Leave blank).

Block 2. Report Date. Full publication date including day, month, and year, if available (e.g. 1 Jan 88). Must cite at least the year.

Block 3. Type of Report and Dates Covered.

State whether report is interim, final, etc. If applicable, enter inclusive report dates (e.g. 10 Jun 87 - 30 Jun 88).

Block 4. Title and Subtitle. A title is taken from the part of the report that provides the most meaningful and complete information. When a report is prepared in more than one volume, repeat the primary title, add volume number, and include subtitle for the specific volume. On classified documents enter the title classification in parentheses.

Block 5. Funding Numbers. To include contract and grant numbers; may include program element number(s), project number(s), task number(s), and work unit number(s). Use the following labels:

C - Contract	PR - Project
G - Grant	TA - Task
PE - Program Element	WU - Work Unit Accession No.

Block 6. Author(s). Name(s) of person(s) responsible for writing the report, performing the research, or credited with the content of the report. If editor or compiler, this should follow the name(s).

Block 7. Performing Organization Name(s) and Address(es). Self-explanatory.

Block 8. Performing Organization Report Number. Enter the unique alphanumeric report number(s) assigned by the organization performing the report.

Block 9. Sponsoring/Monitoring Agency Name(s) and Address(es). Self-explanatory.

Block 10. Sponsoring/Monitoring Agency Report Number. (If known)

Block 11. Supplementary Notes. Enter information not included elsewhere such as: Prepared in cooperation with...; Trans. of...; To be published in.... When a report is revised, include a statement whether the new report supersedes or supplements the older report.

Block 12a. Distribution/Availability Statement.

Denotes public availability or limitations. Cite any availability to the public. Enter additional limitations or special markings in all capitals (e.g. NOFORN, REL, ITAR).

DOD - See DoDD 5230.24, "Distribution Statements on Technical Documents."

DOE - See authorities.

NASA - See Handbook NHB 2200.2.

NTIS - Leave blank.

Block 12b. Distribution Code.

DOD - Leave blank.

DOE - Enter DOE distribution categories from the Standard Distribution for Unclassified Scientific and Technical Reports.

NASA - Leave blank.

NTIS - Leave blank.

Block 13. Abstract. Include a brief (*Maximum 200 words*) factual summary of the most significant information contained in the report.

Block 14. Subject Terms. Keywords or phrases identifying major subjects in the report.

Block 15. Number of Pages. Enter the total number of pages.

Block 16. Price Code. Enter appropriate price code (*NTIS only*).

Blocks 17. - 19. Security Classifications. Self-explanatory. Enter U.S. Security Classification in accordance with U.S. Security Regulations (i.e., UNCLASSIFIED). If form contains classified information, stamp classification on the top and bottom of the page.

Block 20. Limitation of Abstract. This block must be completed to assign a limitation to the abstract. Enter either UL (unlimited) or SAR (same as report). An entry in this block is necessary if the abstract is to be limited. If blank, the abstract is assumed to be unlimited.

ABSTRACT

This report documents work carried out largely over the fifth and final year of the ONR sponsored University Research Initiative (URI) entitled "Materials for Adaptive Structural Acoustic Control." This program has continued to foster the successful development of new electroceramic single crystal and composite material combinations for both sensing and actuation functions in adaptive structural systems.

For the classical perovskite relaxor, dielectrics typified by lead magnesium niobate, continuing studies of properties in the temperature region above the dielectric maximum T_m have added strong additional support to the superparaelectric/spin glass model for the behavior developed earlier in the IMRL. The most exciting and important discovery of the year has been the ultra high strain capability of relaxor ferroelectric single crystal actuators. For crystal in the lead zinc niobate:lead titanate (PZN;PT) solid solution system, at compositions in the rhombohedral phase close to the morphotropic phase boundary to the tetragonal ferroelectric phase at 9 mole % PT in PZN, crystals cut and poled along the 001 cube axis exhibit massive field induced quasi linear anhysteretic strains up to 0.6%. For this poling d_{33} values up to 2,300 pC/N and coupling coefficients k_{33} of 94% have been achieved and it was the original hypothesis that these extreme numbers must be largely due to extrinsic domain wall motion. Now however it is very clear that the exact equivalence of the effect of an 001 oriented E field on the $\bar{1}\bar{1}1, \bar{1}\bar{1}\bar{1}, \bar{1}\bar{1}\bar{1}$, and $\bar{1}\bar{1}\bar{1}$ rhombohedral domains precludes this field from driving domain wall motion so that quite contrary to our earlier expectation the polarization and associated strain phenomena are purely intrinsic. At higher field levels there is an obvious step in both polarization and strain into an induced tetragonal phase which gives total reproducible induced strains up to 1.7%. Clearly the PZN:PT crystals represent a major breakthrough into a completely new regimen for piezoelectric actuation and sensing.

For antiferroelectric:ferroelectric switching compositions in the lead lanthanum zirconated titanate stannate family, new experimental studies have proven that the induced polarization P_3 and the strain x_{33} onset at different field levels. A new domain re-orientation model has been invoked to explain this startlingly unusual behavior. Both barium and strontium additives have also been explored to control hysteresis between forward and backward switching with good success. As well as being interesting for transduction we believe these compositions are sure to be important for energy storage dielectrics.

In composite sensing it is pleasing to report that the moonie flexensional patent has now been licensed to the Input:Output Corporation who have successfully fabricated and sold more than 80,000 moonie sensors. Work is continuing on the cymbal type modification of the moonie with focus now on array structures for large area panels. This topic is transitioning to a joint study between the IMRL and Penn State's ARL, on a new MURI initiative. For the very small hollow PZT spheres produced by blowing, the emphasis has been upon both poling and driving from outer surface electrodes, and exploring both by experiment and by finite element theoretical methods, the resonant mode structures which can be induced. Studies of the 2:2 composite structures confirm the very high effective hydrostatic sensitivity and are permitting closer consonance between measurement and theoretical analysis.

Actuation studies have been dominated by the initial exploration of the fantastic strain capability of the relaxor ferroelectric MPB single crystals. Obviously the induced strains are on order of magnitude larger than for conventional PZT ceramics, but the blocking force has

not yet been determined. It is expected that d_{31} will also be large and anhysteretic in these crystals, as spontaneous strain depends on Q_{44} which is a pure shear constant. The d_{15} however may be significantly more complex as an E_1 field will certainly drive domain walls in these E_3 poled crystals.

Reliability studies of conventional actuators are continuing with emphasis on using acoustic emission to explore and separate domain wall motion and crack propagation. Most earlier studies were indeterminate and difficult to interpret, recently for these strongly piezoelectric samples we have shown that electrical noise in the power supply induces very strong mechanical noise in the sample giving high spurious emission counts. New studies using a long time constant filter in the supply have permitted clear and effective separation. Over the last few years there has been a strong re-awakening of interest in bimorph type transducer amplifiers with new concepts like rainbow, cerambow and thunder appearing. Under our ONR program with Virginia Polytechnic it has been necessary to sort out the conflicting claims for these 'morph' types and these data are included for completeness. We have also begun serious study of the large electrostriction in the soft polyurethane elastomers where it has been necessary to derive new techniques to measure strain with ultra low constraint on the films.

Processing studies now involved both single crystal flux growth and a wide range of powder and ceramic processing. Current needs for integrity and better mechanical properties are driving new needs for fine grained PZT piezoceramics and new processing is permitting retention of excellent properties down to submicron grain sizes.

From the wide range of thin ferroelectric film activities in the laboratory, only those which refer to the thicker films being produced on silicon for MEMS devices are included.

**MATERIALS FOR ADAPTIVE STRUCTURAL
ACOUSTIC CONTROL**

Period February 1, 1996 to January 31, 1997

Final Report

VOLUME IV

OFFICE OF NAVAL RESEARCH
Contract No.: N00014-92-J-1510

APPROVED FOR PUBLIC RELEASE — DISTRIBUTION UNLIMITED

Reproduction in whole or in part is permitted
for any purpose of the United States Government

L. Eric Cross

TABLE OF CONTENTS

APPENDICES LISTING	2
ABSTRACT	11
INTRODUCTION	12
1.0 GENERAL SUMMARY PAPERS	14
2.0 MATERIALS STUDIES	14
3.0 COMPOSITE SENSORS	15
4.0 ACTUATOR STUDIES	16
5.0 INTEGRATION STUDIES	16
6.0 PROCESSING STUDIES	16
7.0 THIN FILM FERROELECTRICS	17
8.0 INSTRUMENTATION	17
9.0 GRADUATE STUDENTS IN THE PROGRAM	17
10.0 HONORS AND AWARDS	17
11.0 APPRENTICE PROGRAM	18
12.0 PAPERS PUBLISHED IN REFERRED JOURNALS	19
13.0 PAPERS SUBMITTED FOR PUBLICATION	22
14.0 PAPERS APPEARING IN NON REFERRED PROCEEDINGS	23
15.0 INVITED PAPERS PRESENTATIONS AT NATIONAL AND INTERNATIONAL MEETINGS	24
16.0 INVITED PAPERS PRESENTED AT UNIVERSITY, INDUSTRY, AND GOVERNMENT LABORATORIES	28
17.0 CONTRIBUTED PAPERS AT NATIONAL AND INTERNATIONAL MEETINGS	31
18.0 BOOKS (AND SECTIONS THERE OF)	36
APPENDICES	

APPENDICES

VOLUME I

General Summary Papers

1. Cross, L.E., "Ferroelectric Materials for Electromechanical Transducer Applications." *Mat. Chem. Phys.* **43**, 108-115 (1996).
2. Cross, L.E., "Ferroelectric Ceramics: Materials and Application Issues." *Ceramic Transactions* **68**, 15-55 (1996).
3. Li, S., J.A. Eastman, Z. Li, C.M. Foster, R.E. Newnham, and L.E. Cross, "Size Effects in Ferroelectrics." *Phys. Lett. A* **212**, 341 (1996).
4. Li, Shaoping, J.A. Eastman, R.E. Newnham, and L.E. Cross, "Susceptibility of Nanostructured Ferroelectrics." *Japanese J. Appl. Physics* **35** (Part 2) [No. 4B], L502-L504 (1996).
5. Newnham, R.E., Chapter: Crystal Chemistry and Crystal Physics, in Innovative Ideas in Ceramics and Materials Curricula, edited by T. Stoebe and W. Huebner. Published by the American Ceramic Society, pp. 65-72 (1996).
6. Uchino, K., "New Applications of Photostriction." *Innovations in Mater. Res.* **1** (1), 11-22 (1996).
7. Aburatani, H. and K. Uchino, "Acoustic Emission (AE) Measurement Technique in Piezoelectric Ceramics." *Jpn. J. Appl. Phys.* **35** (2) [4B], L516-L518 (1996).

Materials Studies

8. Choi, S., J.M. Jung, and A.S. Bhalla, "Dielectric, Pyroelectric and Piezoelectric Properties of Calcium-Modified Lead Magnesium Tantalate-Lead Titanate Ceramics." *Ferroelectric Letters* **21**, 27-33 (1996).
9. Alberta, E. and A.S. Bhalla, "Preparation of Phase Pure Perovskite Lead Indium Niobate Ceramic." *Mater. Lett.* **29**, 127-129 (1996).
10. Zhang, Q.M., J. Zhao, T.R. Shrout, and L.E. Cross, "The Effect of Ferroelastic Coupling in Controlling the Abnormal Aging Behavior in Lead Magnesium Niobate-Lead Titanate Relaxor Ferroelectrics." *J. Mater. Res.* **12** (7), (1997).
11. Alberta, E., A.S. Bhalla, and T. Takenaka, "Piezoelectric, elastic and Dielectric Constants for Ceramics in the Solids Solution: $x\text{PbZrO}_3 - (1-x-z)\text{Pb}(\text{Zn}_{1/3}\text{Nb}_{2/3})\text{O}_3 - z\text{PbTiO}_3$." *Ferroelectrics* **188**, 109-124 (1996).

Materials Studies—continued

12. Zhang, Q.M. and J. Zhao, "Polarization Responses in Lead Magnesium Niobate Based Relaxor Ferroelectrics." *Applied Physics Letters* (submitted).
13. Müller, V. and Q.M. Zhang, "Nonlinearity and Scaling Behavior in Donor Doped Lead Zirconate Titanate Piezoceramic." *Physics Review Letters* (submitted).
14. Zhang, Q.M., J. Zhao, K. Uchino, and J. Zheng, "Change of the Weak-Field Properties of Pb(ZrTi)O₃ Piezoceramics with Compressive Uniaxial Stresses and Its Links to the Effect of Dopants on the Stability of the Polarizations in the Materials." *J. Mat. Res.* **12**, 226 (1997).
15. Markowski, K., S.-E. Park, S. Yoshikawa, and L.E. Cross, "The Effect of Compositional Variations in the Lead Lanthanum Zirconate Stannate Titanate System on Electrical Properties." *J. Amer. Ceram.* **79** (12), 3297-3304 (1996).
16. Park, S.-E., K. Markowski, S. Yoshikawa, and L.E. Cross, "The Effect of Barium and Strontium Additions in the Lead Lanthanum Zirconate Stannate Titanate System on Electrical Properties." *J. Amer. Ceram.* **80** (2), 407-412 (1997).

VOLUME II

17. Yoshikawa, S., K. Markowski, S.-E. Park, M.-J. Pan, and L.E. Cross, "Antiferroelectric-to-Ferroelectric Phase Switching Lead Lanthanum Zirconate Stannate Titanate (PLZST) Ceramics." *SPIE Proceedings IV* (1997).
18. Blue, C.T., J.C. Hicks, S.-E. Park, S. Yoshikawa, and L.E. Cross, "In-situ X-ray Diffraction Study of the Antiferroelectric-Ferroelectric Phase Transition in PLSnZT." *Applied Physics Letter* **68** (21), 2942-2944 (1996).
19. Pan, M.-J., S.-E. Park, K. Markowski, and S. Yoshikawa, "Antiferroelectric-to-Ferroelectric PLZST Ceramics-II: The Effect of Pre-Stress Conditions on the Strain Behavior." Submitted *Proceedings of IEEE International Symposium on the Applications of Ferroelectrics*, Rutgers University, East Brunswick, New Jersey (August 1996).
20. M.-J. Pan, Markowski, K., S.-E. Park, S. Yoshikawa, and L.E. Cross. "Antiferroelectric-to Ferroelectric PLZSnT Ceramics-I: Structure, Compositional Modification and Electric Properties." Submitted *Proceedings of IEEE International Symposium on the Applications of Ferroelectrics*, Rutgers University, East Brunswick, New Jersey (August 1996).

Materials Studies—continued

21. Lopath, P.D., K.K. Shung, S.-E. Park, and T.R. Shrout, "Ultrasonic Transducers Using Piezoelectric Single Crystals Perovskites." Submitted *Proceedings of IEEE International Symposium on the Applications of Ferroelectrics*, Rutgers University, East Brunswick, New Jersey (August 1996).
22. Park, S.-E. and T.R. Shrout, "Characteristics of Relaxor-Based Piezoelectric Single Crystals for Ultrasonic Transducers." Proceedings of 1996 IEEE Ultrasonics Symposium, San Antonio, Texas (November 1996).
23. Park, S.-E., P.D. Lopath, K.K. Shung, and T.R. Shrout, "Relaxor-Based Single Crystal Materials for Ultrasonic Transducer Applications." Proceedings on SPIE's International Symposium on Medical Imaging, Newport Beach, California (February 1997).
24. Lopath, P.D., S.-E. Park, K.K. Shung, and T.R. Shrout, " $\text{Pb}(\text{Zn}_{1/3}\text{Nb}_{2/3})\text{O}_3/\text{PbTiO}_3$ Single Crystal Piezoelectrics for Ultrasonic Transducers." Proceedings on SPIE's International Symposium on Medical Imaging, Newport Beach, California (February 1997).
25. Park, S.-E. and T.R. Shrout, "Relaxor Based Ferroelectric Single Crystals for Electro-Mechanical Actuators." *Innovations in Materials Research* (accepted).
26. Park, S.-E. and T.R. Shrout, "Characteristics of Relaxor-Based Piezoelectric Single Crystals for Ultrasonic Transducers," *IEEE Trans. on Ultrasonics, Ferroelectric and Frequency Control Special Issue on Ultrasonic Transducers* (to be published).
27. Jin, B., R. Guo, and A.S. Bhalla, "Piezoelectric Properties and Equivalent Circuits of Ferroelectric Relaxor Single Crystals."
28. Mulvihill, M.L., K. Uchino, Z. Li, and W. Cao, "In-situ Observation of the Domain Configurations during the Phase Transitions in Barium Titanate." *Phil. Mag. B.* **74** (1), 25-36 (1996).
29. Mulvihill, M.L., L.E. Cross, and K. Uchino, "Dynamic Motion of the Domain Configuration in Relaxor Ferroelectric Single Crystals as a Function of Temperature and Electric Field." *Ferroelectrics* **186**, 325-328 (1996).
30. Sundar, V. and R.E. Newnham, "Conversion Method Measurements of Electrostriction Coefficients in Low-K Dielectrics." *Mat. Res. Bull.* **31** (5), 545-554 (1996).
31. Sundar, V., J.-F., Li, D. Viehland, and R.E. Newnham, "Interferometric Evaluation of Electrostriction Coefficients." *Mat. Res. Bull.* **31** (5), 555-563 (1996).

Materials Studies—continued

32. Sundar, V., N. Kim, C. Randall, R. Yimnirun, and R.E. Newnham, "The Effect of Doping and Grain Size on Electrostriction in $\text{PbZr}_{0.52}\text{Ti}_{0.48}\text{O}_3$." Submitted *Proceedings of IEEE International Symposium on the Applications of Ferroelectrics*, Rutgers University, East Brunswick, New Jersey (August 1996).
33. Erdei, S., L. Galambos, I. Tanaka, L. Hesselik, F.W. Ainger, L.E. Cross, and R.S. Feigelson, "Segregation and Inhomogenities in Photorefractive SBN Fibers." *SPIE Proceedings V-Photorefractive Fiber and Crystal Devices: Materials, Optical Properties, and Applications II*, **2849**, 168-173 (1996).
34. Li, Shaoping, J.A. Eastman, J.M. Vertrone, R.E. Newnham, and L.E. Cross, "Coherent Coupling in Ferroelectric Superlattices." (1996).
35. Su, J., Q.M. Zhang, and R.Y. Ting, "Space Charge Enhanced Electromechanical Response in Thin Film Polyurethane Elastomers." *Applied Physics Letters* (submitted).
36. Zhang, Q.M., J. Su, and C.-H. Kim, "An Experimental Investigation of Electromechanical Responses in a Polyurethane Elastomer." *J. Appl. Phys.* **81** (6), 2770 (1997).

VOLUME III

37. Su, J., Q.M. Zhang, C.H. Kim, R.Y. Ting, and R. Capps, "Effects of Transitional Phenomena on the Electric Field Induced Strain-Electrostrictive Response of a Segmented Polyurethane Elastomer." *J. Appl. Polymer Sci.* (accepted).

Composite Sensors

38. Fernandez, J.F., A. Dogan, Q.M. Zhang, J.F. Tressler, and R.E. Newnham, "Hollow Piezoelectric Composites, Sensors and Actuators." *A: Physical* **51** (2,3), 183-192 (1996).
39. Fernandez, J.F., A. Dogan, Q.M. Zhang, and R.E. Newnham, "Piezoelectric Composites with Enclosed Hollow Spaces." *Proceedings 4th Euroceramics Conference, Electroceramics* **5**, 39-46 (1996).
40. Fernandez, J.F., A. Dogan, J.T. Fielding, K. Uchino, and R.E. Newnham, "Temperature Dependence of New Design Ceramic-Metal Piezocomposites Actuators." *Proceeding 4th Euroceramics Conference, Electroceramics* **5**, 133-138 (1996).

Composite Sensors—continued

41. Newnham, R.E., "Composite Sensors and Actuators," Disordered Materials, edited by G. Milton, K. Godlen, G. Grimmett, and P. Sen, Springer-Verlag, NY (accepted January 1997).
42. Tressler, J.F. and R.E. Newnham, "Doubly Resonant Cymbal Transducers, *IEEE Transactions of UFFC*, Special Issue on Transducers (accepted 1996).
43. Tressler, J.F., W. Cao, K. Uchino, and R.E. Newnham, "Ceramic Metal Composite Transducers for Underwater Acoustic Applications." Submitted *Proceedings of IEEE International Symposium on the Applications of Ferroelectrics*, Rutgers University, East Brunswick, New Jersey (August 1996).
44. Alkoy, S., A. Dogan, A.C. Hladky, J.K. Cochran, and R.E. Newnham, "Vibration Modes of PZT Hollow Sphere Transducers." Submitted *Proceedings of IEEE International Symposium on the Applications of Ferroelectrics*, Rutgers University, East Brunswick, New Jersey (August 1996).
45. Alkoy, S., A. Dogan, A.C. Hladky, and R.E. Newnham, "Miniature Piezoelectric Hollow Sphere Transducers (BBs)." 1996 Proceeding of IEEE International Frequency Control Symposium, pp. 586-594, Honolulu, Hawaii (1996).
46. Alkoy, S., A. Dogan, A.C. Hladky, and R.E. Newnham, "Piezoelectric Hollow Spheres." 1996 Proceeding 3rd Turkish Ceramic Society Meeting., Eds. V. Günay, H. Mandel, S. Ozgen. Istanbul, Turkey (October 1996).
47. Koc, B., A. Dogan, J.F. Fernandez, R.E. Newnham, and K. Uchino, "Accelerometer Application of the Modified Moonie (Cymbal) Transducer." *J. App. Phys.* **35**, 65-67 (1996).

VOLUME IV

48. Kumar, S., A. Bhalla, and L.E. Cross, "Underwater Acoustic Absorption by Collocated Smart Materials." *Ferroelectric Letters* **21**, 11-16 (1996).
49. Geng, X. and Q.M. Zhang, "Evaluation of Piezocomposites for Ultrasonic Transducer Applications—Influence of the Unit Cell Dimensions and the Properties of Constituents the Performance of 2-2 Piezocomposites." *IEEE Transactions of UFFC* (accepted).
50. Zhang, Q.M. and X. Geng, "Acoustic Properties of the Interface of a Uniform Medium-2-2 Piezocomposite and the Field Distributions in the Composite." *J. Appl. Phys.* (accepted).

Actuator Studies

51. Park, S.-E., and T.R. Shrout, "Ultrahigh Strain and Piezoelectric Behavior in Relaxor Based Ferroelectric Single Crystals."
52. Uchino, K. and S. Takahashi, "Multilayer Ceramic Actuators." *Current Opinion, Ceramic, Composites and Intergrowths*, p. 98-705 (1996).
53. Zheng, J., S. Takahashi, S. Yoshikawa, and K. Uchino, "Heat Generation in Multilayer Piezoelectric Actuators." *J. Amer. Ceram.* **79** (12), 3193-3198 (1996).
54. Dogan, A., J.F. Fernandez, K. Uchino, and R.E. Newnham, "New Piezoelectric Composite Actuator Designs for Displacement Amplification." *Proceeding Euroceramic Conference, Electroceramics* (5), 127-132 (1995) (in press).

VOLUME V

55. Poosanaas, P., A. Dogan., A.V. Prasadaraao, S. Komarneni, and K. Uchino, "Photostriction of Sol-Gel Processed PLZT Ceramics." *J. Electroceramics* (1996) (in press).
56. Uchino, K., "Reliability of Ceramic Actuators." Submitted *Proceedings of IEEE International Symposium on the Applications of Ferroelectrics*, Rutgers University, East Brunswick, New Jersey (August 1996).
57. Uchino, K., "High Electromechanical Coupling Piezoelectrics-How High Energy Conversion Rate is Possible?-. " *Proceeding MRS 1996* (1996) (in press).
58. Uchino, K., "Recent Developments in Ceramic Actuators-Comparison Among USA, Japan and Europe."
59. Xu, B., Q.M. Zhang, V.D. Kugel, Q. M. Wang, and L.E. Cross, "Optimization of Bimorph Based Double Amplifier Actuator under Quasistatic Situation." Submitted *Proceedings of IEEE International Symposium on the Applications of Ferroelectrics*, Rutgers University, East Brunswick, New Jersey (August 1996).
60. Kugel, V.D., S. Chandran, and L.E. Cross, "Caterpillar-Type Piezoelectric d_{33} Bimorph Transducer." *Appl. Phys. Lett.* **69** (14), 2021-2023 (1996).
61. Kugel, V.D., Q.M. Zhang, B. Xu, Q.-M. Wang, S. Chandran, and L.E. Cross, "Behavior of Piezoelectric Actuators under High Electric Field." Submitted *Proceedings of IEEE International Symposium on the Applications of Ferroelectrics*, Rutgers University, East Brunswick, New Jersey (August 1996).
62. Kugel, V.D., B. Xu, Q.M. Zhang, and L.E. Cross, "Bimorph-Based Piezoelectric Air Acoustic Transducer Model." *Sensors and Actuators A* (submitted 1996).

Actuator Studies—continued

63. Chandran, S., V.D. Kugel, and L.E. Cross, "CRESCENT: A Novel Piezoelectric Bending Actuator." *Proceeding SPIE's 4th Annual Symposium on Smart Structures* accepted 1997).
64. Kugel, V.D., S. Chandran, and L.E. Cross, "A Comparative Analysis of Piezoelectric Bending-Mode Actuators." Submitted *SPIE Proceedings*, Smart Structures and Materials: Smart Materials Technologies, 3040, 70-80 (1997).
65. Wang, Q.M., B. Xu, V.D. Kugel, and L.E. Cross, "Characteristics of Shear Mode Piezoelectric Actuators," Submitted *Proceedings of IEEE International Symposium on the Applications of Ferroelectrics*, Rutgers University, East Brunswick, New Jersey (August 1996).

Integration Studies

66. Elissalde, C., L.E. Cross, and C.A. Randall, "Structural-Property Relations in a Reduced and Internally Biased Oxide Wafer (RAINBOW) Actuator Material." *J. Amer. Ceram. 79* (8), 2041-2048 (1996).
67. Xu, B., Q.M. Zhang, V.D. Kugel, Q. Wang, and L.E. Cross, "Optimization of Bimorph Based Double Amplifier Transducer under Quasistatic Conditions." Submitted *Proceedings of IEEE International Symposium on the Applications of Ferroelectrics*, Rutgers University, East Brunswick, New Jersey (August 1996).
68. Xu, B., Q. M. Zhang, V.D. Kugel, and L.E. Cross, "Piezoelectric Air Transducer for Active Noise Control." *Proceeding SPIE, Smart Structures and Integrated Systems 271* (7), 388 (1996).

VOLUME VI

69. Chandran, S., V.D. Kugel, and L.E. Cross, "Characterization of the Linear and Non-Linear Dynamic Performance of RAINBOW Actuator." Submitted *Proceedings of IEEE International Symposium on the Applications of Ferroelectrics*, Rutgers University, East Brunswick, New Jersey (August 1996).
70. Wang, H., Q.M. Zhang, L.E. Cross, and C.M. Trottier, "Tailoring Material Properties by Structure Design—Radially Poled Piezoelectric Cylindrical Tube." *Ferroelectrics 173*, 181-189 (1995).

Processing Studies

71. Park, S.-E., M. Mulvihill, P.D. Lopath, M. Zippardo, and T.R. Shrout, "Crystal Growth and Ferroelectric Related Properties of (1-x) Pb (A_{1/3}Nb_{1/3})O₃ - xPbTiO₃(A=Zn²⁺, Mg²⁺).” Submitted *Proceedings of IEEE International Symposium on the Applications of Ferroelectrics*, Rutgers University, East Brunswick, New Jersey (August 1996).
72. Mulvihill, M., S.-E. Park, G. Risch, Z. Li, K. Uchino, and T.R. Shrout, "The Role of Processing Variables in the Flux Growth of PZN-PT Relaxor Ferroelectric Single Crystals." *Jpn. J. Appl. Phys.* **35** (Pt. 1; No. 7), 3984-3990 (1996).
73. Pan, M.-J., S.-E. Park, C.W. Park, K.A. Markowski, S. Yoshikawa, and C. Randall, "Superoxidation and Electrochemical Reactions during Switching in Pb(Zr,Ti)O₃ Ceramics." *J. Amer. Ceram.* **79** (11), 2971-2974 (1996).
74. Park, S.-E., M.L. Mulvihill, G. Risch, and T.R. Shrout, "The Effect of Growth Condition on Dielectric Properties of Pb(Zn_{1/3}Nb_{2/3})O₃ Crystal." *Jpn. J. Appl. Phys.* **36** (1) (1997).
75. Yoshikawa, Y. and K. Uchino, "Chemical Preparation of Lead-Containing Niobate Powders." *J. Amer. Ceram.* **79** (9), 2417-2421 (1996).
76. Ravindrathan, P., V. Srikanth, S. Komarneni, and A.S. Bhalla, "Processing of Pb(Zn_{1/3}Nb_{2/3})O₃: Ceramics at High Pressure." *Ferroelectrics* **188**, 135-141 (1996).
77. Ravindrathan, P., S. Komarneni, A.S. Bhalla, and R. Roy, "Low Temperature Chemical Routes to Smart Materials." *Ferroelectrics* **188**, 125-133 (1996).
78. Alberta, E.F. and A.S. Bhalla, "A Processing and Electrical Property Investigation of the Solid Solution: (x) Pb(In_{1/2}Nb_{1/2})O₃ - (1-x)Pb(Sc_{1/2}Ta_{1/2})O₃." *Ferroelectrics* **188**, 95-107 (1996).

Thin Film Ferroelectrics

79. Chen, H.D., K.R. Udayakumar, C.J. Gaskey, and L.E. Cross, "Fabrication and Electrical Properties of Lead Zirconate Titanate Thick Films." *J. Amer. Ceram. Soc.* **79** (8), 2189-2192 (1996).
80. Chen, H.D., K.K. Li, C.J. Gaskey, and L.E. Cross, "Thickness-Dependent Electrical Properties in Lanthanum-Doped PZT Thick Films." *Mat. Res. Soc. Symp. Proc.* **433**, 325-332 (1996).
81. Ravichandran, D., R. Meyer, Jr., R. Roy, R. Guo, A.S. Bhalla, and L.E. Cross, "Sol-Gel Synthesis of $\text{Ba}(\text{Mg}_{1/3}\text{Ta}_{2/3})\text{O}_3$; Phase Pure Powder and Thin Films." *Mat. Res. Bull.* **31** (7), 817-825 (1996).
82. Ravichandran, D., K. Yamakawa, R. Roy, A.S. Bhalla, S. Trolier-McKinstry, R. Guo, and L.E. Cross, "The Effect of Annealing Temperature on the Formation of $\text{SrBi}_2\text{Ta}_2\text{O}_9$ (SBT) Thin Films." Submitted *Proceedings of IEEE International Symposium on the Applications of Ferroelectrics*, Rutgers University, East Brunswick, New Jersey (August 1996).

Instrumentation

83. Su, J., P. Moses, and Q.M. Zhang, "A Bimorph Based Dilatometer for Field Induced Strain Measurement in Soft and Tin Free Standing Polymer Films." *Reviews of Scientific Instruments* (submitted).

COMPOSITE SENSORS

(continued)

APPENDIX 49

Evaluation of Piezocomposites for Ultrasonic Transducer Applications
---- Influence of the Unit Cell Dimensions and the Properties of Constituents on the
Performance of 2-2 Piezocomposites

X. Geng and Q. M. Zhang

Materials Research Laboratory and Department of Electrical Engineering
Penn State University, University Park, PA 16802

Abstract:

A theoretical model on piezoceramic polymer composites with laminar periodic structure is presented. A salient feature of this model is that it can treat explicitly how the unit cell dimensions and other material properties influence the performance of an ultrasonic transducer made of 2-2 piezocomposites. The model predicts that there exist a series of modes associated with the periodic structure of a composite, which is beyond the stop-band edge resonance prediction. One of the main concerns in designing a composite transducer is how the surface vibration profile changes with frequency and how this is influenced by the aspect ratio of the ceramic plate. It was predicted that as long as the thickness resonance is below the first lateral mode frequency, there is always a frequency f_1 , which is near the thickness resonance and at which the polymer and ceramic vibrate in unison. The effect of aspect ratio is to change the position of f_1 with respect to the thickness resonance frequency and the bandwidth in which polymer and ceramic have nearly the same vibration amplitude and phase. It is also predicted that when operated in a fluid medium such as water, there will be a resonance mode which has a frequency determined by the velocity of the fluid medium and the unit cell length d and is associated with the oscillation of the fluid. The behavior of a composite plate as an acoustic transmitter and receiver and the influence of the aspect ratio of the ceramic plate on them are also investigated.

I. Introduction

To produce a high performance ultrasonic transducer requires the transducer material, which performs the energy conversion between the mechanical form and electrical form, to have a high electromechanical coupling factor, broad operation frequency bandwidth, and adjustable acoustic impedance which can be tuned to match that of the medium. With single phase piezoelectric materials, it is difficult to simultaneously meet all the requirements. Piezoceramic polymer composite materials, which combine the high electromechanical activity of piezoceramics and the low acoustic impedance of polymeric materials, have provided new opportunities to meet these requirements.^{1,2} Since their inception in the seventies, the piezoceramic polymer composites have become one of the most important transducer materials and are being widely used in many areas such as medical imaging, nondestructive evaluation of materials, and underwater vision, etc.

Being a diphasic material, the properties of a piezo-composite can be tailored over a wide range by adjusting the material properties and geometric shapes of constituent phases.^{3,4} It has also been observed that the properties of a composite vary with frequency.⁵ The challenge of understanding the seemingly complex relationship between the performance of a composite and the properties of its constituents and the great opportunities provided by these materials have stimulated, in the past two decades, extensive investigations, both experimental and theoretical, on this class of materials.

The classic work of Newnham et al.,⁶ which classified piezocomposite materials according to the connectivity of the constituent phases, has greatly facilitated the analysis of the composites as the connectivity is one of the key parameters in determining the performance of a composite. For composites with 1-3 and 2-2 connectivities, both analytical and finite element modelings have been carried out which have provided useful guidelines in the design of composite transducers.⁷⁻¹³ The isostrain models developed by Smith et al.³ and Hashimoto et al.⁴ linked the material parameters of the constituents to the effective piezoelectric properties of 1-3 and 2-2 composites respectively and predicted that the thickness coupling factor k_t of a

composite can approach the longitudinal coupling factor k_{33}^l of the piezoceramic rod and k_{33}^w of the plate respectively, which is in good agreement with experiments for composites with a high aspect ratio t/d , where t is the thickness and d is the periodicity of the composites. Auld et al., using the Floquet theory, investigated wave propagations in both the 2-2 and 1-3 composites and showed that due to the periodic structure of these composites, there exist pass bands and stop bands, similar to the band structure in a crystal solid, and that there are piezoelectric resonances associated with the stop band edge resonances.⁷⁻¹⁰ For the design of composite transducers, the recognition of the existence of these modes and the precise prediction of their frequencies are of prime importance since quite often, it is the interference of these modes with the thickness mode of a composite that deteriorates the performance, especially at high frequency operations. Craciun et al. examined the coupling between these lateral modes and thickness mode using a phenomenological approach and the results provided qualitative understanding between the coupling of the two modes and the material properties.¹¹ The results from these investigations have played important roles in the development of ultrasonic composite transducers. However, due to the approximations used in the analysis, there are severe limitations. For instance, various features related to the dynamic behavior of a composite transducer were not treated in a consistent manner, and the effect of finite thickness of a composite on the material properties, that has been shown to be crucial in determining the performance of a piezocomposite, cannot be treated in these analyses. To address these realistic issues of a composite material, finite element analysis has been employed by many authors.¹²⁻¹⁵ For example, the dispersion curves have been evaluated for various modes in a composite and the dependence of the electromechanical coupling factor on the ceramic volume content and the ceramic rod shape was investigated.

For a piezoceramic polymer composite, it has to be recognized that it is the ceramic phase which performs the energy conversion between the electric and mechanical forms and the polymer phase merely acts as a carrier which transfers acoustic energy between the piezoceramic and the external medium. Hence, if the elastic coupling between the two

constituents is not very effective, even if the material exhibits a perfect acoustic impedance matching with the medium and the electromechanical coupling factor is large, the electromechanical performance of the material is still poor. These observations clearly indicate that in modeling piezoceramic polymer composites, one cannot simply use an effective medium approach and has to take into account explicitly this internal degree of freedom.

Recently, we developed an analytical model on the dynamic problem of a piezocomposite material with the 2-2 connectivity.¹⁶⁻¹⁸ In the model, we avoided the approximations made in the earlier works and hence, can address the dynamic responses of 2-2 piezocomposites, such as the frequencies of various modes, the mode coupling, the electromechanical coupling factor, the vibration profiles of composites under different external driving conditions, etc., in a realistic and consistent manner. For example, one of the misconceptions in the early studies of the dynamic behavior of piezocomposites is the direct linkage between the non-uniform surface vibration profile in a composite and the aspect ratio of the ceramic plate (in 2-2 composites) or rod (in 1-3 composites). Here, we will show, which was verified by experiment, that for a composite plate, as long as the thickness resonance frequency is below that of the lateral mode, there is always a frequency near the thickness resonance where the vibration profile of the composite is uniform. The influence of the aspect ratio is on the frequency bandwidth in which the polymer and ceramic vibrate in unison.

The approach taken here to solve the vibration problem in a finite thickness composite plate is based on the method of partial wave expansion where the various elastic and electric fields are expended in terms of the eigenmodes of the structure as shown in figure 1(a) and the coefficients for each eigen-mode are determined by the boundary conditions at $x_3 = t/2$ (figure 1(b)). Some of the results have been presented in early publications. In this paper, we would like to summarize briefly these early results and then, discuss many issues pertinent to the design of piezocomposite ultrasonic transducers based on the results from the model analysis. The paper is organized as the following: First, the details of derivation of the eigenfunctions for a 2-2 piezoceramic polymer composite will be presented. Based on the results, the wave

propagation in an unbounded 2-2 composite is analyzed. For the finite thickness composites, various features of a piezocomposite plate under an external driving electric field in both air and water media are treated. The response behavior of the composite plate under external pressure is also treated. Experiments were conducted to provide comparison with the theoretical results. From the results, we will show explicitly how the aspect ratio t/d influences the transduction performance of a composite plate.

II. General Solutions for Wave Propagation in a 2-2 Piezocomposite

Shown in figure 1(a) is a schematic drawing of a 2-2 composite (unbounded in the x_3 -direction), where plates of piezoceramic and polymer form a parallel array. The coordinate system is chosen such that the x_3 -axis is along the ceramic poling direction, the x_1 -axis is perpendicular to the ceramic polymer interface, and x_2 -axis is in the plane of the plates. For a typical 2-2 composite, the dimensions in the x_1 - and x_2 -directions are much larger than the period d and thickness t . In the treatment here, they can be taken as infinite without much error in the results. Under these conditions, the composite is clamped in the x_2 -direction so that $S_2=0$, where S_2 is the strain in the x_2 -direction, and the problem becomes a two dimensional one with no dependence on the x_2 -coordinate.

The governing equations for the dynamics of a 2-2 composite are¹⁹⁻²¹

$$\begin{aligned} \frac{\partial T_1}{\partial x_1} + \frac{\partial T_5}{\partial x_3} &= \rho \frac{\partial^2 u_1}{\partial t^2} \\ \frac{\partial T_5}{\partial x_1} + \frac{\partial T_3}{\partial x_3} &= \rho \frac{\partial^2 u_3}{\partial t^2} \\ \frac{\partial D_1}{\partial x_1} + \frac{\partial D_3}{\partial x_3} &= 0 \end{aligned} \quad (1)$$

The symbols adopted in this paper are summarized here: T_i and S_i are the stress and strain tensor components, where the Voigt notation is used, u_i is the elastic displacement vector, ρ is the density, and D_i is the electric displacement vector, E_i is the electric field. The relevant

material coefficients are: e_{ij} is the piezoelectric coefficient, c_{ij} is the elastic stiffness, and ϵ_i is the dielectric permittivity. Equation (1) holds for both the polymer and ceramic phases.

The constitutive equations, relating stress T, strain S, electric displacement D, and electric field E, are

$$[T] = [c^E][S] - [e_s][E] \quad (2a)$$

$$[D] = [e][S] + [\epsilon^S][E] \quad (2b)$$

For the polymer phase, e_{ki} in the equation (2) are zero. The superscripts E and S indicate that the coefficients are under the constant E field and constant strain conditions, respectively. Here $[e_s]$ is the transposed $[e]$ array. Under the quasi-electrostatic approximation, the electric field E can be expressed as

$$\bar{E} = -\nabla\Phi \quad (3)$$

where Φ is the electrical potential.

Combining eqs: (1), (2), and (3) yields three second order differential equations, governing the elastic displacement u_1 , u_3 , and electric potential Φ in the ceramic plate, respectively:

$$\begin{aligned} c_{44}^E u_{3,11} + (c_{13}^E + c_{44}^E) u_{1,13} + c_{33}^E u_{3,33} + (e_{33}\Phi_{,33} + e_{15}\Phi_{,11}) &= \rho \ddot{u}_3 \\ c_{11}^E u_{1,11} + (c_{13}^E + c_{44}^E) u_{3,13} + c_{44}^E u_{1,33} + (e_{31} + e_{15})\Phi_{,13} &= \rho \ddot{u}_1 \\ e_{15}u_{3,11} + (e_{15} + e_{31})u_{1,13} + e_{33}u_{3,33} - (\epsilon_{33}^S\Phi_{,33} + \epsilon_{11}^S\Phi_{,11}) &= 0 \end{aligned} \quad (4)$$

For the polymer phase, e_{ij} in eq. (4) should be taken to zero.

For an unbounded composite, the solutions to eq. (4) have the form

$$\begin{aligned} u_3 &= A \exp(j(hx_1 + \beta x_3 - \omega t)) \\ u_1 &= B \exp(j(hx_1 + \beta x_3 - \omega t)) \\ \Phi &= C \exp(j(hx_1 + \beta x_3 - \omega t)) \end{aligned} \quad (5)$$

where A, B, and C are three constants, ω is the angular frequency, h and β are the wave vector components in the x_1 - and x_3 - directions, respectively.

Substituting eq. (5) into (4) yields three homogeneous equations with the undetermined constants A, B, and C,

$$[M_{ij}]A_i = 0 \quad (6)$$

where $[A_i] = [A, B, C]^T$ and

$$[M_{ij}] = \begin{pmatrix} c_{33}^E \beta^2 + c_{44}^E h^2 - \rho \omega^2 & (c_{13}^E + c_{44}^E) h \beta & e_{33} \beta^2 + e_{15} h^2 \\ (c_{13}^E + c_{44}^E) h \beta & c_{11}^E h^2 + c_{44}^E \beta^2 - \rho \omega^2 & (e_{15} + e_{31}) h \beta \\ e_{33} \beta^2 + e_{15} h^2 & (e_{15} + e_{31}) h \beta & -(e_{11}^S h^2 + e_{33}^S \beta^2) \end{pmatrix} \quad (7)$$

The condition for a nontrivial solutions is such that the determinant of the coefficient matrix vanishes, i.e.,

$$|M_{ij}| = 0 \quad (8)$$

Equation (8) is a cubic equation of h^2 . For a given ω and β , eq. (8), in general, has three roots of h^2 , denoted as h_1^c , h_2^c and h_3^c , corresponding to the quasi-electromagnetic, quasi-longitudinal, and quasi-shear waves in the piezoelectric plate, respectively. For each h_i^c , the ratio among A, B, and C can be determined from eq. (6). Since we are concerned only with the waves in the x_3 direction which correspond to piezo-active modes in a finite thickness composite plate, the general solutions become

$$\begin{aligned} u_3^c &= \sum_i R_i^c f_i^c \cos(h_i^c x_1) \sin(\beta x_3) \\ u_1^c &= \sum_i R_i^c g_i^c \sin(h_i^c x_1) \cos(\beta x_3) \\ \Phi^c &= \sum_i R_i^c t_i^c \cos(h_i^c x_1) \sin(\beta x_3) \end{aligned} \quad (9)$$

where i runs from 1 to 3. f_i , g_i and t_i are the cofactors of $A_{k1}(i)$, $A_{k2}(i)$, and $A_{k3}(i)$ of the determinant (8) (where h is replaced by h_i^c for $i=1, 2$, and 3 , respectively). The $\exp(-j\omega t)$ term in eq. (9) is omitted.

Following the similar procedure, the solutions for the polymer phase can be obtained (the center of the polymer plate is at $x_1 = d/2$)

$$\begin{aligned} u_3^P &= \sum_i R_i^P f_i^P \cos(h_i^P(x_1 - \frac{d}{2})) \sin(\beta x_3) \\ u_1^P &= \sum_i R_i^P g_i^P \sin(h_i^P(x_1 - \frac{d}{2})) \cos(\beta x_3) \\ \Phi^P &= C^P \cosh(\beta(x_1 - \frac{d}{2})) \sin(\beta x_3) \end{aligned} \quad (10)$$

where $i = 1, 2$. f_i^P and g_i^P are the cofactors of $A_{k1}(i)$, $A_{k2}(i)$ of the determinant (8) with all the material parameters replaced by those of the polymer phase, and

$$(h_1^P)^2 = (k_L^P)^2 - \beta^2 \text{ and } (h_2^P)^2 = (k_T^P)^2 - \beta^2$$

where $k_L^P = \frac{\omega}{v_L^P}$, $k_T^P = \frac{\omega}{v_T^P}$, v_L^P and v_T^P are the longitudinal and shear wave velocities of the polymer phase, respectively.

The expressions of the stresses and the electric displacement in the ceramic plate can be obtained by substituting eq. (9) into eq. (2):

$$\begin{aligned} T_1^C &= \sum_i T_{11}^C(i) R_i^C \cos(h_i^C x_1) \cos(\beta x_3) \\ T_3^C &= \sum_i T_{33}^C(i) R_i^C \cos(h_i^C x_1) \cos(\beta x_3) \\ T_s^C &= \sum_i T_{31}^C(i) R_i^C \sin(h_i^C x_1) \sin(\beta x_3) \end{aligned} \quad (11)$$

where

$$\begin{aligned} T_{11}^C(i) &= c_{11}^E h_i^C g_i^C + (c_{13}^E f_i^C + e_{31} t_i^C) \beta \\ T_{33}^C(i) &= c_{13}^E h_i^C g_i^C + (c_{33}^E f_i^C + e_{33} t_i^C) \beta \\ T_{31}^C(i) &= -c_{44}^E (\beta g_i^C + h_i^C f_i^C) - e_{15} h_i^C t_i^C \end{aligned} \quad (12)$$

where $i = 1, 2, 3$ for ceramic phase. The electric displacements are:

$$D_1^C = \sum_i D_1^C(i) R_i^C \sin(h_i^C x_1) \sin(\beta x_3) \quad (13a)$$

$$D_3^C = \sum_i D_3^C(i) R_i^C \cos(h_i^C x_1) \cos(\beta x_3) \quad (13b)$$

where $D_1^C(i) = -e_{15}(\beta g_i^C + h_i^C f_i^C) + \epsilon_{11}^S h_i^C t_i^C$ and $D_3^C(i) = e_{31} h_i^C g_i^C + e_{33} \beta f_i^C - \epsilon_{33}^C \beta t_i^C$. Similar expressions can be obtained for the polymer plate. For instance, the electric displacements are:

$$D_1^P = -\epsilon_{11}^P \beta C^P \sinh(\beta(x_1 - \frac{d}{2})) \sin(\beta x_3) \quad (14c)$$

$$D_3^P = -\epsilon_{11}^P \beta C^P \cosh(\beta(x_1 - \frac{d}{2})) \cos(\beta x_3) \quad (14d)$$

Making use of the boundary conditions at the ceramic-polymer interface ($x_1 = vd/2$, where v is the volume fraction of the ceramic in a composite), which are

$$u_1^C = u_1^P, \quad u_3^C = u_3^P, \quad T_1^C = T_1^P \quad \text{and} \quad T_3^C = T_3^P \quad (15a)$$

$$\text{and } \Phi^C = \Phi^P \quad \text{and} \quad D_1^C = D_1^P \quad (15b)$$

R_i^C , R_j^P and C^P ($i=1, 2, 3$ and $j=1, 2$) can be determined. Expanding Eqs. (15) in terms of eqs. (9), (10), (11), (13) and (14) yields the following six homogeneous linear equations:

$$\begin{pmatrix} K_{11} & K_{12} & K_{13} & K_{14} & K_{15} & 0 \\ K_{21} & K_{22} & K_{23} & K_{24} & K_{25} & 0 \\ K_{31} & K_{32} & K_{33} & K_{34} & K_{35} & 0 \\ K_{41} & K_{42} & K_{43} & K_{44} & K_{45} & 0 \\ 0 & 0 & K_{53} & K_{54} & K_{55} & K_{56} \\ 0 & 0 & K_{63} & K_{64} & K_{65} & K_{66} \end{pmatrix} \begin{pmatrix} R_1^P \\ R_2^P \\ R_1^C \\ R_2^C \\ R_3^C \\ C^P \end{pmatrix} = 0 \quad (16)$$

where the matrix elements K_{ij} are functions of β , ω , d , v , and the material parameters of both the polymer and piezoceramic. The condition that the determinant

$$|K_{ij}| = 0 \quad (17)$$

yields the relationship between ω and β , the dispersion relations in the composite. For each pair of ω and β , the relationships among R_i^C , R_j^P and C^P can be obtained. Hence, the various stress, strain, electric field distributions in the composite can be determined.

III. Dispersion Curves, Modes and Modes Coupling of a 2-2 Piezocomposite

Eq. (17) allows us to determine the relationship between β and ω , the dispersion curves, for a composite if the materials parameters of piezoceramic and polymer and the geometric parameters, such as d and v , are known. Eq. (17) is a transcendental function which cannot be solved analytically. A computer code was developed and the dispersion curves were evaluated numerically.

Shown in figure 2 (the solid curves) are the two lowest branches of the dispersion curves for a 2-2 composite made of PZT-5H piezoceramic and Spurr epoxy with the ceramic volume fraction of 44%.²² For all the composites discussed in this paper, except otherwise specified, PZT-5H piezoceramic and Spurr epoxy are used as the constituents. The parameters of PZT-5H and Spurr epoxy are presented in Table I. The general trend of the dispersion curves in figure 2 resembles that of the symmetric Lamb waves in a plate.¹⁹ As will be shown later, at small βd limit, the first branch corresponds to the longitudinal wave propagation along the x_3 -direction, that is, u_3 is the dominant displacement which is more or less uniform and in phase in the x_1 -direction, and its phase velocity is the effective longitudinal wave velocity of the composite. The second branch corresponds to the lateral resonance which arises from the periodic structure of the composite, that is, it is a stationary shear wave along the x_1 -direction, and it can be shown that the displacement u_3 of the polymer phase is much larger than that of the ceramic phase and the phase difference between them is 180°. Hence, it is the so called stop-band edge resonance as predicted by Auld et al.^{7,8}

Under the assumption that the wave length λ in the x_3 -direction ($\beta = 2\pi/\lambda$) is equal to two times the composite thickness t (the condition for the thickness resonance), the theoretical dispersion curves can be compared with the experimental results, obtained from composites with different thickness. At low βd on the dispersion curves, where d is the period of the composite, the frequency of the fundamental thickness mode from the experiment falls on the first branch as marked by the black dots, and the frequency of the first lateral mode falls on the second branch as marked by the open circles. After the crossover region B, the modes interchange the positions on the dispersion curves where the thickness mode is in the second branch while there is a weak resonance at a frequency below the thickness mode and it falls on the first branch. Here, the thickness mode is defined as the one with higher electromechanical coupling factor. The mode on the first branch gradually diminishes at high βd values. The result is presented in figure 2. Clearly, there is an excellent accord between the theoretically derived resonance frequencies and experimentally observed ones.

Shown in figures 3(a) and figure 3(b) are the 3-dimensional dispersion curves for 2-2 composites with 15% and 44% ceramic volume fraction, respectively. Obviously, there are imaginary and complex branches of the dispersion curves. The modes on these branches are non-propagating modes (imaginary branches) and attenuated modes (complex branches), respectively. These modes do not exist in an unbounded composite, however, they are important in the vibration problems of finite thickness plates as well as in semi-infinite mediums, where they correspond to the evanescent waves at the surface which will be discussed later in the paper.

Figure 4 presents the effect of the stiffness of the polymer phase on the dispersion curves of a 2-2 composite with 30% ceramic content where PZT-5H is used as the piezoceramic phase. It is apparent that the frequency position of the second branch is very sensitive to properties of the polymer phase. This is quite understandable since as will be shown later, the frequency position of this branch is directly related to the shear velocity of the polymer matrix for

composites at this ceramic content. The lower the shear wave velocity of the polymer phase is, the lower the frequency of the second branch will be. Therefore, for a transducer operated at high frequencies, in order to avoid the interference from the lateral modes, a polymer matrix with a high shear velocity should be utilized even though the thickness coupling factor k_t of this composite may be reduced as a result of the stiffer polymer matrix.^{3,4}

In order to further elucidate the origins of these resonant modes, it is instructive to make a comparison between the dispersion curves of a composite and those of single piezoceramic and polymer plates with appropriate boundary conditions.²³ In general, in piezoceramic polymer composites, the elastic stiffness of the piezoceramic is more than one order of magnitude higher than that of the polymer. It is reasonable to assume that the piezoceramic plates in a 2-2 composite are stress free at the ceramic-polymer interface, that is, the stress components T_1 and T_3 are zero at the interface. Similarly, the polymer plates can be approximated as under the fixed boundary conditions, that is, u_1 and u_3 are zero at the interface. Under these assumptions, the dispersion curves of both single ceramic and single polymer plates are calculated for the plates with different widths corresponding to 2-2 composites with different ceramic volume fractions. The results are presented in figures 5(a), 5(b), and 5(c) corresponding to 2-2 composites with 15%, 44% and 80% ceramic content, respectively. In these figures, the solid lines are the dispersion curves of the 2-2 composites, the dashed lines are those of the ceramic plate, and dotted lines are the dispersion curves of the polymer plate.

The results from these figures reveal that there are many resemblance between the dispersion curves of 2-2 composites and the dispersion curves of the single ceramic and single polymer plates with appropriate boundary conditions. For instance, at small βd , the first branch in the dispersion curves of the 2-2 composites with 44% and 80% ceramic volume content is very close to the first branch of the ceramic plate. On the other hand, for 2-2 composites with low ceramic volume content, a large difference between these two is found for the first branch. These results are consistent with those from Smith et al. and from Hashimoto et al. based on an effective medium model.^{3,4} For the second branch which corresponds to the

lateral resonant mode in a composite plate, at low and medium ceramic volume content, it is close to the first branch of the polymer plate which frequency at small βd is equal to $V_T^P / 2d_p$, where V_T^P and d_p are shear wave velocity and width of the polymer plate, respectively. However, for composites with high ceramic volume content such as the one shown here (80%), the second branch is related to the longitudinal resonance of the ceramic plate along the width (or x_1 -) direction while the shear resonance associated with the polymer plate lies on the third branch of the dispersion curves.

Obviously, the coupling between the two phases through the interface boundary conditions will influence the dispersion curves of the waves in the two phases. It is well known that the dispersion curves for the uncoupled waves are split at their crossover points when coupling is introduced.¹¹ Far from the crossover region, the coupled wave dispersion curves should nearly coincide with those of the uncoupled waves. If the coupling is very strong as for the 15% and 44% piezocomposites, the coupled waves exhibit large departure from the uncoupled curves in the crossover region, which is clearly shown in figure 5(a) and figure 5(b). While for the composite with 80% ceramic content, the coupling between the first and the second branches is through the coupling of P wave and SV wave in the ceramic plate where the interface does not have a significant effect on it.

IV. Vibration of a Finite Thickness Composite Plate under an Electric Field in Air

In the previous section, the properties of guided wave propagation in laminated 2-2 piezocomposites have been analyzed. In spite of the fact that many effective parameters of the material can be derived by this simple method, one key issue in the design of a composite transducer, i.e., the influence of the aspect ratio of the ceramic plates (or the unit cell) in a composite on the performance of the transducer cannot be addressed. In this section, we will treat the vibration problem of a finite thickness composite plate under an external driving electric field and situated in air. From the analysis, one can obtain detailed information on how

the surface vibration profile changes with frequency and its dependence on the aspect ratio of the ceramic plate (or the unit cell dimension), the possible resonant modes in a composite transducer, and the dependence of the electromechanical coupling factor on the aspect ratio of the ceramic plate, etc. We will also show that as long as the thickness resonance frequency is below the lateral mode frequency, the aspect ratio will not have a direct effect on the vibration uniformity of a composite near the thickness resonance. The influence is on the bandwidth in which the ceramic and polymer vibrate with nearly same amplitude and phase.

A composite plate with a thickness t is drawn schematically in figure 1(b). For the problem treated here, the two free surfaces of the composite plate are electroded with conducting material and an AC electric field of a frequency f is applied between the two electrodes.

It is well known that there exist no simple solutions for the vibration problem of a finite thickness plate such as the piezocomposite treated here. One of the most frequently used approximation methods is to expand the elastic and electric fields in a material in terms of the eigenfunctions in an unbounded one.²¹ Different techniques such as the variational technique and the method of least squares can be used to determine the expansion coefficients. For the composite plate treated here, we found that the variational technique is more appropriate in treating the boundary problem than the method of least squares because of the large difference in the vibration amplitudes between the two phases in the composite.

For the ceramic phase in the composite plate, the elastic displacements u_3 and u_1 , and the electric potential Φ are expended in terms of the eigenfunctions derived:

$$\begin{aligned} u_3^C &= \sum_{n=1}^m \sum_{i=1}^3 R_{ni}^C f_{ni}^C \cos(h_{ni}^C x_1) \sin(\beta_n x_3) A_n \\ u_1^C &= \sum_{n=1}^m \sum_{i=1}^3 R_{ni}^C g_{ni}^C \sin(h_{ni}^C x_1) \cos(\beta_n x_3) A_n + CR_0^C \sin(h_{01}^C x_1) \\ \Phi^C &= \sum_{n=1}^m \sum_{i=1}^3 R_{ni}^C t_{ni}^C \cos(h_{ni}^C x_1) \sin(\beta_n x_3) A_n + Cx_3 \end{aligned} \quad (18)$$

Similarly, for the polymer phase in the composite plate:

$$\begin{aligned}
u_3^P &= \sum_{n=1}^m \sum_{i=1}^2 R_{ni}^P f_{ni}^P \cos(h_{ni}^P(x_1 - \frac{d}{2})) \sin(\beta_n x_3) A_n \\
u_1^P &= \sum_{n=1}^m \sum_{i=1}^2 R_{ni}^P g_{ni}^P \sin(h_{ni}^P(x_1 - \frac{d}{2})) \cos(\beta_n x_3) A_n + C R_0^P \sin(h_{01}^P(x_1 - \frac{d}{2})) \\
\Phi^P &= \sum_{n=1}^m C_n^P \cosh(\beta_n(x_1 - \frac{d}{2})) \sin(\beta_n x_3) A_n + C x_3
\end{aligned} \tag{19}$$

where R_{n1}^C , R_{n2}^C , R_{n3}^C , R_{n1}^P , R_{n2}^P and C_n^P are determined in eq. (16), β_n , h_{ni}^C and h_{ni}^P are the wave vector components of the nth mode in the x_3 - and x_1 -directions where the superscripts c and p stand for the ceramic and polymer, respectively. h_{01}^C and h_{01}^P are related to the mode in

which β is equal to zero: $h_{01}^C = \sqrt{\frac{\rho^C}{c_{11}^E}} \omega$ and $h_{01}^P = \sqrt{\frac{\rho^P}{c_{11}^P}} \omega$. R_0^C and R_0^P are determined by eq.

(16) in which β is set to zero. The mode with $\beta=0$ is generated due to the fact that the velocity of the electromagnetic wave is much faster than that of the elastic waves and the composite plate is clamped in the x_3 -direction ($S_3 = 0$). A_n and C are the coefficients which will be determined by the boundary conditions which are traction free and $\Phi = \pm V/2$ (here $\exp(-j\omega t)$ is omitted) at $x_3 = \pm d/2$.

The stresses T_3 , T_5 and electric displacement D_3 are expressed as:

$$T_3^C = \sum_{n=1}^m \sum_{i=1}^3 T_{33}^C(n, i) \cos(h_{ni}^C x_1) \cos(\beta_n x_3) A_n + (e_{33} + T_0^C \cos(h_{01}^C x_1)) C \tag{20a}$$

$$T_5^C = \sum_{n=1}^m \sum_{i=1}^3 T_{13}^C(n, i) \sin(h_{ni}^C x_1) \sin(\beta_n x_3) A_n \tag{20b}$$

$$D_3^C = \sum_{n=1}^m \sum_{i=1}^3 D_3^C(n, i) \cos(h_{ni}^C x_1) \cos(\beta_n x_3) A_n + (-\varepsilon_{33}^S + D_0^C \cos(h_{01}^C x_1)) C \tag{20c}$$

$$T_3^P = \sum_{n=1}^m \sum_{i=1}^2 T_{33}^P(n, i) \cos(h_{ni}^P(x_1 - \frac{d}{2})) \cos(\beta_n x_3) A_n + T_0^P \cos(h_{01}^P(x_1 - \frac{d}{2})) C \tag{20d}$$

$$T_5^P = \sum_{n=1}^m \sum_{i=1}^2 T_{13}^P(n,i) \sin(h_{ni}^P(x_1 - \frac{d}{2})) \sin(\beta_n x_3) A_n \quad (20e)$$

$$D_3^P = \sum_{n=1}^m \sum_{i=1}^2 D_3^P(n,i) \cos(h_{ni}^P(x_1 - \frac{d}{2})) \cos(\beta_n x_3) A_n - \epsilon_{11}^P C \quad (20f)$$

Where $T_{33}^C(n,i)$, $T_{13}^C(n,i)$, $D_3^C(n,i)$, $T_{33}^P(n,i)$, $T_{13}^P(n,i)$ and $D_3^P(n,i)$ are the same as $T_{33}^C(i)$, $T_{31}^C(i)$, $D_3^C(i)$, $T_{33}^P(i)$, $T_{31}^P(i)$, and $D_3^P(i)$ in equations (11) to (14) if the subscript i there is replaced by n and i for i-th partial wave of n-th mode here. And

$$T_0^C = c_{13}^E h_{01}^C R_0^C, T_0^P = c_{12}^P h_{01}^P R_0^P, D_0^C = e_{31} h_{01}^C R_0^C.$$

The number of the eigenfunctions, m, required in the expansion is determined by the accuracy needed for the solution. For the problem treated here, we found that it is adequate to use eight eigen-modes in the expansion. In the frequency range studied ($fd < 2 \text{ MHz} \cdot \text{mm}$), there are two branches having real β and the other branches having either imaginary or complex β , which corresponds to the modes confined at the surface of $x_3 = \pm t/2$.

For the problem treated here, all the stress components in air are zero and for the sake of simplicity, D in air is also assumed to be zero since the dielectric permittivity of the composite is much higher than air. Under these conditions, the variational formula takes the following form:

$$\int_V [(T_{k,t} - \rho \ddot{u}_t) \delta \dot{u}_t + D_{k,t} \delta \Phi^*] dV + \int_S [(-T_{k,t}) \delta \dot{u}_t + (\Phi - \bar{\Phi}) \delta D_k^*] dS = 0 \quad (21)$$

where the integration over time has been performed to take into account of the complex notations for the quantities in the integrands.^{19,21} The * represents the complex conjugate of the corresponding quantity. The first integral is over the volume of the 2-2 composite plate and it can be shown that it is equal to zero since all the quantities in the integrand satisfy eq. (1). The second integral is over the surfaces of the composite plate at $x_3 = \pm t/2$ where $\bar{\Phi} = \pm V/2$ at $x_3 = \pm t/2$ where V is the applied voltage. The periodic condition of the composite in the x_1 -direction and

the symmetric condition of the solutions and the boundary conditions about the plane of $x_3 = 0$ allow the second integration to be performed over one unit cell at $x_3 = t/2$.

Substituting T_3 , T_5 , u_1, u_3 , Φ and D_3 into equation (21) yields the following linear algebraic equation:

$$(M_{ij})(A_j) = (V_i) \quad (22)$$

where (M_{ij}) is a 9×9 matrix, $(A_j) = (A_1, A_2, A_3, A_4, A_5, A_6, A_7, A_8, C)^T$, (V_i) is a 9×1 matrix whose elements depend only on V , the applied voltage. For a given frequency f , one can solve eq. (22) to obtain A_j and C . From A_j and C , eqs. (18), (19), and (20) yield all the characteristic properties related to the vibration of a 2-2 composite plate with different thickness and different ceramic volume fraction such as the electrical impedance, surface displacement distribution, resonant modes, electromechanical coupling coefficient, etc.

For the composite plate treated here, the electrical impedance for a single repeating unit can be found from:

$$Z = \frac{V}{I} \quad (23)$$

where I is the current which is equal to $I = \frac{dQ}{dt} = -j\omega Q = -j2ab \int_0^t D_3 dx_1$, where Q and b are

the electric charge and the length in the x_2 -direction of the plate respectively. To compare with the experimental result, the current I should be multiplied by N , the number of repeating unit in a composite plate.

Shown in figure 6(a) is the electric impedance curve calculated from eqs. (22) and (23) for a composite plate with $t/d=4.5$ and the ceramic volume fraction $v=44\%$. The electric impedance measured experimentally from the same composite plate is shown in figure 6(b) and clearly the theoretical impedance curve reproduces the experimental data quite well. The difference in the sharpness of the resonant peaks between the experimental data and the theoretical curve is due

to the fact that in the theoretical analysis, the electrical and mechanical losses of the ceramic and polymer phases were not included.

In figure 6(c), the peak positions from the experimental data are compared with the dispersion curves for this composite which shows excellent agreement between the two. In order to elucidate the nature of these modes, the spatial distribution of u_3 at each mode at the composite surface is presented in figure 7 which are evaluated based on eqs. (18) and (19). Apparently, f_{L1} is the fundamental thickness resonance and f_{11} is the first lateral mode as revealed by the fact that the ceramic and polymer vibrate 180° out of phase at this mode, as predicted in the earlier theoretical work.^{7,8} The frequency position and the distribution of u_3 along the x_3 axis indicate that f_{L3} is the third harmonic of the thickness mode. However, the appearance of f_{12} is not expected from the earlier theoretical works in which the ceramic and polymer vibrate in phase. By examining the equations of the boundary conditions at $x_3 = \pm t/2$, it can be deduced that a resonance will occur whenever $\beta = (1+2n)\pi/t$, i.e., $\cos(\beta t/2) = 0$. Hence, the dispersion curves of real β , as shown in figure 6(c), reveal that the fundamental thickness resonance and the first lateral resonance occur at $\beta = \pi/t$ (f_{L1} and f_{11}). Similarly, when $\beta = 3\pi/t$, the third harmonic of the thickness mode will occur at f_{L3} . In addition, a mode f_{12} will also show up at the branch 1 which is at a frequency near and above f_{11} . By the same argument, it would be expected that f_{L5} , f_{13} , etc. may also be observed, depending on the electromechanical coupling factors of these modes. As shown later, the effective coupling factor for the modes in the first branch will decrease with increasing βd , i.e., reducing thickness, and on the other hand, the effective coupling factor for the modes in the second branch will increase with β . As the ratio of t/d decreases, the frequency of the thickness mode will gradually move towards the first lateral mode which will become stronger (coupling factor increases), and the second lateral mode (f_{12}) becomes weaker and finally it will disappear.

experimental observations on how various modes change with temperature (which causes reduction of the shear velocity of the polymer phase) and the composite thickness.⁵

Both the experimental results and the theoretical data indicate that the ceramic and polymer vibrate in phase for all the modes on the first branch and out of phase for modes on the second branch.

The electromechanical coupling factor for the thickness resonance can be evaluated based on the definition of IEEE:¹⁹

$$k_t^2 = \frac{\pi}{2} \frac{f_s}{f_p} \tan\left(\frac{\pi}{2} \frac{f_p - f_s}{f_p}\right) \quad (24)$$

where k_t is the thickness mode coupling factor, f_s and f_p are the series and parallel resonance frequencies, respectively. Eq. (24) is used here to calculate the coupling factor for the modes in both the first and second branches. Shown in figure 9 is the results for a 2-2 composite plate with 44% ceramic volume content for different d/t , where both theoretical and experimental results are presented. As the ratio of d/t increases, the coupling factor of the mode (thickness mode) in the first branch gradually decreases, while the coupling factor of the mode in the second branch gradually increases due to the modes coupling. As d/t is further increased, the thickness mode will jump to the second branch when the coupling factor in the second branch surpasses that of the first branch. Although in this region the coupling factor for the thickness mode can still be quite high, the distribution of the u_z is not uniform on the composite surface and the ceramic and polymer vibrate 180° out of phase which is not desirable since the polymer phase will not be able to perform properly the function of transferring the acoustic energy between the ceramic plates and the external medium.

For a composite plate to work effectively as an electromechanical transduction material, it is required that the ceramic and the polymer plates in the composite vibrate in phase with nearly the same amplitude in the x_3 -direction. The evolution of the vibration pattern in the two phases with frequency and the effect of the aspect ratio t/d of a composite plate on this distribution are

investigated. Shown in figure 10(a) is the variation of the ratio u_3^P/u_3^C at the surface of the composite plate, where u_3^P and u_3^C are u_3 at the centers of the polymer ($x_1=d/2$) and the ceramic plates ($x_1=0$), respectively, with frequency for the composite plate of $t/d=4$ where both the experimental results and theoretically calculated curve are presented. The experimental data were acquired using a laser dilatometer.²⁴ Hence, at frequencies far below any resonant mode, u_3^P/u_3^C is always less than one, which is true as long as the composite is driven electrically. For a given frequency, as t/d increases, this ratio increases and approaches one. These are consistent with the results of the earlier theoretical work on the static properties of composites.²⁵ As frequency increases, the ratio u_3^P/u_3^C increases towards one. At a frequency f_1 which is near f_s of the thickness mode, $u_3^P/u_3^C = 1$. This ratio will surpass one as the frequency is further increased. This is true as long as $f_{L1} < f_{11}$. In figure 10(b), the change of f_1/f_s vs. the ratio of d/t is presented. Clearly, f_1/f_s is close to but larger than one except for composite plates with a small aspect ratio. Hence, the aspect ratio t/d does not have a significant effect on the ratio of u_3^P/u_3^C at frequencies very near f_s of the thickness mode, where u_3^P/u_3^C is always near one if the thickness mode is below the first lateral mode frequency. However, it will affect the bandwidth in which u_3^P/u_3^C is near one. For example, the bandwidth $\Delta f/f_1$, where Δf is defined here as the frequency width in which $0.9 < u_3^P/u_3^C < 1.1$, increases as the ratio of d/t decreases, which is shown in figure 10(b). The experimental data points are also presented in figure 10(b) and the agreement between the two is quite good.

V. Forced Vibration of a Piezocomposite Plate in a Fluid Medium

Following a similar procedure as outlined in the preceding section, the vibration problem of a composite plate in a fluid medium can also be analyzed which are more relevant to the practical design and application of a composite transducer. The fluid medium chosen for the

study is water and two situations will be investigated: the composite plate as a transmitter, i.e., under a harmonic electric field, and the composite as a receiver, i.e., under a harmonic acoustic pressure in water.

(5.1) Forced Vibration of a Composite Plate in Water under an AC Electric Field

For the sake of convenience, we will treat the system as a symmetric one in which the composite plate is loaded by water on both surfaces, hence, the boundary conditions at the composite-water interface are:

$$T_3^{Cm} = T_3^W, \quad T_5^{Cm} = 0, \quad u_3^{Cm} = u_3^W \quad \text{and} \quad \Phi = \pm \frac{V}{2} \quad \text{at } x_3 = \pm \frac{t}{2} \quad (25)$$

where superscripts Cm and W denote the quantities in the composite and water, and the factor $e^{-j\omega t}$ is omitted in electric potential Φ . The variational formula for this problem can be derived

$$\text{as} \quad \int_{S^+} \frac{1}{2} \left[(T_3^W - T_3^{Cm})(\delta(u_3^W)^* + \delta(u_3^{Cm})^*) + (u_3^{Cm} - u_3^W)(\delta(T_3^W)^* + \delta(T_3^{Cm})^*) \right] dS \\ + \int_{S^+} [(\Phi^{Cm} - \bar{\Phi})\delta(D_3^{Cm})^* - T_5^{Cm}\delta(u_1^{Cm})^*] dS = 0 \quad (26)$$

where S^+ indicates that the integration is over the two composite-water interfaces (at $x_3 = \pm t/2$), and the factor $e^{-j\omega t}$ is omitted in electric potential Φ depending on the angular velocity ω and the integration over the volume has been omitted since it is equal to zero.

Here, the expressions for the elastic displacement vectors and the electrical potential Φ in the composite are those in eq. (18) and (19). Because of the periodic nature of the composite plate in the x_1 -direction, the solutions in water have the form:

$$u_1^W = j \sum_{n=0}^J h_n^W \sin(h_n^W x_1) \exp(\pm j\beta_n^W x_3) R_n^W \\ u_3^W = \sum_{n=0}^J \beta_n^W \cos(h_n^W x_1) \exp(\pm j\beta_n^W x_3) R_n^W \\ T_3^W = j T_0^W \sum_{n=0}^J \cos(h_n^W x_1) \exp(\pm j\beta_n^W x_3) R_n^W \quad (27)$$

where $h_n^w = \frac{2n\pi}{d}$, $\beta_n^w = \sqrt{\frac{\omega^2}{(V^w)^2} - (h_n^w)^2}$, $T_0^w = c^w(\beta_0^w)^2$, $\beta_0^w = \frac{\omega}{V^w}$, $V^w = \sqrt{\frac{c^w}{\rho^w}}$ is the longitudinal wave velocity of water, c^w is the bulk modulus of water. \pm correspond to the solutions in $x_3 > 0$ region and $x_3 < 0$ region, respectively. h and β are the wave vector components in the x_1 - and x_3 -directions in water. R_n^w is determined by the boundary conditions through the variational principle formula eq. (26).

Substituting equations (18), (19) and (27) into equation (26) yields a set of linear algebraic equations:

$$(M_{ij})(A_j) = (V_i) \quad (28)$$

where (M_{ij}) is a matrix in which its elements are related to the parameters of water, ceramic and polymer and the geometrical parameters v and d , as well as ω , β and h . $(A_j) = (A_1, \dots, A_m, C, R_0^w, \dots, R_J^w)$, where m and J are the numbers of the eigenfunctions used in the expansions for the quantities in the composite and in water, respectively, and how many eigenfunctions should be used in the expansion depends on the accuracy desired. In this calculation, $m=8$ and $J=6$. Hence, (V_i) is a 16×1 matrix which elements depend on the applied voltage V . Equation (28) is solved numerically.

Shown in figure 11(a) is a theoretical electrical impedance curve for a 2-2 composite plate of 44% ceramic volume content and the aspect ratio $t/d = 3.8$ loaded with water. For the comparison, the experimental curve for the same composite plate is shown in figure 11(b). The agreement between the experimental result and the theoretical one is quite good. The relatively sharp resonant peaks in the theoretical curve compared with the experimental one are due to the fact that in the theoretical calculation, the elastic and dielectric losses of the composite plate are not included. Comparison between figure 11 with figure 6, which is the electrical impedance for a similar composite plate in air, reveals that the resonance is severely damped in water as shown by the marked broadening of the resonant peaks in the impedance curve. For the lateral

modes (modes 1 and 2 in figure 11) which is mainly determined by the shear resonance of the polymer phase in the 2-2 composite investigated, because the acoustic impedance between the polymer and water is very close, the change in the amplitude is quite significant. One interesting feature of the influence of the water loading on a composite plate is the appearance of a mode which is labeled 3 in the figure. It can be shown that the resonant frequency for this mode does not change very much as the thickness of the composite plate changes. From the stress distribution pattern in the water, it is not difficult to show that this mode is related to the coupling between the composite and water and its frequency is determined by the periodicity d and the acoustic wave velocity of water ($f = V^w/d$). And it corresponds to the local oscillation of water within one unit cell.

In analogous to the situation in air, it is also found that in water, at frequencies far below any resonant mode, the ratio of u_3^P/u_3^C is always less than one and will approach one as the aspect ratio t/d increases. As the frequency increases towards the thickness resonant frequency, u_3^P/u_3^C increases towards one. At a frequency f_1 near the thickness resonant frequency f_s , this ratio becomes one and above that, this ratio is larger than one (figure 12(a)).

Figure 12(b) presents f_1/f_s and $\Delta f/f_1$ vs. the ratio of d/t for a composite with 44% ceramic content. Clearly, the effect of the aspect ratio t/d on the surface uniformity of a composite plate is to change the frequency position f_1 with respect to the thickness resonance and the frequency width Δf in which u_3^P/u_3^C is near one which are very similar to that found in air. However, the bandwidth $\Delta f/f_1$ in water is larger than that in air, indicating that the surface distribution of the displacement of the two phases is much flatter in water than in air which is quite understandable. Because of the water loading, the vibration amplitude of the polymer phase is significantly reduced. Figure 12(a) shows how the ratio of u_3^P/u_3^C at the composite surface varies with frequency ($t/d=4$). One noticeable change between the surface profiles in air and in

water is that in water, even at the lateral mode frequency, this ratio does not become very large (not shown in the figure since the lateral mode frequency is at about 1.5 MHz).

(5.2) Forced Vibration of a Composite Plate in Water under Harmonic Acoustic Pressure

Now we turn to investigate the vibration behavior of a composite plate in water under harmonic acoustic pressure, that is, to study issues related to the receiving sensitivity of a simple 2-2 composite transducer. For simplicity, we shall restrict the treatment to the symmetric system. In this case, as sketched in figure 13, the incident acoustic waves impinge normally on the two surfaces of the composite plate from opposite directions and the boundary conditions for this problem are:

$$T_3^{Cm} = T_3^W, \quad T_5^{Cm} = 0, \quad u_3^{Cm} = u_3^W \quad \text{and} \quad D_3^{Cm} = 0 \quad \text{at } x_3 = \pm \frac{t}{2} \quad (29)$$

The appropriate variational formula is

$$\begin{aligned} & \int_{S^*} \frac{1}{2} \left[(T_3^W - T_3^{Cm})(\delta(u_3^W)^* + \delta(u_3^{Cm})^*) + (u_3^{Cm} - u_3^W)(\delta(T_3^W)^* + \delta(T_3^{Cm})^*) \right] dS \\ & - \int_{S^*} [D_3^{Cm} \delta(\Phi^{Cm})^* + T_5^{Cm} \delta(u_1^{Cm})^*] dS = 0 \end{aligned} \quad (30)$$

The expressions of the displacements and electrical potential in the composite plate are those in equations (18) and (19) except now the mode of $\beta=0$ should not be included since there is no externally applied electric field. To account for the incident wave in water, equation (27) is modified and the solutions in the $x_3 > 0$ region are:

$$\begin{aligned} u_1^W &= j \sum_{n=0}^J h_n^W \sin(h_n^W x_1) \exp(j\beta_n^W x_3) R_n^W \\ u_3^W &= -\beta_0 \exp(-j\beta_0 x_3) + \sum_{n=0}^J \beta_n^W \cos(h_n^W x_1) \exp(j\beta_n^W x_3) R_n^W \\ T_3^W &= j T_0^W \left[\exp(-j\beta_0 x_3) + \sum_{n=0}^J \cos(h_n^W x_1) \exp(j\beta_n^W x_3) R_n^W \right] \end{aligned} \quad (31)$$

where the term of $-\beta_0 \exp(-j\beta_0 x_3)$ corresponds to the incident plane wave. By substituting equations (18), (19) and (31) into (30), we obtain a set of linear algebraic equations:

$$(M_{ij})(A_j) = (V_i) \quad (32)$$

where (M_{ij}) is a 15×15 matrix, $(A_j) = (A_1, \dots, A_m, R_0^W, \dots, R^W)$ with $m=8$ and $J=6$, and (V_i) is a 15×1 matrix related to the incident wave. By solving equation (32) one can obtain all of the properties related to the behaviors of a composite plate under a harmonic acoustic pressure.

Shown in figure 14 is the open circuit voltage receiving sensitivity V/p , where V is the voltage output and p is the pressure of the incident wave, for a 44% 2-2 composite plate at the thickness resonance vs. d/t for the thickness resonance mode where the cross over region (point B in figure 2) is at $d/t = 0.65$.²⁶ That is, at $d/t < 0.65$, the thickness mode is in the first branch of the dispersion curves and above that, the thickness resonance is at the second branch of the dispersion curves where the polymer and ceramic vibrate out of phase. Since the problems treated in this paper are related only to the piezo-materials, the open-circuit receiving sensitivity is used here which, as pointed out by Kojima, is a system independent parameter.²⁶ The bandwidth is defined as the 3dB width about the peak frequency (f_p for the receiving mode). For a single phase material, it can be derived from the KLM model that the sensitivity here should be proportional to t , the thickness of the transducer. Hence, in figure 14, the V/p vs. d/t curve for a single phase material should fall off as t (solid line in the figure) while the bandwidth should stay constant. The results show that the sensitivity of the thickness mode for a 2-2 composite decreases slowly as d/t becomes larger than 0.4, but the bandwidth increases gradually. The increase in the bandwidth is due to the merger of the two resonant modes in water. After that, there are anomalous changes in both the bandwidth and the sensitivity in the cross-over region. At higher values of d/t (thin composite plates), both the sensitivity and the bandwidth fall much below the values of single phase material (solid line). If we define the figure of merit (FOM) here as the product of sensitivity and bandwidth, as shown in figure 14(b), at $d/t < 0.5$, the FOM falls off with t . At $d/t > 0.5$, the FOM drops to

much smaller value. Therefore, in order to gain a high receiving sensitivity and a broad bandwidth of a 2-2 composite transducer, it is desirable to have d/t less than 0.5. The results here can be compared with what shown in figures 2, 8, 9, and 12. At d/t above 0.5, the coupling factor shows a precipitous drop (figure 9) and the thickness mode frequency also shows an apparent deviation from the extrapolated value (the dashed line in figure 2). Figure 8 also shows that there is a significant coupling between the two modes. Although the results presented are for a composite with 44% ceramic content, it is approximately true for composites with other volume fractions.

VI. Summary

The details of a theoretical model on piezoceramic polymer composites with laminar periodic structure are presented. The result shows that the various resonant modes in a composite structure can be traced back to the modes in either an isolated ceramic plate or polymer plate with appropriate boundary conditions (stress free for the ceramic plate and strain free for the polymer plate). It also shows that there exist a series of modes associated with the periodic structure of a composite, which is beyond the stop-band edge resonance prediction. One of the main concerns in designing a composite transducer is how the surface vibration profile changes with frequency and how this is influenced by the aspect ratio t/d . It was predicted and verified by experiment that as long as the thickness resonance is below the first lateral mode frequency, there is always a frequency f_1 , which is near the thickness resonance and at which the polymer and ceramic vibrate in unison. The effect of t/d is to change the position of f_1 with respect to the thickness resonance frequency and the bandwidth in which polymer and ceramic have nearly the same vibration amplitude and phase. It is also predicted that when operated in a fluid medium such as water, there will be a resonance mode whose frequency is determined by the velocity of the fluid medium and the unit cell length d and is associated with the oscillation of the fluid, causing the polymer and ceramic to vibrate 180° out of phase. The difference in the surface vibration profiles between in air and in water indicates

the need to characterize the vibration pattern of a composite in a fluid medium since it is much closer to the real application environment.

In general, the maximum transmitting voltage sensitivity of a transducer is at a frequency near f_s , and the maximum open circuit receiving sensitivity is near f_p of the thickness mode ($f_p > f_s$), and hence it is expected that the influence of the lateral mode (hence, the aspect ratio t/d) will be more severe on the receiving sensitivity. From the data analysis, it is shown that when an FOM which is the product of the sensitivity and the bandwidth is introduced as the criterion of the performance of a composite transducer as a receiver, the performance deteriorates when $d/t > 0.5$ for the composite discussed here. Experimental results confirm this finding where as shown in figure 15, the insertion loss of a 2-2 piezocomposite shows large increases at d/t near and above 0.5.

VII. Acknowledgment

The authors wish to thank Dr. J. Yuan and Dr. H. Kunkel of ATL/Echo ultrasound for stimulating discussions. This work was supported by the Office of Naval Research under the Grant No: N00014-96-0357.

Table I. The material properties of PZT-5H and Spurr epoxy used for the 2-2 composites in the investigation.

PZT-5H: $e_{33} = 23.09 \text{ C/m}^2$, $e_{31} = -6.603 \text{ C/m}^2$, $e_{15} = 17.0 \text{ C/m}^2$, $c_{11} = 12.72 \times 10^{10} \text{ N/m}^2$, $c_{44} = 2.3 \times 10^{10} \text{ N/m}^2$, $c_{33} = 11.74 \times 10^{10} \text{ N/m}^2$, $c_{13} = 8.47 \times 10^{10} \text{ N/m}^2$, $K_{11} = 1700$, $K_{33} = 1470$, $\rho = 7500 \text{ kg/m}^3$.

Spurr epoxy: $c_{11} = 5.4 \times 10^9 \text{ N/m}^2$, $c_{44} = 1.3 \times 10^9 \text{ N/m}^2$, $\rho = 1100 \text{ kg/m}^3$.

References:

1. W. A. Smith, "The application of 1-3 piezocomposites in acoustic transducers," Proc. 1990 IEEE ISAF7 (Urbana, Illinois 1990) pp. 145-152, 1990.
2. T. R. Gururaja, A. Safari, R. E. Newnham, and L. E. Cross, "Piezoelectric ceramic-polymer composites for transducer applications," in Electronic ceramics, ed. L. M. Levinson, pp. 92-128, Marcel Dekker, New York, 1987.
3. W. A. Smith and B. A. Auld, "Modeling 1-3 composite piezoelectrics: Thickness-mode oscillations," IEEE Trans. UFFC Vol. 38, pp. 40-47, 1988.
4. K. Y. Hashimoto and M. Yamaguchi, "Elastic, piezoelectric and dielectric properties of composite materials," Proc. 1986 IEEE Ultrasonics Symp. (Williamsburg, VA), pp. 697-702, 1986.
5. T. R. Gururaja, W. A. Schulze, L. E. Cross, R. E. Newnham, B. A. Auld, and J. Wang, "Piezoelectric Composite Materials for Ultrasonic Transducer Applications. Part I: Resonant Modes of Vibration of PZT-Rod-Polymer Composites," IEEE Trans. Sonics and Ultrasonics, Vol. SU 32, pp 481-498, 1985.
6. R. E. Newnham, D. P. Skinner, and L. E. Cross, "Connectivity and piezoelectric-pyroelectric composites," Mater. Res. Bull. Vol. 13, pp. 525-536, 1984.
7. B. A. Auld, H. Kunkel, Y. A. Shui, and Y. Wang, "Dynamic behavior of periodic piezoelectric composites," Proc. 1983 IEEE Ultrasonics Symp. (Atlanta, GA), pp. 554-558, 1983.
8. B. A. Auld, Y. A. Shui, and Y. Wang, "Elastic wave propagation in three-dimensional periodic composite materials," Journal de Physique, Vol. 45, pp. 159-163, 1984.
9. Y. Wang, E. Schmidt, and B. A. Auld, "Acoustic wave transmission through one-dimensional PZT-epoxy composites," Proc. 1986 IEEE Ultrasonics Symp. (Williamsburg, VA), pp. 685-689, 1986.
10. Y. Wang, "Waves and Vibrations in Elastic Superlattice Composites," Ph. D. Thesis, Stanford University, December 1986.

11. F. Craciun, L. Sorba, E. Molinari, and M Pappalardo, "A cooupled-mode theory for periodic piezoelectric composites," IEEE Trans. UFFC Vol. 36, pp. 50-56, 1989.
12. M. Yamaguchi, K. Y. Hashimoto, and H. Makita, "Finite element method analysis of dispersion characteristics for the 1-3 type piezoelectric composites," Proc. 1987 IEEE Ultrasonics Symp. (Denver, CO), pp. 657-661, 1987.
13. J. A. Hossack and G. Hayward, "Finite element analysis of 1-3 composite transducers," IEEE Trans. UFFC Vol. 38, pp. 618-629, 1991.
14. Anne-Christine, Hladky-Hennion, and Jean-Noel Decarpigny, "Finite element modeling of active periodic structures: Application to 1-3 piezocomposites," J. Acoust. Soc. Am., Vol. 94, pp. 621-635, 1993.
15. J. Sato, M. Kawabuchi, J. Fukumoto, "Dependence of Electromechanical Coupling Coefficient on the Width to the Thickness Ratio of Plate Shaped Piezoelectric Transducers Used in Electrically Scanned Ultrasonic Diagnostic Systems," J. Acous. Soc. Am., Vol. 66, pp 1609-1611, 1979.
16. Q. M. Zhang and X. Geng, "Dynamic modeling of piezoceramic polymer composite with 2-2 connectivity," J. Appl. Phys. Vol.76, pp. 6014-6016, 1994.
17. Y. A. Shui, X. Geng, and Q. M. Zhang, "Theoretical modeling of resonant modes of composite ultrasonic transducers," IEEE Trans. UFFC Vol.42, pp. 766-773, 1995.
18. X. Geng and Q. M. Zhang, "Dynamic Behavior of Periodic Piezoceramic-Polymer Composite Plates," Appl. Phys. Lett. Vol. 67, pp 3093-3095, 1995.
19. B. A. Auld, Acoustic Fields and Waves in Solid, John Wiley & Sons, N. Y., 1973.
20. IEEE Standard on Piezoelectricity (ANSI/IEEE Standard 176-1987,1988).
21. H. F. Tiersten, Linear Piezoelectric Plate Vibrations, Plenum, New York, 1969.
22. PZT-5H is the trade-mark of Morgan Mattroc Inc. (Beddford, OH 44146) for one of its PZT piezoceramics. Spurr epoxy is the trade-mark of Polysciences, Inc. (Warrington, PA 18976).

23. C. G. Oakley, "Geometric Effects on the Stopband Structures of 2-2 Piezoelectric Composite Plates," Proc. 1991 IEEE Ultrasonics Symp. pp. 657-661, 1991
24. Q. M. Zhang, S. J. Jang, and L. E. Cross, "High-frequency Strain Response in Ferroelectrics and Its Measurement Using a Modified Mach-Zehnder Interferometer," J. Appl. Phys. Vol. 65, 2807-2815, 1989.
25. Q. M. Zhang, W. Cao, J. Zhao, and L. E. Cross, "Piezoelectric performance of piezoceramic-polymer composites with 2-2 connectivity: A combined theoretical and experimental study," IEEE Trans. UFFC Vol. 41, pp. 556-562, 1994.
26. T. Kojima, "A New Method for Estimating the System-Independent Characteristics of an Ultrasonic Piezoelectric Transducer," 1981 IEEE Ultra Symp. pp. 649-654, 1981.

Figure captions:

Figure 1. (a) Schematic drawing of a 2-2 piezoceramic polymer composite which is unbounded in all three orthogonal directions. The period of the composite is d . (b) Schematic drawing of a 2-2 piezoceramic polymer composite plate with a thickness t situated in air. An external voltage is applied to the composite.

Figure 2. The first and second branches of the dispersion curves (solid lines) and the experimentally measured thickness mode (solid circles) and lateral mode (open circles) for a 2-2 composite made of PZT-5H and Spurr epoxy with 44% ceramic content. After the crossover region, the thickness mode jumps to the second branch. The criterion for the thickness mode is that it is the one with the larger effective coupling factor.

Figure 3. The dispersion curves for a 2-2 composite (figure 1(a))made of PZT-5H and Spurr epoxy for (a) 15% ceramic volume content and (b) 44% ceramic volume content.

Figure 4. The effect of the properties of the polymer matrix on the dispersion curves of 2-2 composites with PZT-5H ceramic, derived from the model. The properties of the polymer phase are: curve 1: $c_{11} = 7.72 \times 10^9 \text{ N/m}^2$, $c_{44} = 1.588 \times 10^9 \text{ N/m}^2$, $\rho = 1160 \text{ kg/m}^3$; curve 2: $c_{11} = 1.3634 \times 10^{10} \text{ N/m}^2$, $c_{44} = 3.432 \times 10^9 \text{ N/m}^2$, $\rho = 1610 \text{ kg/m}^3$; curve 3: $c_{11} = 3.173 \times 10^9 \text{ N/m}^2$, $c_{44} = 0.696 \times 10^9 \text{ N/m}^2$, $\rho = 1060 \text{ kg/m}^3$; curve 4: $c_{11} = 1.622 \times 10^9 \text{ N/m}^2$, $c_{44} = 1.646 \times 10^8 \text{ N/m}^2$, $\rho = 890 \text{ kg/m}^3$.

Figure 5. Comparison of the dispersion curves in 2-2 composites with those in a single piezoceramic plate and a polymer plate for composites with (a) 15% ceramic content; (b) 44% ceramic; and (c) 80% ceramic content. PZT-5H is used as the piezoceramic and Spurr epoxy as the polymer phase.

Figure 6. The electric impedance curve for a 2-2 composite plate with PZT-5H and Spurr epoxy (44% ceramic) measured in air: (a) the theoretical curve and (b) the experimental curve. The thickness t of the composite is $t/d = 4.5$ and $d=0.635 \text{ mm}$. f_{L1} and f_{L3} are the fundamental

and third harmonic of the thickness mode and t_1 and t_2 are the modes arose from the periodicity of the composite. (c) The dispersion curves elucidating the origin of the resonant modes f_{11} and f_{12} . In general, any modes on the dispersion curves will show up whenever $\beta d = (2n+1)/2$, $n=0,1,2, \dots$ is satisfied, where $\beta=2\pi/\lambda$ and $\lambda=2t$.

Figure 7. The distribution of the elastic displacement u_3 for f_{L1} , f_{L3} , f_{11} , and f_{12} of a 2-2 composite with $t/d=4$, where (a) and (b) are the distributions along the x_3 -direction when $x_1=0$ (at the center line of the ceramic plate, figure 1(b)), $x_3=0$ is at the center and $x_3=2$ is at the ceramic surface; (c) and (d) are surface vibration profiles at $x_3=2$, $x_1=0$ corresponds to the center of the ceramic plate and $x_1=0.5$ is at the center of the polymer plate.

Figure 8. The evolution of various modes in a 2-2 composite made of PZT-5H (44% ceramic) and Spurr epoxy with the thickness t of composite plate: (a) $t/d = 4$, (b) $t/d = 2$, and (c) $t/d = 1$. There is already substantial coupling between the thickness and lateral modes at $t/d = 2$ for this composite. At low t/d values (thin samples), the lateral mode will disappear.

Figure 9. The evolution of the coupling factor for the modes on the first and second branches of the dispersion curves with the composite thickness d/t for a composite made of PZT-5H and Spurr epoxy with 44% ceramic content.

Figure 10. (a) The ratio of u_3^P/u_3^C vs. frequency for a composite made of PZT-5H and Spurr epoxy (44% ceramic content) at a thickness of $t/d = 4$ ($d=0.635$ mm) measured in air. u_3^P and u_3^C are the surface displacements at the centers of the polymer plate and ceramic plate, respectively. The black dots are the experimental data measured using a laser dilatometer and the solid line is derived from the model.

(b) The ratio f_1/f_s as a function of the ratio d/t of the composite plate, where f_1 is the frequency at which $u_3^P/u_3^C=1$ and f_s is the series resonant frequency for the thickness mode. The black dots are experimental data and the solid lines are derived from the model calculation.

(c) The bandwidth as a function of the ratio d/t of the composite plate. The black dots are experimental data and the solid lines are derived from the model calculation.

Figure 11. The electrical impedance magnitude for a 2-2 composite of PZT-5H and Spurr epoxy with 44% ceramic content measured in water. The thickness of the composite is $t/d=3.8$ and $d=0.635$ mm. (a) is derived from the model and (b) is the experimental results. The modes 1 and 2 are the lateral modes (f_{11} and f_{12} in figure 6(c)) and mode 3 arises from the coupling of water to the periodic structure of the composite surface.

Figure 12. (a) The ratio of u_3^p/u_3^c vs. frequency for a composite made of PZT-5H and Spurr epoxy (44% ceramic content) at a thickness of $t/d = 4$ ($d=0.635$ mm) measured in water. u_3^p and u_3^c are the surface displacements at the centers of the polymer plate and ceramic plate, respectively. The results are derived from the model.

(b) The ratio f_1/f_s as a function of d/t of the composite plate, where f_1 is the frequency at which $u_3^p/u_3^c=1$ and f_s is the series resonant frequency for the thickness mode. The results are derived from the model.

(c) The bandwidth as a function of d/t of the composite plate. The results here can be compared with those in figure 10 and apparently, and the water loading improves the uniformity of the vibration profile at the composite surface. The results are derived from the model.

Figure 13. Schematic drawing of a 2-2 composite plate under normal incident of a pressure wave from the water.

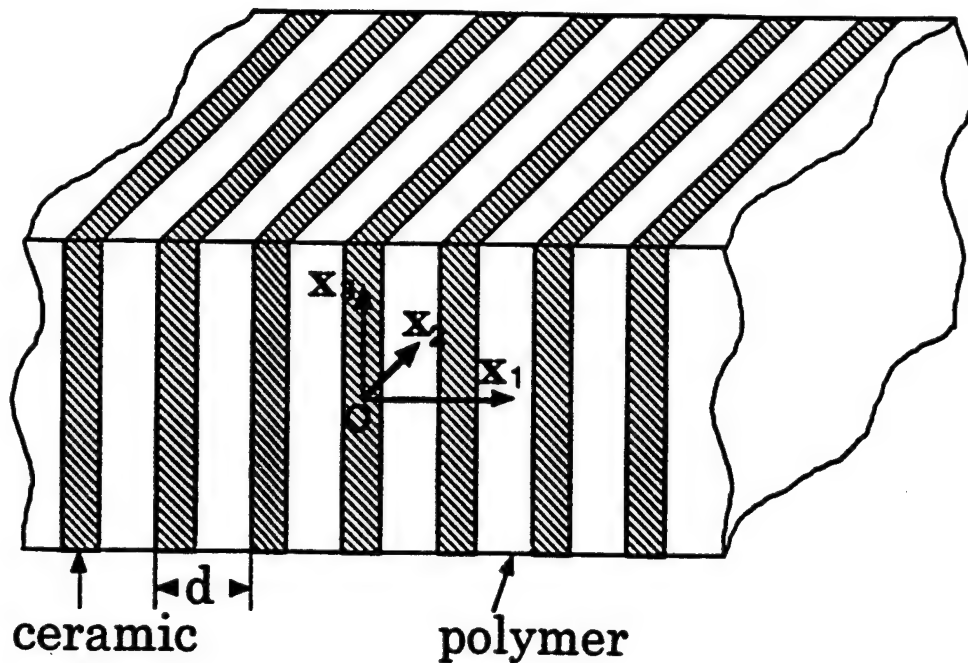
Figure 14. (a) The influence of the unit cell dimension ratio of d/t on the open circuit voltage sensitivity of a 2-2 composite with 44% PZT-5H and Spurr epoxy matrix. Solid dots are V/p at the peak frequency (f_p) and the solid line is the sensitivity of a single phase material with the effective properties of the composite. The results are derived from the model.

(b) The 3 dB bandwidth as a function of d/t for a composite transducer derived from the model.

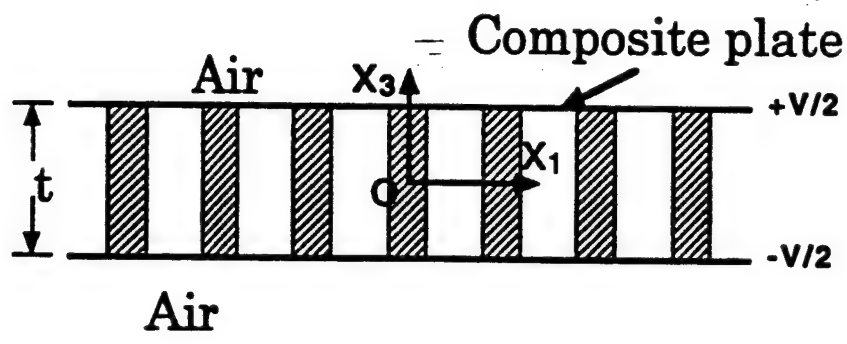
(c) FOM (solid dots, the product of the sensitivity and the bandwidth) for the 2-2 composite in (a) as a function of d/t . The solid line is FOM for a single phase material with the

effective properties of the composite. At $d/t > 0.5$, FOM drops much below the single phase material value. The results are derived from the model.

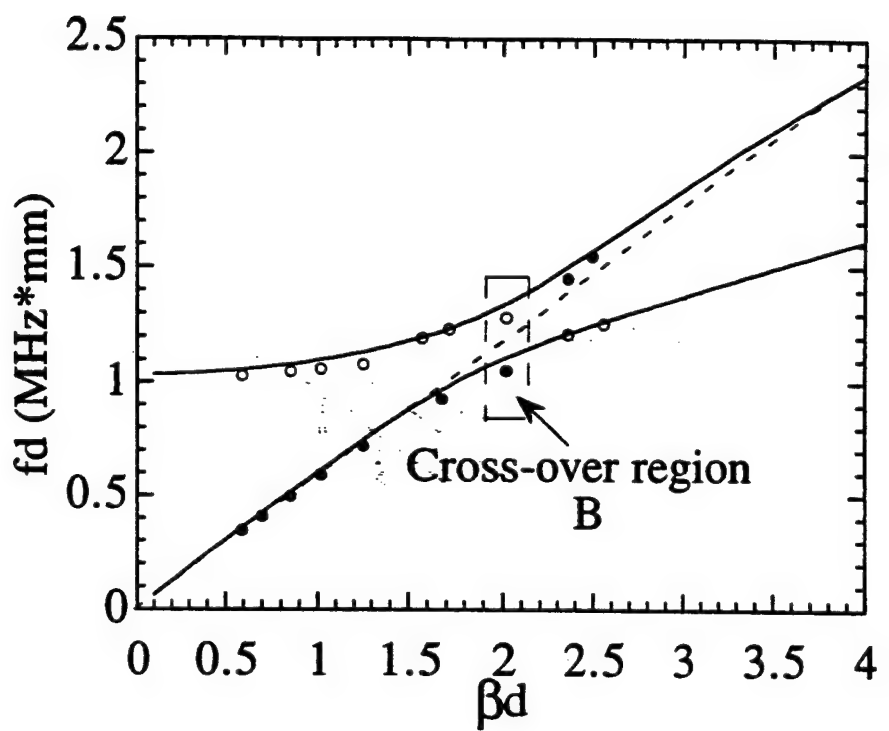
Figure 15. The experimental data on the insertion loss (open circles) and 6 dB bandwidth (solid dots) of 2-2 composites with 44% volume content of PZT-5H and Spurr epoxy polymer matrix measured by the pulse echo method for different ratio of d/t ($d=0.635$ mm). The solid lines are drawn to guide eyes.

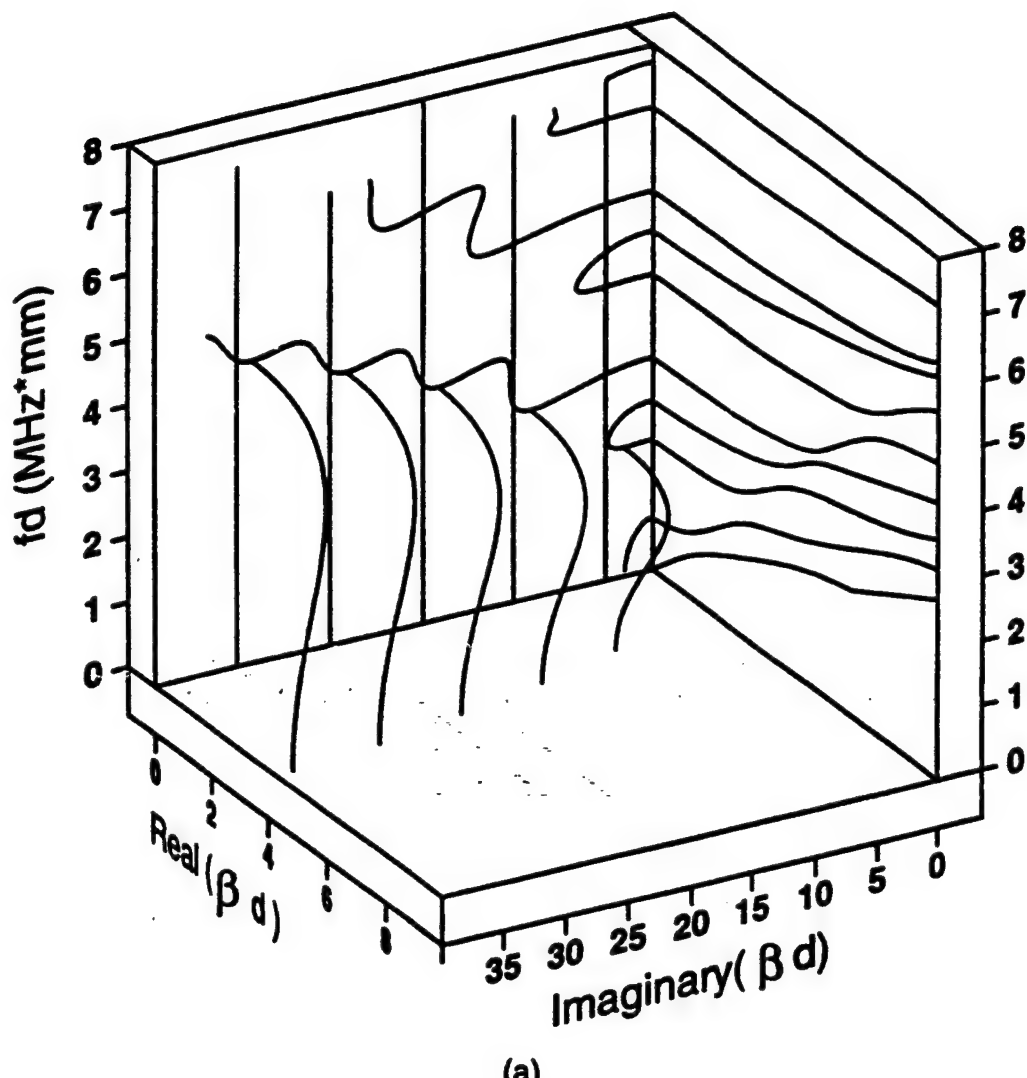


(a)

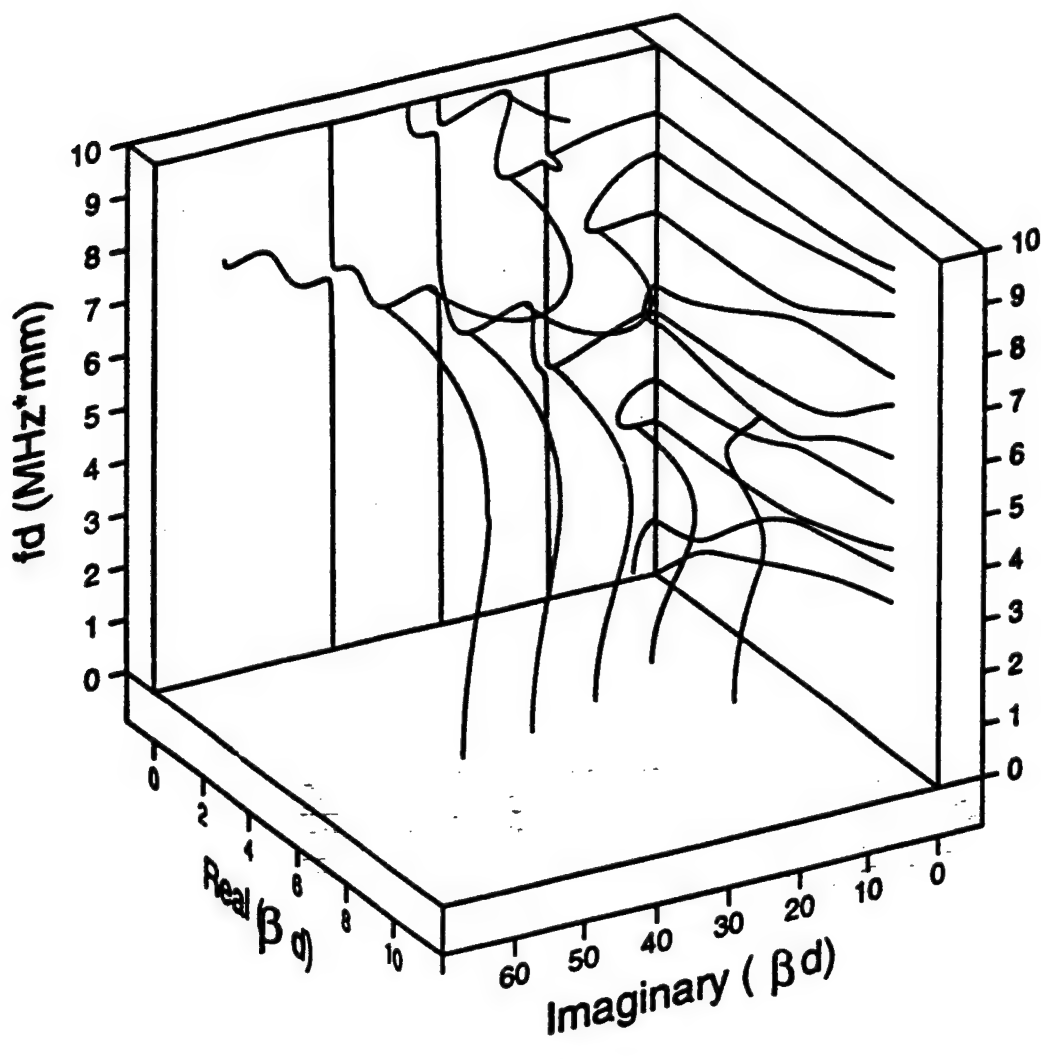


(b)



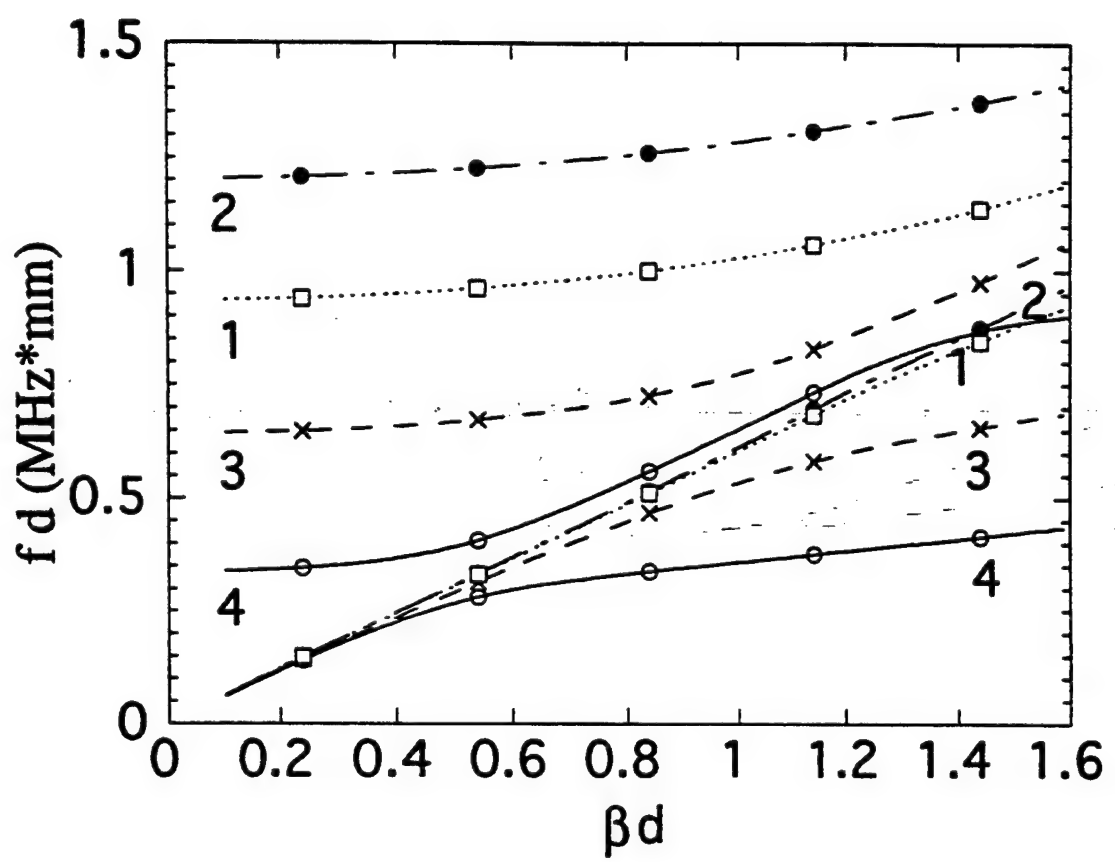


F 3(a)

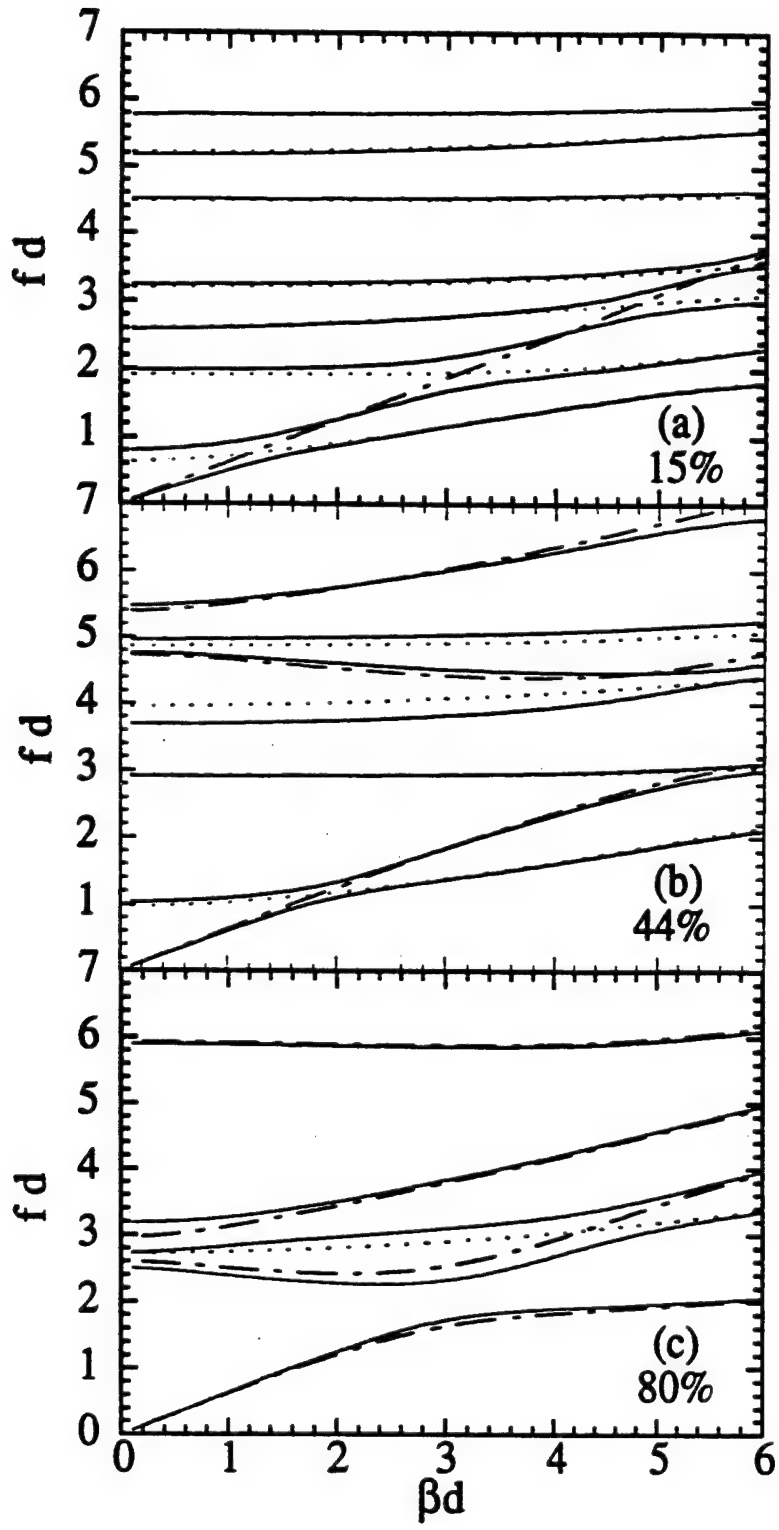


(b)

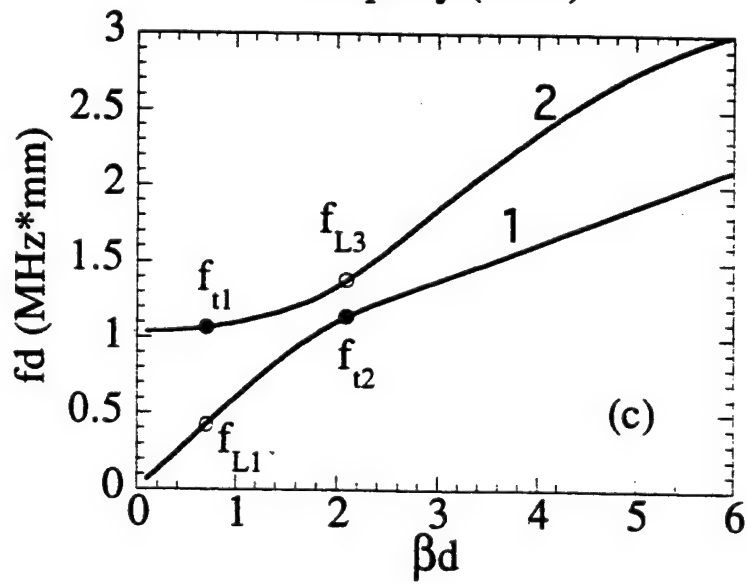
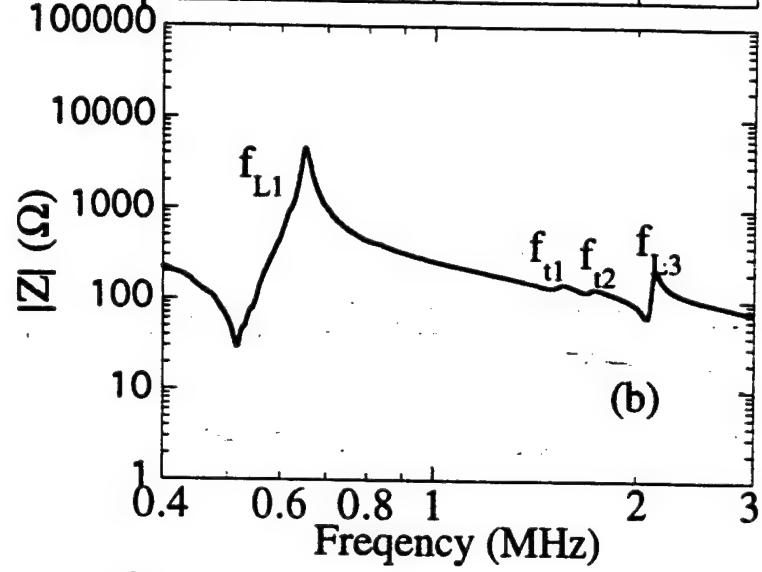
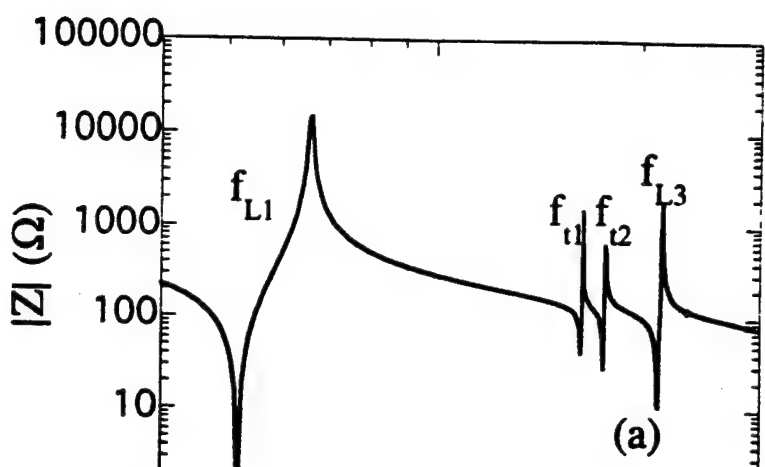
F 3(b)



F. 4



F.



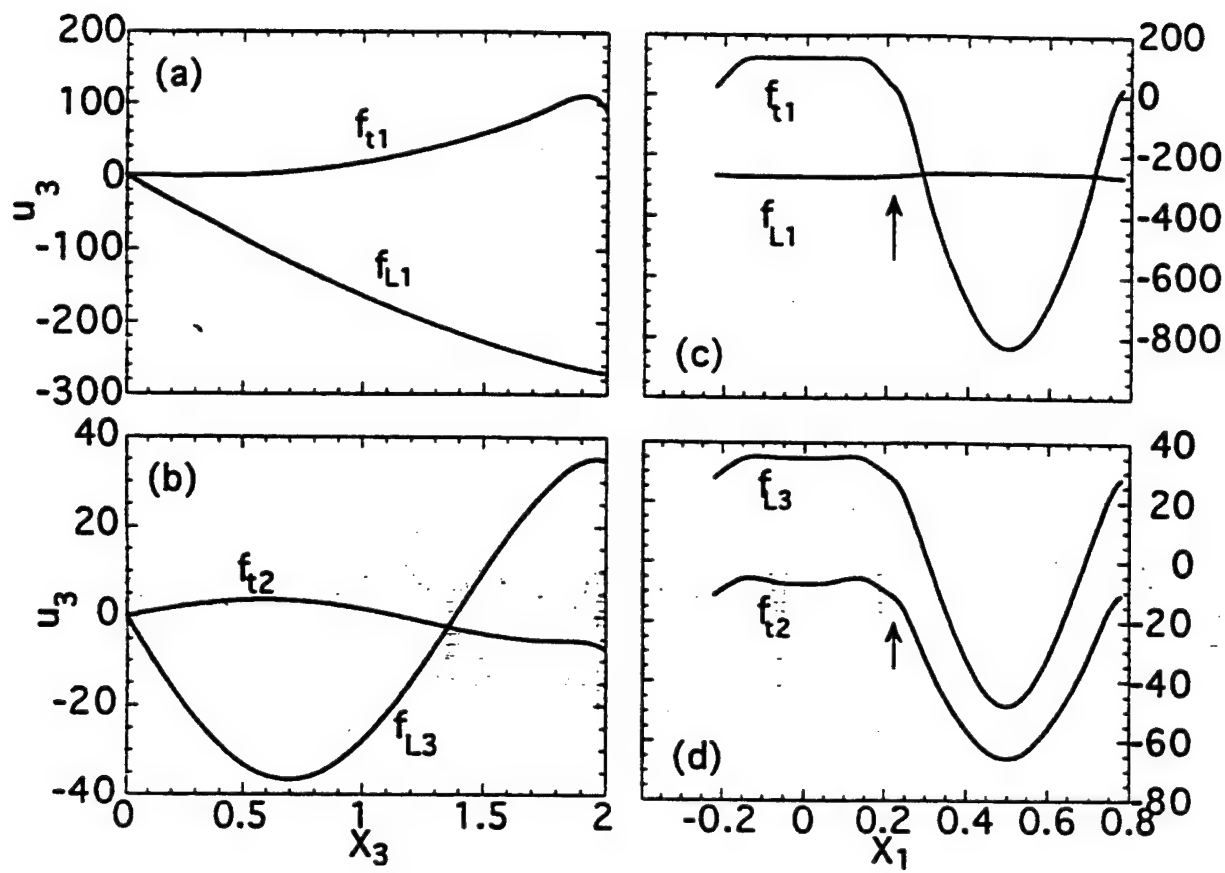
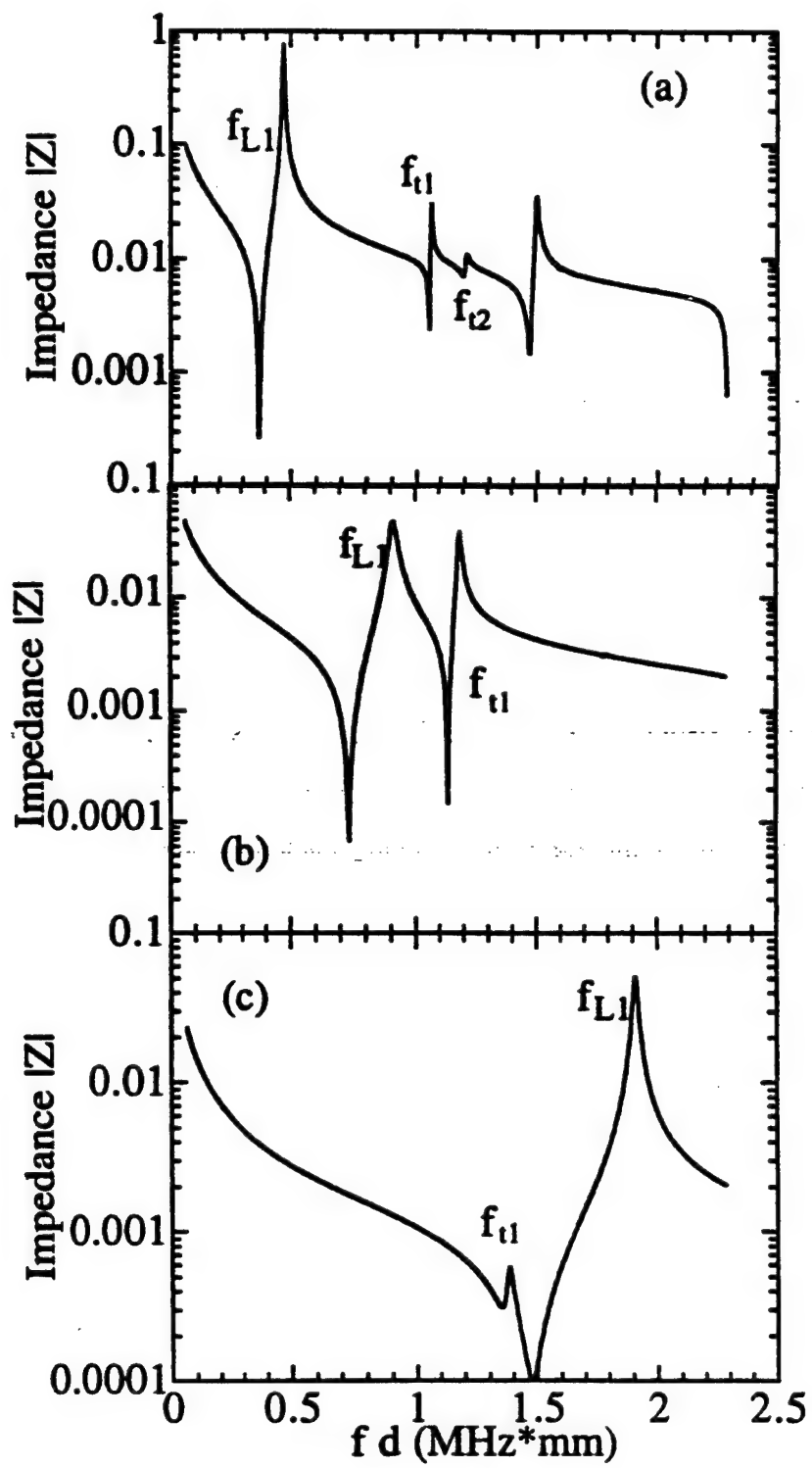


Fig.



These features are summarized in figure 8 which provide understanding on the earlier experimental observations on how various modes change with temperature (which causes reduction of the shear velocity of the polymer phase) and the composite thickness.⁵

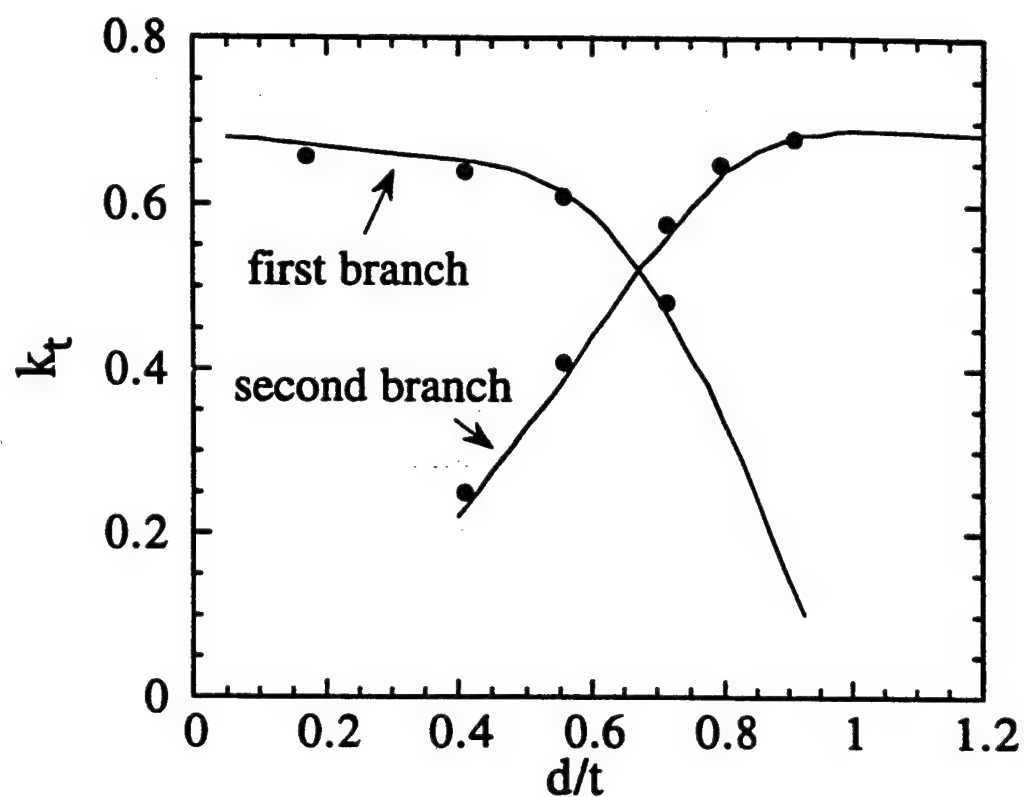
Both the experimental results and the theoretical data indicate that the ceramic and polymer vibrate in phase for all the modes on the first branch and out of phase for modes on the second branch.

The electromechanical coupling factor for the thickness resonance can be evaluated based on the definition of IEEE:²⁰

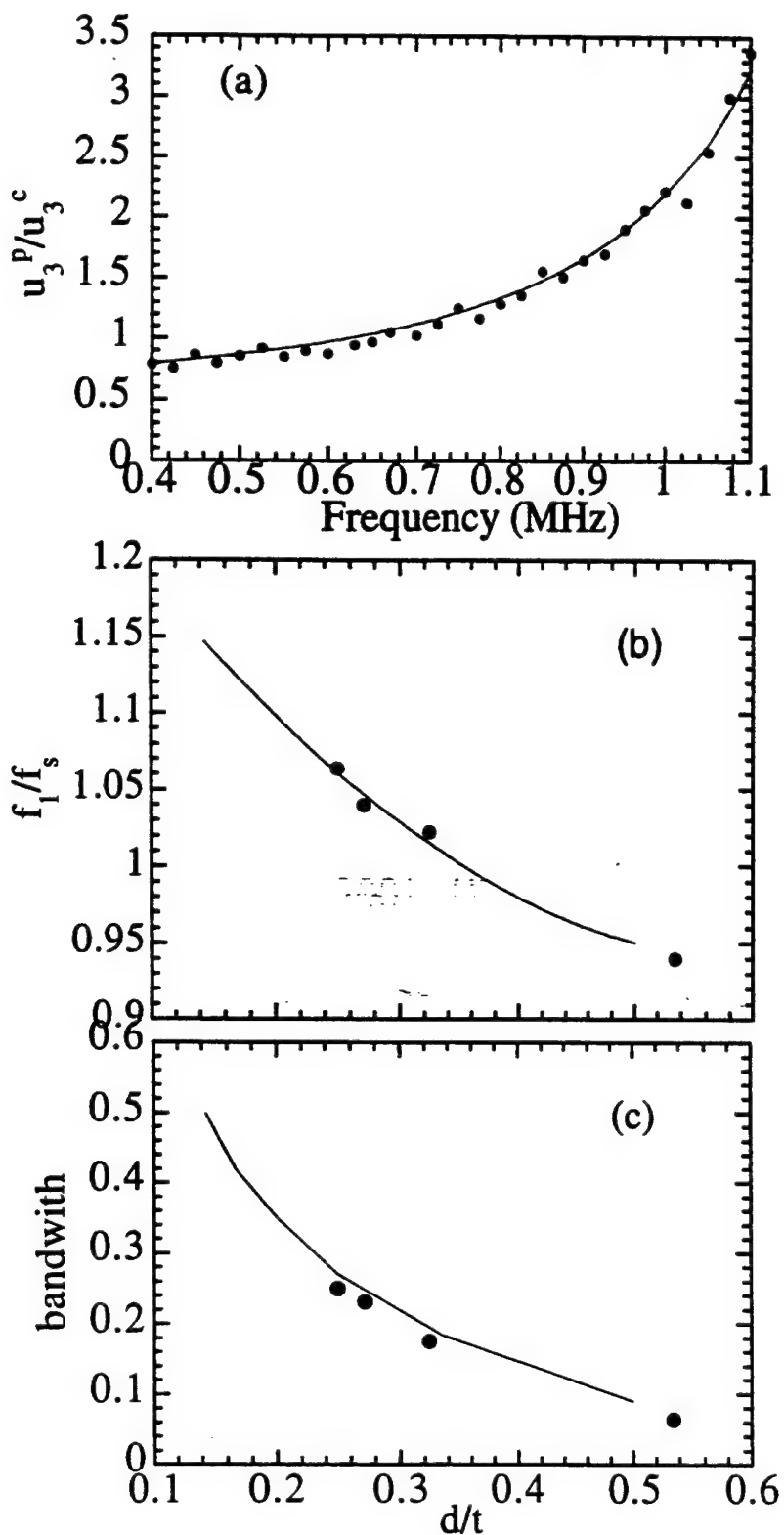
$$k_t^2 = \frac{\pi}{2} \frac{f_s}{f_p} \tan\left(\frac{\pi}{2} \frac{f_p - f_s}{f_p}\right) \quad (24)$$

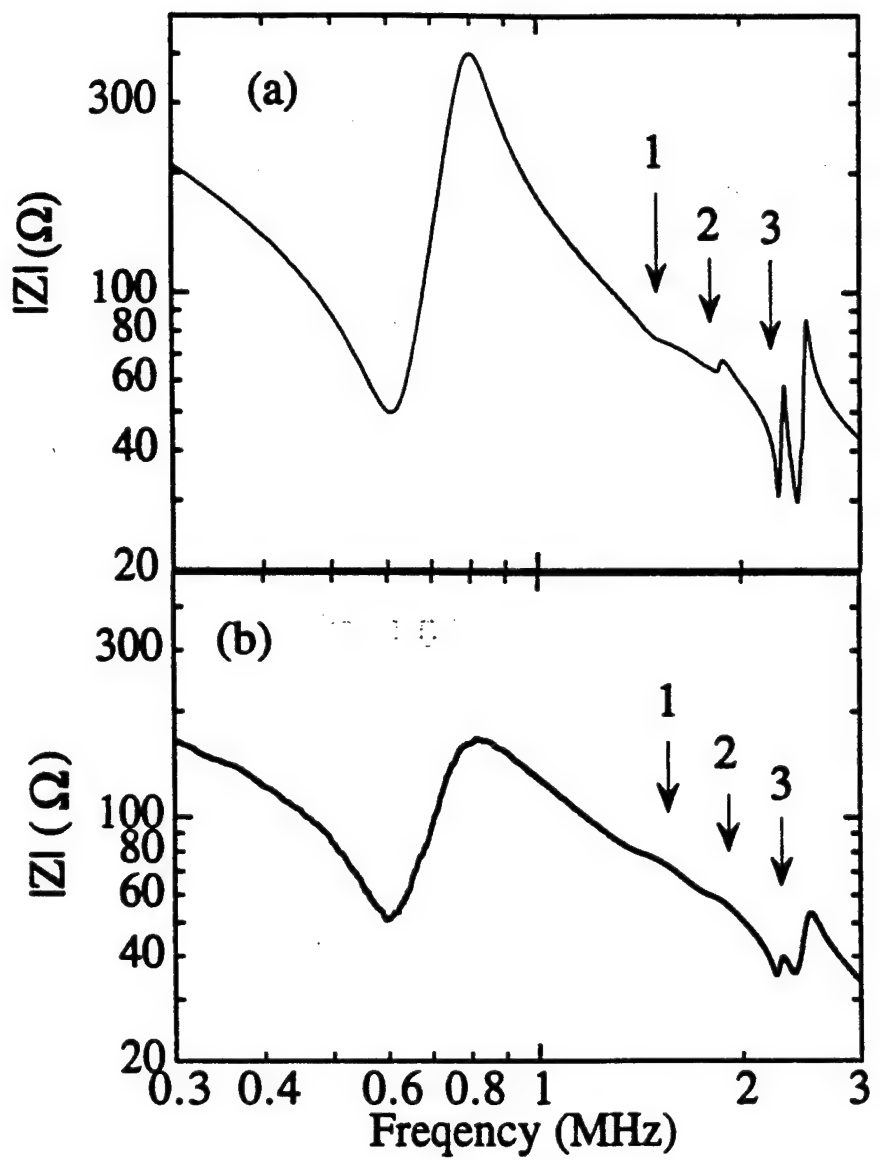
where k_t is the thickness mode coupling factor, f_s and f_p are the series and parallel resonance frequencies, respectively. Eq. (24) is used here to calculate the coupling factor for the modes in both the first and second branches. Shown in figure 9 is the results for a 2-2 composite plate with 44% ceramic volume content for different d/t , where both theoretical and experimental results are presented. As the ratio of d/t increases, the coupling factor of the mode (thickness mode) in the first branch gradually decreases, while the coupling factor of the mode in the second branch gradually increases due to the modes coupling. As d/t increases further, the thickness mode will jump to the second branch when the coupling factor in the second branch surpasses that of the first branch. Although in this region the coupling factor for the thickness mode can still be quite high, the distribution of u_z is not uniform on the composite surface and the ceramic and polymer vibrate 180° out of phase which is not desirable since the polymer phase will not be able to perform properly the function of transferring the acoustic energy between the ceramic plates and the external medium.

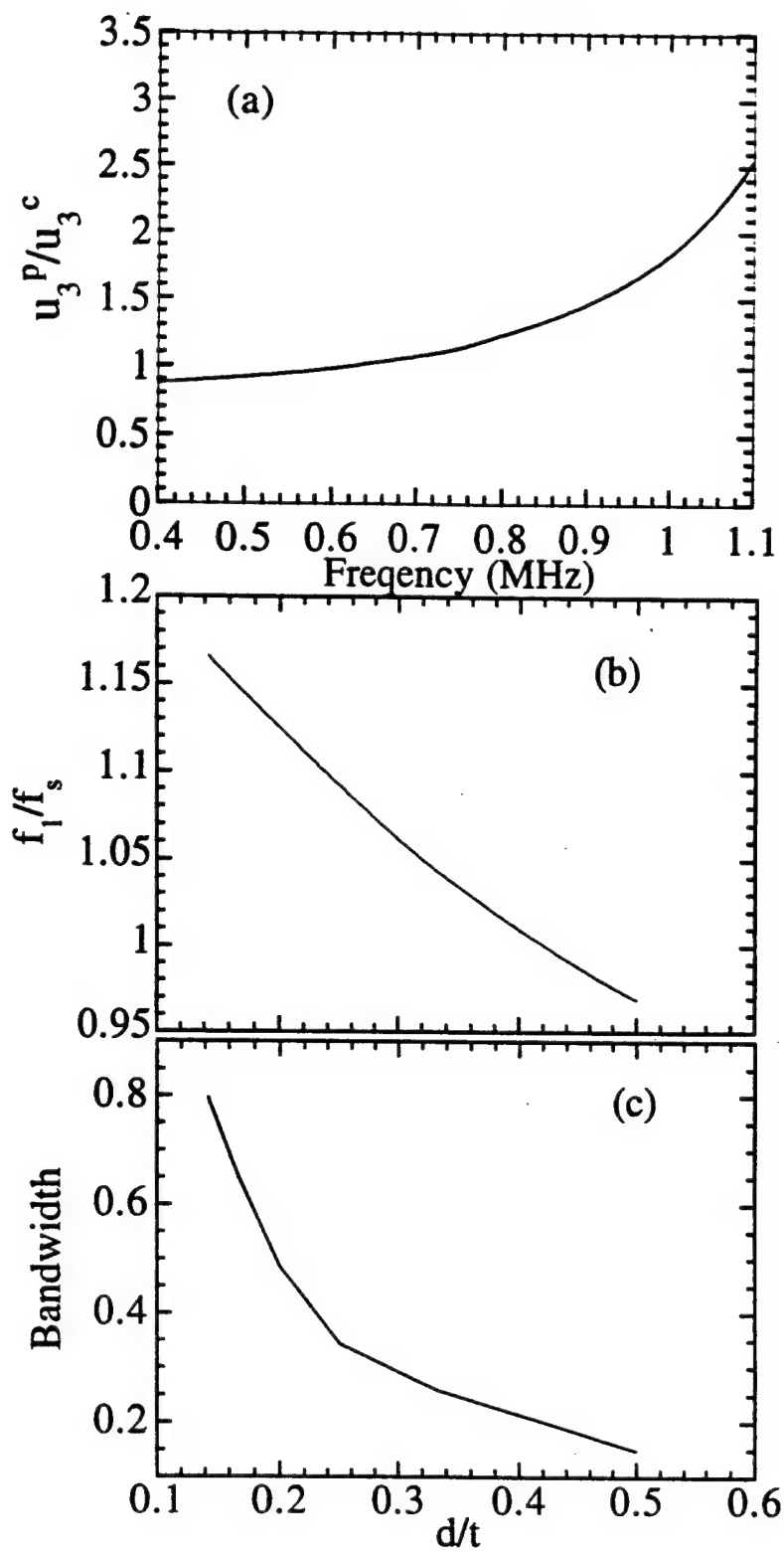
For a composite plate to work effectively as an electromechanical transduction material, it is required that the ceramic and the polymer plates in the composite vibrate in phase with nearly the same amplitude in the x_3 -direction. The evolution of the vibration pattern in the two phases with frequency and the effect of the aspect ratio t/d of a composite plate on this distribution are

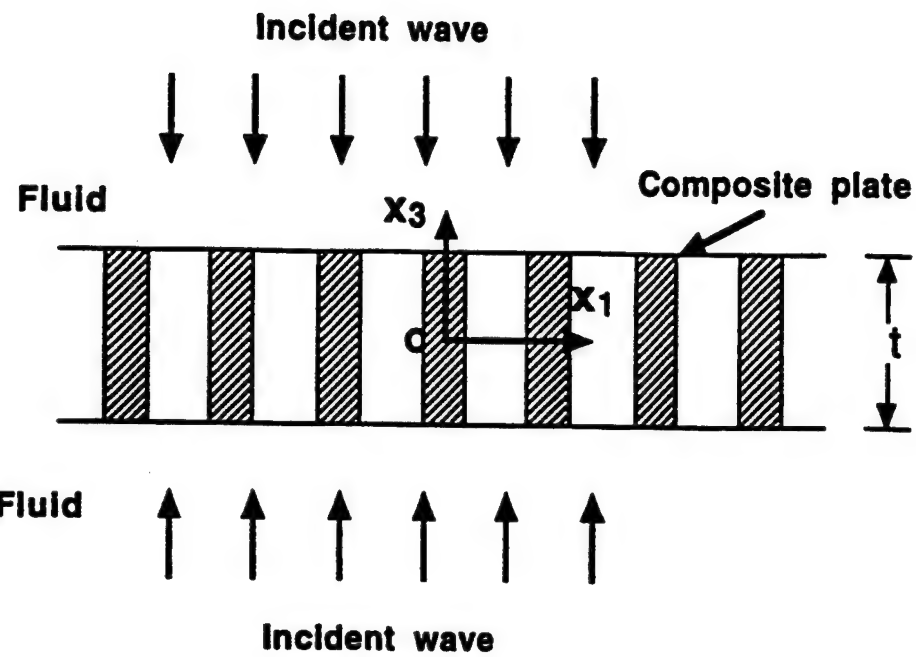


F.c

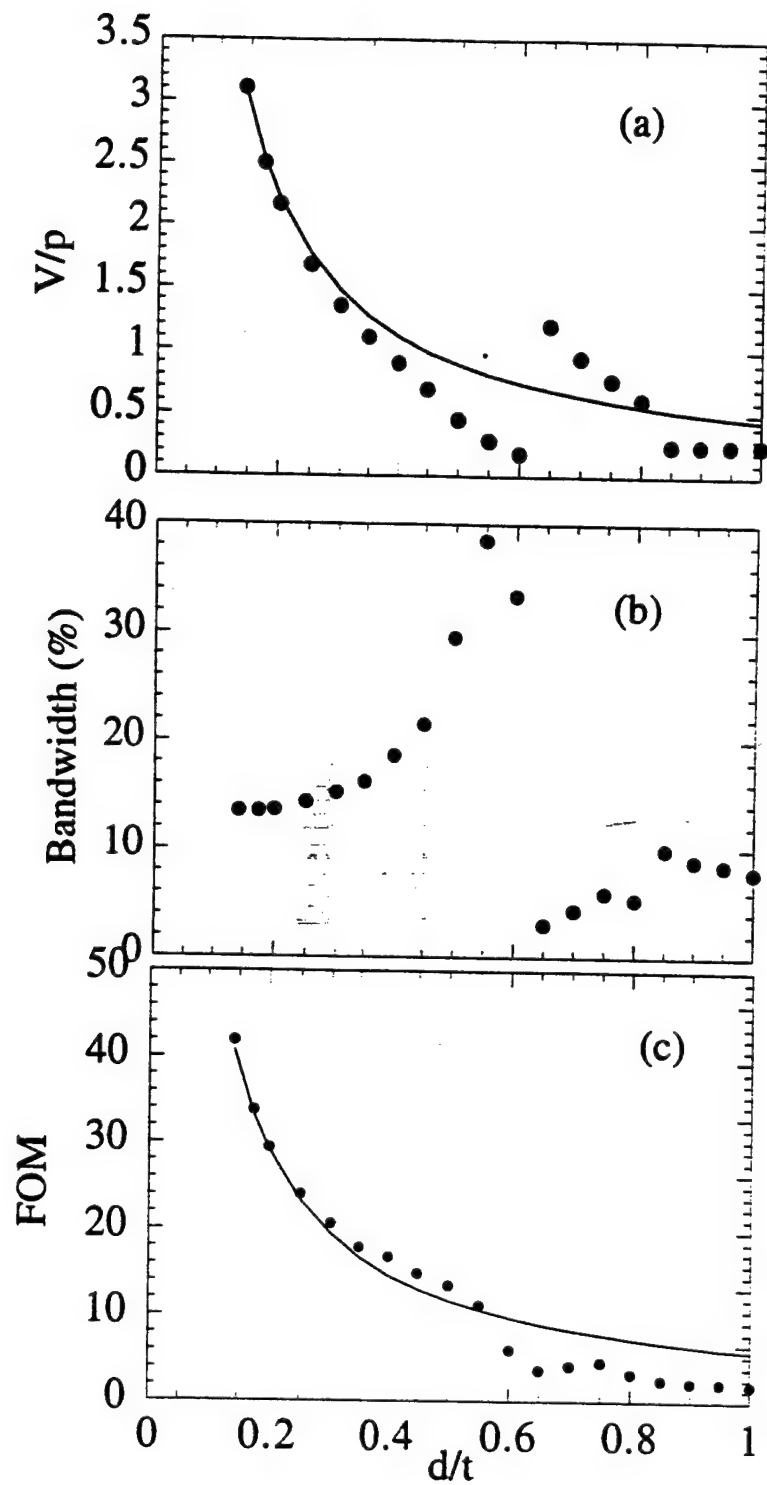


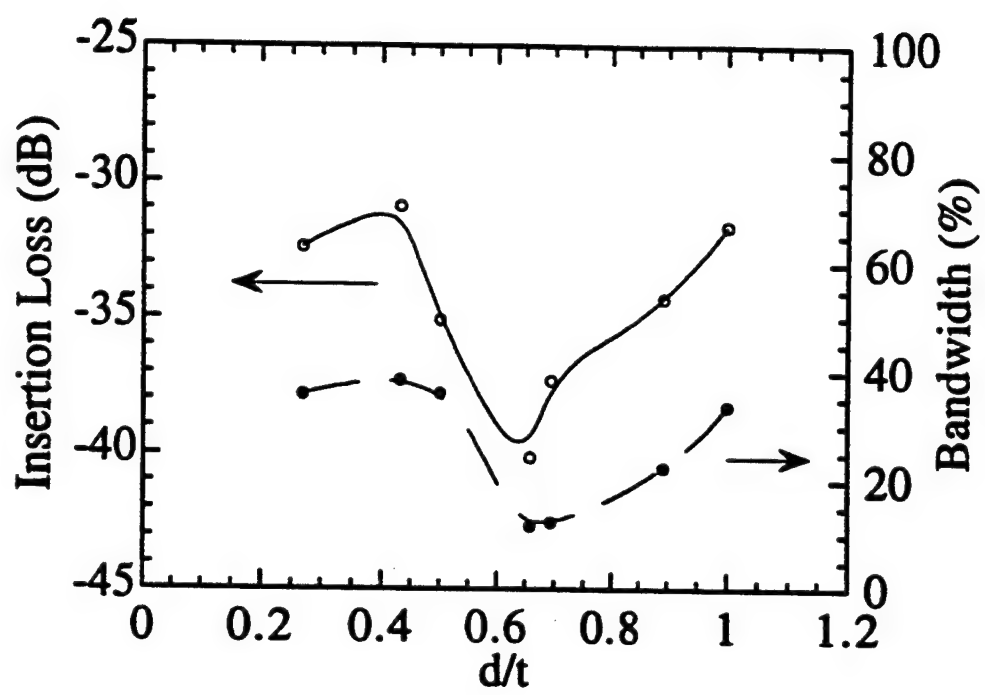






F. 13





F. 15

APPENDIX 50

Acoustic Properties of the Interface of a Uniform Medium-2-2 Piezocomposite
and the Field Distributions in the Composite

Q. M. Zhang and Xuecang Geng

Materials Research Laboratory and Department of Electrical Engineering

The Pennsylvania State University, University Park, PA 16802

Abstract:

The acoustic properties of a medium-composite interface and the field distributions in a 2-2 composite are analyzed based on an approach developed recently. It is shown that the reflection coefficient from the interface is a complex number and the reflected wave suffers a more than 180° phase change. In addition to that the effective input acoustic impedance Z_{in} of the composite is a complex number, it is found that Z_{in} also shows dependence on the shear stiffness constant of the medium in contact, which is related to the non-uniform vibration distribution at the composite surface. Since for a piezoceramic polymer composite, it is the ceramic phase which performs the energy conversion between the acoustic and electric forms, the amount of acoustic energy which can enter the ceramic region is one of the most important parameters in a composite transducer design. In the paper, we show that even though the effective transmission coefficient increases as the frequency is increased, the amount of acoustic energy entering the ceramic region actually decreases. From the fact that there is more than 180° phase change in the reflection wave from the medium-composite interface, it is shown that the matching layer thickness is no longer equal to the quarter wavelength, but smaller. These predictions are confirmed experimentally.

PACS No: 43.35. -c, 68.35. Gy, 85.50.Ly

Accepted JAP

I. Introduction:

Transmission and reflection of a wave at an interface is of great importance in many areas of modern technology such as the optical, electromagnetic, acoustic, and materials nondestructive evaluations. For homogeneous materials, a quantitative understanding of how the material properties at the interface influence the transmission and reflection of various wave components has been well established.^{1,2} However, for materials with heterogeneity such as composites, much work remains to be done in order to provide both qualitative and quantitative understandings on how a composite structure affect flows of waves at an interface between a composite and a homogeneous fluid or solid medium.

For the piezoceramic polymer composites used for ultrasonic transducer applications,³⁻⁶ in addition to the wave transmission and reflection at the interface, one has also to deal with the acoustic energy transfer between the two constituents, i.e., the piezoceramic and polymer phases. In a piezoceramic polymer composite, because the energy conversion can only be carried out in the ceramic phase and the polymer phase acts as a carrier to transfer the acoustic energy between the piezoceramic and the external medium to which the transducer is interacting. Clearly, to establish a structure performance relationship in this type of material, both the propagation of the acoustic energy at the composite-medium interface and the effectiveness of the energy transfer between the polymer and ceramic inside a composite have to be considered.

The objective of this paper is to examine quantitatively how the material properties at the two sides of the interface, i.e., the properties of a piezoceramic polymer composite and a uniform medium, either a liquid or a solid, influence the wave transmission and reflection at the interface and the acoustic energy transfer inside the composite, and how these affect the parameters of the matching layer at the interface. The approach taken here is based on the eigen-mode expansion method and variational technique.^{2,7,8}

The organization of the paper is as follows: In section II, the general formula used to treat the wave propagation at the interface is briefly presented and the results for the fluid-composite

interface are derived. The definition of the input acoustic impedance of the composite at the interface is also discussed. The acoustic energy transfer between the ceramic and polymer is analyzed. In section III, the wave propagation at a interface between a solid and a piezocomposite is analyzed. In section IV, the issues related to the anti-reflection quarter wave matching layer at a composite-medium interface are examined. And in section V, a brief summary and discussion are presented.

In the paper, the piezoceramic polymer composites used in the model calculations and in experiments are those made of PZT-5H piezoceramic and Spurr epoxy polymer matrix.⁹ The composites have a 2-2 connectivity (a terminology introduced by Newnham),⁵ i.e., the ceramic and polymer form a periodic laminated structure as shown schematically in figure 1(a).

II. Plane acoustic wave propagation at a fluid-2-2 composite interface

(2.1) Eigen-modes in a 2-2 piezocomposite and fluid medium and variational formula at their interface

The schematic of the interface system is shown in figure 1(b) where a plane acoustic wave is normally incident upon the boundary between a fluid and a 2-2 piezocomposite. The coordinate system is chosen such that the x_3 -axis is perpendicular to the interface, the x_1 -axis is parallel to the interface as shown in the figure, and the x_2 -axis is perpendicular to both the x_1 and x_3 axes (pointing out of the paper). The fluid occupies the space of $x_3 < 0$ and the 2-2 composite is in $x_3 > 0$. Since the dimension in the x_2 -direction is much larger than the period d of the 2-2 composite and the wave fields are uniform in that direction, it can be taken as infinite without much error in the results. Hence, for the dynamic problem to be considered, the 2-2 composite can be regarded as elastically clamped in the x_2 -direction so that $S_2 = 0$, where S_2 is the strain in that direction, and we have a two dimensional problem with no dependence on the x_2 -variable.

The governing equations for this problem are

$$\begin{aligned} T_{ij,i} &= \rho \ddot{u}_j \\ D_{i,i} &= 0 \end{aligned} \quad (1)$$

Where i and $j=1$ and 3 . The symbols adopted in this paper are summarized here: T_{ij} and S_{ij} are the stress and strain tensor components, where the matrix notation is used, u_i is the elastic displacement vector, ρ is the mass density, D_i is the electric displacement vector, and E_i is the electric field. The relevant material coefficients are: e_{ij} is the piezoelectric coefficient, c_{ij} is the elastic stiffness, and ϵ_i is the dielectric permittivity.

The constitutive equations in the composite are:

$$\begin{aligned} [T] &= [c^E][S] - [e_t][E] \\ [D] &= [e][S] + [\epsilon^S][E] \end{aligned} \quad (2)$$

The boundary conditions at the fluid-2-2 composite interface for the problem are

$$\begin{aligned} T_{33}^{Cm} &= T_{33}^W, \quad T_{13}^{Cm} = 0, \quad u_3^{Cm} = u_3^W \\ \Phi^{Cm} &= \Phi^W, \quad D_3^{Cm} = D_3^W \end{aligned} \quad \text{at } x_3=0 \quad (3)$$

The superscripts Cm and W represent the 2-2 composite and the fluid. And Φ is the electric potential.

In the 2-2 composite, as has been shown in earlier publications,^{8,10} the displacements and electric potential in the ceramic phase can be expressed as

$$\begin{aligned} u_3^c &= \sum_i R_i^c f_i^c \cos(h_i^c x_1) \exp(j\beta x_3) \\ u_1^c &= j \sum_i R_i^c g_i^c \sin(h_i^c x_1) \exp(j\beta x_3) \\ \Phi^c &= \sum_i R_i^c t_i^c \cos(h_i^c x_1) \exp(j\beta x_3) \end{aligned} \quad (4)$$

where i runs from 1 to 3. In eq. (4), h_i and β are the wave vector components in the x_1 - and x_3 -directions, respectively. For each β , there are three h_i correspond to the quasi-longitudinal, quasi-shear, and quasi-electric waves, respectively. For the polymer phase, we have the similar expressions,

$$\begin{aligned} u_3^P &= \sum_i R_i^P f_i^P \cos(h_i^P(x_1 - \frac{d}{2})) \exp(j\beta x_3) \\ u_1^P &= j \sum_i R_i^P g_i^P \sin(h_i^P(x_1 - \frac{d}{2})) \exp(j\beta x_3) \end{aligned} \quad (5)$$

$$\Phi^P = C^P \cosh(\beta(x_1 - \frac{d}{2})) \exp(j\beta x_3)$$

where $i=1$ and 2 . In equations (4) and (5), f_i^c , g_i^c , t_i^c , f_i^p , and g_i^p are the coefficients and superscripts c and p refer to the ceramic and polymer regions. In these equations, the time dependent term, i.e., $\exp(-j\omega t)$, is omitted for the sake of simplicity.

By imposing the boundary conditions at the ceramic-polymer interface, one can obtain the dispersion relations in a 2-2 composite for waves in the x_3 -direction. As an example, the dispersion curves for a 2-2 composite made of PZT-5H piezoceramic and Spurr epoxy with 44% ceramic volume content are shown in figure 2. In addition, the relations among $R_1^c, R_2^c, R_3^c, R_1^p, R_2^p$ and C^p are determined and for a given mode (a given β), there is only one independent variable among these 6 coefficients. Therefore, they can be expressed as $(R_1^c, R_2^c, R_3^c, R_1^p, R_2^p, C^p)^t A$, where A is an undetermined constant. Hence, eqs. (4) and (5) constitute the eigenfunctions in a 2-2 composite for a wave propagating in the x_3 -direction.

In the fluid medium, the constitutive relation has the form

$$T_{11} = T_{33} = \lambda^W (\frac{\partial u_1}{\partial x_1} + \frac{\partial u_3}{\partial x_3}) \quad (6)$$

where λ^W is the bulk modulus of the fluid. The periodic condition in the x_1 -direction due to the composite structure also imposes the constraints on the solutions to the equation (1) in the fluid region:

$$\begin{aligned} u_1^W &= j h_n^W \sin(h_n^W x_1) \exp(j\beta_n^W x_3) R_n^W \\ u_3^W &= \beta_n^W \cos(h_n^W x_1) \exp(j\beta_n^W x_3) R_n^W \end{aligned} \quad (7)$$

where $h_n^W = \frac{2n\pi}{d}$ and $\beta_n^W = \sqrt{\frac{\omega^2}{(V^W)^2} - (h_n^W)^2}$ ($n=0,1,2,3\dots$) are the wave vector

components in the x_1 - and x_3 -directions in the fluid region, $V^W = \sqrt{\frac{\lambda^W}{\rho^W}}$ is the acoustic wave velocity of fluid. In eq. (7), R_n^W is an undetermined constant.

In order to satisfy the boundary conditions at the composite-fluid interface, the elastic and electric fields in the two regions are expanded in terms of the eigenfunctions obtained. The coefficient of each mode is determined by the variational method.¹⁰

$$\begin{aligned} & \int_S \frac{1}{2} [(T_{33}^W - T_{33}^{Cm})(\delta u_3^W + \delta u_3^{Cm})^* - 2T_{13}^{Cm}(\delta u_1^{Cm})^* \\ & + (u_3^{Cm} - u_3^W)(\delta T_{33}^{Cm} + \delta T_{33}^W)^* + (D_3^W - D_3^{Cm})(\delta \Phi^W + \delta \Phi^{Cm})^* \\ & + (\Phi^W - \Phi^{Cm})(\delta D_3^W + \delta D_3^{Cm})^*] dS = 0 \end{aligned} \quad (8)$$

where the surface integral is performed at $x_3=0$ over one unit cell ($-\frac{d}{2} \leq x_1 \leq \frac{d}{2}$), W and Cm

refer to the fluid and composite, respectively, and * denotes the complex conjugate.

For the situation considered here, in the fluid medium, there are incident wave and reflected wave, therefore, in terms of the eigenfunctions in the fluid medium, the elastic displacement and electric potential in the fluid can be expressed as

$$\begin{aligned} u_1^W &= j \sum_{n=0}^G h_n^W \sin(h_n^W x_1) \exp(-j\beta_n^W x_3) R_n^W \\ u_3^W &= \beta_0^W \exp(j\beta_0^W x_3) - \sum_{n=0}^G \beta_n^W \cos(h_n^W x_1) \exp(-j\beta_n^W x_3) R_n^W \\ \Phi^W &= \sum_{n=0}^G \cos(h_n^W x_1) \exp(h_n^W x_3) R_n^W \end{aligned} \quad (9)$$

where $\beta_0^W = \frac{\omega}{V^W}$ and $\beta_0^W \exp(j\beta_0^W x_3)$ corresponds to the incident wave normal to the interface. R_n^W are the coefficients determined by equation (8).

In the composite region, only the transmitted wave exists. In the ceramic phase, the elastic displacements and the electric potential are

$$\begin{aligned} u_3^C &= \sum_{n=1}^m \sum_{i=1}^3 R_{ni}^C f_{ni}^C \cos(h_{ni}^C x_1) \exp(j\beta_n x_3) A_n \\ u_1^C &= j \sum_{n=1}^m \sum_{i=1}^3 R_{ni}^C g_{ni}^C \sin(h_{ni}^C x_1) \exp(j\beta_n x_3) A_n \\ \Phi^C &= \sum_{n=1}^m \sum_{i=1}^3 R_{ni}^C t_{ni}^C \cos(h_{ni}^C x_1) \exp(j\beta_n x_3) A_n \end{aligned} \quad (10)$$

and in the polymer phase, they are

$$\begin{aligned} u_3^P &= \sum_{n=1}^m \sum_{i=1}^2 R_{ni}^P f_{ni}^P \cos(h_{ni}^P(x_1 - \frac{d}{2})) \exp(j\beta_n x_3) A_n \\ u_1^P &= j \sum_{n=1}^m \sum_{i=1}^2 R_{ni}^P g_{ni}^P \sin(h_{ni}^P(x_1 - \frac{d}{2})) \exp(j\beta_n x_3) A_n \\ \Phi^P &= \sum_{n=1}^m C_n^P \cosh(\beta_n(x_1 - \frac{d}{2})) \exp(j\beta_n x_3) A_n \end{aligned} \quad (11)$$

where A_n are coefficients to be determined from eq. (8). In the expansions (9), (10) and (11), the number of modes used are determined by the accuracy needed. Making use of the constitutive equations in the ceramic and polymer phases, the stress and electric displacement in the composite region can be obtained. Substituting these quantities into eq. (8) yields the following algebraic equation:

$$(M_{ij})R_j = (V_i) \quad (12)$$

where $(R_j) = (R_0, R_1, \dots, R_G, A_1, \dots, A_m)^T$, (M_{ij}) is a $(G+m+1) \times (G+m+1)$ matrix, and (V_i) is a $(G+m+1) \times 1$ matrix. In the problem treated, $G=7$ and $m=9$ are used. From eq. (12), the coefficients R_j and A_j are determined.

(2.2) Reflection coefficient and input acoustic impedance at the interface and field distributions in the composite

In this section, we will first derive the reflection coefficient for a composite in contact with water based on the results derived in the preceding sections. As we have pointed out, in the expression (9), $\beta_0^w \exp(j\beta_0^w x_3)$ is the incident wave and other terms are from the reflected wave. The zeroth order reflected wave, i.e., $n=0$ and $h_0^w=0$, represents the normal reflection. For $n \neq 0$, in the frequency of interest, i.e., below the first lateral mode frequency, it can be shown that β_n^w is nearly equal to $j(2n\pi/d)$ which implies that the amplitude of these waves will decay as $\exp(-2n\pi x_3/d)$ as the waves depart from the interface and hence they are evanescent waves which are important only in the boundary region. In this sense, the reflection coefficient which can be measured experimentally is equal to $-R_0$.

Figure 3(a) shows the reflection coefficient derived for a plane acoustic wave on the boundary between water and a 2-2 composite in which the volume fraction of ceramic phase is 44%. At lower frequencies where the periodicity d of the 2-2 composite in the x_1 -direction is much smaller than the wavelength of the incident wave, the 2-2 composite behaves like an effective homogeneous medium, and the reflection coefficient is real and can be fully characterized by the acoustic impedance of the two materials, i.e., the effective acoustic impedance of the composite derived based on effective medium theory and the characteristic impedance of water.^{11,12} As the frequency increases, however, the vibration displacement at the surface of the 2-2 composite becomes nonuniform, which implies that it could no longer be regarded as a homogeneous medium. Hence, the reflection coefficient at the water and composite interface will be dispersive and become a complex number as shown in figure 3(a) where the magnitude of the reflection coefficient decreases gradually and meanwhile, the phase of the reflection coefficient becomes larger than 180° and increases with frequency.

To verify the results, an experiment was conducted to measure the reflection coefficient from the interface between water and a 2-2 composite of 44% ceramic. The schematic of the experimental set-up is shown in figure 4, where the reflected signals, both the amplitude and

time delay, from a 2-2 composite of 44% ceramic volume and a standard reflector made of a stainless steel rod, were compared. Since the acoustic impedance of the stainless steel standard is known, the reflection coefficient from the water-composite interface can be determined. To approximate the plane wave condition, the distance between the transducer and the water-composite interface is smaller than the radius of the transducer. Because the main purpose of this experiment is to determine the phase angle of the reflection coefficient from the water-composite interface, it is crucial to ensure the separation between the probing transducer and the composite the same as that between the transducer and stainless steel standard.

The result thus obtained is shown in figure 3(a). At frequencies below the lateral resonant mode ($f_d < 1 \text{ MHz mm}$), the agreement between the model result and experimental result is quite good, especially the phase. The fluctuation in the experimental data in the amplitude of R around $f_d = 0.65 \text{ (MHz mm)}$ is probably due to the existence of other weak modes at the composite surface. At frequencies near the lateral mode ($f_d = 1 \text{ MHz mm}$), even though the model prediction does not reproduce the experimental data, it still follows the trend of the data. Near a resonance, any small error in the input parameters in the model, especially the elastic loss in the polymer phase which is not included in the model, can cause large effect. This could be the reason for the discrepancy between the model results and experimental data.

In figure 3(b), the reflection coefficient for a 2-2 composite with 15% ceramic content is presented. Clearly, the trend is quite similar to that in figure 3(a), although the magnitude and the phase of the reflection coefficient are more sensitive to the frequency of incident wave which is apparently due to the small volume content of the ceramic phase in the composite and lower lateral mode frequency ($f_d = 0.8 \text{ MHz}^*\text{mm}$).

One important parameter related closely to the reflection and transmission of an acoustic wave at an interface is the acoustic impedance of the media at the two sides of the boundary which also depends on the nature of the wave such as plane wave or spherical wave.^{2,13} For homogeneous isotropic materials, the acoustic impedance for a plane wave is the characteristic acoustic impedance which is simply the product of the mass density ρ and the wave

(longitudinal wave or shear wave) velocity V .^{1,2} ¹³ For nonuniform materials (such as piezocomposite materials), on the other hand, no characteristic impedance can be defined in such a simple manner due to the dispersive nature of the properties as has been shown. However, the acoustic impedance of a material can still be found, for example, from the reflection coefficient or other methods. It should be pointed out that although there exist several definitions for determining the acoustic impedance at an interface (input acoustic impedance), for a heterogeneous material, the results obtained by using different definitions may not be the same.^{14,15} However, since the input acoustic impedance is not a direct physical quantity but rather a parameter introduced for the convenience of the analysis, a situation in analogy to the complex notation introduced in many engineering fields, which definition is more appropriate really depends on the situation where it is used. In dealing with the energy transfer across an interface, one might have to use the formula derived under energy flow consideration. On the other hand, in designing matching layers and dealing with the reflection and transmission of acoustic waves in a multilayer medium, the amplitude and phase of the wave components are crucial which may not be included in the coefficients related to the transmission and reflection of the acoustic energy. In the discussion here, we will adopt the definition related to the wave reflection and transmission problems.^{12,14}

From the reflection coefficient R , the input acoustic impedance of the composite at the interface can be found as

$$Z_{in} = \frac{1-R}{1+R} Z^W \quad (13)$$

where Z_{in} is the effective input impedance of the 2-2 composite, Z^W is the characteristic impedance of water. Using the results in figure 3, the effective input acoustic impedance of 2-2 composites with 44% and 15% ceramic volume content is evaluated and presented in figures 5(a) and 5(b). Apparently, there is a large change of the magnitude and phase of the input acoustic impedance as the frequency increases.

In analogy to the electrical impedance, the specific impedance at the interface can also be found from the ratio of the stress (in analogy to the voltage) to the displacement velocity (in analogy to the current):

$$Z(x_1, 0) = \frac{T_3^{Cm}(x_1, 0)}{v_3^{Cm}(x_1, 0)} \quad (14)$$

where v_3^{Cm} is the particle displacement velocity in the 2-2 composite. Eq. (14) is used widely in the equivalent circuit model of transducers.¹⁶⁻¹⁸ Apparently, for a 2-2 composite considered, Z from eq. (14) is a function of x_1 due to the variation of T_3 and v_3 in that direction. To eliminate this variation, the approach taken by Miller and Pursey is adopted here.¹⁴ That is, the averaged T_3 and averaged v_3 in the x_1 -direction are used:

$$Z_{in} = \frac{\int T_3^{Cm}(x_1, 0) dx_1}{\int v_3^{Cm}(x_1, 0) dx_1} \quad (15)$$

where the integration is taken in one unit cell. This expression seems physically meaningful since it reflects an averaged mechanical impedance of the composite at the interface. Z_{in} calculated from eq. (15) for composites with 44% and 15% ceramic contents is shown in figure 6 which is quite close to those in figure 5. In the following discussion, eq. (15) is used to calculate Z_{in} in the composite.

One interesting question is whether the acoustic impedance of the fluid phase will affect the effective input impedance of the composite at the interface. To answer this question, the effective input impedance of the composite at the interface is evaluated for fluid phases with different acoustic impedance (by varying the bulk modulus) and the results are presented in figure 7. Clearly, the effective acoustic impedance of a 2-2 composite is independent of the acoustic impedance of the fluid at the interface.

In order to shed light on the large change of the input acoustic impedance with frequency, the surface displacement u_3 is evaluated at the center of the ceramic plate ($x_1=0$) and polymer plate ($x_1=d/2$) and the results are presented in figure 8(a). At low frequencies, the surface displacements in the polymer and ceramic regions are in unison which indicate that the isostain

model used in many earlier modelings on ultrasonic composite transducers is valid in this frequency region.^{11,12} As the frequency increases, even at frequencies still far below the first lateral mode (at f_d near 1), the surface vibration amplitudes in the two regions become quite different. At the frequency near the first lateral mode, the vibrations in the polymer and ceramic regions are 180 out of phase and in this frequency region, the effective input acoustic impedance of the composite is very near that of water and the reflection coefficient exhibits a minimum as shown in figure 3.

As has been pointed out in the introduction, for an ultrasonic piezoceramic polymer composite, one of the most important factors in determining the performance is the effective acoustic energy exchange between the ceramic and the external medium. As seen in figure 3 and 5 where at frequencies near the lateral mode, the input acoustic impedance of the composite is close to that of water and the reflection coefficient reaches a minimum, the question is how much of that energy enters into the ceramic plates. Figure 8(b) shows how the total acoustic powers entering into the ceramic region and polymer region vary with frequency. Clearly, at the high frequency region, in spite of the fact that the effective transmission coefficient of the composite increases, the amount entering into the ceramic plate actually decreases.

It is also interesting to examine how this acoustic energy distribution in the polymer and ceramic regions changes along the x_3 -direction since the interaction between the ceramic and polymer through the joint region will cause the acoustic energy transfer between the two. In figure 9, the acoustic energy distribution along the x_3 -direction at three frequencies ($f \ll f_l$, $f = f_l/2$, and $f = f_l$, where f_l is the first lateral mode frequency) is shown. In all the cases, there is a redistribution of the acoustic energy along the x_3 -axis and the acoustic energy in the polymer is gradually transferred to the ceramic plate. However, at low frequencies, the transition region is much shorter than that at high frequencies (with respect to the wave length at that frequency). For instance, in figure 9(a), the reduced length x_3/λ is about 0.01 for the acoustic power in the ceramic to reach 90% of the final value, while in figure 9(b), this region

increases to about 0.1, and in figure 9(c), it becomes near 0.2. It should be reminded that in a thickness mode transducer, the thickness of the piezocomposite is $\lambda/2$.

In figure 10, the change of the displacement u_3 in the polymer and ceramic regions along the x_3 -direction at the three frequencies is presented and it shows that at high frequencies, the displacement amplitude in the polymer and ceramic regions is no longer the same even deep inside the composite.

The change of the input acoustic impedance from eq. (15) along the x_3 -direction in the composite is also evaluated. Figure 11 are the results of the 2-2 composite with 44% ceramic content at different frequencies. Apparently, at high frequencies there is a large change of the effective acoustic impedance from the surface into the interior of the composites and even in the interior of the composite, the effective impedance is not the same as that derived from the effective medium theory.^{11,12}

III. Wave reflection and transmission at solid-2-2 composite interfaces

In general, a piezoelectric ultrasonic transducer has a multilayer structure in which there are one or two quarter wavelength impedance matching layers in front of the piezoelectric element and a backing material in the back. The piezoelectric element in the transducer does not contact directly with fluid medium. Therefore, the investigation of the interaction between a 2-2 composite and solid medium has practical importance for composite transducers.

The issues investigated in this section are quite similar to those studied in the preceding section. The difference is that a solid medium can support shear waves while a fluid cannot. Due to this difference, the boundary conditions (3) must be modified to:

$$\begin{aligned} T_{33}^{Cm} &= T_{33}^S, \quad T_{13}^{Cm} = T_{13}^S, \quad u_3^{Cm} = u_3^S, \quad u_1^{Cm} = u_1^S \\ \Phi^{Cm} &= \Phi^S, \quad D_3^{Cm} = D_3^S, \end{aligned} \tag{16}$$

where the superscript S refers to the variables in the solid medium. Hence, the variational formula for the problem becomes

$$\begin{aligned} & \int_S \frac{1}{2} [(T_{33}^S - T_{33}^{Cm})(\delta u_3^S + \delta u_3^{Cm})^* + (T_{13}^S - T_{13}^{Cm})(\delta u_1^S + \delta u_1^{Cm})^* \\ & + (u_3^{Cm} - u_3^S)(\delta T_{33}^{Cm} + \delta T_{33}^S)^* + (u_1^{Cm} - u_1^S)(\delta T_{13}^{Cm} + \delta T_{13}^S)^* \\ & + (D_3^S - D_3^{Cm})(\delta \Phi^S + \delta \Phi^{Cm})^* + (\Phi^S - \Phi^{Cm})(\delta D_3^S + \delta D_3^{Cm})^*] dS = 0 \end{aligned} \quad (17)$$

where the surface integral is performed at $x_3=0$ over one repeat unit in the x_1 -direction of the composite. The elastic displacement u_1^S, u_3^S , and the electrical potential Φ^S in the solid medium are expanded in terms of the eigenfunctions:

$$\begin{aligned} u_1^S &= j \sum_n \sum_{i=1}^2 g_{ni}^S \sin(h_n^S x_1) \exp(-j\beta_{ni}^S x_3) R_n^S \\ u_3^S &= \beta_0^S \exp(j\beta_0^S x_3) - j \sum_n \sum_{i=1}^2 f_{ni}^S \cos(h_n^S x_1) \exp(-j\beta_{ni}^S x_3) R_n^S \\ \Phi^S &= \sum_n \cos(h_n^S x_1) \exp(h_n^S x_3) R_n^S \end{aligned} \quad (18)$$

where $\beta_0^S \exp(j\beta_0^S x_3)$ is the incident wave and other terms are from the reflected waves in which both the longitudinal and shear components exist except the one with $n=0$ where the reflected wave is a pure longitudinal one. Substituting the elastic and electrical variables in the 2-2 composite and eq. (18) into equation (17), the coefficients of the expansions can be obtained.

Figure 12 presents the dispersion curve of the reflection coefficient at the interface for 2-2 piezocomposites with 44% ceramic volume content and the acoustic impedance calculated from eq. (13) where the characteristic impedance of the solid medium is $Z=2.4$ MRayls.

By comparing the results in figure 12 and figure 5, it can be found that the input acoustic impedance of 2-2 composites calculated here is different from that in the fluid case. In addition, it is also found that at a solid medium-2-2 composite interface, the input acoustic impedance also depends on the characteristic impedance of the solid medium at the interface, which seems to be quite different from the fluid medium interface.

To understand this phenomenon, we notice that the difference between a solid medium and a fluid one is that a solid medium has a non-zero shear stiffness constant. Therefore, Z_{in} for a

2-2 composite (44% ceramic content) in contact with solid medium is evaluated where ρ (mass density) and c_{11} are kept as constant and c_{44} is varied and the results are presented in figure 13(a). Similarly, Z_{in} for a 2-2 composite in contact with solid medium is also evaluated where ρ and c_{44} are kept constant and c_{11} is varied and the results are shown in figure 13(b). The results demonstrate that for a plane incident wave, even if the characteristic longitudinal impedance of the solid medium is kept constant, the effective input impedance of a composite and, hence, the reflection coefficient from the interface will change if the shear stiffness coefficient of the solid medium changes. On the other hand, if the shear stiffness constant is kept constant and the characteristic longitudinal impedance is varied in the solid medium, the effective input acoustic impedance of a composite will not have much change. This phenomenon is directly related to the surface uniformity of the composite and as has been shown earlier, the enhanced stress transfer between the ceramic and polymer regions is through the shear action.¹⁹

To illustrate this, the surface vibration distribution in the ceramic and polymer regions is also evaluated for the 2-2 composite in contact with solid media of different c_{11} and c_{44} and the results are presented in figure 14. There is very little difference in the surface vibration profile for solid media with the same c_{44} and different c_{11} . In contrast, the surface vibration profile will change as c_{44} is changed (figures 14(a) and 14(b)).

Figure 15 illustrates the input acoustic impedance of a composite as a function of x_3 for different solid media at the interface. It shows the length of the transition region in the composite where the evanescent waves are important decreases as the acoustic impedance of the medium, especially the shear modulus, increases.

IV. Reflection and transmission from the boundary between fluid and acoustic impedance matching layer

We now proceed to investigate how the various effects observed in the preceding sections affect the selection of anti-reflection matching layers at the interface. Figure 16 is a schematic of an acoustic system which consists of a fluid medium, a matching layer and a 2-2 composite. In this case, there are two interfaces with different boundary conditions to be treated. One of the interfaces is between the 2-2 composite and matching layer where the boundary conditions are those of equation (16). Another one is the fluid and matching layer interface where the boundary conditions are:

$$T_{33}^S = T_{33}^W, T_{13}^S = 0, u_3^S = u_3^W, \Phi^S = \Phi^W, D_3^S = D_3^W \quad \text{at } x_3=-t \quad (19)$$

where t is the thickness of the matching layer and the other notations are the same as before.

The variational formula for this problem can be derived:

$$\begin{aligned} & \int_{S_1} \frac{1}{2} [(T_{33}^S - T_{33}^{Cm})(\delta u_3^S + \delta u_3^{Cm})^* + (T_{13}^S - T_{13}^{Cm})(\delta u_1^{Cm} + \delta u_1^S)^* \\ & + (u_3^{Cm} - u_3^S)(\delta T_{33}^{Cm} + \delta T_{33}^S)^* + (u_1^{Cm} - u_1^S)(\delta T_{13}^{Cm} + \delta T_{13}^S)^* \\ & + (D_3^S - D_3^{Cm})(\delta \Phi^S + \delta \Phi^{Cm})^* + (\Phi^S - \Phi^{Cm})(\delta D_3^S + \delta D_3^{Cm})^*] dS \\ & + \int_{S_2} \frac{1}{2} [(T_{33}^W - T_{33}^S)(\delta u_3^S + \delta u_3^W)^* + 2T_{13}^S(\delta u_1^S)^* + (u_3^S - u_3^W)(\delta T_{33}^S + \delta T_{33}^W)^* \\ & + (D_3^W - D_3^S)(\delta \Phi^S + \delta \Phi^W)^* + (\Phi^W - \Phi^S)(\delta D_3^S + \delta D_3^W)^*] dS = 0 \end{aligned} \quad (20)$$

where the surface integrals S_1 and S_2 are performed at $x_3=0$ and $x_3=-t$ planes, respectively, from $x_1=0$ to $x_1=d/2$.

In the matching layer region, there are waves which propagate in both the $+x_3$ and $-x_3$ directions due to the two interfaces at $x_3=0$ and $x_3=-t$. Hence, the expressions for the elastic and electrical variables become:

$$\begin{aligned} u_1^S &= j \sum_n \sum_i g_{ni}^S(\beta_{ni}^S) \sin(h_n^S x_1) [-\exp(-j\beta_{ni}^S x_3) R_n^1 + \exp(j\beta_{ni}^S x_3) R_n^2] \\ u_3^S &= \sum_n \sum_i f_{ni}^S(\beta_{ni}^S) \cos(h_n^S x_1) [-\exp(-j\beta_{ni}^S x_3) R_n^1 + \exp(j\beta_{ni}^S x_3) R_n^2] \quad (21) \\ \Phi^S &= \sum_n \cos(h_n^S x_1) [-\exp(-h_n^S x_3) R_n^1 + \exp(h_n^S x_3) R_n^2] \end{aligned}$$

The solutions in the composite and in the fluid medium are those of eqs. (9), (10) and (11). Substituting those expressions into equation (20), the undetermined coefficients in these equations can be found and various quantities in different regions can be evaluated.

In general, for homogeneous materials, the reflection coefficient from the boundary between a fluid and a matching layer will be zero when the thickness of the matching layer is quarter wavelength and its acoustic impedance Z^M is

$$Z^M = \sqrt{Z^W Z^S} \quad (22)$$

where Z^W and Z^S are the acoustic impedance of the media on the two sides of the matching layer, respectively.^{1,2}

For a composite material, from the results obtained in the preceding sections, it is expected that the parameters of the anti-reflection matching layer will be modified. Figure 17 illustrates the derived reflection coefficient from the boundary between the fluid and matching layer for different matching layer materials where the thickness of the matching layer is chose so that the frequency of the reflection coefficient minimum is at $fd=0.335$ MHz*mm. From results, it is found that the acoustic impedance of the matching layer from which the reflection coefficient becomes zero satisfies approximately equation (22) if Z^S is replaced by the effective input acoustic impedance of the 2-2 composite at the low frequency. However, the thickness of the matching layer is no longer quarter wavelength and in fact, it is shorter than $\lambda/4$. These results are summarized in figure 18. The data in figure 18(a) is the acoustic impedance of the matching layer in order for the reflection coefficient to be zero as a function of frequency. In figure 18(b), the change of the matching layer thickness as a function of frequency is presented where $t=1$ corresponds to the thickness of $\lambda/4$ at that frequency. Therefore, as the frequency increases, both the acoustic impedance and the thickness of the matching layer decrease. For example, when the frequency changes from 0.05 MHz*mm to 0.5 MHz*mm, the acoustic impedance of the matching layer changes from 4.70 MRayls to 4.45 MRayls and the thickness t changes from about $\lambda/4$ to $0.86*\lambda/4$. The reduction in the matching layer thickness is a

direct result of the fact that the incident plane wave suffers more than 180° phase loss upon the reflection from the interface.

From the fact that in the frequency range of interest, the evanescent waves at the interface will decay approximately as $\exp(-2\pi x_3/d)$, the effect of the interface of $x_3=t$, where t is approximately $\lambda/4$, to the surface vibration distribution at the composite-matching layer interface will be quite small. Therefore, the reflection coefficient introduced in the section III between the composite and a solid medium can be used to approximate the reflection at the matching layer-composite interface. Hence, the reflection coefficient R from the system in figure 16 can be approximated as:

$$R = \frac{R_{12} + R_{23}e^{2j\beta_o t}}{1 + R_{12}R_{23}e^{2j\beta_o t}} \quad (23)$$

where R_{12} and R_{23} are the reflection coefficients at the fluid-matching layer interface and matching layer-2-2 composite interface, respectively. In eq. (23), R_{12} is the reflection coefficient from the interface of two semi-infinite media of the fluid and solid, and R_{23} is that derived in the section III (the reflection coefficient from the solid medium-composite interface). From equation (23), the requirements to the matching layer to achieve the total transmission ($R=0$) can be derived. The acoustic impedance of the matching layer is

$$Z^M = \sqrt{Z^W |Z^{Cm}| \frac{|Z^{Cm}| - Z^W \cos(\theta)}{|Z^{Cm}| \cos(\theta) - Z^W}} \quad (24)$$

where θ is the phase angle of the acoustic impedance of the 2-2 composite. The thickness of the matching layer is

$$t = \frac{\lambda}{4} \left\{ 1 - \frac{1}{\pi} \arctan \left(\frac{2Z^M |Z^{Cm}| \sin(\vartheta)}{|Z^{Cm}|^2 - (Z^M)^2} \right) \right\} \quad (25)$$

In the frequency range of interest, the results from eqs. (24) and (25) are almost identical to those derived from the numerical calculation presented in figure 18.

In order to verify the theoretical predictions, the reflection coefficient from a fluid-matching layer interface was measured as a function of frequency utilizing the experimental set-up shown in figure 4 where a stainless steel standard was used as the reference. For a 2-2 composite with 44% PZT-5H ceramic in a Spurr epoxy matrix, the required acoustic impedance for the matching layer in frequencies near $f d = 0.5$ (MHz mm) is about 4.45 MRayls. A series of polymer were examined and the acoustic velocity was determined from the time of flight technique. Combined with the data on the density, the acoustic impedance of the material can be obtained. A Hysol epoxy (EE1068) was chosen because the acoustic impedance $Z = 4.68$ Mrayls ($\rho = 1610 \text{ kg/m}^2$, $c_{11} = 1.3634 \times 10^{10} \text{ N/m}^2$, and $c_{44} = 3.432 \times 10^9 \text{ N/m}^2$) is quite close to the required value.²⁰ For a fixed thickness t of the matching layer, the frequency position of the minimum reflection can be determined and the ratio of $4t/\lambda$ is obtained. By varying the thickness of the matching layer, the dependence of $4t/\lambda$ on the frequency can be obtained. The data is presented in Fig. 18(b) (open circles) and apparently, there is an excellent accord between the theoretical prediction and experimental data.

V. Summary and Acknowledgment:

The reflection and transmission of a plane acoustic wave at a medium-composite interface and the issues related to the design of matching layer for a composite are analyzed based on an approach developed recently, which can address explicitly the non-uniform field distributions due to the heterogeneity structure of a piezoceramic polymer composite. It has been shown that the reflection coefficient from the interface is a complex and the reflected wave suffers a more than 180° phase change. The effective input acoustic impedance Z_{in} of the composite at the interface was evaluated and both the amplitude and phase show a strong frequency dependence. For a fluid medium, it was found that Z_{in} does not change with the acoustic impedance of the medium. However, for a solid medium, Z_{in} will change if the shear stiffness

constant of the medium changes. It was demonstrated that this difference originates from the non-uniformity of the surface vibration distribution of the composite at the interface which depends crucially on the shear stiffness constant of the medium.

Since for a piezoceramic polymer composite, it is the ceramic phase which performs the energy conversion between the acoustic and electric forms, how much acoustic energy can enter the ceramic region is one of the most important parameters in a composite transducer design. In the paper, we show that even though the effective transmission coefficient increases as the frequency is increased, the amount of acoustic energy entering the ceramic region actually decreases. Therefore, there may be a trade-off between the bandwidth, which is related to the transmission coefficient, and the sensitivity in the composite transducer design.

From the fact that there is more than 180° phase change in the reflection from the medium-composite interface, it is shown that the matching layer thickness is no longer equal to the quarter wavelength but smaller than that. In addition, the acoustic impedance of the matching layer will also be affected by the phase of Z_{in} of the composite, although the effect is not as significant as that in the thickness of the matching layer.

Reflection experiment was conducted from both the fluid-composite interface and the fluid-matching layer interface and the agreement between the experimental results and theoretical prediction is quite good.

The authors wish to thank Dr. J. Yuan of ATL/Echo Ultrasound for the assistance during this investigation. This work was supported by the Office of Naval Research under the Grant No: N00014-96-0357.

References:

1. L. M. Berkhovskikh, "Waves in Layered Media" (Academic Press, New York 1980).
2. B. A. Auld, "Acoustic Fields and Waves in Solids" Vol. I & II (John Wiley & Sons, New York 1973).
3. T. R. Gururaja, W. A. Schulze, L. E. Cross, R. E. Newnham, B. A. Auld, and J. Wang, IEEE Trans UFFC SU32, 481 (1985).
4. W. A. Smith, Proc. 1990 IEEE 7th ISAF (Urbana, Illinois 1990), 145.
5. R. E. Newnham, D. P. Skinner, and L. E. Cross, Mater. Res. Bull. 13, 525 (1978).
6. B. A. Auld, Mater. Sci. & Eng. A122, 65 (1989).
7. H. F. Tiersten, "Linear Piezoelectric Plate Vibrations" (Plenum, New York, 1969).
8. Q. M. Zhang and Xuecang Geng, J. Appl. Phys. 80, 5503 (1996).
9. PZT-5H is the trade-mark of Morgan Mattroc Inc. (Beddford, OH 44146) for one of its PZT piezoceramics. Spurr epoxy is the trade-mark of Polysciences, Inc. (Warrington, PA 18976). Their parameters are: PZT-5H: $e_{33} = 23.09 \text{ C/m}^2$, $e_{31} = -6.603 \text{ C/m}^2$, $e_{15} = 17.0 \text{ C/m}^2$, $c_{11} = 12.72 \times 10^{10} \text{ N/m}^2$, $c_{44} = 2.3 \times 10^{10} \text{ N/m}^2$, $c_{33} = 11.74 \times 10^{10} \text{ N/m}^2$, $c_{13} = 8.47 \times 10^{10} \text{ N/m}^2$, $K_{11} = 1700$, $K_{33} = 1470$, $\rho = 7500 \text{ kg/m}^3$. Spurr epoxy: $c_{11} = 5.4 \times 10^9 \text{ N/m}^2$, $c_{44} = 1.3 \times 10^9 \text{ N/m}^2$, $\rho = 1100 \text{ kg/m}^3$.
10. Xuecang and Q. M. Zhang, Submitted to IEEE Trans. UFFC (1996).
11. W. A. Smith and B. Auld, IEEE Trans. UFFC 38, 40 (1988).
12. K. Y. Hashimoto and M. Yamaguchi, Proc. 1986 IEEE Ultrasonics Symp. (Williamsburg, VA), 697 (1986).
13. Donald E. Hall, "Basic Acoustics" (Happer & Row, Publishers, NY 1987).
14. G. F. Miller and H. Pursey, Proc. Royal Soc. of London 223, 521 (1954).
15. C. S. Desilets, Ph. D. Thesis, Stanford University (1978).
16. G. S. Kino, "Acoustic Waves: Devices, Imaging, & Analog Signal Processing" (Prentice-Hall, Inc. Englewood Cliffs, New Jersey 1987).

17. D. A. Berlincourt, D. R. Curran, and H. Jaffe, in "Physical Acoustics" Vol. I, part A, ed. W. P. Mason (Academic Press, NY 1964).
18. D. Leedom, R. Krimholtz, and G. Matthaei, IEEE Trans. on Sonics and Ultrasonics, SU-18, 128 (1971).
19. Wenwu Cao, Q. M. Zhang, J. Zhao, and L. E. Cross, IEEE Trans. UFFC 42, 37 (1995).
20. Hysol epoxy is from Hysol electronic chemicals division, CA 91746.

Figure captions:

Figure 1. (a) Schematic of a 2-2 piezoceramic polymer composite where the dimensions in both the x_1 and x_2 directions are much larger than the period d . (b) Schematic of an interface between a fluid and a 2-2 piezocomposite where a plane acoustic wave normally incents to the interface from the fluid medium. The composite occupies the semi-infinite space $x_3 > 0$.

Figure 2. The dispersion curves for the 2-2 composite of PZT-5H ceramic and Spurrs epoxy where the ceramic content is 44%.

Figure 3. The reflection coefficient (both the amplitude and phase) as a function of frequency for 2-2 composites with (a) 44% ceramic and (b) 15% ceramic content. The anomalous changes at $fd = 1$ in (a) and $fd = 0.8$ in (b) are related to the lateral resonant mode in these composites, respectively. The experimental data are shown in (a) where the open circles are the amplitude and solid circles are the phase of the measured reflection coefficient.

Figure 4. Schematic of the set-up used to measure the reflection coefficient of 2-2 composites. In order to obtain phase information of the reflection coefficient, the distance between the probe transducer and the 2-2 composite is maintained the same as that between the probe and the stainless steel standard.

Figure 5. (a) The effective input acoustic impedance Z_{in} of the 2-2 composite with 44% ceramic content calculated from the data in figure 3 (the reflection coefficient). (b) Z_{in} for the 2-2 composite with 15% ceramic volume content.

Figure 6. The effective input impedance Z_{in} calculated from eq. (16) for (a) the composite of 44% ceramic volume content and (b) the composite of 15% ceramic content. The results here are nearly the same as those in figure 5 except at frequencies above the first lateral mode.

Figure 7. Z_{in} of the composite of 44% volume content derived from the reflection coefficient for fluid media with different acoustic impedance: $Z_1 = 1.48$ Mrayls (water), and $Z_2 = 2.09$ Mrayls. Apparently, Z_{in} of the composite for the two cases overlaps with each other indicating that it does not change with the acoustic impedance of the fluid medium.

Figure 8. (a) The surface vibration distribution as a function of frequency for the 2-2 composite with 44% ceramic content at the interface with water and under an acoustic field. u_3^p and u_3^c are the displacement at the center of the polymer plate ($x_1=d/2$) and ceramic plate ($x_1=0$). (b) The acoustic energy (in reduced units) entering the ceramic and polymer regions as a function of frequency evaluated at the interface ($x_3=0$) where P_0 is the total energy in the incident wave.

Figure 9. The energy redistribution inside the composite along the x_3 -direction where $x_3=0$ is the interface. There is an energy transfer from the polymer to the ceramic inside the composite. As shown in the figures, the width of the transition region increases as the frequency increases (in reduced length unit).

Figure 10. The vibration profile as a function of the distance from the interface with water ($x_3=0$) where u_3^p and u_3^c are the displacement at the center of the polymer plate ($x_1=d/2$) and ceramic plate ($x_1=0$). At low frequencies, the polymer and ceramic vibrate with the same amplitude and phase while at high frequencies, even far away from the interface, the vibration amplitude of the two is still not the same while the phase becomes the same.

Figure 11. The effective input impedance from eq. (16) as a function of the distance from the interface with water ($x_3=0$) at three typical frequencies: far below the lateral mode, at about the half of the lateral mode frequency, and near the lateral mode frequency.

Figure 12. (a) The reflection coefficient at a interface between a solid medium ($Z=2.4$ MRayls) and a 2-2 composite of 44% ceramic volume content as a function of frequency. (b) The effective input acoustic imedance of a 2-2 composite of 44% ceramic volume content as a function of frequency. Z_{in} is calculated from the reflection coefficient.

Figure 13. Data illustrate the dependence of the input acoustic impedance of a composite on the elastic properties of the solid medium at the interface. (a) The solid medium for the curve 1 is $\rho=1.61 \text{ g/cm}^3$, $c_{11} = 1.36*10^{10} \text{ N/m}^2$, and $c_{44} = 3.43*10^9 \text{ N/m}^2$, and for the curve 2 and curve 3, both ρ and c_{11} are kept constant and $c_{44} = 6.86*10^9 \text{ N/m}^2$ and $c_{44} = 1.72*10^9$

N/m^2 . (b) Here both ρ and c_{44} are kept constant, and $c_{11} = 0.68 * 10^{10}$, $c_{11} = 1.36 * 10^{10}$, and $c_{11} = 2.72 * 10^{10} \text{ N/m}^2$. The amplitude of Z_{in} does not change much with c_{11} except a small change in the phase.

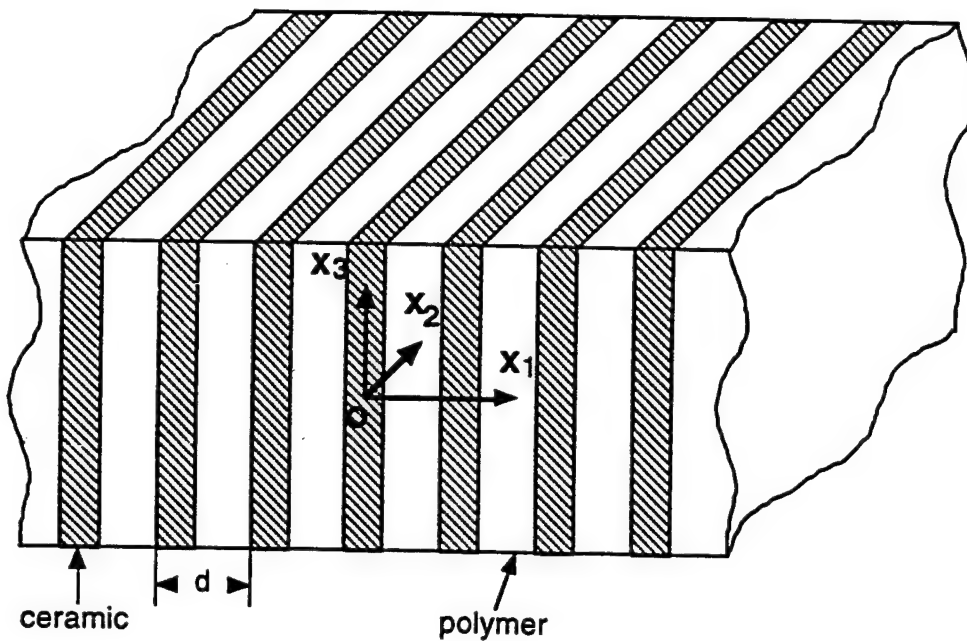
Figure 14. The figures illustrate the effect of c_{11} and c_{44} of the solid medium on the surface vibration profile of the composite. (a) The parameters of the solid medium for the data of dashed curve is $\rho=1.61 \text{ g/cm}^3$, $c_{11} = 1.36 * 10^{10} \text{ N/m}^2$, and $c_{44} = 3.43 * 10^9 \text{ N/m}^2$, and for the solid curve, both ρ , c_{44} are the same except $c_{11}=2.72*10^{10} \text{ N/m}^2$. (b) The parameters for the solid medium is $\rho=1.61 \text{ g/cm}^3$, $c_{11} = 1.36 * 10^{10} \text{ N/m}^2$, and $c_{44} = 6.86 * 10^9 \text{ N/m}^2$. Notice the effect of c_{44} on the surface vibration profile of the composite.

Figure 15. The figures illustrate the effect of the elastic properties of the solid medium at the interface on the effective input impedance distribution along the x_3 -axis at a frequency $f*d = 0.446 \text{ MHz*mm}$ where $x_3=0$ is the interface. (a) The dashed line: $\rho=1.16 \text{ g/cm}^3$, $c_{11}=7.72 * 10^9 \text{ N/m}^2$, and $c_{44} = 1.588 * 10^9 \text{ N/m}^2$. The solid line: $\rho=1.1 \text{ g/cm}^3$, $c_{11} = 5.41 * 10^9 \text{ N/m}^2$, and $c_{44} = 1.307 * 10^9 \text{ N/m}^2$ (Spurrs epoxy). (b) The parameters for the solid medium is: $\rho=1.61 \text{ g/cm}^3$, $c_{11} = 1.36 * 10^{10} \text{ N/m}^2$, and $c_{44} = 3.43 * 10^9 \text{ N/m}^2$.

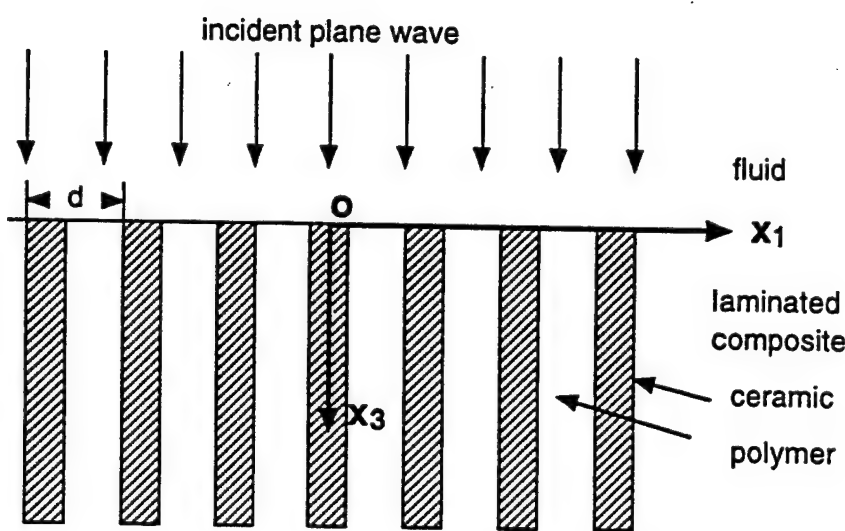
Figure 16. Schematic of an interface system consisting of a fluid medium (medium 1), a matching layer, and a 2-2 composite. The thickness of the matching layer is t and the period of the composite is d .

Figure 17. The reflection coefficient from the matching layer system where the total transmission occurs at $f*d = 0.334 \text{ MHz*mm}$ for the matching layer with $t = 2.02*d = 0.91*(\lambda/4)$ (at $f*d = 0.334 \text{ MHz*mm}$) and $Z^M=4.68 \text{ Mrayls}$ ($\rho=1.61 \text{ g/cm}^3$, $c_{11} = 1.36 * 10^{10} \text{ N/m}^2$, and $c_{44} = 3.43 * 10^9 \text{ N/m}^2$) (the curve 1). For the comparison, the reflection coefficient from the matching layers with other parameters is also shown here: for the curve 2, $Z^M = 3.0 \text{ Mrayls}$ and $t = 1.85*d$, and for the curve 3, $Z^M = 2.44 \text{ Mrayls}$ and $t = 1.58*d$.

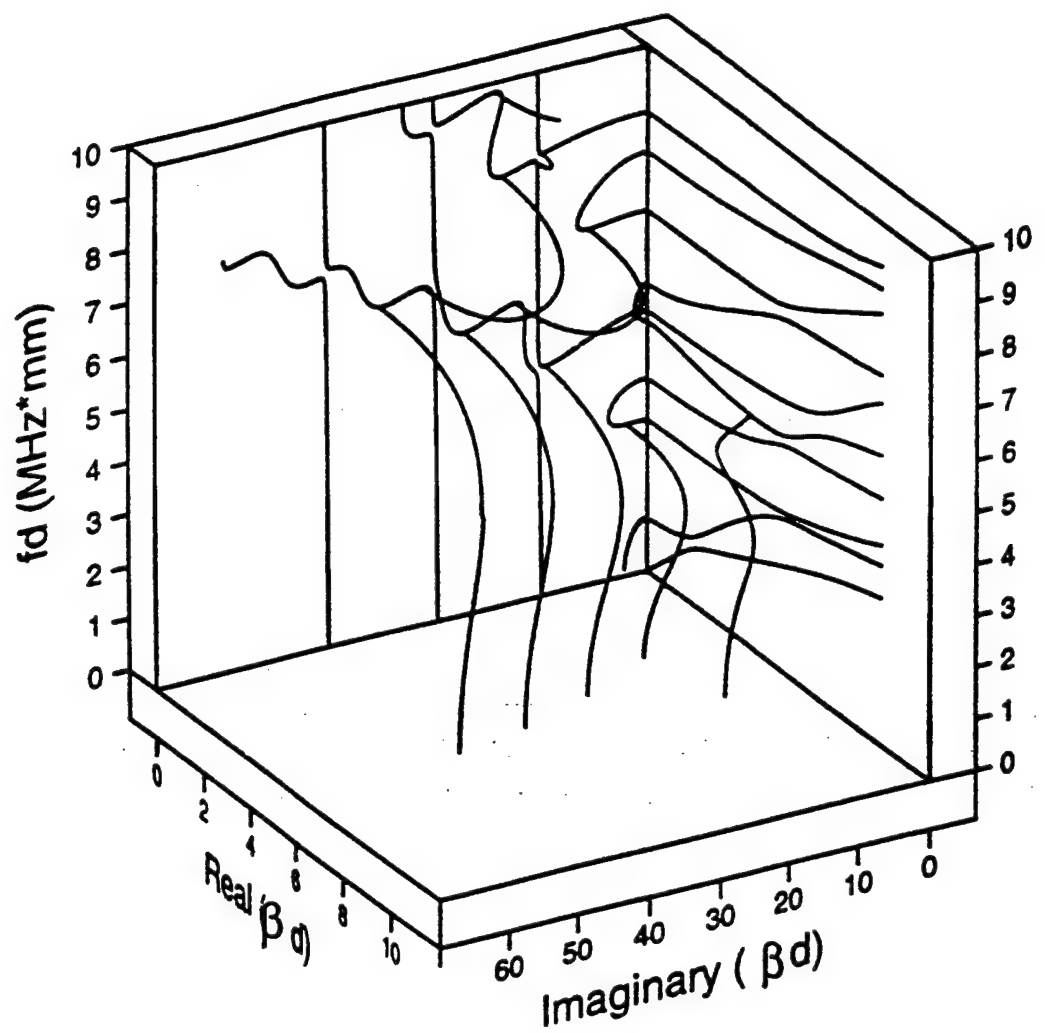
Figure 18. The required parameters for (a) Z^M and (b) t of the matching layer to have total transmission as a function of frequency for a water-2-2 composite (44% ceramic volume content) interface (solid lines are the theoretical predictions). The experimental data was presented in (b) as open circles.



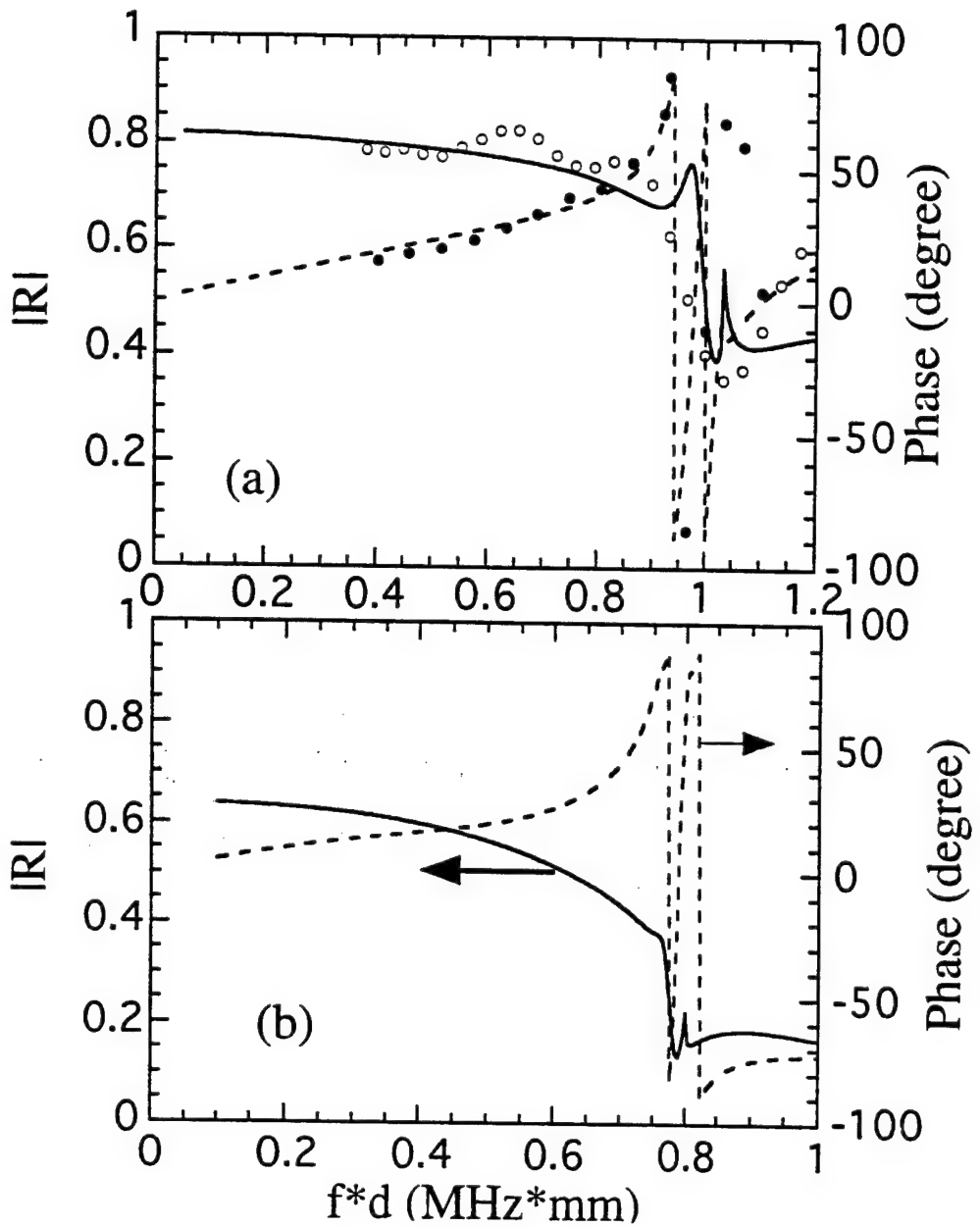
(a)



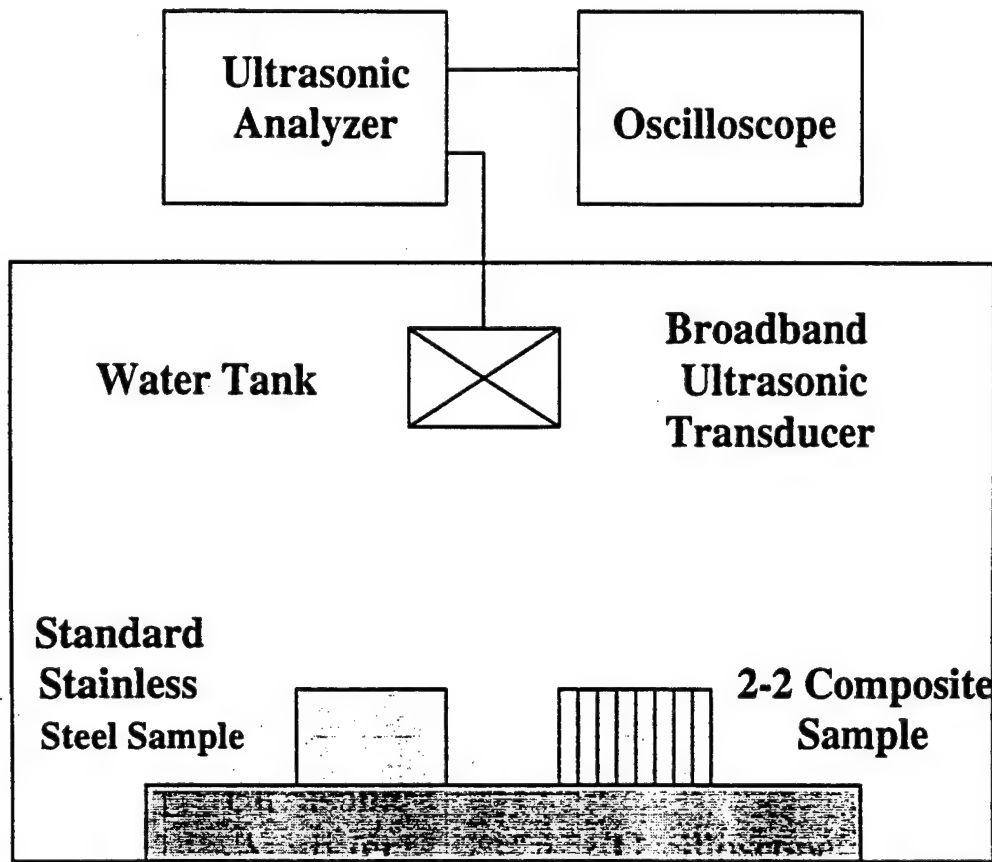
(b)

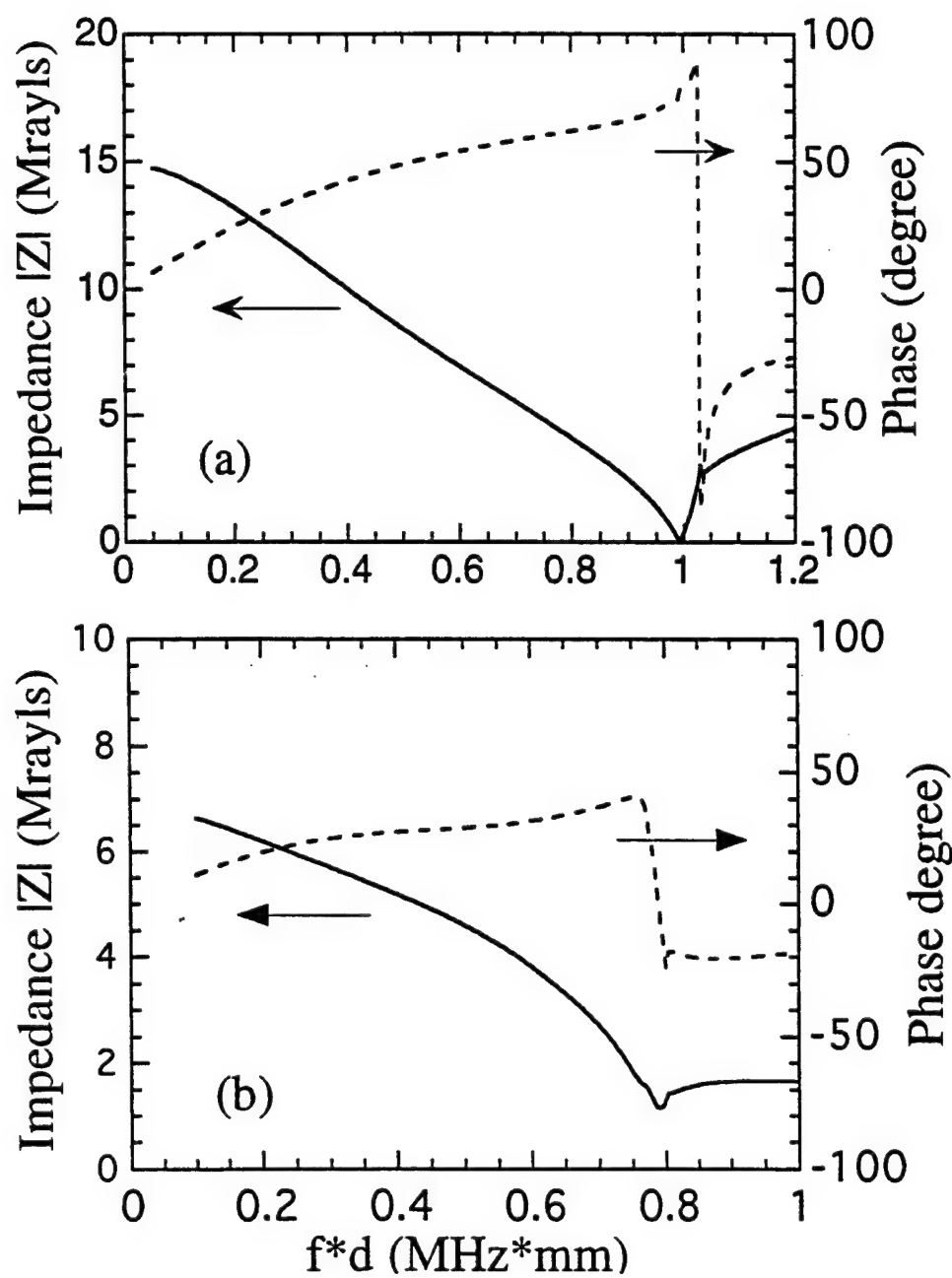


F2

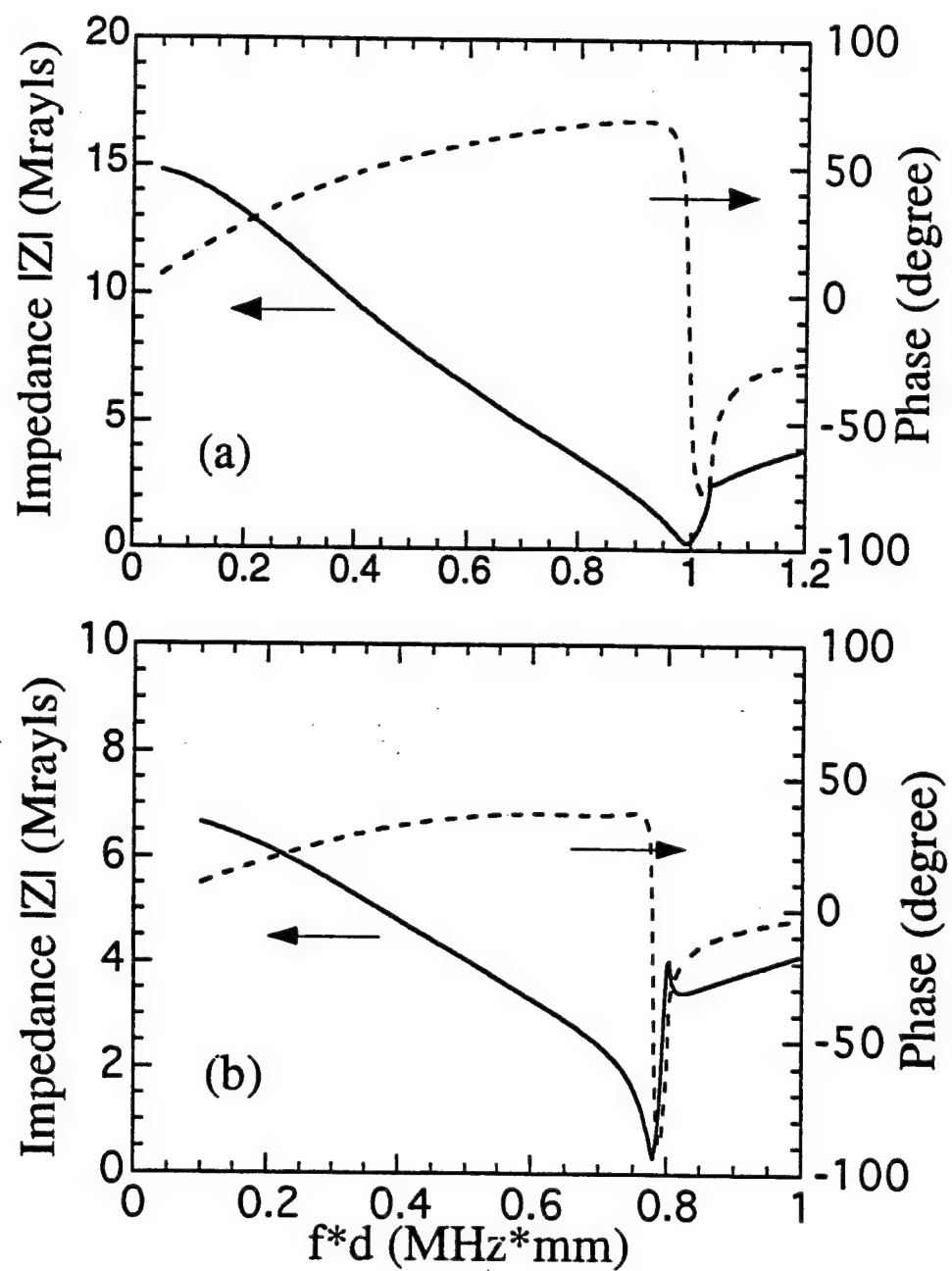


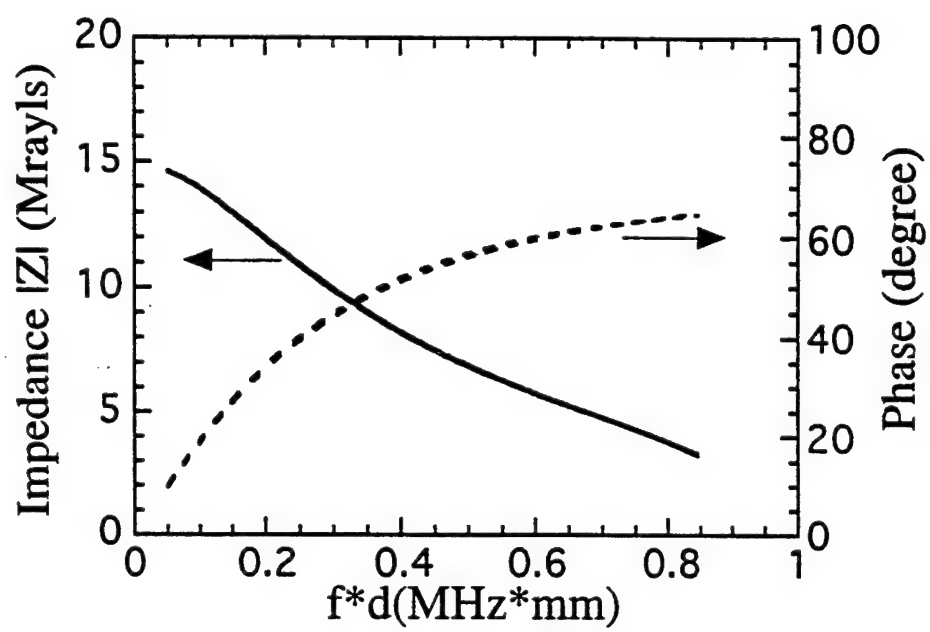
F.3



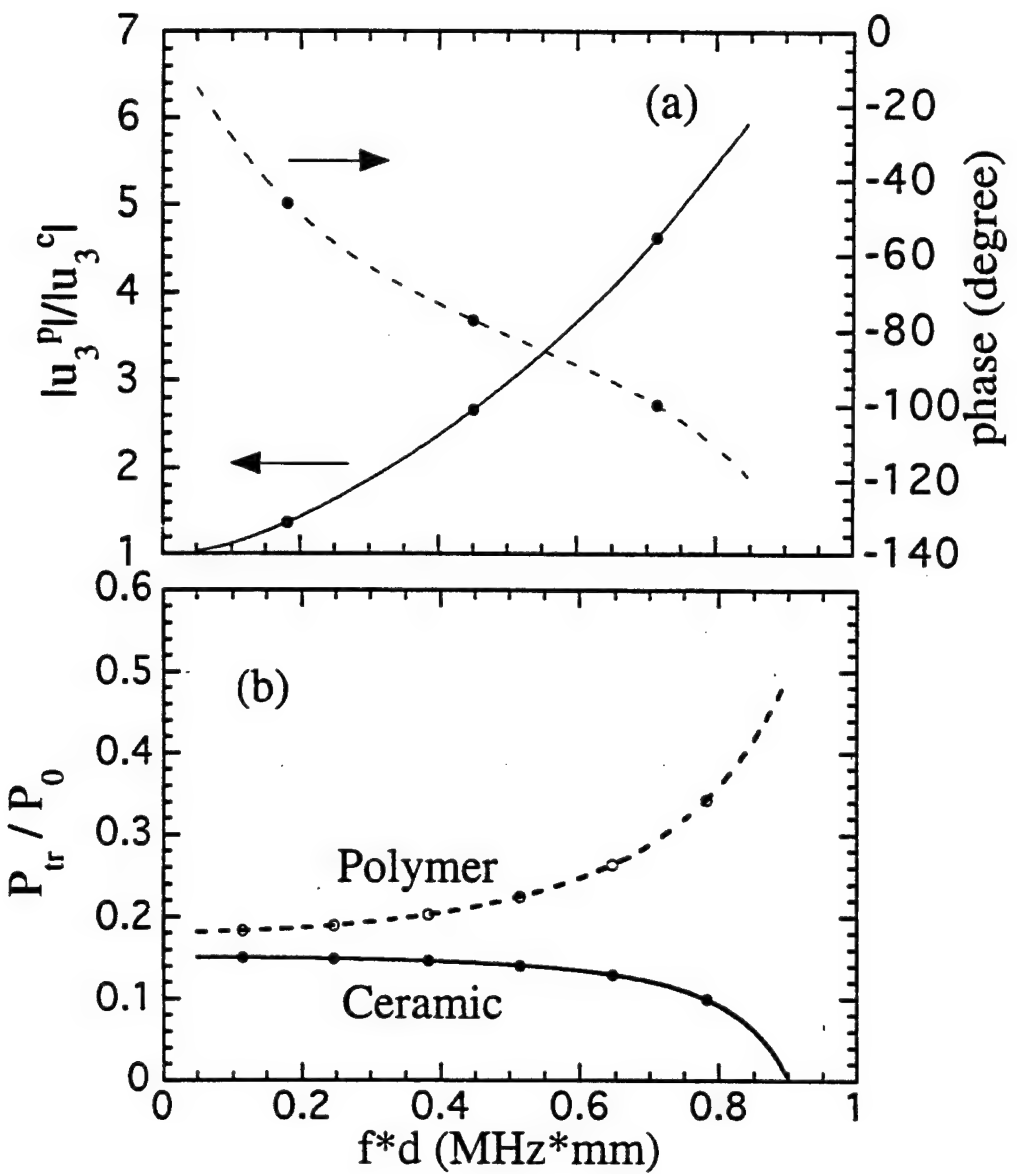


F.5

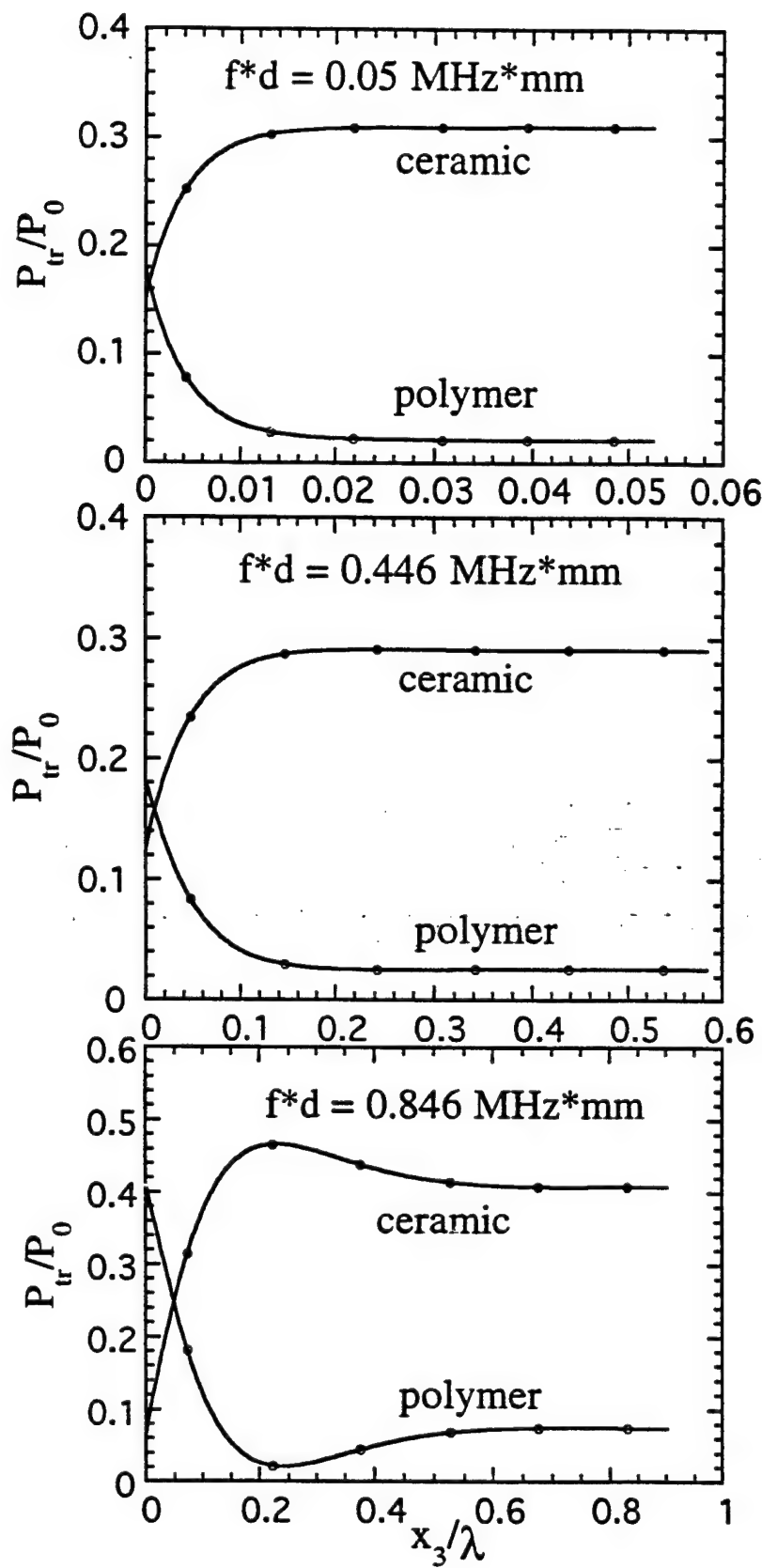


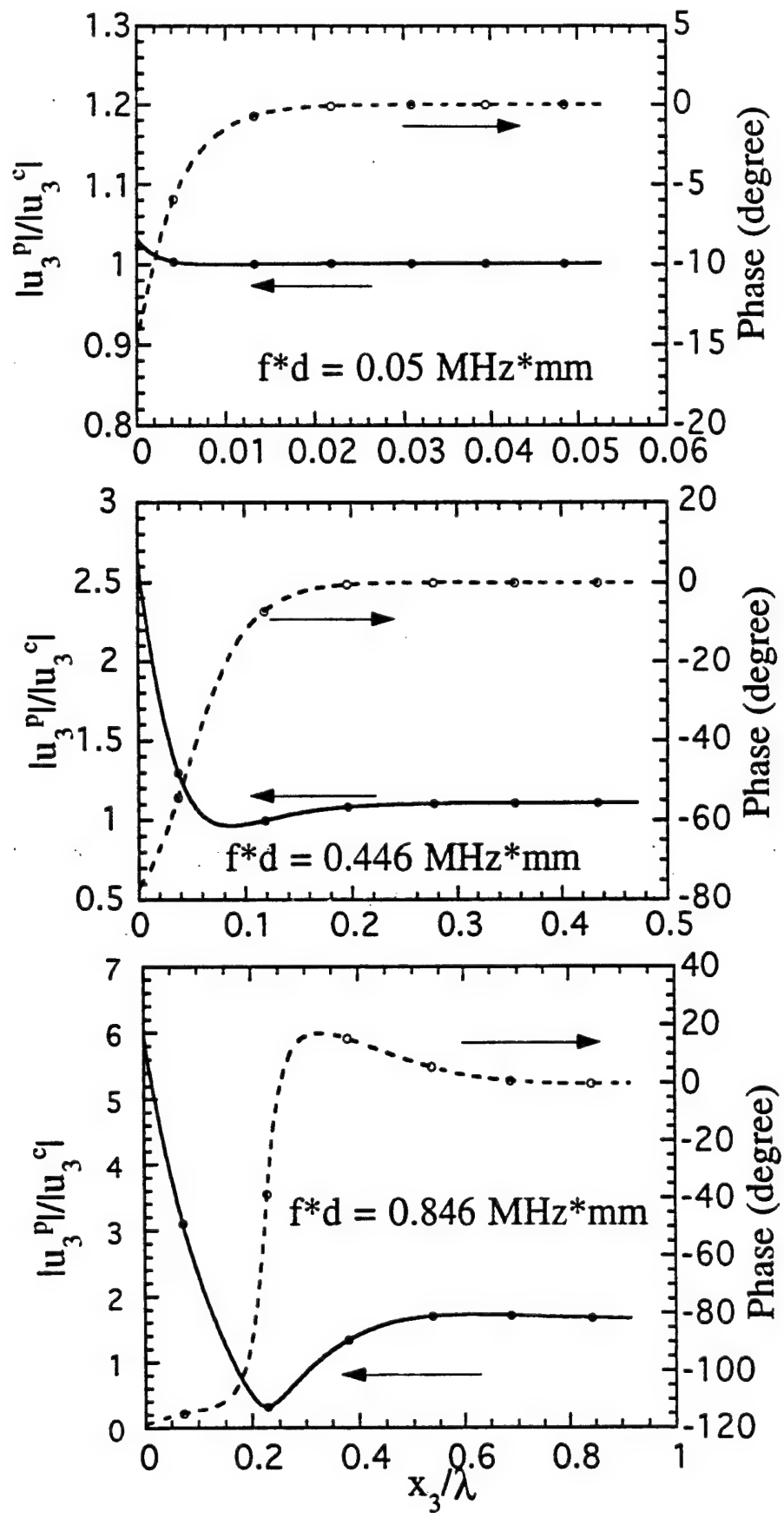


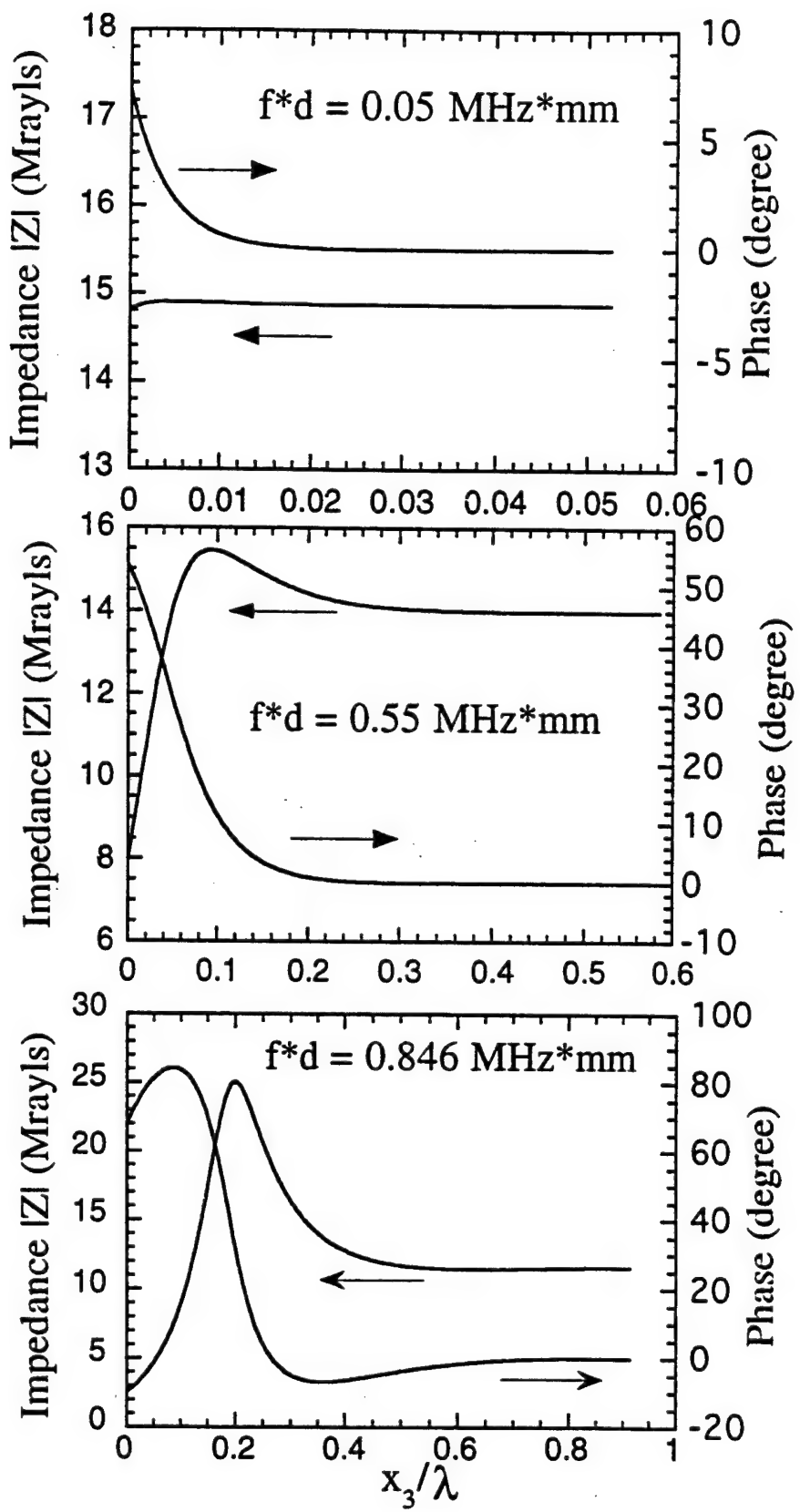
F.7

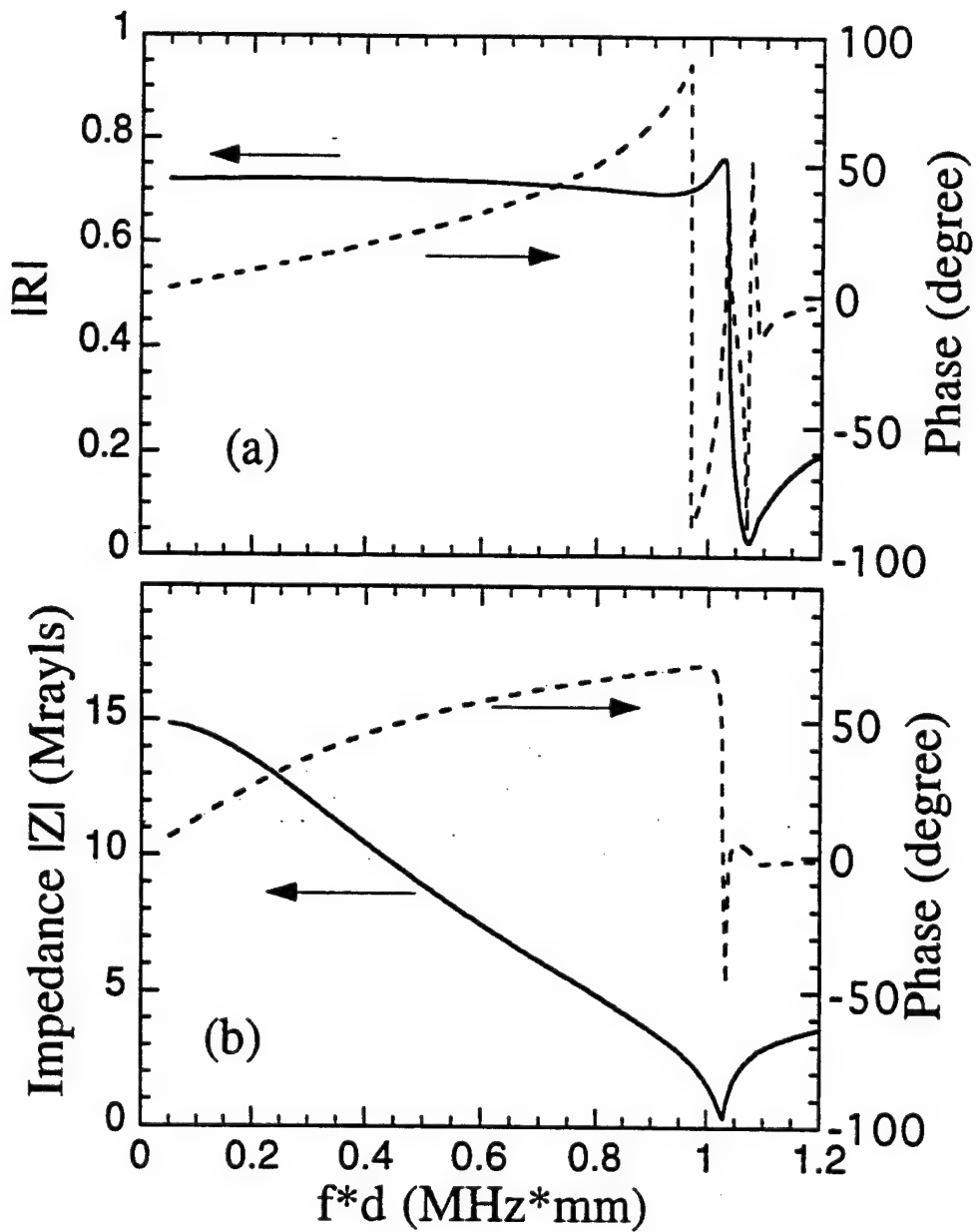


7

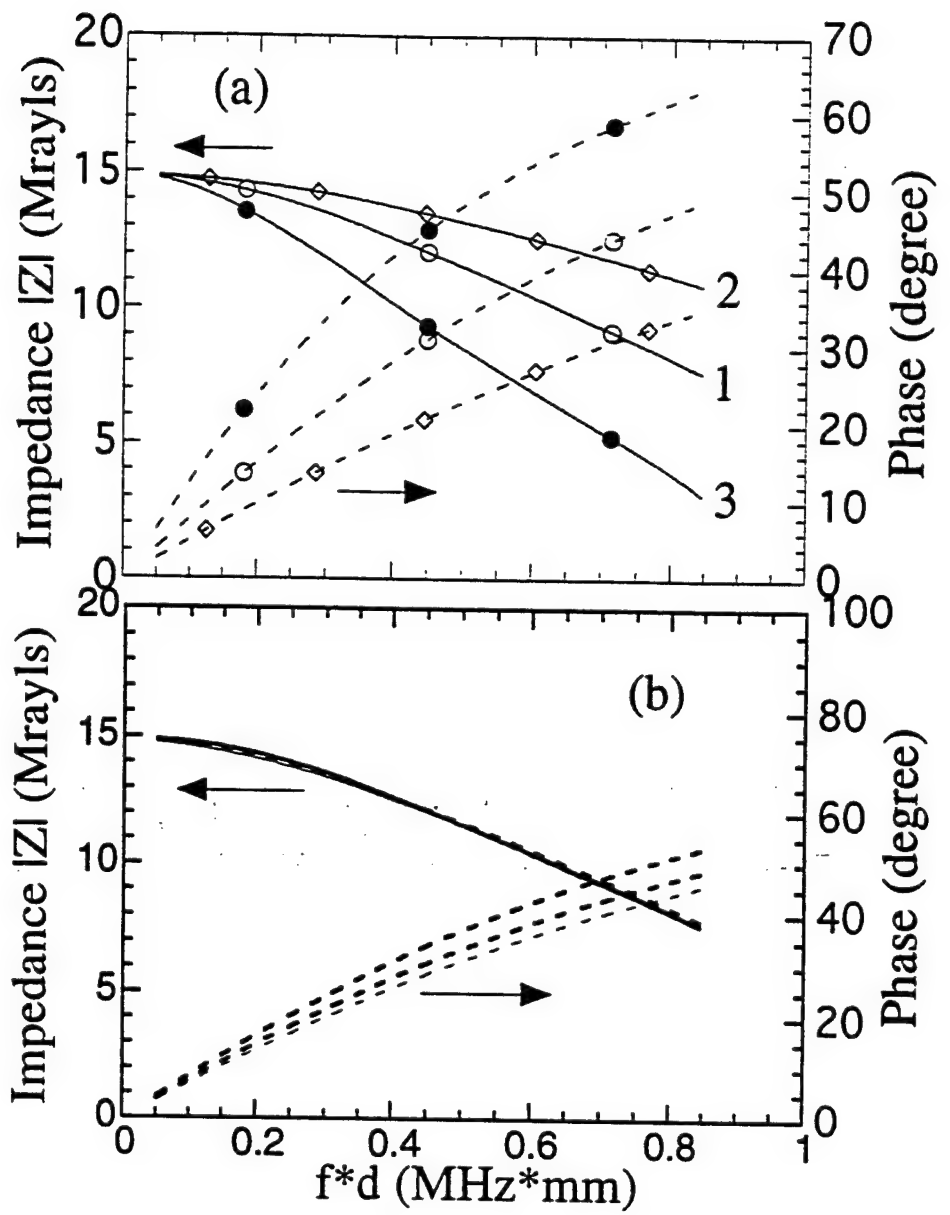




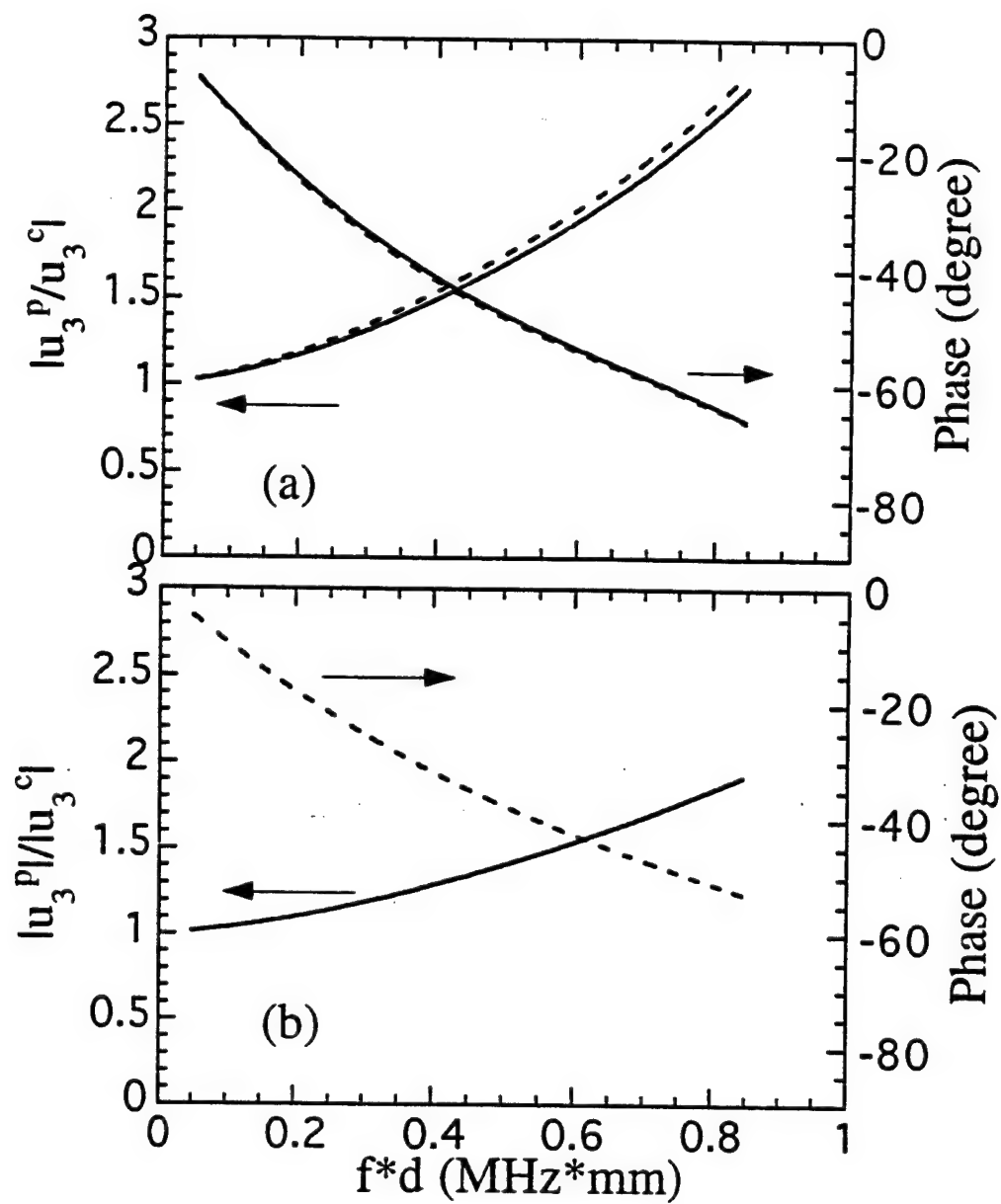


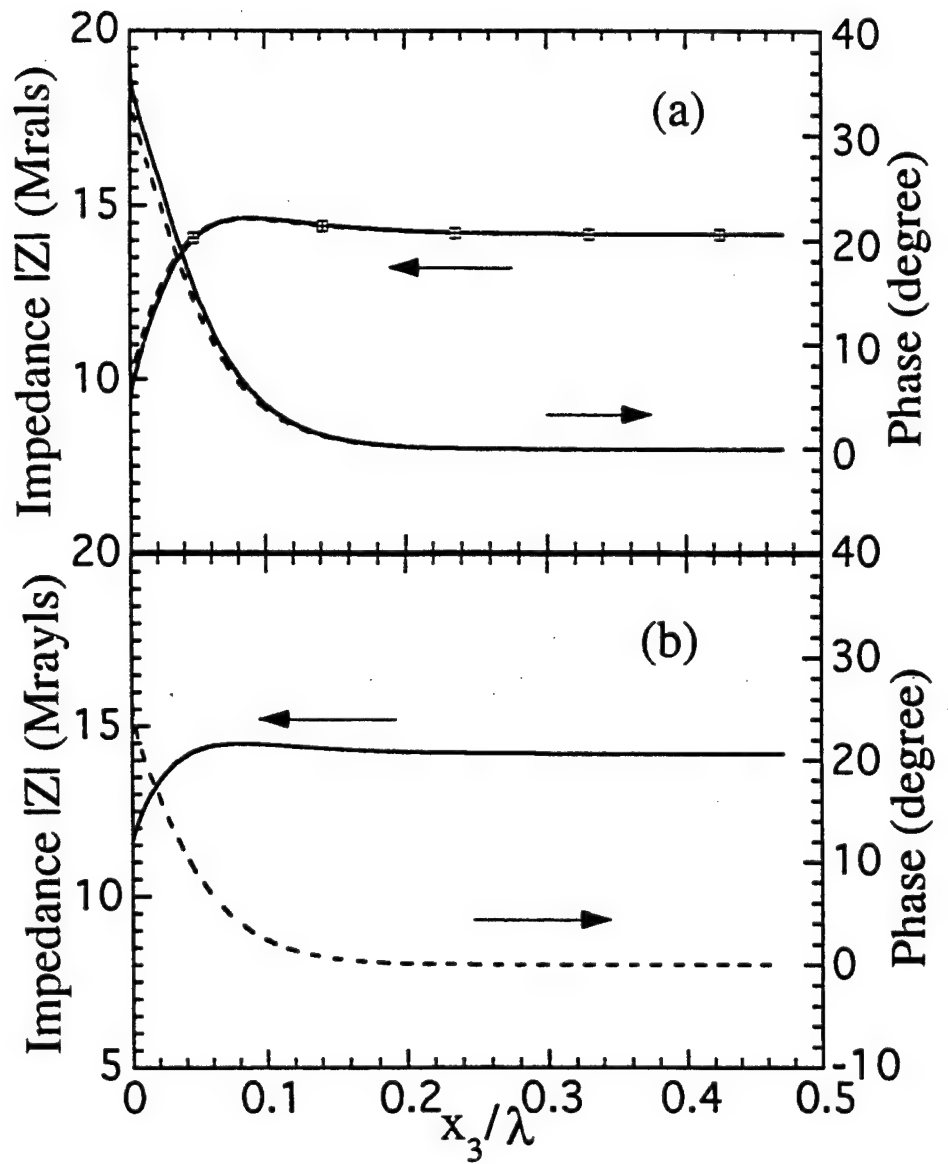


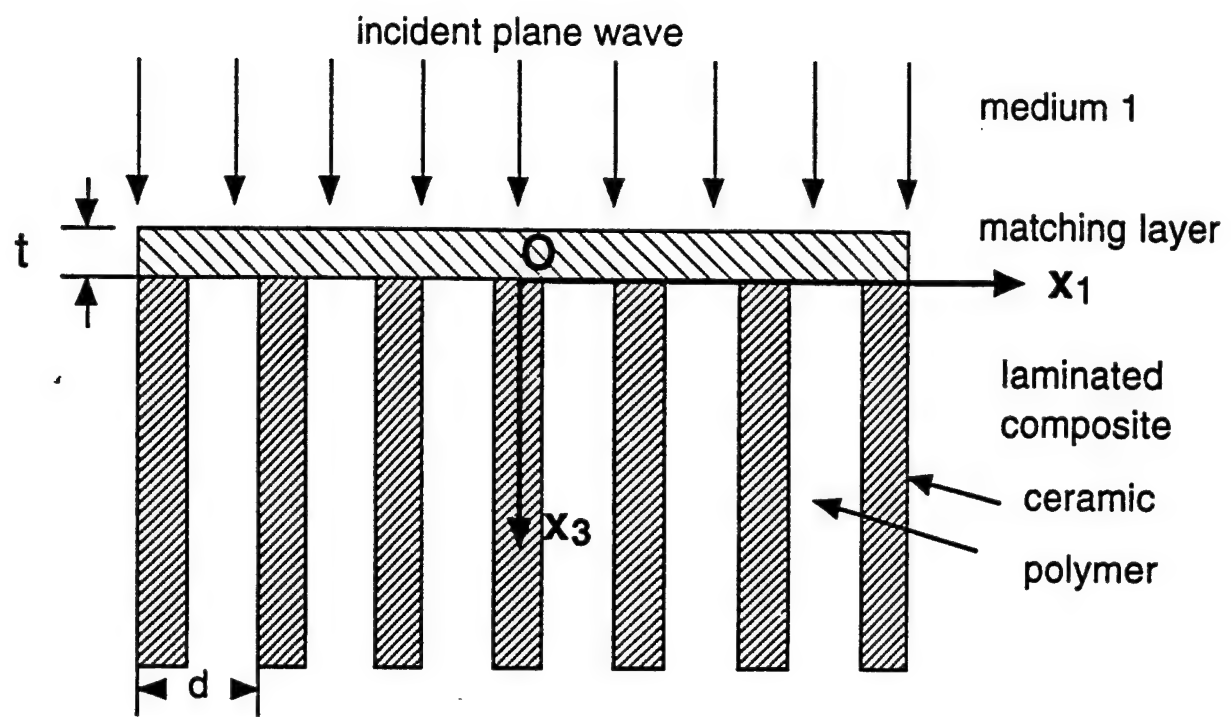
F. 12



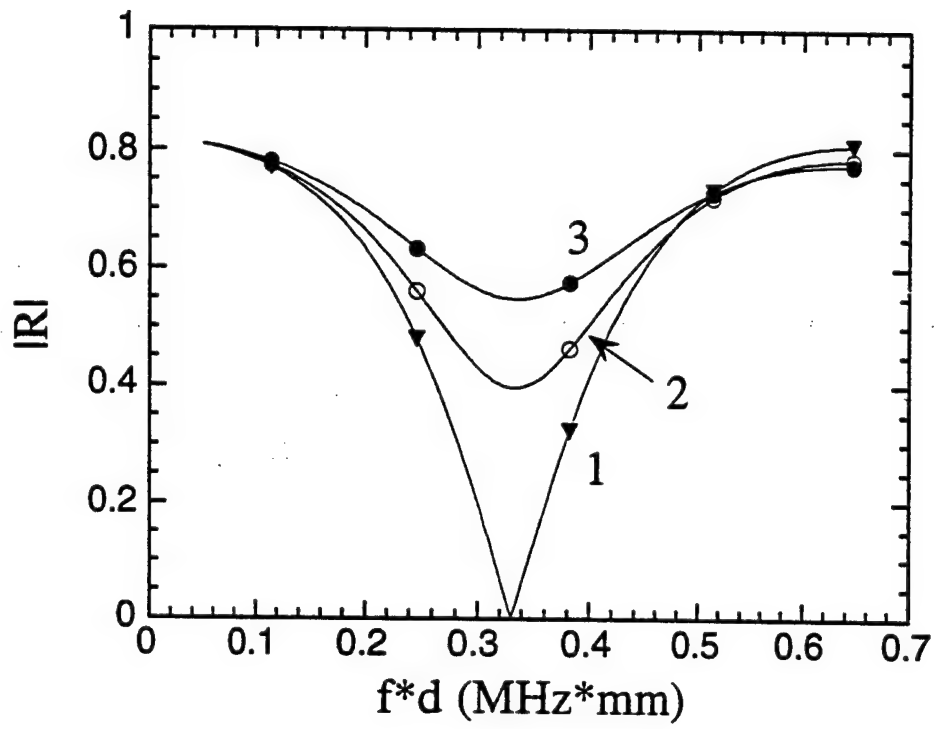
F.13



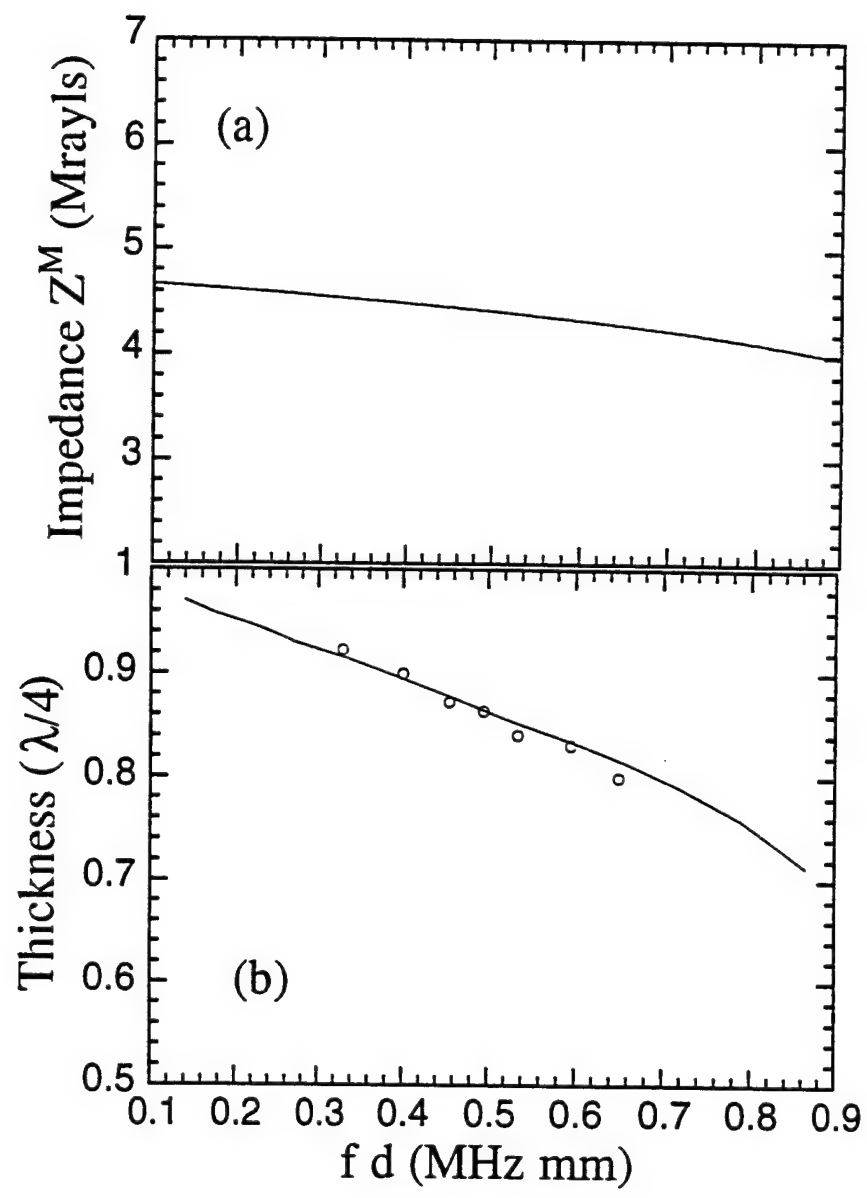




F.16



F. 17



ACTUATOR STUDIES

APPENDIX 51

ULTRAHIGH STRAIN AND PIEZOELECTRIC BEHAVIOR IN RELAXOR BASED FERROELECTRIC SINGLE CRYSTALS

Seung-Eek Park and Thomas R. Shrout

Materials Research Laboratory, The Pennsylvania State University, University Park, PA 16802

Abstract

The piezoelectric properties of relaxor based ferroelectric single crystals, such as $\text{Pb}(\text{Zn}_{1/3}\text{Nb}_{2/3})\text{O}_3 - \text{PbTiO}_3$ (PZN-PT) and $\text{Pb}(\text{Mg}_{1/3}\text{Nb}_{2/3})\text{O}_3 - \text{PbTiO}_3$ (PMN-PT) were investigated for electromechanical actuators. In contrast to polycrystalline materials such as $\text{Pb}(\text{Zr},\text{Ti})\text{O}_3$ (PZT's), morphotropic phase boundary (MPB) compositions were not essential for high piezoelectric strain. Piezoelectric coefficients (d_{33} 's) $> 2500 \text{ pC/N}$ and subsequent strain levels up to $>0.6\%$ with minimal hysteresis were observed. Crystallographically, high strains are achieved for $<001>$ oriented rhombohedral crystals, though $<111>$ is the polar direction. Ultrahigh strain levels up to 1.7%, an order of magnitude larger than those available from conventional piezoelectric and electrostrictive ceramics could be achieved, being related to an E-field induced phase transformation. High electromechanical coupling (k_{33}) $> 90\%$ and low dielectric loss $<1\%$, along with large strain make these crystals promising candidates for high performance solid state actuators.

Keywords : Relaxor ferroelectrics, single crystal, actuator, piezoelectrics, phase transformations, hysteresis, domains.

1. Introduction

Electromechanical actuators directly transform input electrical energy into mechanical energy. Of the many types of actuator materials including, magnetostrictive, photostrictive, and shape memory alloys, piezoelectric and electrostrictive ceramics are widely used in applications requiring high generative force, high frequency operation, accurate displacement, quick response time, or small device size [1]. Generally, among the material properties determining actuator performance, the electric field (E-field) induced strain is the most important parameter for actuators. This is demonstrated by strain energy density which is a measure of the energy per unit mass an actuator can deliver,

$$e_{max} = 1/\rho \cdot 1/4 \cdot (1/2 \cdot E(s_{max})^2) \quad (1)$$

where e_{max} is the strain energy density, E is the actuator's elastic modulus, s_{max} is the maximum field induced strain, and ρ is the actuator's density. [1] $1/4$ is a factor of appropriate for an actuator with its impedance matching to that of its surroundings. In designing an actuator, the maximum strain energy density should be as high as possible. In electroactive ceramics, density and elastic modulus vary little from material to material, therefore, the level of strain and maximum strain achievable with a reasonable electric field (<50kV/cm) dominates the energy density. The piezoelectric coefficient (d_{ij}), determining the level of induced strain at a given electric field, is the most widely used parameter describing actuator performance.

It is the objective of this paper to report ultrahigh piezoelectric coefficients (d_{33}) and ultrahigh strain levels with low hysteresis observed for single crystals of relaxor perovskite

$\text{Pb}(\text{Zn}_{1/3}\text{Nb}_{2/3})\text{O}_3$ - PbTiO_3 (PZN-PT) and $\text{Pb}(\text{Mg}_{1/3}\text{Nb}_{2/3})\text{O}_3$ - PbTiO_3 (PMN-PT). Strain behavior as a function of E-field will be discussed with respect to crystal structure, orientation, domain configuration and anticipated actuator performance.

2. Background

2.1 Morphotropic phase boundary and electrostrictive ceramics

$\text{Pb}(\text{Zr}_{1-x}\text{Ti}_x)\text{O}_3$ (PZT) ceramics have been the mainstay for high performance actuator applications. Compositionally, PZT ceramics lie near the morphotropic phase boundary (MPB) between the tetragonal and rhombohedral phases as shown in figure 1. MPB compositions exhibit anomalously high dielectric and piezoelectric properties as a result of enhanced polarizability arising from the coupling between two equivalent energy states, i.e. the tetragonal and rhombohedral phases, allowing optimum domain reorientation during the poling process. Alternate MPB systems can be found in Relaxor- PbTiO_3 , also as shown in figure 1. Lead based relaxor materials are complex perovskites with the general formula $\text{Pb}(\text{B}_1\text{B}_2)\text{O}_3$, ($\text{B}_1=\text{Mg}^{2+}, \text{Zn}^{2+}, \text{Ni}^{2+}, \text{Sc}^{3+} \dots, \text{B}_2=\text{Nb}^{5+}, \text{Ta}^{5+}, \text{W}^{6+} \dots$). Characteristic of relaxors is a broad and frequency dispersive dielectric maxima [2].

To achieve a high piezoelectric coefficient, MPB-based ceramics are further engineered by compositionaly adjusting the Curie temperature (T_c) downward relative to room temperature. The effect of transition temperature (T_c) on the piezoelectric properties is clearly evident in figure 2. As shown, the room temperature values of d_{33} are plotted as a function of T_c for a variety of modified PZT ceramics, including Relaxor-PT systems. Enhanced piezoelectric activity of MPB-based ceramics, achieved by compositionaly adjusting T_c downward relative to

room temperature, results in ‘soft’ piezoelectric ceramics. This enhanced piezoelectric effect, therefore, comes with the expense of more temperature dependent properties, and less polarization stability, i.e. aging and loss of piezoelectric activity. Further details on the relationship between dielectric/piezoelectric properties and Curie temperature (T_c) of piezoelectric ceramics can be found in the article by S.-E. Park et al. [3]

Most importantly, a consequence of increased piezoelectric activity for these “soft” ceramics is large hysteresis in the strain vs. E-field behavior as a result of domain motion. Strain vs. E-field behavior for PZT-5H (Navy type -VI) is shown in figure 3 as an example. Though the piezoelectric coefficient (d_{33}) of PZT-5H ceramics is in the range of ~600 to 700 pC/N [4] (implying ~0.06 to 0.07% strain at 10 kV/cm), strain as high as 0.1% can be observed at 10kV/cm. This enhanced nonlinear strain is the result of domain motion, and therefore, accompanied by significant hysteresis, resulting in poor positioning accuracy. The area within the strain vs. E-field curve, or dielectric loss, also results in significant heat generation during operation. Heat generation combined with a decreased temperature usage range, results in poor temperature stability and limits these ceramics to low frequency applications.

Strain vs. E-field hysteresis can be minimized with the use of the “hard” piezoelectric ceramics. Hard piezoelectric ceramics such as PZT-8 (Navy type III) offer very low hysteresis as shown in figure 3. However, the reduction in hysteresis and loss comes at the expense of d_{33} and subsequent strain level. Typically d_{33} values, for ‘hard’ PZTs range from ~200 to 300 pC/N [4].

Another category of ceramic materials used in commercial actuators are electrostrictors. Electrostrictive strain is proportional to the square of polarization. A few materials such as PMN and its solid solution with PT exhibit significant electrostrictive strain (> 0.1%) with virtually no

hysteresis as shown in figure 3. Effective d_{33} 's > ~800 pC/N calculated directly from the strain vs. E-field curve can be achieved, but only over a very narrow range of E-field and temperature. For hard piezoelectric and electrostrictive ceramics, strain level with low hysteresis does not exceed 0.15%. This limitation originates from the material's dielectric breakdown strength and polarization saturation.

In summary, piezoelectric and electrostrictive ceramics offer strain levels up to ~ 0.15%. Soft PZT's, exhibiting piezoelectric coefficients (d_{33}) as high as 750 pC/N, are inherently limited due to hysteresis caused by domain motion. Hysteresis can be minimized with the use of hard piezoelectric ceramics, but d_{33} values of only ~200 to 300 pC/N are available. Even though electrostrictive ceramics offer effective d_{33} 's ~ 800 pC/N, maximum strain level is limited by its dielectric breakdown strength and polarization saturation. To achieve E-field induced strain levels > 0.15%, electroactive materials should possess high piezoelectric coefficients (d_{33} >1000 pC/N) and high dielectric breakdown strength.

2.2 Single crystal piezoelectrics

Single crystal piezoelectrics such as quartz (SiO_2), lithium niobate (LiNbO_3), and the analogue lithium tantalate (LiTaO_3) are widely employed in specific applications that include oscillators, surface acoustic wave (SAW) devices, and in optics. In contrast to PZT ceramics, however, these single crystals offer inferior piezoelectric properties, with d_{33} 's < 50 pC/N.

Attempts to grow single crystals of MPB PZTs have been made by numerous researchers, resulting in crystallites too small to allow adequate property measurements [5,6,7,8,9]. In contrast to PZT crystal growth, relaxor-PT materials can be readily grown in single crystal form.

This key distinction was first realized by Nomura and co-workers for the PZN and PZN-PT systems [10,11] and later by Shrout for the PMN-PT [12]. In general, most $\text{Pb}(\text{B}_1,\text{B}_2)\text{O}_3$ -PT crystals can be grown by high temperature solution growth using Pb-based fluxes.[13,14]

Piezoelectric coefficients as high as $\sim 1500 \text{ pC/N}$ have been reported [11,12] for MPB Relaxor-PT crystals. However, it should be noted that piezoelectric coefficients are generally determined using low-field ($< 0.1\text{kV/cm}$) techniques such as the resonance method (IEEE standard) [15]. Therefore, direct observation of the strain vs. E-field behavior is essential in order to investigate hysteresis and maximum levels of strain, key experiments to directly confirm actuator performance. In relation to actuators, several questions arise, 1) How do the high d_{33} values determined using low field techniques correlate to direct measurements? As for piezoelectric and electrostrictive ceramics, will the strain level saturate with increased E-field? 2) How much hysteresis accompanies the strain?, 3) Is morphotropy essential for enhanced piezoelectric properties?, 4) Are there optimum crystallographic cuts as in the case of the other piezoelectric crystals? In the following sections, we will attempt to answer these questions, reporting piezoelectric properties and direct observation of strain behavior as a function of crystallographic orientation and electric field for Relaxor-PT single crystals.

Commonalities inherent to Relaxor-PT systems have been discussed in reviews by Shrout [16] and Randall [17]. Based on these commonalities, our research was limited to two representative systems, PZN-PT and PMN-PT. Though PMN-PT MPB crystals exhibit piezoelectric properties comparable with PZN-PT, more focus was given to the PZN system owing to its relatively lower PT content for MPB, allowing more uniform crystal growth of these solid solution materials.

3. Experimental Procedure

3.1 Crystal growth

Crystals of PZN, PMN and their solid solutions with PT were grown using the high temperature flux technique. High purity (>99.9%) powders of Pb₃O₄ (Aldrich, WI), ZnO (Johnson Matthey, MA), MgCO₃ (Johnson Matthey, MA), Nb₂O₅ (Aldrich, WI), and TiO₂ (Aldrich, WI) were used. Raw powders were weighed with desired molar ratio with excess Pb₃O₄ as a flux. The powders were dry mixed for a desired period of time using a tumbling mill. The mixed powders were loaded into a Platinum crucible, which was placed in an alumina crucible sealed with an alumina lid and alumina cement to minimize PbO volatilization. The crucible and powder were placed in a tube furnace and held at soak temperatures (1100 to 1200°C), followed by slow cooling (1 to 5°C/hr). The crucible was then furnace-cooled to room temperature. Hot HNO₃ is used to separate the crystals out of the rest of the melt. Typically crystal size ranged from 3 to 20 mm. Further details on the flux growth technique of these crystals can be found in ref. [13,14].

2.2 X-ray diffraction (XRD) analysis

Single crystals were ground into a fine powder for XRD analysis ranging from 20° - 80° 2θ with a step size of 0.01 and a counting time of 3 sec, in order to confirm phase pure perovskite and to calculate lattice parameter. Individual crystals were oriented along various crystallographic directions such as their pseudocubic <001> and the <111> axis using a Laue back reflection camera.

2.3 Electrical characterization

Dielectric and piezoelectric properties were measured using direct observation of strain as a function of electric field as well as low-field property measurements using the IEEE resonance technique. [15] For electrical characterization, samples were prepared by polishing with silicon carbide and alumina polishing powders to achieve flat and parallel surfaces onto which gold electrodes were sputtered. High-field measurements included polarization and strain hysteresis using a modified Sawyer-Tower circuit and linear variable differential transducer (LVDT) driven by a lock-in amplifier (Stanford Research Systems, Model SR830). Plate shape samples with thickness ranging from 0.2 mm to 0.5 mm were used. Electric fields as high as ~140 kV/cm were applied using an amplified unipolar wave form at 0.2 Hz, using a Trek 609C-6 high voltage DC amplifier. During testing the samples were submerged in Fluorinert (FC-40, 3M, St. Paul, MN), an insulating liquid, to prevent arcing. For piezoelectric coefficient(d_{33}) determination, bar shape samples with lengths ranging from 3 mm to 5 mm were tested. Samples were poled either by field cooling (10kV/cm) from temperatures above the dielectric maximum temperature (T_{max}) or by applying 40kV/cm at room temperature. Figure 4 presents, from left to right, a representative of an as grown crystal, an aligned sample using the Laue camera, a cut and polished sample, an electroded sample for direct strain observation as well as for low field planar mode resonant sample, and a low field longitudinal mode resonant sample, for PZN-9.5%PT, respectively.

4. Results and Discussion

4.1 Low field measurements

Piezoelectric coefficients as a function of composition and crystal orientation for PZN-PT, calculated based on IEEE standards, are presented in figure 5. As shown, large piezoelectric coefficients ($d_{33} \sim 1600$ pC/N) were found for PZN-PT with MPB compositions (9.5% PT), as previously reported by Kuwata [11]. PMN-PT crystals with MPB compositions (PMN-35% PT) also exhibited large piezoelectric coefficients ($d_{33} \sim 1500$ pC/N).[3] It should be noted, however, that all rhombohedral crystals oriented along their pseudocubic $\langle 001 \rangle$ direction exhibited large piezoelectric coefficients. As shown in figure 5, d_{33} increased with increased amount of PbTiO_3 for $\langle 001 \rangle$ oriented rhombohedral crystal. Maximum d_{33} values of ~ 2500 pC/N were determined with domain engineered rhombohedral PZN-8%PT crystals*. In contrast to PZT's, d_{33} dramatically decreases at MPB to levels ~ 500 pC/N for tetragonal composition. Though $\langle 111 \rangle$ is the polar direction for rhombohedral crystals, such cuts exhibited low piezoelectric coefficient as shown in figure 5. In the following section the origin of apparent anisotropy will be discussed by direct strain observation as a function of electric field.

4.2 Domain (in)stability and associated anisotropy

Table 1 presents dielectric and piezoelectric properties for two rhombohedral crystals, pure PZN and PZN-8%PT, as a function of crystallographic orientation. Dielectric loss values $< 1\%$ and electromechanical coupling constant values ($k_{33} > 90\%$), attractive for transducer applications and essential for high performance solid state actuators, could be achieved with $\langle 001 \rangle$ oriented crystals, with further details found in ref. [3]. Oriented, $\langle 001 \rangle$ rhombohedral

* Rhombohedral crystals oriented and poled along pseudocubic $\langle 001 \rangle$ direction. Crystallographically, polar direction of rhombohedral crystal is pseudocubic $\langle 111 \rangle$ direction.

crystals exhibited ultrahigh piezoelectric coefficients (d_{33}) of ~1100 pC/N (PZN) up to 2500 pC/N (PZN-8%PT), and d_{33} values increased with increased PbTiO_3 content as presented in figure 5. However, electromechanical couplings (k_{33}) and piezoelectric coefficients (d_{33}) of <111> oriented rhombohedral crystals are only ~35% and ~80 pC/N, respectively, regardless of composition. This composition-independence of piezoelectric properties must have the origins other than the inherent crystallographic anisotropy.

Polarization and strain as a function of E-field (bipolar) for <111> oriented PZN crystal are presented in figures 6a and 6b, respectively. Subsequent unipolar strain behavior after poling (field cooling under 20 kV/cm from 200°C to room temperature) is shown in figure 7a. As <111> is polar direction, complete poling results in a single domain state and piezoelectric strain behavior is expected to be hysteresis free for <111> poled PZN crystals. However, as shown in figure 7a, significant hysteresis together with abnormally high strain values (0.1% at 10 kV/cm) indicates domain reorientation under bias, as discussed in section 2.1. Domain motion along with increased strain must include 109° or 71° domain reorientation, starting at $E \sim 2 \text{kV/cm}$ in this case (figure 7a), followed by strain saturation. It should be noted that remnant strain values of ~0.04% after E-field is removed and, original sample dimension recovered its zero strain point a few seconds after E-field is removed, as presented in figure 7a. This behavior obviously reflects domain motion, including depoling as well as reorientation. As in case of "soft" ceramics, this domain motion is the origin of abnormally high strain values and hysteresis. Piezoelectric coefficient (d_{33}) values ~ 80 pC/N determined by low-field resonance technique could be explained by the slope of strain vs. E-field at low field region, as given in figure 7a. Various d_{33} 's calculated by the slope of strain vs. E-field are given, too. Therefore, the inferior piezoelectric

properties of <111> oriented rhombohedral crystals detected by low-field resonance method are strongly related to domain instability. Complete domain orientation and single domain configuration under bias may cause elastic energy in crystals to increase, however, resulting in depoling after removing E-field.

In contrast, the domain configuration of <001> oriented rhombohedral crystals was found to be stable. Polarization and strain vs. E-field (bipolar) curves of <001> oriented PZN crystals are presented in figure 6c and 6d, respectively. Domain switching by bipolar field abruptly occurs at Ec (~3kV/cm), similar behavior found with single domain ferroelectric crystals. Schematics of domain configurations for <001> poled rhombohedral crystals are shown in figure 8. Since <111> is the polar direction, <001> poled crystals must have the configuration that each domain has one of four possible polar directions - <111>, <-111>, <1-11>, and <-1-11>. Remnant polarization ($P_r \sim 25 \mu\text{C}/\text{cm}^2$) of <001> oriented rhombohedral PZN crystal must be $1/\sqrt{3}$ of <111> oriented crystal's according to figure 8, which explains $\sim 25 \mu\text{C}/\text{cm}^2$ for $P_{r,<001>}$ out of $P_{r,<111>} \sim 43 \mu\text{C}/\text{cm}^2$. Therefore, abrupt domain switching at Ec (~3kV/cm) is expected to be 71° domain switching, as shown in figure 9. In figure 7b, <001> poled PZN crystals exhibit almost hysteresis-free strain behavior, a consequence of engineered-domain stability. From the slope of strain vs. E-field curve revealed d_{33} value of $\sim 1100 \text{ pC/N}$, as determined by low-field resonance technique. This behavior for <001> oriented rhombohedral crystals will be discussed in the following section.

The observed domain (in)stability as a function of crystallographic orientation holds for all rhombohedral crystals of PZN-PT and PMN-PT. Owing to low hysteresis as well as ultrahigh piezoelectric coefficient (d_{33}), <001> oriented rhombohedral crystal may be attractive candidates

for actuators. Although domain (in)stability is clearly a function of crystallographic orientation, in-situ domain observation using optical microscopy is necessary and will be reported elsewhere.

[19]

4.3 Optimum crystallographic orientation

As discussed in section 2.2, optimum crystallographic cuts was one of the merits uniquely utilized with single crystals. For conventional piezoelectric single crystals, however, an “optimum cut” was determined from a single domain crystal, whereas engineered multidomain state is being utilized in this study. The term “optimum orientation” includes crystallographic direction not only for poling but for actuator driving to obtain hysteresis (strain) values as low (high) as possible, respectively.

Though it was determined that $<001>$ is superior to $<111>$, multidomain rhombohedral crystals may allow other crystallographic directions as optimum for higher strain values with comparably low hysteresis. To investigate this possibility, piezoelectric samples oriented along $<001> + \alpha$ were made, where α is the degree of deviation from $<001>$ toward $<111>$, as shown in figure 9, using PZN-4.5%PT crystal. In figure 10 remnant polarization (P_r) approaches the $P_r_{<111>}$ value ($\sim 43 \mu\text{C}/\text{cm}^2$) as orientation (α) approaches $<111>$ (54.7°), respectively. Ec value also increase with increased α . Figure 11 presents unipolar strain behavior as a function of α for $<001>$ poled PZN-4.5%PT crystals. At low field, strain values do not vary significantly as a function of α , attributed to strain induced by domain reorientation when $\alpha \neq 0$. For example, the strain value of a sample ($\alpha = 10^\circ$) is higher than that for a $<001>$ oriented sample ($\alpha = 0^\circ$). This increased domain motion with increased α is presented in figure 12, with hysteresis vs. α

calculated from the area of polarization vs. unipolar E-field curves (20kV/cm). The amount of hysteresis can be translated into degree of depoling, because more depoling consequently involves more domain reorientation, resulting in increased hysteresis. Therefore, domain becomes more unstable with the increased α . From these observations, the closer to $<001>$ is rhombohedral crystal orientation, the more stable domain configuration and the higher strain value are achieved. Therefore the optimum crystallographic orientation is $<001>$.

High-field strain behavior is shown in figure 13 for $<001>$ oriented PZN-4.5%PT crystals. Strain saturation becomes more significant as α increases (orientation approaches $<111>$). At high fields, strain level decreases with increased α , the result of polarization saturation and subsequent strain saturation. However crystals oriented close to $<001>$ ($\alpha < 20^\circ$) exhibit no saturation, and furthermore, an apparent jump in strain to values over 1%. The question arises, does this strain jump originated from domain reorientation? This question is addressed in the following section.

4.4 Strain vs. E-field behaviors for $<001>$ oriented rhombohedral crystals

Strain as a function of electric field for various $<001>$ oriented rhombohedral crystals (pure PZN, PZN-4.5%PT, PZN-8%PT, and PMN-24%PT) are presented in figure 14. Also, E-field induced strains of various electromechanical ceramics such as soft PZT (PZT-5H), hard PZT (PZT-8) and electrostrictive ceramics (PMN-PT) are compared. Piezoelectric coefficients (d_{33}) directly calculated from the slope of strain vs. electric field curves confirmed the piezoelectric coefficients determined by the low-field resonance method. Strains as high as 0.6% were observed with low hysteresis for these crystals, significantly larger than that for polycrystalline

ceramics. The limitation of achievable strain for polycrystalline ceramics is the result of low piezoelectric coefficient, polarization saturation and subsequent saturation on strain and breakdown strength.

Figure 15 schematically presents engineered domain state and their piezoelectric response under bias for rhombohedral crystals oriented and poled along <001>. When actuation is induced by an E-field along <001>, the polar direction is expected to incline close to E-field direction in each domain (step A in figure 15), possibly resulting in increased rhombohedral lattice distortion. Domain reorientation is not necessary during this step because neighboring domains must involve equal amount of induced distortion, nullifying all strains in individual domains, the reason of stable domain configuration and, therefore, the origin of hysteresis-free or low-hysteresis strain behavior for <001> oriented rhombohedral crystals.

Strain saturation for <001> oriented rhombohedral crystals was investigated until dielectric breakdown, as presented in figure 16. Far from saturation, the strain abruptly increased with strain levels as high as 0.8% being achieved for all crystals tested. Strain levels >1.2% for the PZN-4.5%PT crystal were the result of higher breakdown voltage (compare with figure 13). The observed strain behavior is believed to be associated with an E-field induced rhombohedral-tetragonal phase transition. Polarization inclination towards <001> finally result in collapse of all polarization's into <001> direction, step B in figure 17. This E-field induced phase transition is more apparent in figure 17, presenting the E-field induced strain behavior of the <001> oriented PZN-8%PT crystal. At ~120kV/cm, the induced strain along with high dielectric breakdown strength resulted in a strain levels as high as 1.7%. The piezoelectric coefficient (d_{33}) ~ 480 pC/N calculated directly from the slope of strain vs. E-field in the high field region (between 40 and

120 kV/cm in figure 17) corresponded to values determined for tetragonal phase with a d_{33} value (~500 pC/N, in figure 5). Individual steps of piezoelectricity (step A) and phase transition (step B) shown in figure 15 are given in figure 17. Although phase transition is a likely explanation for the ultrahigh strain level, direct observation of phase transition using in-situ XRD is required.

5. Conclusion

Pseudocubic <001> oriented relaxor based rhombohedral crystals such as (1-x)PZN-xPT ($x<0.09$) and (1-x) PMN- xPT ($x<0.35$) exhibited actuation levels not available with current piezoelectric ceramics. Ultrahigh piezoelectric coefficients ($d_{33}>\sim 2500$ pC/N and strain levels up to 0.6% with low hysteresis were observed. Optimum crystallographic orientation was found to be pseudocubic <001> for rhombohedral crystals, exhibiting high-strain and low-hysteresis behavior. Domain instability could explain the composition-independently inferior piezoelectric properties for <111> oriented rhombohedral crystals. Ultrahigh strain levels up to 1.7% could be achieved for <001> oriented rhombohedral single crystals as a result of E-field induced rhombohedral-tetragonal phase transition. Other relaxor based rhombohedral crystals are expected to exhibit similar strain vs. E-field behavior. <001> textured polycrystalline ceramics are expected to exhibit high strain behaviors. Though clearly promising candidates for high performance actuators, further investigations in crystal growth and pre-stress testing are required for single crystal piezoelectrics to become the next generation material of actuators.

Acknowledgment

This research has been supported by Office of Naval Research and Whitaker Center for Ultrasonic Imaging. The authors would like to thank L. E. Cross and C. Randall for their helpful suggestions, and Wesley Hackenberger, Patrick D. Lopath, Michael J. Zipparo for their helps with the property measurements, and Shi-Fang Liu and Hua Lei for their helps with crystal growing and sample preparation, respectively.

References

1. V. Giurgiutiu, Z. Chaudhry, and C. A. Rogers, "Energy-based Comparison of Solid-State Actuators," Report No. CIMSS 95-101, Virginia Polytechnic Institute and State University, September 1995.
2. L. E. Cross, "Relaxor Ferroelectrics," *Ferroelectrics*, vol. 76, pp. 241-267, 1987.
3. Seung-Eek Park, Thomas R. Shrout, "Characteristics of Relaxor-Based Piezoelectric Single Crystals for Ultrasonic Transducers," in press *IEEE Trans. on Ultrasonics, Ferroelectric and Frequency Control Special Issue on Ultrasonic Transducers*, 1997.
4. H. Jaffe and D. A. Berlincourt, "Piezoelectric Transducer Materials," *Proceedings of IEEE*, vol. 53 no. 10, pp. 1372-1386, 1965.
5. S. Fushimi and T. Ikeda, "Phase Equilibrium in the System PbO-TiO₂-ZrO₂," *Journal of the American Ceramic Society*, vol. 50, no. 3, pp. 129-132, March 1967.

6. V. A. Kuznetzov, "Crystallization of Titanium, Zirconium and Hafnium Oxides and Some Titanate and Zirconate Compounds under Hydrothermal Conditions," *Journal of Crystal Growth*, vol. 34, pp. 405 - 410, 1968.
7. R. Clarke and R. W. Whatmore, "The Growth and Characterization of $PbZr_xTi_{1-x}O_3$ Single Crystals," *Journal of Crystal Growth*, vol. 33, pp. 29-38, 1976.
8. T. Hatanaka and H. Hasegawa, "Dielectric Properties of $Pb(Zr_xTi_{1-x})O_3$ Single Crystals Including Monoclinic Zirconia," *Japanese Journal of Applied Physics*, vol. 34, pp. 5446-5448, Sept. 1995.
9. K. Yanagisawa, H. Kanai, and Y. Yamashita, "Hydrothermal Crystal Growth of Lanthanum-Modified Lead Zirconate Titanate," *Japanese Journal of Applied Physics*, vol. 34, pp. 536-538 Sept. 1995.
10. J. Kuwata, K. Uchino, and S. Nomura, "Phase Transitions in the $Pb(Zn_{1/3}Nb_{2/3})O_3$ - $PbTiO_3$ System," *Ferroelectrics*, vol. 37, pp. 579-582, 1981.
11. J. Kuwata, K. Uchino, and S. Nomura, "Dielectric and Piezoelectric Properties of 0.91 $Pb(Zn_{1/3}Nb_{2/3})O_3$ - 0.09 $PbTiO_3$ Single Crystals," *Japanese Journal of Applied Physics*, vol. 21, no. 9, pp. 1298-1302, Sept. 1982.
12. T. R. Shrout, Z. P. Chang, N. Kim, and S. Markgraf, "Dielectric Behavior of Single Crystals near the $(1-x)Pb(Mg_{1/3}Nb_{2/3})O_3$ - $(x)PbTiO_3$ Morphotropic Phase Boundary," *Ferroelectric Letters*, vol. 12, pp. 63-69, 1990.
13. M. L. Mulvihill, S. -E. Park, G. Risch, Z. Li, K. Uchino, T. R. Shrout, "The Role of Processing Variables in the Flux Growth of Lead Zinc Niobate-Lead Titanate Relaxor

Ferroelectric Single Crystals," *Japanese Journal of Applied Physics*, vol. 35, no. 7, pp. 51-57, July 1996.

14. S. -E. Park, M. L. Mulvihill, G. Risch, and T. R. Shrout, "The Effect of Growth Condition on Dielectric Properties of $\text{Pb}(\text{Zn}_{1/3}\text{Nb}_{2/3})\text{O}_3$ Crystal," *Japanese Journal of Applied Physics*, Pt. 1, vol. 36, no. 3, March 1997.
15. IEEE Standard on Piezoelectricity, American National Standards Institute, 1976.
16. T. R. Shrout and J. Fielding, Jr., "Relaxor Ferroelectric Materials," in *Proceedings of the 1990 IEEE Ultrasonics Symposium*, 1990, pp. 711-715.
17. C. A. Randall, A. S. Bhalla, T. R. Shrout, and L. E. Cross, "Classification and Consequences of Complex Lead Perovskite Ferroelectrics with regard to B-site Cation Order," *Journal of Materials Research*, vol. 5, no. 4, pp. 829-834, 1990.
18. S.-E. Park and T. R. Shrout, presented at 9th International Meeting on Ferroelectricity, Seoul, Korea, 24-27 August, 1997.
19. S. Wada, S.-E. Park, L. E. Cross, and T. R. Shrout, presented at 9th International Meeting on Ferroelectricity, Seoul, Korea, 24-27 August, 1997.
20. Y. Yamashita, "Large Electromechanical Coupling Factors in Perovskite Binary Material System," *Japanese Journal of Applied Physics*, 33, Pt. 1[9B], 5328-5331 (1994).

Figure Caption

Figure 1 Ternary diagram depicting MPBs in PZT and Relaxor-PT systems for piezoelectric ceramic.

Figure 2 Piezoelectric coefficient (d_{33}) as a function of transition temperature (T_c) for piezoelectric ceramics, including PZT, modified PZTs, and Relaxor-PT systems. Data were compiled from references, commercial brochures and internal investigations.

Figure 3 Strain vs. E-field behavior for various electromechanical ceramics.

Figure 4 An as grown crystal, an aligned sample using the Laue camera, a cut and polished sample, an electroded sample for direct strain observation as well as for low field planar mode resonant sample, and a low field longitudinal mode resonant sample, for PZN-9.5%PT, respectively (from left to right).

Figure 5 d_{33} as a function of crystal composition and orientation.

Figure 6 Polarization and strain vs. E-field (bipolar) curves for PZN crystals oriented along $<111>$ (a,b) and $<001>$ (c,d).

Figure 7 Strain vs. E-field (unipolar) curves for PZN crystals oriented along $<111>$ (a) and $<001>$ (b).

Figure 8 Schematics of engineered domain configuration for $<001>$ poled rhombohedral crystals.

Figure 9 Schematic diagram of sample preparation for investigating optimum crystallographic orientation.

Figure 10 Ferroelectric hysteresis for PZN-4.5%PT crystals oriented along $<001> + \alpha$, where α is the degree of deviation from $<001>$ toward $<111>$, (a) $\alpha=0^\circ$, (b) $\alpha=10^\circ$, (c) $\alpha=20^\circ$, (d) $\alpha=30^\circ$, (e) $\alpha=40^\circ$.

Figure 11 Strain vs. E-field (unipolar) PZN-4.5%PT crystals oriented along $<001> + \alpha$, where α is the degree of deviation from $<001>$ toward $<111>$, (a) $\alpha=0^\circ$, (b) $\alpha=10^\circ$, (c) $\alpha=20^\circ$, (d) $\alpha=30^\circ$, (e) $\alpha=40^\circ$.

Figure 12 Hysteresis as a function of α , where α is the degree of deviation from $<001>$ toward $<111>$. Hysteresis values are calculated from the area of unipolar polarization curve when maximum E-field is 20 kV/cm.

Figure 13 Strain vs. E-field (unipolar) PZN-4.5%PT crystals oriented along $<001> + \alpha$, where α is the degree of deviation from $<001>$ toward $<111>$. Maximum field is limited either by dielectric breakdown or by voltage limit of the apparatus.

Figure 14 Strain vs. E-field behavior for $<001>$ oriented rhombohedral crystals of PZN-PT and PMN-PT and for various electromechanical ceramics.

Figure 15 Schematic diagram of domain configurations in $<001>$ oriented rhombohedral crystals under bias (step A - piezoelectricity, step B - induced phase transition).

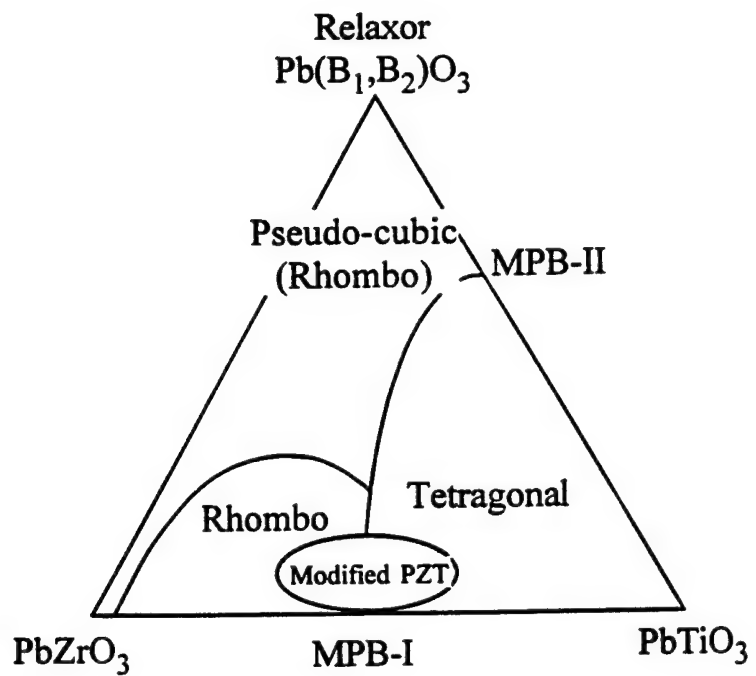
Figure 16 Strain vs. E-field behavior for $<001>$ oriented rhombohedral crystals of PZN-PT and PMN-PT and for various electromechanical ceramics. Maximum field was limited either by dielectric breakdown or by voltage limit of the apparatus.

Figure 17 Strain vs. E-field behavior for $<001>$ oriented PZN-8%PT crystal. Maximum field is limited by voltage limit of the apparatus.

Table 1 Dielectric and piezoelectric properties as a function of crystallographic orientation for rhombohedral $\text{Pb}(\text{Zn}_{1/3}\text{Nb}_{2/3})\text{O}_3$ (PZN) and $\text{Pb}(\text{Zn}_{1/3}\text{Nb}_{2/3})\text{O}_3 - 8\%\text{PbTiO}_3$ (PZN-8%PT).

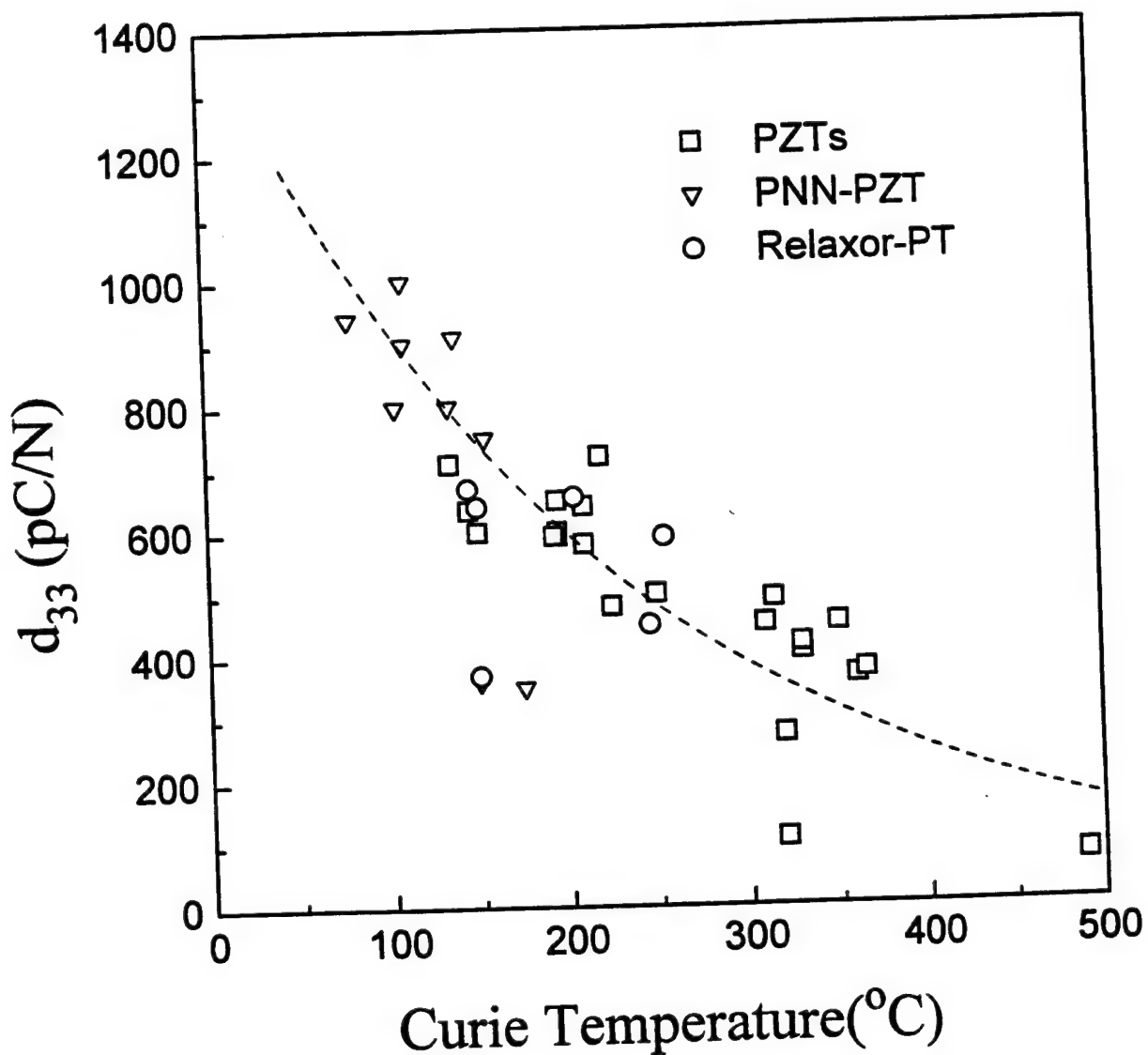
Crystal Orientation	Composition	mode	coup-ling	$s_{33}^E (10^{-12} \text{m}^2/\text{N})$	Dielectric Constant	Loss	d_{33} (pC/N)
111	PZN	k_{33}	0.38	7.4	900	0.012	83
	PZN-8%PT	k_{33}	0.39	7.4	1000	0.012	84
001	PZN	k_{33}	0.85	48	3600	0.008	1100
	PZN-8%PT	k_{33}	0.94	130	5000	0.010	2500

* Samples were poled by field cooling from 200°C with applying 20kV/cm.



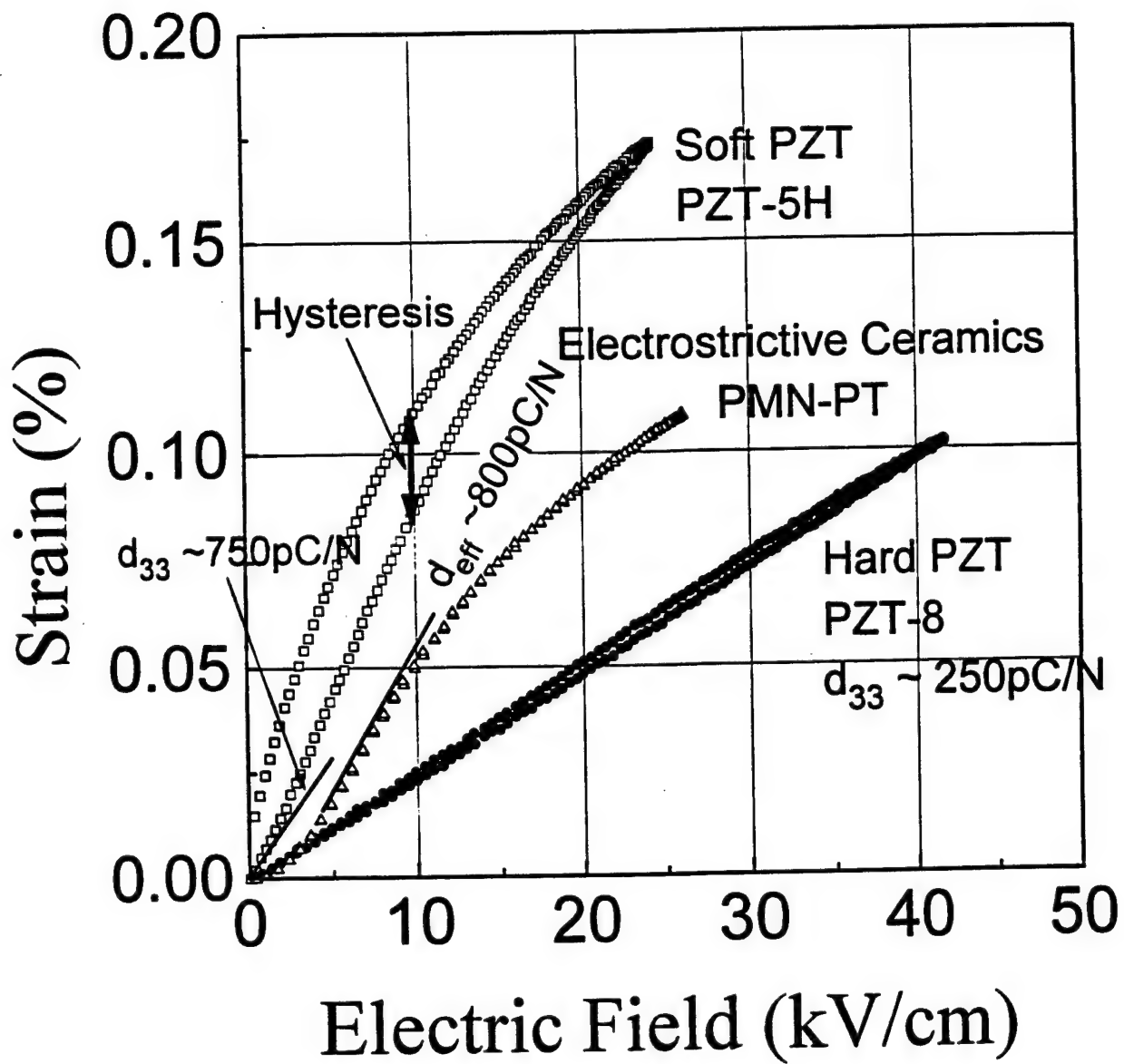
S.-E. Park and T. R. Shrout

Figure 1. Ternary diagram depicting MPBs in PZT and Relaxor-PT systems for piezoelectric ceramic [20].



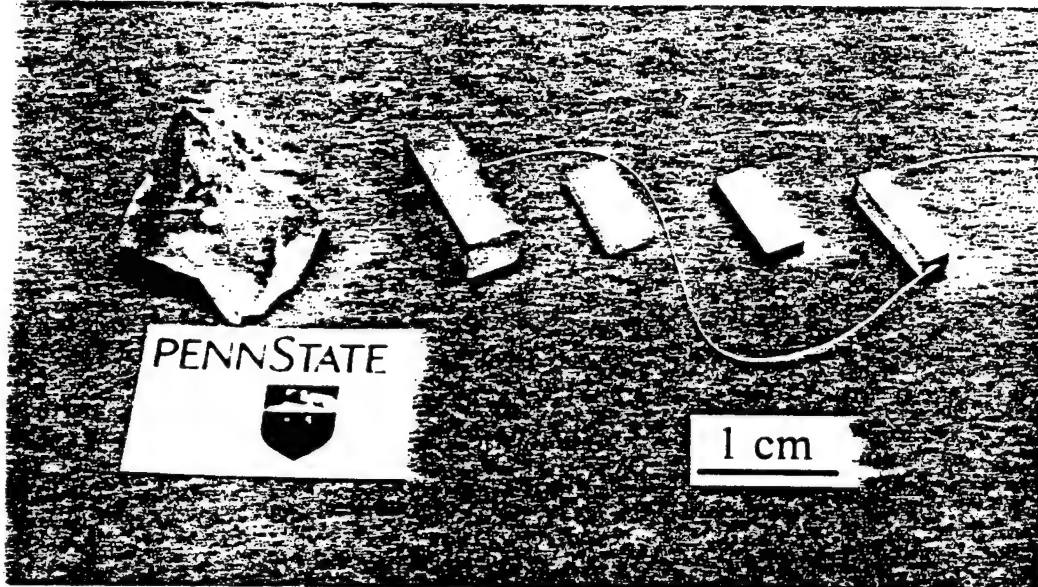
Seung-Eek Park and Thomas R. Shrout

Figure 2 Piezoelectric coefficient (d_{33}) as a function of transition temperature (T_c) for piezoelectric ceramics, including PZT, modified PZTs, and Relaxor-PT systems. Data were compiled from references, commercial brochures and internal investigations.



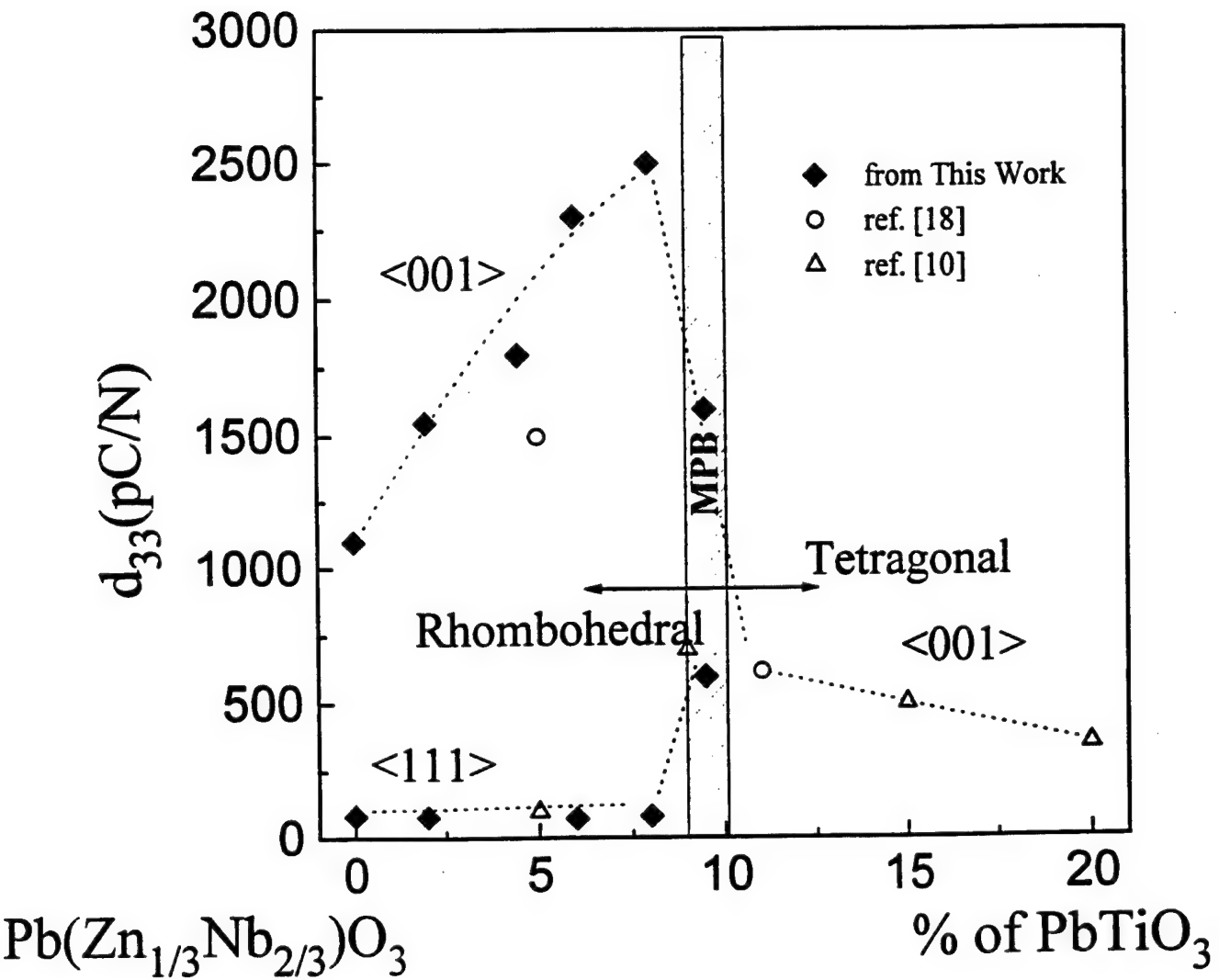
S.-E. Park and T. R. Shrout

Figure 3 Strain vs. E-field behaviors for various electromechanical ceramics



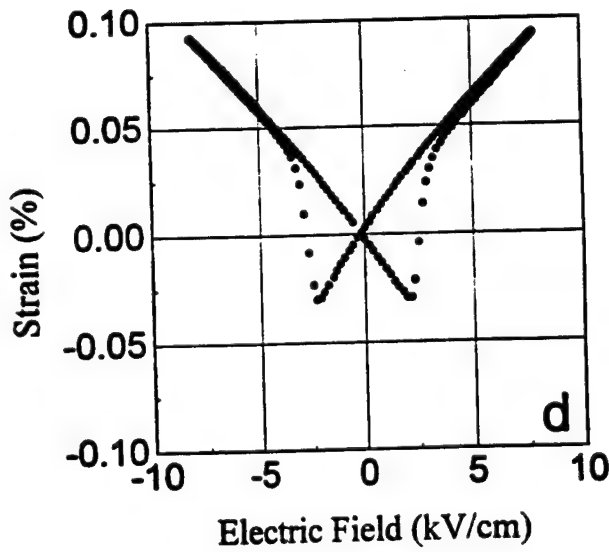
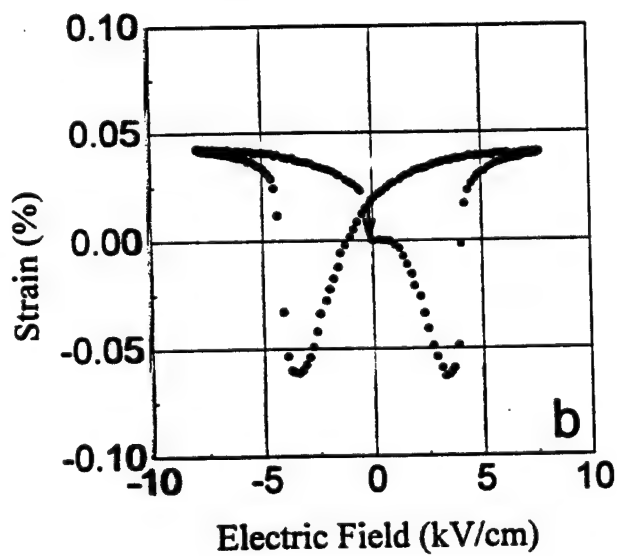
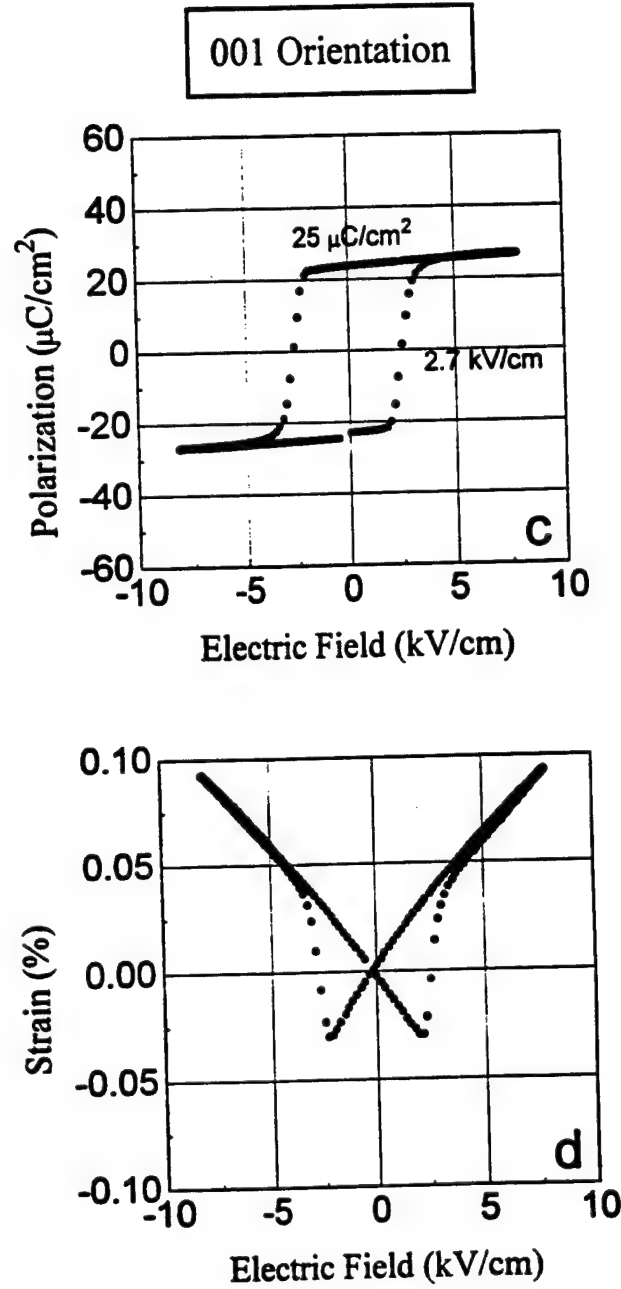
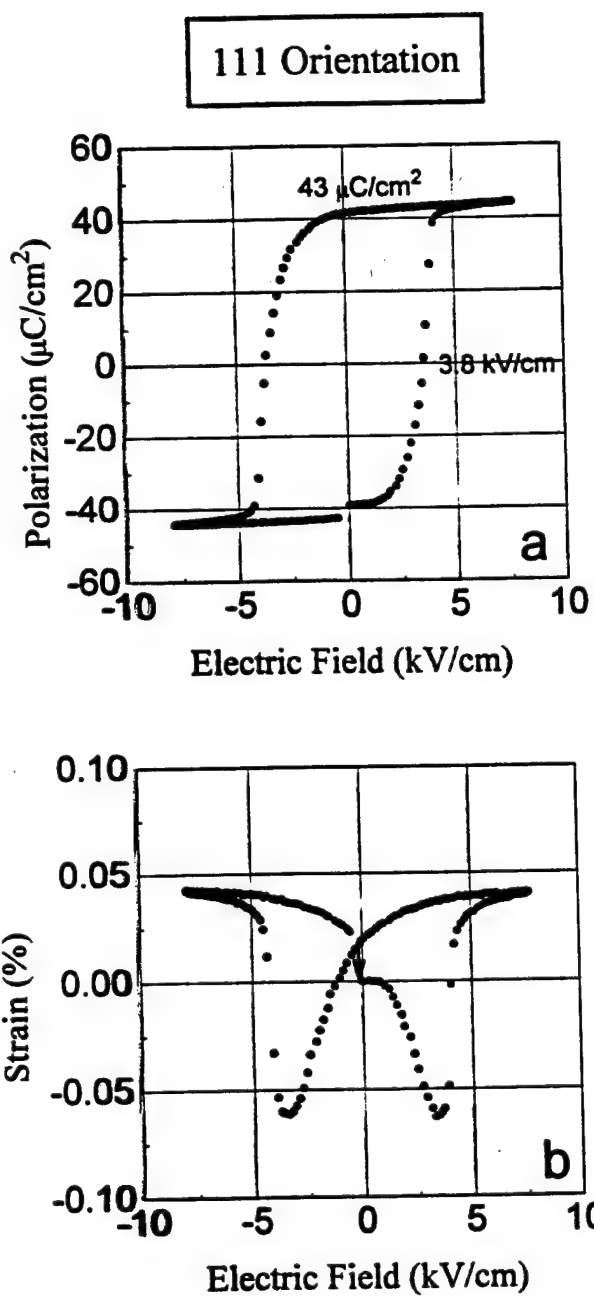
S.-E. Park and T. R. Shroud

Figure 4 An as grown crystal, an aligned sample using the Laue camera, a cut and polished sample, an electroded sample for direct strain observation as well as for low field planar mode resonant sample, and a low field longitudinal mode resonant sample, for PZN-9.5%PT, respectively (from left to right).



S.-E. Park and T. R. Shroud

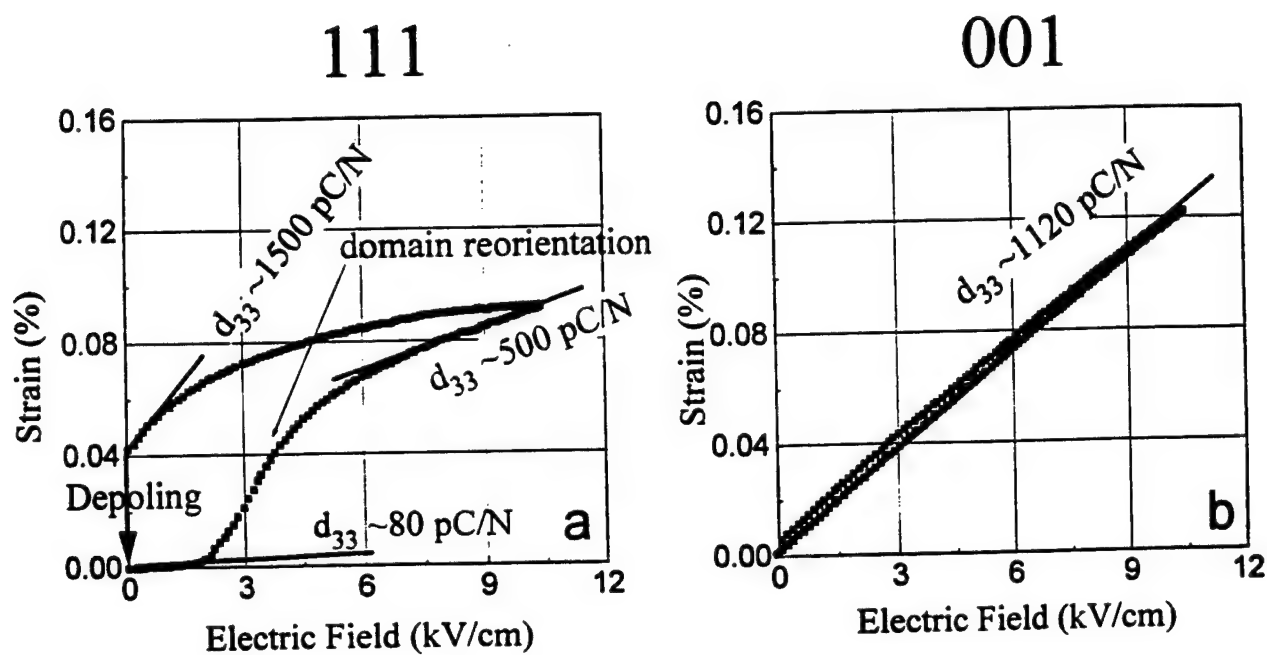
Figure 5 d_{33} as a function of crystal composition and orientation



S.-E. Park and T. R. Shroud

Figure 6 Polarization and strain vs. E-field curves

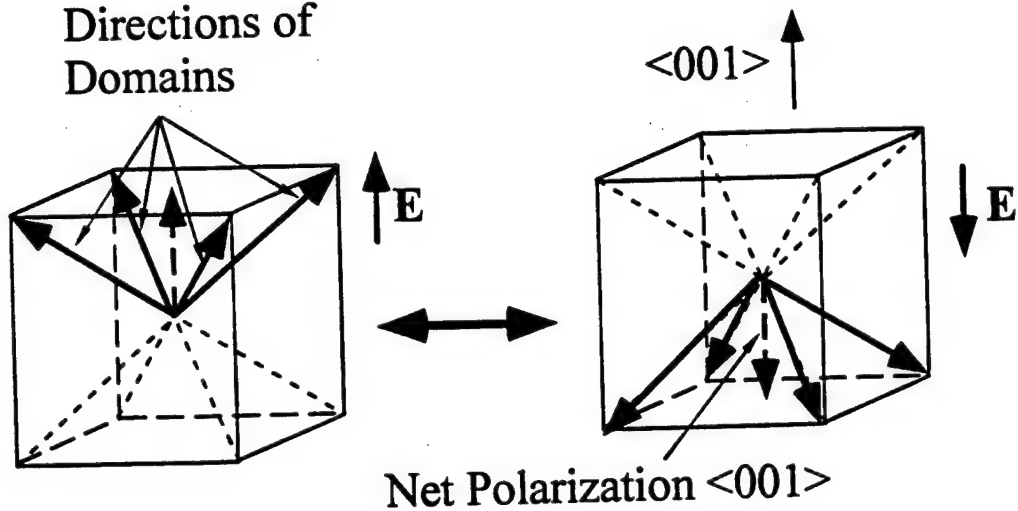
for PZN crystals oriented along $<111>$ (a,b) and $<001>$ (c,d).



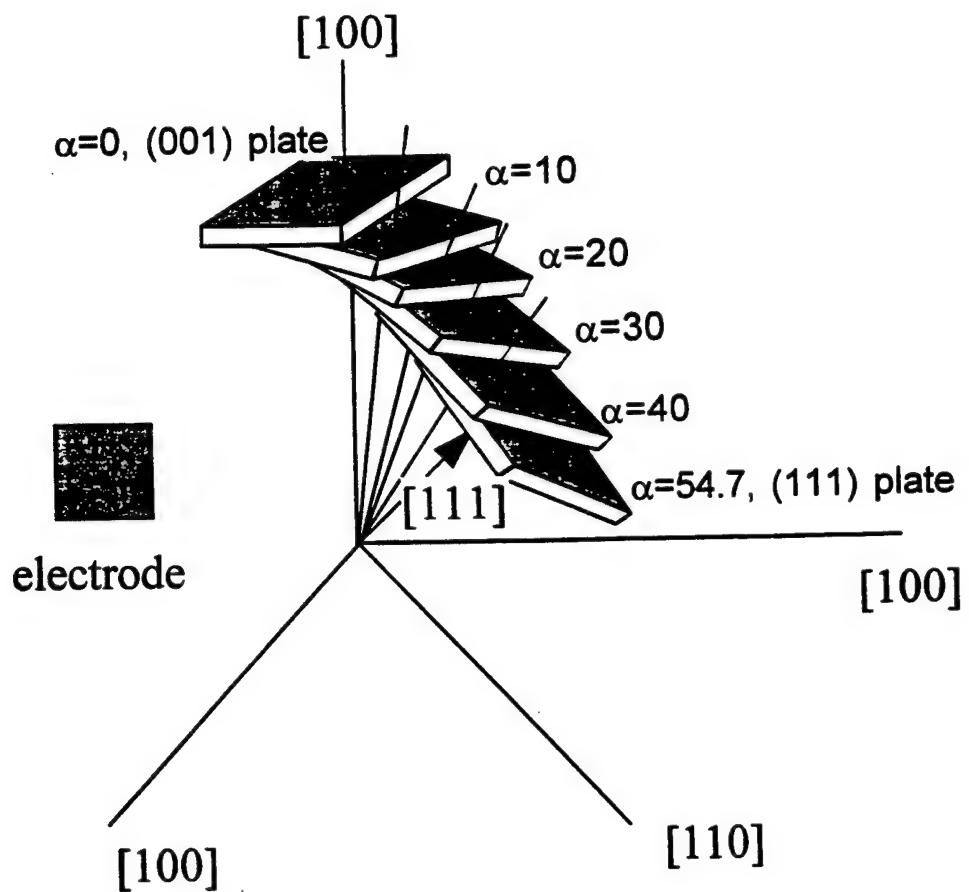
S.-E. Park and T. R. Shroud

Figure 7 Polarization and strain vs. E-field curves (unipolar)
for PZN crystals oriented and poled along <111> (a) and <001> (b).

Possible
Polarization
Directions of
Domains

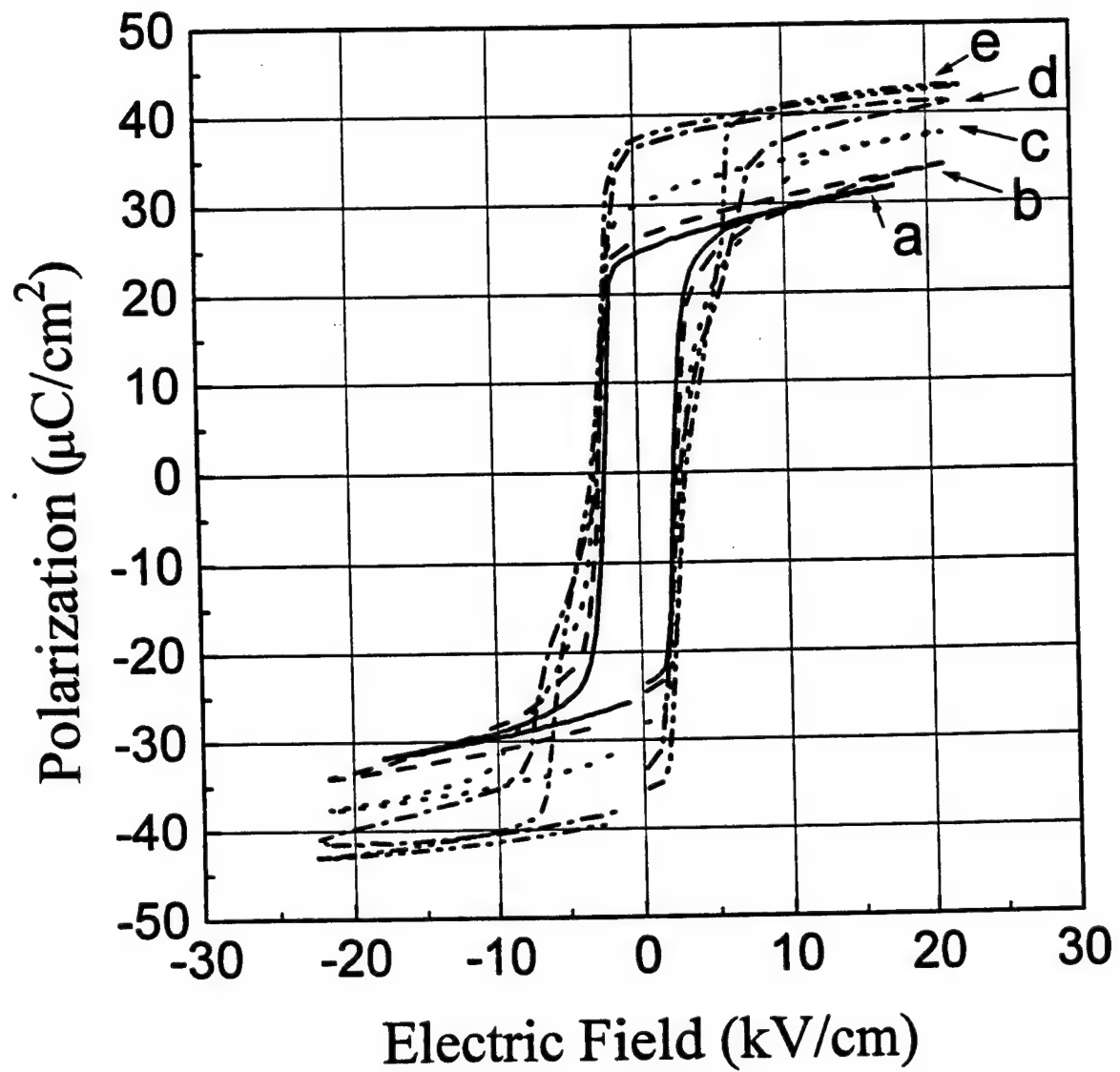


S.-E. Park and T. R. Shroud
Figure 8 Schematics of engineered domain configuration
for $<001>$ poled rhombohedral crystals



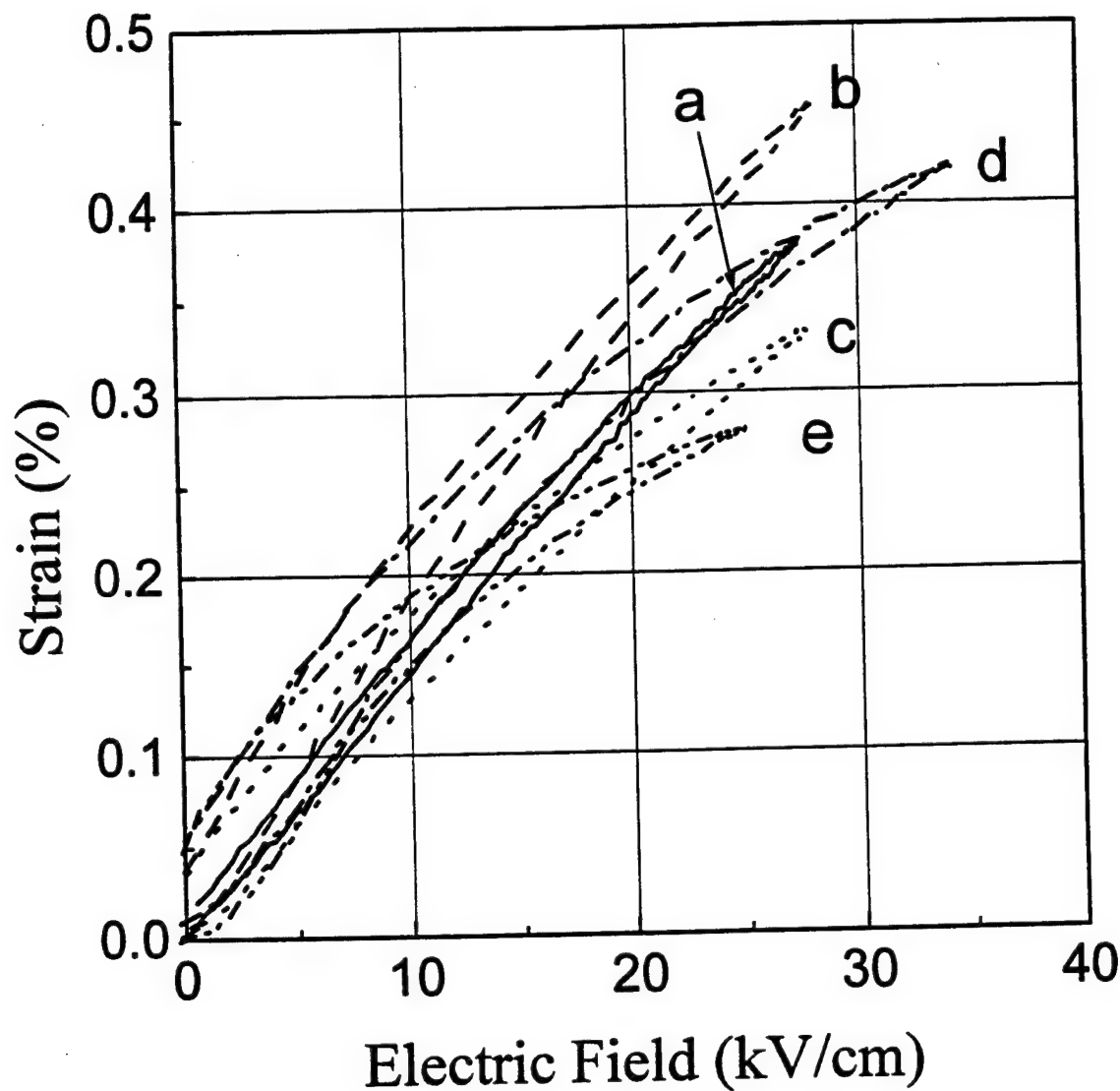
S.-E. Park and T. R. Shrout

Figure 9 Schematic diagram of sample preparation
for investigating optimum crystallographic orientation



S.-E. Park and T. R. Shroud

Figure 10 Ferroelectric hysteresis for PZN-4.5%PT crystals oriented along $<001> + \alpha$, where α is the degree of deviation from $<001>$ toward $<111>$,
 (a) $\alpha=0^\circ$, (b) $\alpha=10^\circ$, (c) $\alpha=20^\circ$, (d) $\alpha=30^\circ$, (e) $\alpha=40^\circ$.



S.-E. Park and T. R. Shrout

Figure 11 Strain vs. E-field (unipolar) PZN-4.5%PT crystals oriented along $<001> +$
where α is the degree of deviation from $<001>$ toward $<111>$,

(a) $\alpha=0^\circ$, (b) $\alpha=10^\circ$, (c) $\alpha=20^\circ$, (d) $\alpha=30^\circ$, (e) $\alpha=40^\circ$.

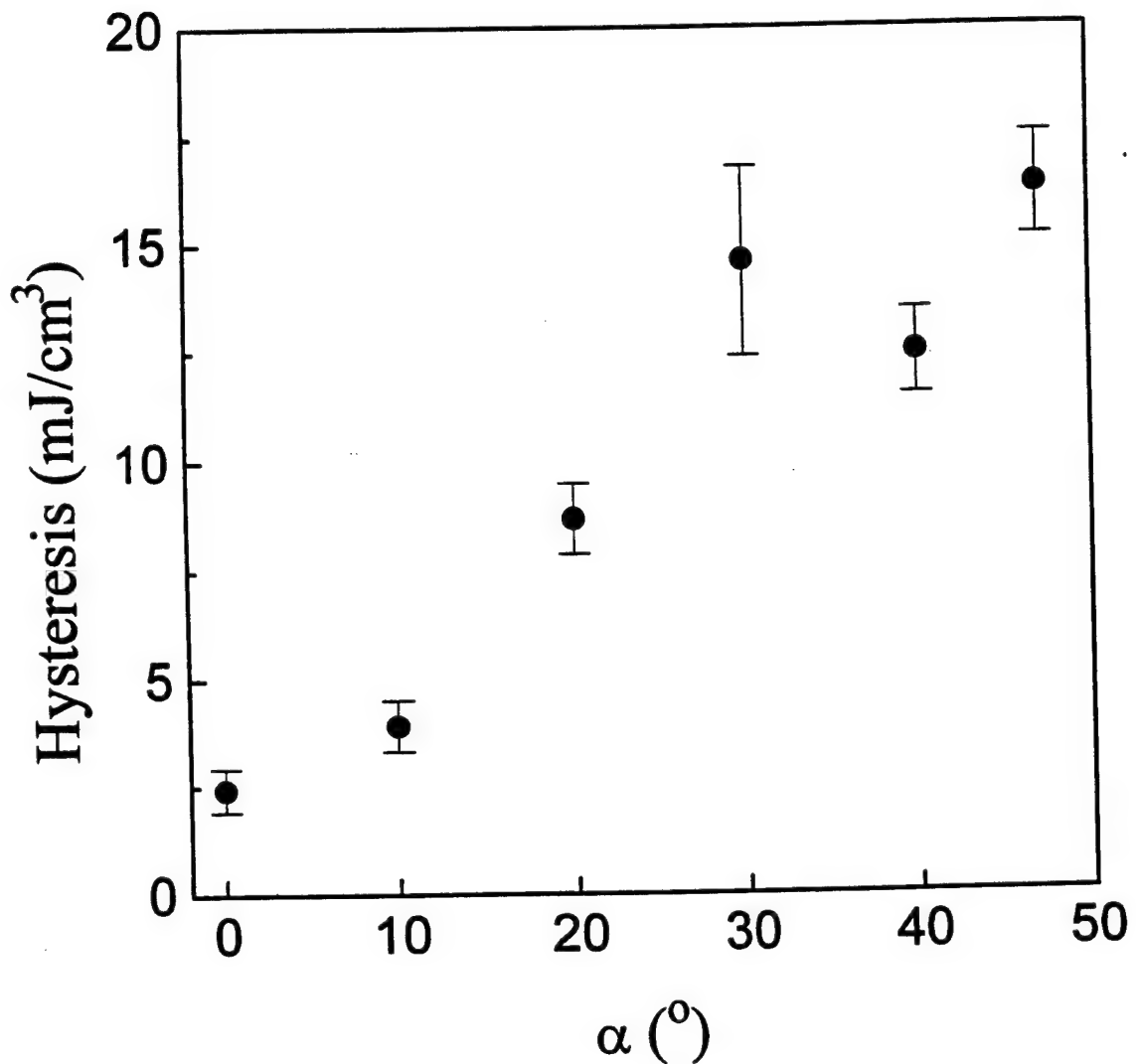
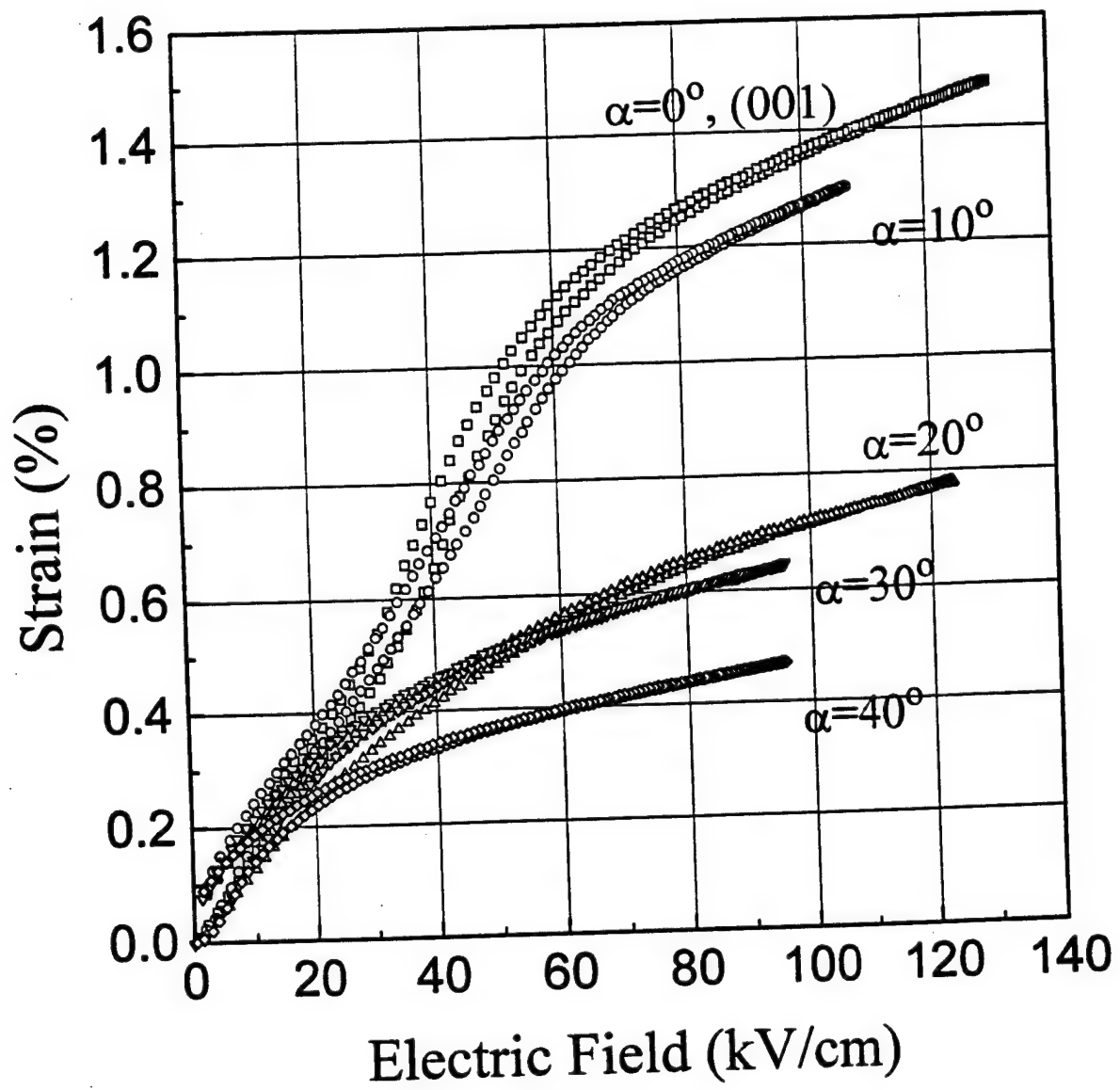
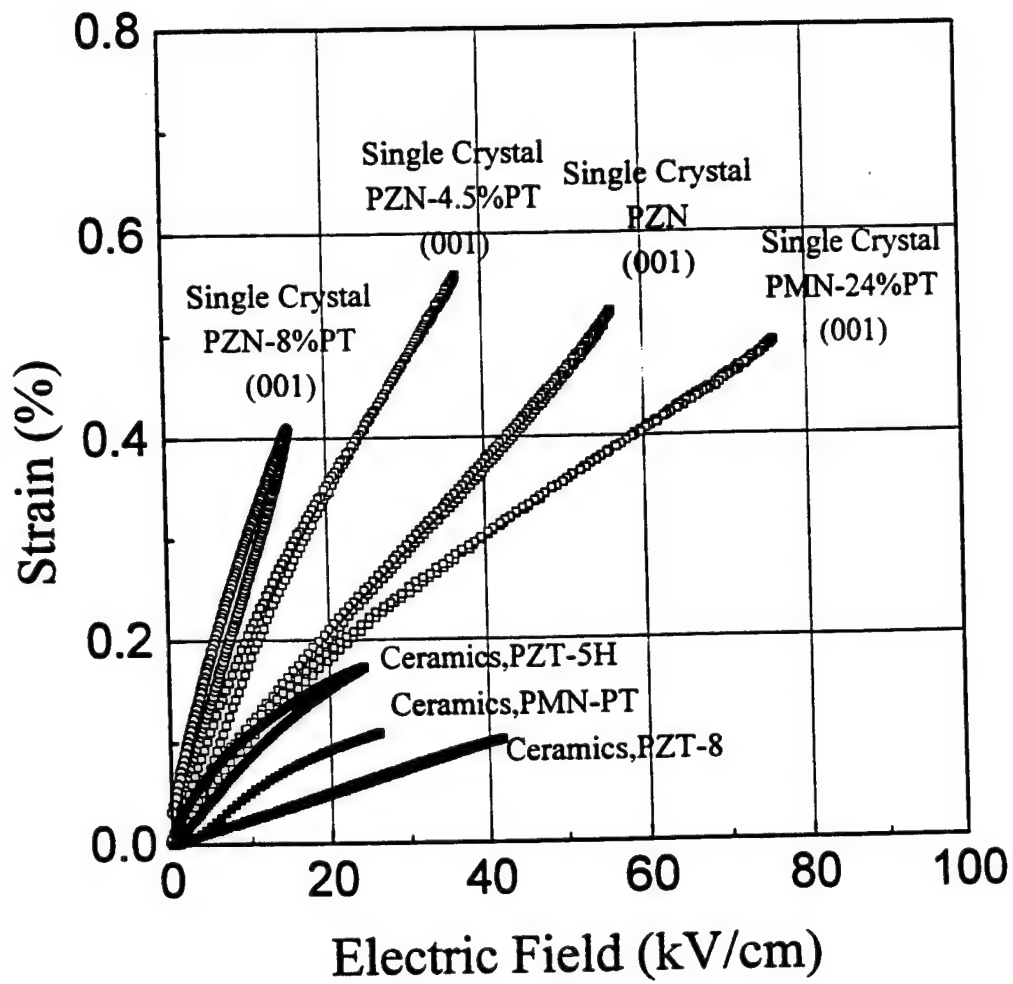


Figure 12 Hysteresis as a function of α , where α is the degree of deviation from $<001>$ toward $<111>$. Hysteresis values are calculated from the area of unipolar polarization curve when maximum E-field is 20 kV/cm.



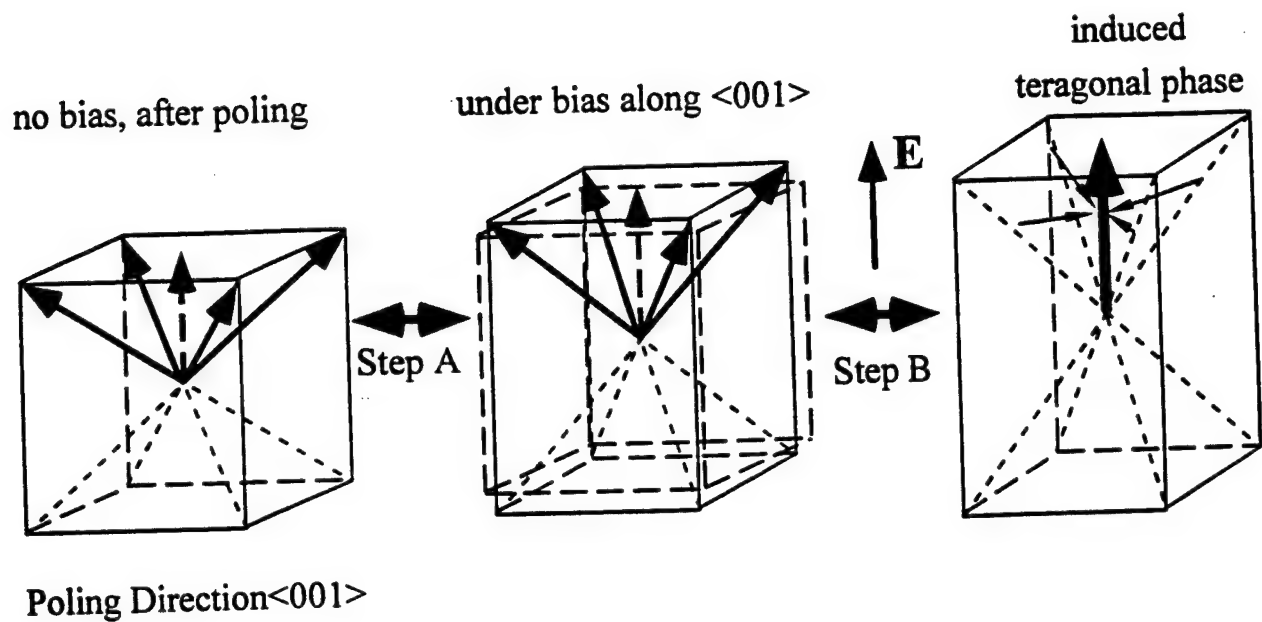
S.-E. Park and T. R. Shroud

Figure 13 Strain vs. E-field (unipolar) PZN-4.5%PT crystals oriented along $<001> + \alpha$, where α is the degree of deviation from $<001>$ toward $<111>$. Maximum field is limited either by dielectric breakdown or by voltage limit of the apparatus.



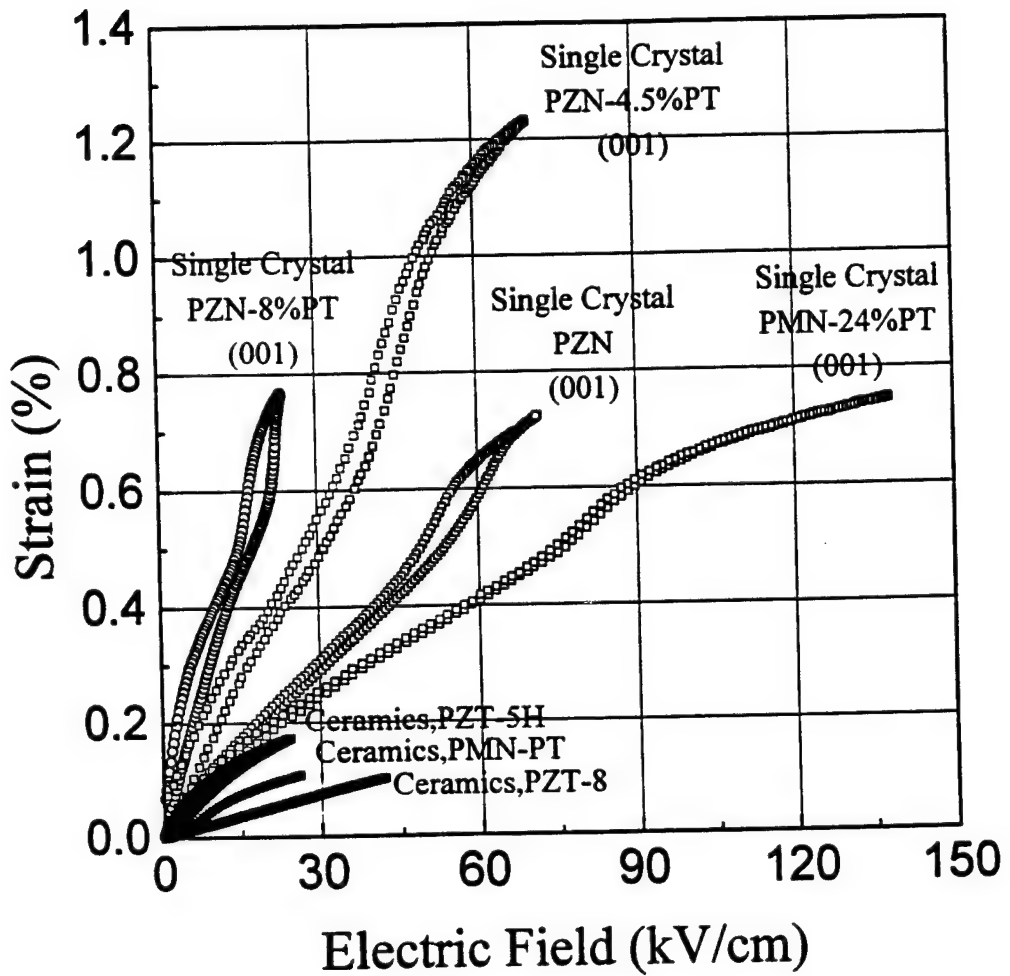
S.-E. Park and T. R. Shrout

Figure 14 Strain vs. E-field behaviors for crystals of PZN-PT and PMN-PT, and for various electromechanical ceramics.



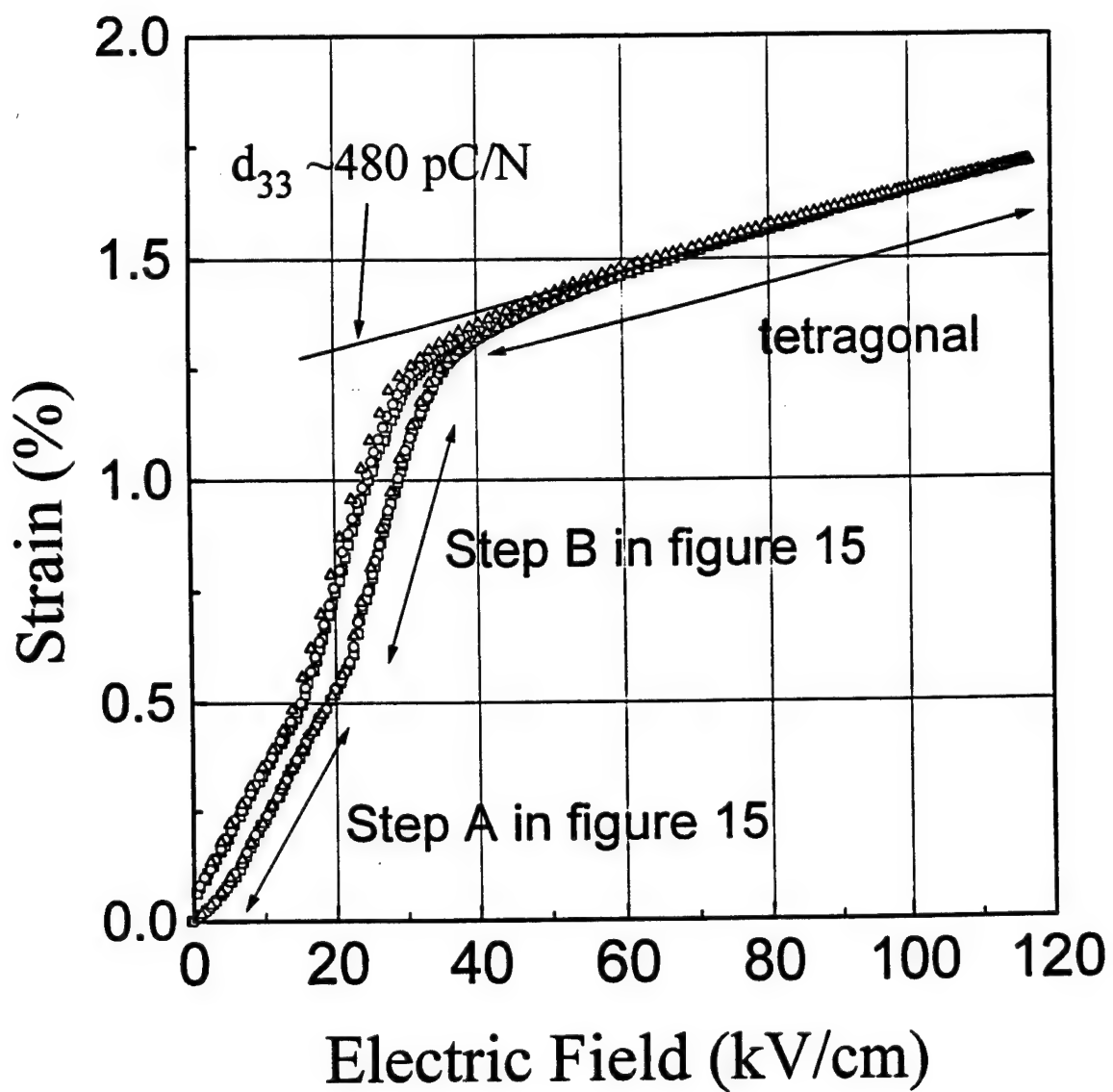
S.-E. Park and T. R. Shroud

Figure 15 Schematic diagram of domain configurations in $<001>$ oriented rhombohedral crystals



S.-E. Park and T. R. Shrout

Figure 16 Strain vs. E-field behaviors for crystals of PZN-PT and PMN-PT, and for various electromechanical ceramics. Maximum field was limited either by dielectric breakdown or by voltage limit of the apparatus.



S.-E. Park and T. R. Shrout

Figure 17 Strain vs. E-field behavior for <001> oriented PZN-8%PT crystal.
Maximum field is limited by voltage limit of the apparatus.

APPENDIX 52

Multilayer ceramic actuators

Kenji Uchino* and Sadayuki Takahashi†

Piezoelectric and electrostrictive ceramic materials have now become key components in smart actuator/sensor systems used as precision positioners, miniature ultrasonic motors and adaptive mechanical dampers. In particular, multilayer structures have been intensively investigated in order to improve their reliability and to expand their applications. There have been recent developments in the USA, Japan and Europe.

Addresses

*134 Materials Research Laboratory, The Pennsylvania State University, University Park, PA 16802, USA; e-mail:

KenjiUchino@Alpha.MRL.PSU.edu

†R&D Group, NEC Corporation, 4-1-1 Miyazaki, Miyamae Kawasaki 216, Japan

Current Opinion in Solid State & Materials Science 1996,
1:698–705

© Current Chemistry Ltd ISSN 1359-0286

Introduction

Piezoelectric actuators are forming a new field midway between electronic and structural ceramics [1^o,2–4]. Application fields can be classified into three categories: positioners, motors, and vibration suppressors. The manufacturing precision of optical instruments such as lasers and cameras, and the positioning accuracy for fabricating semiconductor chips, which are adjusted using solid-state actuators, is of the order of 0.1 mm. Tiny motors smaller than 1 cm³ are often required in office or factory automation equipment, and conventional electromagnetic motors which have sufficient energy efficiency are rather difficult to produce. Ultrasonic motors whose efficiency is insensitive to size are superior in the mini-motor area. Vibration suppression in space structures and military vehicles using piezoelectric actuators is also a promising technology.

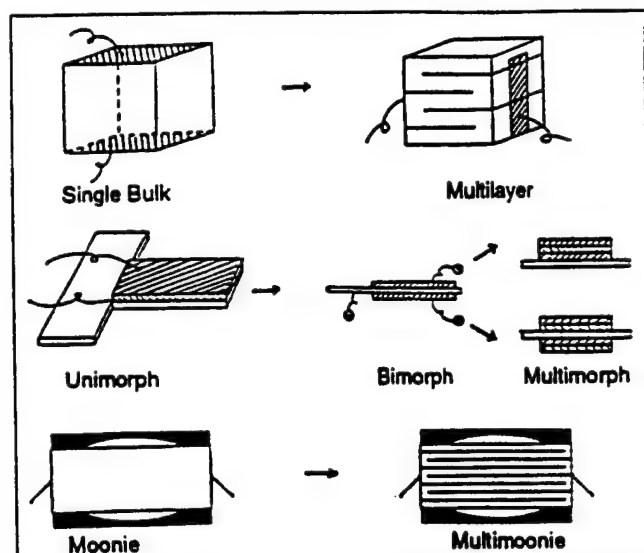
Multilayer structures are mainly used for practical applications because of their low drive voltage, high energy density, quick response and long lifetime [5,6^o]. Figure 1 illustrates multilayer, multimorph and multilayer-moonie structures, which will be covered in this review. Recent investigations have focused on the improvement of reliability and durability in multilayer actuators.

This article reviews the investigations of device structures, reliability issues, and recent applications of multilayer actuators, comparing developments in the USA, Japan and Europe.

Multilayer structures

Two preparation processes are possible for multilayer ceramic devices: a cut-and-bond method or a tape-casting method. The tape-casting method requires expensive

Figure 1



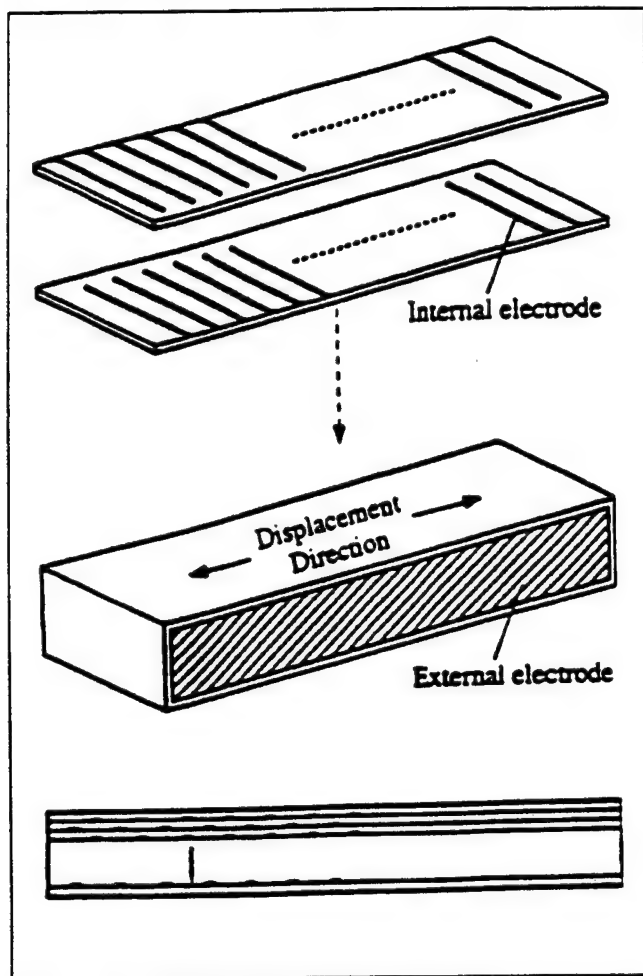
Examples of multilayer, multimorph and multilayer-moonie structures.

fabrication facilities and sophisticated techniques, but is suitable for the mass production of thousands of devices per month. Tape-casting also provides thin dielectric layers, leading to low drive voltages of 40–100 V [7^o,8].

A multilayer actuator with interdigital internal electrodes has been developed by Tokin [9,10]. In contrast to the conventional electrode configuration in Figure 1, line electrodes are printed on piezoelectric ceramic green sheets, and are stacked so that alternating electrode lines are displaced by one-half pitch (see Fig. 2). This actuator generates motions at right angles to the stacking direction using the longitudinal piezoelectric effect. Long ceramic actuators up to 74 mm in length are manufactured.

A three-dimensional positioning actuator with a stacked structure has been proposed by PI Ceramic (Fig. 3), in which shear strain is utilized to generate x and y displacements [11].

Composite actuator structures called 'moonies' and 'cymbals' have been developed at The Pennsylvania State University to provide characteristics intermediate between the multilayer and bimorph actuators. These transducers exhibit an order of magnitude larger displacement than the multilayer, and much a larger generative force with a quicker response than the bimorph [12,13^o]. The device consists of a thin multilayer piezoelectric element and two metal plates with narrow moon-shaped cavities bonded together as shown in Figure 1. A moonie 5×5×2.5 mm³ in size can generate a 20 mm displacement under 60 V.

Figure 2

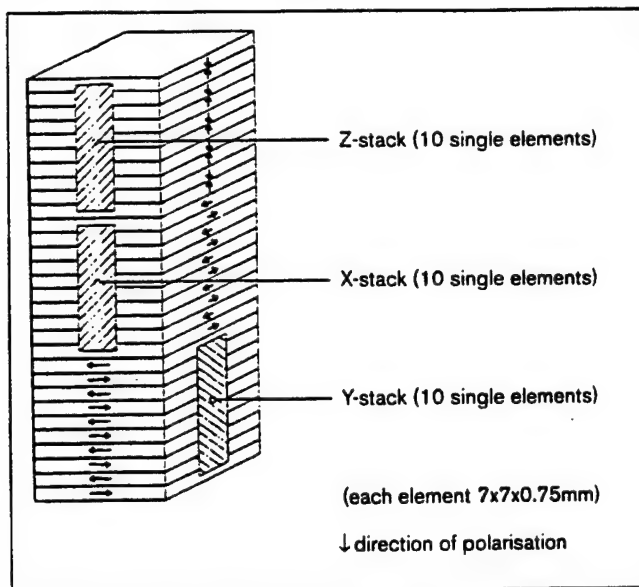
Structure of an internal interdigital electrode actuator.

eight times as large as the displacement of a multilayer of the same size [14]. This new compact actuator has been used to make a miniaturized laser beam scanner [14]. Moonic/cymbal characteristics have been investigated for various constituent materials and sizes [15,16].

Reliability of multilayer actuators

As the application fields expand, the reliability and durability issues for multilayer actuators become increasingly important. The reliability of ceramic actuators depends on a number of complex factors, which can be divided into three major categories: reliability of the ceramic itself, reliability of the device design, and drive technique.

Compositional changes of actuator ceramics and the effect of doping are the primary issues used in stabilizing the temperature and stress dependence of the induced strains. A multilayer piezoactuator for use at high temperatures (150°C) has been developed by Hitachi Metal, using Sb_2O_3 doped $(\text{Pb},\text{Sr})(\text{Zr},\text{Ti})\text{O}_3$ ceramics [17]. Systematic data on the uniaxial stress dependence of piezoelectric

Figure 3

3D controllable multilayer piezoelectric actuator.

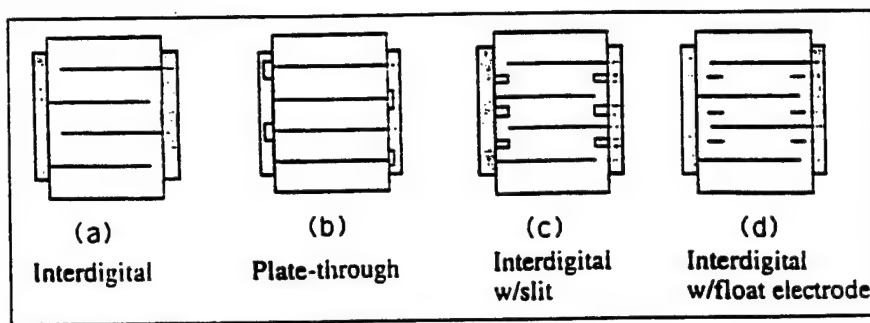
characteristics have been collected on various Navy PZT ($\text{Pb}(\text{Zr},\text{Ti})\text{O}_3$) materials [18]. The grain size and porosity control of the ceramics are also important in controlling the reproducibility of actuators [19]. Aging phenomena, especially the degradation of the strain response, are, in general, strongly dependent on the applied electric field as well as on temperature, humidity and mechanical bias stress [20].

The design of the device strongly affects its durability and lifetime. Silver electrode metal tends to migrate into the piezoceramic under a high electric field in high humidity. Silver-palladium alloys suppress this behavior effectively. Resistive coatings of the device should also be taken into account [21]. To overcome electrode delamination, improved adhesion can be achieved by using a mesh-type electrode or an electrode material with mixed metal and ceramic (the matrix composition!) powders. Pure ceramic electrode materials have also been developed using semiconductive perovskite oxides (barium titanate-based PTCR [positive temperature coefficient of resistivity] ceramics) [22]. The lifetime characteristics of a multilayer actuator with applied DC or unipolar AC voltage at various temperatures [23,24**] and at various humidities [25] have been investigated by Nagata and Kinoshitao. The relationship between the logarithm of the lifetime and the reciprocal of the absolute temperature showed linear characteristics similar to the Arrhenius type. Nevertheless, the degradation mechanism remains a critical problem.

In multilayer actuators, reduction of the tensile stress concentration around the internal electrode edge of the conventional interdigital configuration is the central

Figure 4

Various internal electrode configurations in multilayer actuators. (a) Interdigital, (b) Plate-through, (c) Slit-insert, and (d) Float electrode.



problem. With regard to the destruction mechanism of multilayer ceramic actuators, systematic data collection and analysis have led to considerable progress [26–32,33°]. Two typical crack patterns are generated in a conventional interdigital multilayer device: one is a Y-shaped crack located on the edge of an internal electrode, and the other is a vertical crack located in a layer adjacent to the top or bottom inactive layer, connecting a pair of internal electrodes.

To overcome this crack problem, three electrode configurations have been proposed (see Fig. 4): plate-through, interdigital and slit, and interdigital and float electrode types. The 'float electrode' type is an especially promising design which can be fabricated using almost the same process as the conventional multilayer actuator, and can lead to much longer lifetimes [34°]. An empirical rule 'the thinner the layer, the tougher the device' [27,28] is also very intriguing, and will receive more theoretical investigation in the near future.

Failure detection or lifetime prediction methods are expected to remarkably increase the reliability of multilayer actuators. Acoustic emission and surface potential monitoring are promising methods [35]. The Pennsylvania State University has developed a modified multilayer actuator containing a strain gauge as an internal electrode [36]. This internal strain gauge electrode can detect the crack initiation sensitively and monitor the field-induced strain [37°°].

When considering drive techniques for ceramic actuators, the pulse drive and AC drive require special attention. The vibration overshoot associated with a sharp-rise step/pulse voltage causes a large tensile force, leading to delamination of the multistacked structure, while the long-term application of an AC voltage generates considerable heat. A special pulse drive technique using a mechanical bias stress is required in the first case, and heat generation can be suppressed by changing the device design. An analytical approach to the heat generation mechanism in multilayer actuators has been reported, indicating the importance of a larger surface area [38]. Heat generation in piezoelectric ceramics is

mainly attributed to the P-E (polarization-electric field) hysteresis loss under large electric field drive [39°,40]. For ultrasonic motors, antiresonance drive is preferable to resonance drive because of higher efficiency and lower heat generation for the same vibration level [41].

Applications of multilayer actuators

Table 1 compares a variety of ceramic actuator developments in the USA, Japan and Europe. Additional details will be described below.

USA

The principal target is military-oriented applications such as vibration suppression in space structures and military vehicles. Substantial up-sizing of the actuators is required for these purposes. A typical example is found in the aircraft wing proposed by NASA [42]. A piezoelectric actuator was installed near the support of the wing, allowing immediate suppression of unwanted mechanical vibrations. Several papers have been reported on damper and noise cancellation applications [43,44].

Passive dampers constitute another important application of piezoelectrics, where mechanical noise vibration is radically suppressed by the converted electric energy dissipation through Joule heat when a suitable resistance, equal to an impedance of the piezoelectric element $1/\omega C$, is connected to the piezoelement [45].

A widely-publicized application occurred with the repair of the Hubble telescope launched by the Space Shuttle. Multilayer PMN ($\text{Pb}(\text{Mg}_{1/3}\text{Nb}_{2/3})\text{O}_3$) electrostrictive actuators corrected the image by adjusting the phase of the incident light wave (Fig. 5) [46]. PMN electrostrictors provided superior adjustment of the telescope image because of negligible strain hysteresis.

Japan

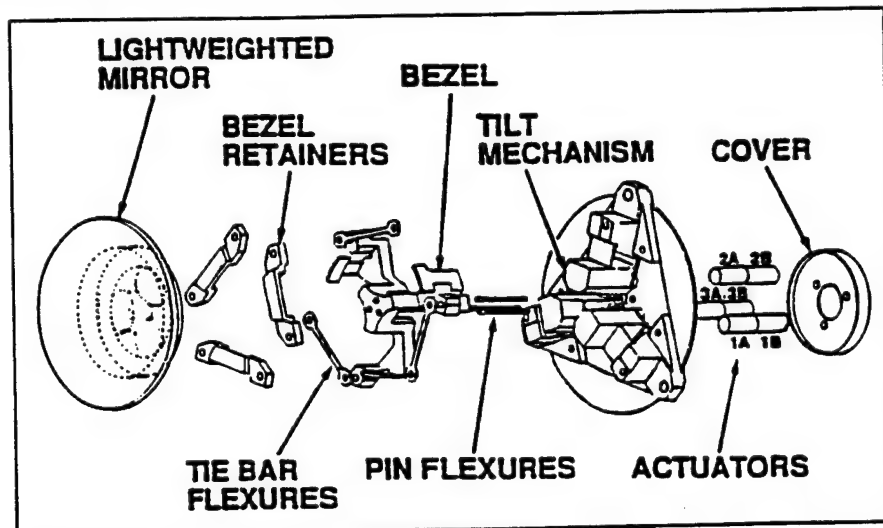
Japanese industries seek to develop mass-consumer products, especially mini-motors and micropositioners, aiming at applications such as office equipment and cameras/video cameras. Tiny actuators smaller than 1 cm^3 are the main focus in these products.

Table 1

Ceramic actuator developments in the USA, Japan and Europe.

	USA	Japan	Europe
Target	Military-oriented products	Mass-consumer products	Laboratory equipment
Category	Vibration suppressor	Mini-motor positioner	Mini-motor positioner Vibration suppressor
Application field	Space structure Military vehicle	Office equipment Cameras Precision machines Automobiles	Lab stage-stepper Airplanes Automobiles Hydraulic systems
Actuator size	Up-sizing (30 cm)	Down-sizing (1 cm)	Intermediate size (10 cm)
Major manufacturer	AVX/Kyocera Morgan Matroc Itek Opt. Systems Burleigh AlliedSignal	Tokin Corp. NEC Hitachi Metal Mitsui-Sekka Canon Seiko Instruments	Philips Siemens Hoechst Ceram Tec. Ferroperm Physik Instrumente

Figure 5

Articulating fold mirror using $Pb(Mg_{1/3}Nb_{2/3})O_3$ multilayer actuators.

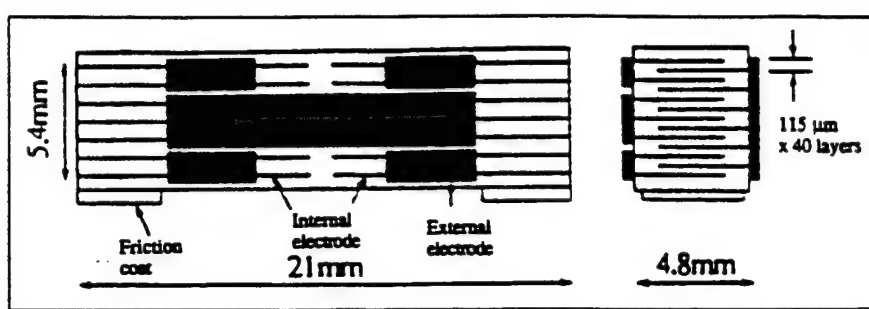
A dot matrix printer was the first widely-commercialized product using multilayer ceramic actuators [47]. Each character formed by such a printer was composed of a 24×24 dot matrix in which a printing ribbon was impacted by a multiwire array. The printing element was composed of a multilayer piezoelectric device with a sophisticated hinge lever magnification mechanism. The magnification by a factor of 30 resulted in an amplified displacement of 0.5 mm and an energy transfer efficiency greater than 50%. A modified impact printer head has been developed by Tokin, using new interdigital internal electrode type actuators, which have lowered the production cost [48]. A color ink-jet printer has also been commercialized by Seiko Epson, using multilayer piezoactuators [49].

Automotive applications by Toyota Motor have recently been accelerated. Multilayer actuators have been introduced to an electronically controlled suspension [50] and a pilot injection system for diesel engines [51].

Efforts have been made to develop high-power ultrasonic vibrators as replacements for conventional electromagnetic motors. The ultrasonic motor is characterized by 'low speed and high torque,' which is contrasted with the 'high speed and low torque' of the electromagnetic motors. Since the invention of π -shaped linear motors [52], various modifications have been reported [53,54•]. The Mitsui Petrochemical model is of particular interest because the motor body is composed of only one component prepared

Figure 6

Monolithic multilayer piezoelectric linear motor.



by a cofiring method as illustrated in Figure 6 [54^{**}]. A maximum speed of 200 mm/s and a maximum thrust of 60 gf have been reported for this motor.

Camera motors utilize a traveling elastic wave induced by a thin piezoelectric ring. A ring-type slider in contact with the 'rippled' surface of the elastic body bonded onto the piezoelectric can be driven in both directions by exchanging the sine and cosine voltage inputs. Another advantage is its thin design, making it suitable for installation in cameras as an automatic focusing device. Nearly 80% of the exchange lenses in Canon's 'EOS' camera series have been replaced by ultrasonic motor mechanisms [55^{*}].

Intriguing research programs are underway in Japan on the vibration damping of earthquakes, using piezoelectric actuators [56,57]. Active damping of a multilayer piezoactuator has been tested using an actual size H-type steel girder, and has been verified to be effective during earthquakes.

Europe

Ceramic actuator development began relatively recently in Europe with a wide range of research topics. Several major manufacturers are currently focusing on laboratory equipment products such as laboratory stages and steppers with rather sophisticated structures.

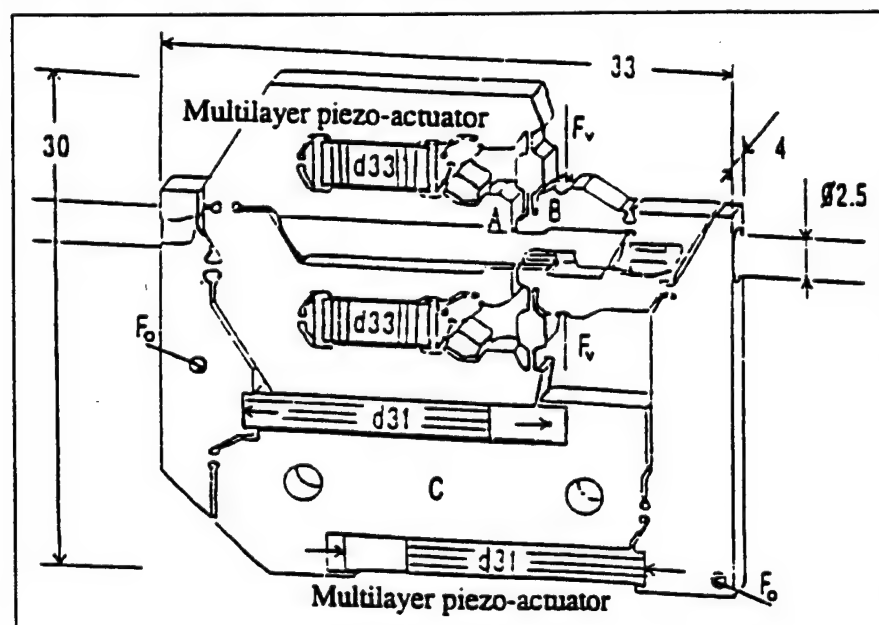
Figure 7 shows a walking piezomotor with four multilayer actuators made by Philips [58]. Two short actuators function as clamps while the longer two provide a proceeding distance in an inchworm mechanism. Physik Instrumente has developed more complicated two-leg type walkers [59].

Conclusions

The intensive development of piezoelectric actuators began in Japan 18 years ago and then spread worldwide. At present, attention is being focused on practical device applications. This article has reviewed several reliability issues for the multilayer ceramic actuators as well as new

Figure 7

An inchworm using multilayer piezoelectric actuators.



actuator structures, and compared the developments of recent applications in the USA, Japan and Europe.

The markets in USA are chiefly limited to military and defense applications, and it is difficult to estimate the amount of sales. The current Navy needs include smart submarine skins, hydrophone actuators, and prop noise cancellation. Smart aircraft skins are an Air Force objective, while the Army requires helicopter rotor twisting, aeroservoelastic control and cabin noise/seat vibration cancellation.

Meanwhile in Japan, piezoelectric shutters (Minolta Camera) and automatic focusing mechanisms in cameras (Canon), dot-matrix printers (NEC) and part-feeders (Sanki) are mass-produced by tens of thousands of pieces per month. During the commercialization, new designs and drive-control techniques of the ceramic actuators have been developed mainly over the past few years. A number of patent disclosures have been generated by NEC, TOTO Corporation, Matsushita Electric, Brother Industry, Toyota Motors, Tokin, Hitachi Metal, and Toshiba.

If we estimate the annual sales in 2001 (neglecting the current economic recession in Japan), ceramic actuator units, camera-related devices and ultrasonic motors are expected to reach \$500 million, \$300 million and \$150 million, respectively. A total of \$10 billion is a realistic target for the overall sales actuator-related products [55].

Future research trends can be divided in two ways: up-sizing in space structures and down-sizing in office equipment. Further down-sizing will also be required in medical diagnostic applications such as blood test kits and surgical catheters.

Key words for the future of multilayer ceramic actuators are 'miniaturization' and 'hybridization'. Layers thinner than 10 µm, corresponding to current multilayer capacitor technology, will also be introduced in actuator devices replacing the present 100 µm sheets. Piezoelectric thin films compatible with silicon technology are a focus in micro-electromechanical systems. Ultrasonic rotary motors as small as 2 mm in diameter [60] and a two-dimensional micro-optical-scanner [61], both of which were fabricated on a silicon membrane are good examples.

Nonuniform configurations or heterostructures of different materials, layer thickness, or electrode patterns will be adopted for practical devices. Functionally gradient piezoelectric actuators now being prototyped indicate a new trend [62].

References and recommended reading

Papers of particular interest, published within the annual period of review, have been highlighted as:

- of special interest
- of outstanding interest

1. Uchino K: *Piezoelectric actuators/ultrasonic motors*. Norwell, Massachusetts: Kluwer Academic Publishers; 1996.
This textbook covers theoretical background, material and device developments, and most important applications, placing particular emphasis on the cofired multilayer structures invented by the author. Recommended reading for beginners and experts.
2. Uchino K: Ceramic actuators: principles and applications. *MRS Bull* 1993, 18:42-48.
3. Uchino K: Materials update: advances in ceramic actuator materials. *Mater Lett* 1995, 22:1-4.
4. Uchino K: New piezoelectric devices for smart actuator/sensor systems. In *Proceedings of the 4th International Conference on Electronic Ceramics and Applications: 1994*; Germany. Edited by Waser R. Aachen, Germany: Verlag der Augustinus Buchhandlung; 1995:179-191.
5. Yoshikawa S, Shrout T: Multilayer piezoelectric actuators - structures and reliability. *AIAA/ASME/ASCE/AHS/ASC Struct Struct Dyn Mater Conference* 1993, 34:3581-3586.
6. Uchino K: Manufacturing technology of multilayered transducers. In *Proceedings Amer Ceram Soc, Manufacture of Ceramic Components: 1995*; Ohio. Edited by Hiramat BV. Westerville, Ohio: The American Ceramic Society Inc; 1995:81-93.
General problems for manufacturing multilayer ceramic devices are discussed, and possible solutions are introduced in this paper. Recommended reading for experts.
7. Dibbern U: Piezoelectric actuators in multilayer technique. In *Proceedings of the 4th International Conference on New Actuators (Actuator '94)*; 1994; Germany. Bremen, Germany: AXON Technologie Consult GmbH; 1995:114-118.
The thinnest layer (20 µm) actuators manufactured by Philips are reviewed in comparison with those by NEC, Siemens, and other manufacturers.
8. Takada S, Inoue Y, Oya K, Inagawa M: 100 V DC driving type multilayer piezoelectric actuator. *NEC Giho* 1994, 47:98-102.
9. Ohashi J, Fuda Y, Ohno T: Multilayer piezoelectric ceramic actuator with interdigital internal electrodes. *Jpn J Appl Phys* 1993, 32:2412-2414.
10. Ohashi J, Fuda Y, Ohno T: Multilayer piezoelectric ceramic actuator with interdigital internal electrodes. *Tokin Tech Rev* 1993, 19:55-60.
11. Bauer A, Moller F: Piezo actuator special design. In *Proceedings 4th International Conference New Actuators (Actuator '94)* 1994; Germany. Bremen, Germany: AXON Technologie Consult GmbH; 1995:128-132.
12. Sugawara Y, Onitsuka K, Yoshikawa S, Xu QC, Newnham RE, Uchino K: Metal-ceramic composite actuators. *J Amer Ceram Soc* 1992, 75:996-998.
13. Onitsuka K, Dogan A, Tressler JF, Xu QC, Yoshikawa S, Newnham RE: Metal-ceramic composite transducer, the 'moonie'. *Intelligent Mater Systems Struct* 1995, 6:447-455.
Good review paper on the 'moonie' actuators and sensors.
14. Goto H, Imanaka K, Uchino K: Piezoelectric actuators for light beam scanners. *Ultrasonic Technol* 1992, 5:48-51.
15. Tressler JF, Xu QC, Yoshikawa S, Uchino K, Newnham RE: Composite flexensional transducers for sensing and actuating. (*Proceedings of the 8th International Meeting Ferroelectricity*) *Ferroelectrics* 1994, 156:67-72.
16. Dogan A, Fernandez JF, Uchino K, Newnham RE: New piezoelectric composite actuator designs for displacement

- amplification. *Proceedings of the 4th Euro Ceramics 1994*, 5:127-132.
17. Watanabe J, Sometsugu T, Watanabe Y, Johmura S, Kurihara K, Kazama Y: Multilayer piezoelectric ceramic actuator for high temperature use. *Hitachi Metal Goho* 1993, 9:59-64.
 18. Zhang QM, Zhao JZ, Uchino K, Zheng JH: Change of the weak field properties of $Pb(Zr,Ti)O_3$ piezoceramics with compressive uniaxial stresses and its links to the effect of dopants on the stability of the polarizations in the materials. *J Mater Res* 1996, in press.
 19. Okada N, Ishikawa K, Murakami K, Nomura T, Ogino M: Improving hysteresis of piezoelectric pzt actuator. *Bull Shizuoka Univ Electron Sci Grad School* 1993, 14:7-13.
 20. Sakai T, Ishikiriyama M, Terai Y, Shimazaki R: Improvement in the durability of PZT ceramics for an actuator. *Toyota Tech Rev* 1992, 42:52-59.
 21. Takada S: Quality improvement of multilayer piezoelectric actuator. *NEC Goho* 1992, 45:109-113.
 22. Abe K, Uchino K, Nomura Late S: Barium titanate-based actuator with ceramic internal electrodes. *Ferroelectrics* 1986, 68:215-223.
 23. Nagata K, Kinoshita S: Life time of multilayer ceramic actuator at high temperature. *J Powder Metallurgy* 1994, 41:975-979.
 24. Nagata K, Kinoshita S: Relationship between lifetime of multilayer ceramic actuator and temperature. *Jpn J Appl Phys* 1995, 34:5266-5269.
 - The lifetime evaluation, which is the 'must' experiment, but has not been actually carried out so far, is described in this paper. Combined with [25], we can obtain practical data on the lifetime of multilayer actuators.
 25. Nagata K, Kinoshita S: Effect of humidity on life time of multilayer ceramic actuator. *J Powder Metallurgy* 1995, 42:623-627.
 26. Furuta A, Uchino K: Dynamic observation of crack propagation in piezoelectric multilayer actuators. *J Amer Ceram Soc* 1993, 76:1615-1617.
 27. Aburatani H, Harada S, Uchino K, Furuta A, Fuda Y: Destruction mechanisms in ceramic multilayer actuators. *Jpn J Appl Phys* 1994, 33:3091-3094.
 28. Furuta A, Uchino K: Destruction mechanism of multilayer ceramic actuators: case of antiferroelectrics. *Ferroelectrics* 1994, 160:277-285.
 29. Wang H, Singh RN: Electric field effects on the crack propagation in a electro-strictive PMN-PT ceramic. *Ferroelectrics* 1995, 168:281-291.
 30. Cao HC, Evans AG: Electric-field-induced fatigue crack growth in piezoelectrics. *J Amer Ceram Soc* 1994, 77:1783-1786.
 31. Schneider GA, Rostek A, Zickgraf B, Aldinger F: Crack growth in ferroelectric ceramics under mechanical and electrical loading. In *Proceedings of the 4th International Conference on Electronic Ceramics and Applications: 1994*; Germany. Edited by Waser R. Aachen, Germany: Verlag der Augustinus Buchhandlung; 1994:1211-1216.
 32. Suo Z: Models for breakdown resistant dielectric and ferroelectric ceramics. *J Mech Phys Solids* 1993, 41:1155-1176.
 33. Hao TH, Gong X, Suo Z: Fracture mechanics for the design of ceramic multilayer actuators. *J Mech Phys Solids* 1996, in press. Comprehensive theoretical approach to explain the crack propagation in multilayer piezoelectric actuators.
 34. Aburatani H, Uchino K, Furuta A and Fuda Y: Destruction mechanism and destruction detection technique for multilayer ceramic actuators. In *Proceedings of the 9th International Symposium Applied Ferroelectrics IEEE: 1994*; Pennsylvania. Edited by Pandey RK, Liu M, Safar A. Piscataway, New Jersey: IEEE; 1995, 750-752.
 - Float internal electrode idea has been introduced to improve the durability of multilayer ceramic actuators while retaining the easy and cheap fabrication process.
 35. Uchino K, Aburatani H: Destruction detection techniques for safety piezoelectric actuator systems. In *Proceedings 2nd International Conference on Intelligent Materials: 1994*, Edited by Rogers C. Technomic Publication; 1994:1248-1256.
 36. Sano M, Ohya K, Hamada K, Inoue Y, Kajino Y: Multilayer piezoelectric actuator with strain gauge. *NEC Goho* 1993, 46:100-103.
 37. Aburatani H, Uchino K: Stress and fatigue estimation in multilayer ceramic actuators using an internal strain gauge. *Annual Meeting and Exposition of the American Ceramic Society International Symposium on Solid-State Sensors and Actuators, 1996*. Abstract SXIX-37:96:191.
 - This paper proposes a unique concept for detecting both the induced strain and the crack initiation simultaneously, using an embedded strain gauge type electrode.
 38. Zheng JH, Takahashi S, Yoshikawa S, Uchino K: Heat generation in multilayer piezoelectric actuators. *J Amer Ceram Soc* 1996, in press.
 39. Hirose S, Takahashi S, Uchino K, Aoyagi M, Tomikawa Y: Measuring methods for high-power characteristics of piezoelectric materials. In *Proceedings Mater Res Soc, '94 Fall Mtg: 1994 Nov 28-30; Boston, Massachusetts*. Edited by George EP, Takahashi S, McKinstry ST, Uchino K, Won-Fogle. MRS Symposium Proceedings Vol 360, Materials for Smart Systems; 1995, 360:15-20.
 - Review of measuring methods for high-power piezoelectric characteristics using a constant current method, which is completely different from the conventional constant voltage method.
 40. Takahashi S, Sakaki Y, Hirose S, Uchino K: Stability of $PbZrO_3$ - $PbTiO_3$ - $Pb(Mn_{1/3}Sb_{2/3})O_3$ piezoelectric ceramics under vibration-level change. *Jpn J Appl Phys* 1995, 34:5328-5331.
 41. Hirose S, Aoyagi M, Tomikawa Y, Takahashi S, Uchino K: High-power characteristics at antiresonance frequency of piezoelectric transducers. In *Proceedings of the Ultrasonic International Conference: July 4-7; Edinburgh, UK* 1995, 1-4.
 42. Heeg J: *Analytical and Experimental Investigation of Flutter Suppression by Piezoelectric Actuation 1993*. NASA, USA. [NASA Tech Pap, NASA-TP-3241 1993, 47].
 43. Mather GP, Tran BN: Aircraft cabin noise reduction tests using active structural acoustic control. *Pap Amer Inst Aeronaut Astronaut* 1993, AIAA-93-4437: 7.
 44. Agrawal BN, Bang H: Active vibration control of flexible space structures by using piezoelectric sensors and actuators. *Amer Soc Mech Eng Des Eng Div* 1993, 61:169-179.
 45. Uchino K, Ishii T: Mechanical damper using piezoelectric ceramics. *J Jpn Ceram Soc* 1988, 96:863-867.
 46. Wada B: *Summary of Precision Actuators for Space Application - March 1993*. Pasadena, California: Jet Repulsion Laboratory; 1993. [JPL Document D-10659].
 47. Yano T, Fukui I, Sato E, Inui O, Miyazaki Y: Impact dot-matrix printer head using multilayer piezoelectric actuators. *Proc Electr Commun Soc* 1984, 1:156.
 48. Ono Y, Fuda Y: Multilayer piezoelectric ceramic actuator with interdigital internal electrodes for impact dot-matrix printers. In *Proceedings of the 6th Symposium on Electro-Magnetic Related Dynamics: 1994*; Japan. Edited by The Committee of Electro-magnetic Related Dynamics. Sendai, Japan; 1994:135-138.
 49. Yonekubo S: Color inkjet printer by multi-layer piezoelectric actuator. *J Electron Photo Soc* 1995, 34:226-228.
 50. Fukami A, Yano M, Tokuda H, Ohki M, Kizu R: Development of piezo-electric actuators and sensors for electronically controlled suspension. *Int J Veh Des* 1994, 15:348-357.
 51. Abe S, Igashira T, Sakakibara Y, Kobayashi F: Development of pilot injection system equipped with piezoelectric actuator for diesel engine. *JSAE Rev (Soc Automot Eng Jpn)* 1994, 15:201-208.
 52. Tohda M, Ichikawa S, Uchino K, Kato K: Ultrasonic linear motor using a multilayered piezoelectric actuator. *Ferroelectrics (Proceedings ECAPD-1/ISAF '88):1988; Switzerland*. *Ferroelectrics* 1989, 93:287-294.
 53. Funakubo T, Tsubata T, Taniguchi Y, Kumei K, Fujumura T, Abe C: Ultrasonic linear motor using multilayer piezoelectric actuators. *Jpn J Appl Phys* 1995, 34:2756-2759.

54. Saigoh H, Kawasaki M, Maruko N, Kanayama K: Multilayer piezoelectric motor using the first longitudinal and the second bending vibrations. *Jpn J Appl Phys* 1995, 34:2760-2764.
Very innovative work. The motor body is fabricated by one component, a cofired multilayer actuator, which upset the conventional design concept of a combination of a piezo-driver and a vibratory piece.
55. Uchino K: Piezoelectric actuators/ultrasonic motors-their developments and markets. In *Proceedings of the 9th International Symposium of Applied Ferroelectrics IEEE: 1994; Pennsylvania*. Edited by Pandey RK, Liu M, Safari A. Piscataway, New Jersey: IEEE; 1995;319-324.
Original data on the market prediction can be found in this paper. A useful paper for developers of multilayer ceramic actuators.
56. Shimoda H, Ohmata J, Okamoto F: Seismic response control of a piping system by a semiactive damper with piezoelectric actuators. *J Precision Engr Jpn* 1992, 58:2111-2117.
57. Fujita T: Can piezoelectric actuators control vibrations of buildings? *New Ceramics* 1994, 7:52-55.
58. Koster MP: A Walking Piezo Motor. In *Proceedings 4th International Conference New Actuators (Actuator '94)*; 1994; Germany, Bremen, Germany: AXON Technologie Consult GmbH; 1994:144-148.
59. Gross R: A High Resolution Piezo Walk Drive. In *Proceedings 4th International Conference New Actuators, (Actuator '94)*; 1994; Germany, Bremen, Germany: AXON Technologie Consult GmbH; 1994:190-192.
60. Flynn AM, Tavrow LS, Bart SF, Brooks RA, Ehrlich DJ, Udayakumar KR, Cross LE: Piezoelectric Micromotors for Microrobots. *IEEE J Microelectromechanical Systems* 1992, 1:44-51.
61. Goto H: Miniature 2D optical scanner and its application to an optical sensor. *J Opt Tech Contact* 1994, 32:322-330.
62. Kim HS, Choi SC, Lee JK, Jung HJ: Fabrication and piezoelectric strain characteristics of PLZT functionally gradient piezoelectric actuator by doctor blade process. *J Korean Ceram Soc* 1992, 29:695-704.

APPENDIX 53

Heat Generation in Multilayer Piezoelectric Actuators

Jiehui Zheng,¹ Sadayuki Takahashi,^{1,*} Shoko Yoshikawa,¹ and Kenji Uchino²

International Center for Actuators and Transducers, Materials Research Laboratory,
The Pennsylvania State University, University Park, Pennsylvania 16802

J. W. C. de Vries

Ceramic Innovation Center, Philips Components B.V., Bredeweg 10, 6042 GG Roermond, The Netherlands

Multilayer piezoelectric actuators when driven under high frequency, generate significant heat, which influences the reliability and other piezoelectric properties. In this paper, heat generation in various types of multilayer PZT-based actuators was studied. Experimental results showed that heat generation is mainly caused by ferroelectric hysteresis loss in the stress-free state. A simplified analytic method was established to evaluate the temperature rise, which is useful for the design of multilayer and other high-power actuators.

I. Introduction

MULTILAYER piezoelectric actuators have been under intensive development during the past decade¹⁻⁶ and have led to some applications such as impact printer heads,^{7,8} ultrasonic linear motors,⁹ and x-y stages.¹⁰ Today, low voltages are the trend for electronic systems, cars, and medical devices.¹¹ This trend has made the multilayer structure with thin layers necessary. Efforts have been made and thin layers down to 20 μm have been achieved.⁵

In order to obtain maximum displacement of the actuator, an electric field of 1–3 kV/mm is usually necessary. For some applications, like the commercialized high-speed impact printer head with a printing speed of 3 kHz,⁷ a high-frequency voltage is applied to the actuator. Under such continuous high frequency, and driving with a high electric field, fairly large heat generation has been observed.¹² Heat generation influences the reliability and other properties and may also limit the applications of the actuators. Therefore, a comprehensive investigation of heat generation becomes very important.

This paper has studied heat generation in various types of multilayer PZT-based actuators. A simplified analytic method was established to evaluate the temperature rise, which is very useful for the design of multilayer and other high-power actuators.

II. Experimental Procedure

Multilayer PZT-based ceramic actuators of various types (see Table I) were prepared by a tape casting technique. The thickness of the active layers was 20 or 40 μm . After cutting

and the application of the end termination, the samples were poled by applying a high voltage at an elevated temperature.

The heat generation experiment was carried out by monitoring the temperature rise of the actuators under continuous voltage driving. The actuators were floated in free air supported by two rigid paper legs. Under this condition, heat conduction through the holder was minimized. When the actuator was put directly on a certain surface, the heat conduction through the sample surface was increased. The former sample holder was used in this study.

The actuators were driven by continuous triangular unipolar voltages. The voltages were generated by an NF 1940 Function Synthesizer, amplified through an NF 4010 High Speed Power Amplifier (the voltage being in the range of 300 V, current range 1.2 A), and then applied to the actuators.

The temperature rise of the actuators was measured by attaching a very fine ($\phi = 0.001$ in.) chromel-alumel thermocouple (CHAL-001, OMEGA Engineering Inc.) to the center of the sample surface. Silicone grease was used as a connective material. The temperature was read through a thermometer (OMEGA HH11) with an accuracy of 0.1°C.

III. Results

(1) Temperature Rise Phenomena

Heat generation for various size actuators, while driving under 3 kV/mm at 300 Hz, is shown in Fig. 1. It is seen from the figure that the actuator temperature initially increases exponentially with an increase in the driving time (t), and then it reaches equilibrium. Temperature rise ΔT is defined as

$$\Delta T = T - T_0$$

where T and T_0 indicate the maximum and initial actuator temperatures. The relationship between ΔT and v_e/A , where v_e is the effective volume where electric field is applied, and A is the total surface area of the sample, is shown in Fig. 2. Temperature rise ΔT is approximately proportional to the value v_e/A , because the heat generation is assumed to be proportional to the " v_e " defined above, and the heat dissipation is proportional to the surface area A .

Heat generation depends on driving frequency (f). The frequency dependence of the temperature rise ΔT is given in Fig. 3 for various applied electric fields. At the low electric field level, ΔT increases almost linearly with increasing driving frequency. As the electric field level becomes higher (>1 kV/mm), the $\Delta T \sim f$ curves gradually deviate from the linear trend.

Heat generation is also electric field (E) dependent. The temperature as a function of time for the actuator with dimensions of 7 mm \times 7 mm \times 2 mm is shown in Fig. 4. Figure 5 gives the temperature rise ΔT as a function of applied electric field at various frequencies. The ΔT is initially proportional to E^2 . But the curves then deviate from this square relationship under higher electric field levels.

W. Huebner—contributing editor

Manuscript No. 192336. Received September 6, 1995; approved June 7, 1996.
Presented at the 97th Annual Meeting of the American Ceramic Society, Cincinnati,
OH, May 1, 1995 (Electronics Division, Paper No. E-14-95).

Supported by Philips Components.

*Member, American Ceramic Society.

¹Permanent address: R & D Group, NEC Corporation, Miyazaki, Miyamae-ku,
Kawasaki 216, Japan.

Table I. Various Sizes of Multilayer Actuators

Actuator type	Dimensions (mm)	Layer thickness (μm)	Surface area A (mm^2)	Effective volume ^a v_e (mm^3)	v_e/A (mm)
d_{33}	4.5 × 3.5 × 2	20	63.5	18.8	0.293
	7 × 7 × 2	40	154	72.3	0.470
	5 × 5 × 20	40	450	308	0.882
	17 × 3.5 × 1	20	160	40.2	0.251
Multimorph	31 × 9 × 0.3	20	582	34.7	0.078

^aEffective volume is a volume that actually generates heat.

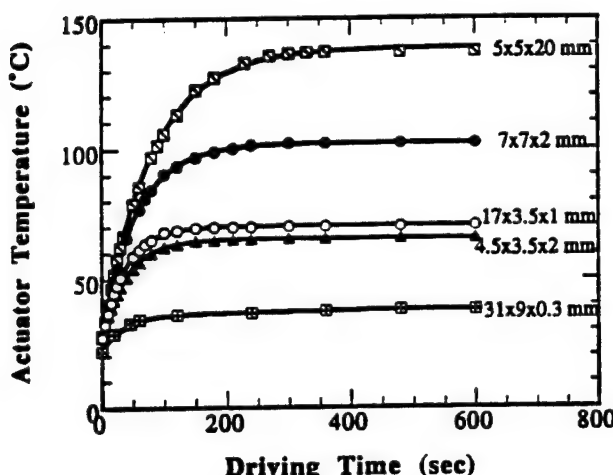
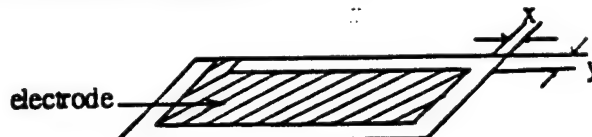


Fig. 1. Heat generation for various actuators (driven at 3 kV/mm, 300 Hz).

(2) P-E Hysteresis Loss

Heat generation in piezoelectric actuators is considered to be caused by losses, such as mechanical loss and dielectric loss.¹²⁻¹⁴ Since the major contribution to dielectric loss is from the ferroelectric hysteresis loss under high electric fields (higher than the threshold field at which domain wall motions start),^{15,16} in this paper, the ferroelectric loss was studied. With the well-known Sawyer-Tower circuit, the polarization (*P*)–electric field (*E*) hysteresis loops were observed. The *P*–*E* hysteresis loops of different size actuators are almost the same, because all of the actuators are made of the same composition. However,

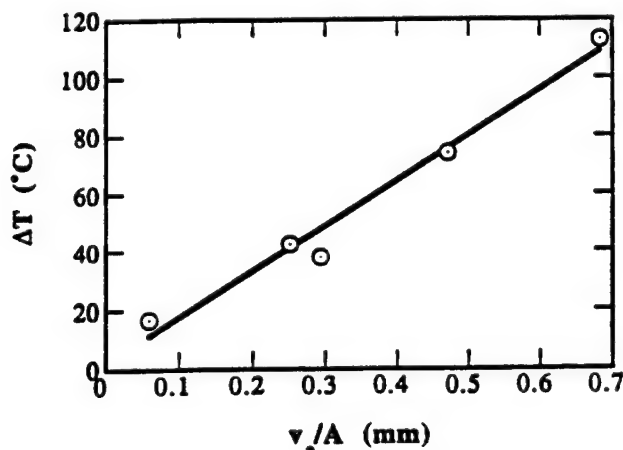


Fig. 2. Temperature rise vs v_e/A (3 kV/mm, 300 Hz).

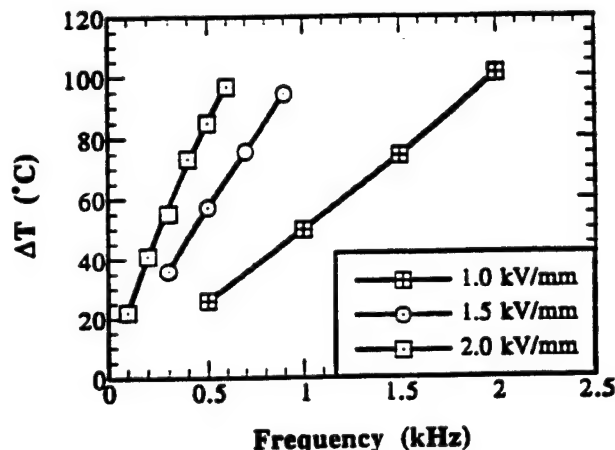


Fig. 3. Temperature rise vs frequency under various applied electric fields (data from the actuator with dimensions of 7 mm × 7 mm × 7 mm).

the hysteresis loops depend on temperature, frequency, and the electric field. At different sample temperatures, hysteresis loops are slightly different. Figure 6 shows the *P*–*E* hysteresis loops at 25° and 98°C, while driving under 3 kV/mm, 300 Hz. The hysteresis areas represent the ferroelectric loss per driving cycle, *u*. The ferroelectric loss *u* as a function of sample temperature is shown in Fig. 7. It is seen that *u* decreases slightly with an increase of the sample temperature. The *P*–*E* hysteresis

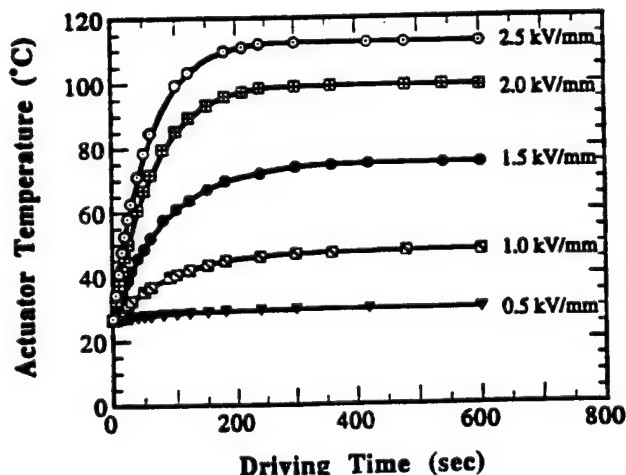


Fig. 4. Heat generation while driving under various electric fields at 400 Hz (data from the actuator with dimensions of 7 mm × 7 mm × 2 mm).

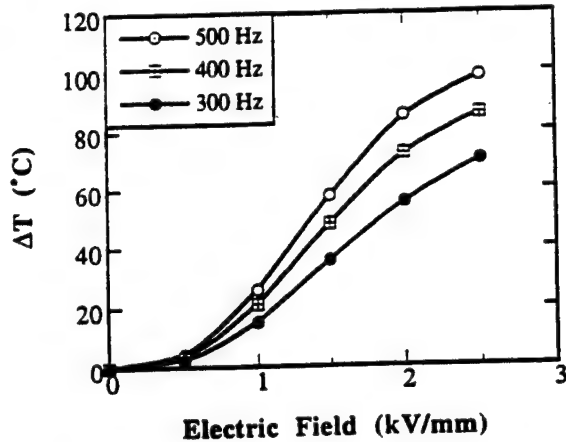


Fig. 5. Temperature rise as a function of applied electric fields (data from the actuator with dimensions of 7 mm \times 7 mm \times 2 mm).

loss also decreases slightly with increasing frequency (Fig. 8). However, it increases noticeably when the applied electric field is increased (Fig. 9). The hysteresis loss is approximately proportional to E^2 (Fig. 10).

IV. Theoretical Analysis and Discussion

According to the law of energy conservation, the rate of heat storage in the actuator resulting from heat generation and dissipation effects can be expressed as (assuming uniform temperature distribution in the sample)

$$\dot{q}_G - \dot{q}_{out} = vpc \left(\frac{dT}{dt} \right) \quad (1)$$

where v , p , c are total volume, density, and specific heat, respectively.

As stated above, heat generation is considered to be caused by losses. Thus, the rate of heat generation (\dot{q}_G) in the actuator can be expressed as

$$\dot{q}_G = u f v_e \quad (2)$$

where u is the loss of the sample per driving cycle per unit volume, f is the driving frequency, v_e is the effective volume which actually generates heat (as defined above).

Since the conduction heat transfer rate through the lead wire in this experiment is negligibly small (i.e., roughly 1/25 of the

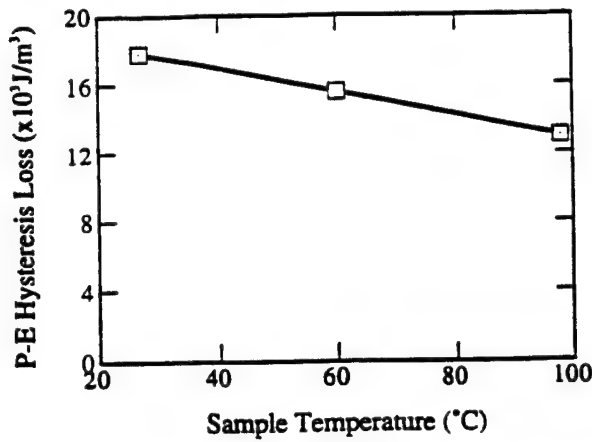


Fig. 7. P - E hysteresis loss as a function of sample temperatures (3 kV/mm, 300 Hz).

convection), the rate of heat dissipation (\dot{q}_{out}) from the actuator is the sum of the rates of heat flow by radiation (\dot{q}_r) and convection (\dot{q}_c)

$$\begin{aligned} \dot{q}_{out} &= \dot{q}_r + \dot{q}_c \\ &= \sigma \epsilon A (T^4 - T_0^4) + \bar{h}_c A (T - T_0) \end{aligned} \quad (3)$$

where σ is the Stefan-Boltzmann constant (5.67×10^{-8} W/(m²·K⁴)), ϵ is the emissivity of the sample, and \bar{h}_c is the average convective heat transfer coefficient.

Thus, by substituting \dot{q}_G and \dot{q}_{out} from Eqs. (2) and (3), Eq. (1) becomes

$$ufv_e - A[\sigma\epsilon(T^4 - T_0^4) + \bar{h}_c(T - T_0)] = vpc \left(\frac{dT}{dt} \right) \quad (4)$$

The above equation can be written in the form

$$ufv_e - Ak(T)(T - T_0) = vpc(dT/dt) \quad (5)$$

where

$$k(T) = \sigma\epsilon(T^4 + T_0^4)(T + T_0) + \bar{h}_c \quad (6)$$

is defined as the overall heat transfer coefficient. The first term of $k(T)$, $\sigma\epsilon(T^4 - T_0^4)(T + T_0)$, is 5.58 W/(m²·K) at 25°C and 9.08 W/(m²·K) at 125°C, if we take ϵ of the sample as 0.93 (similar to rough fused quartz), while \bar{h}_c has the magnitude of

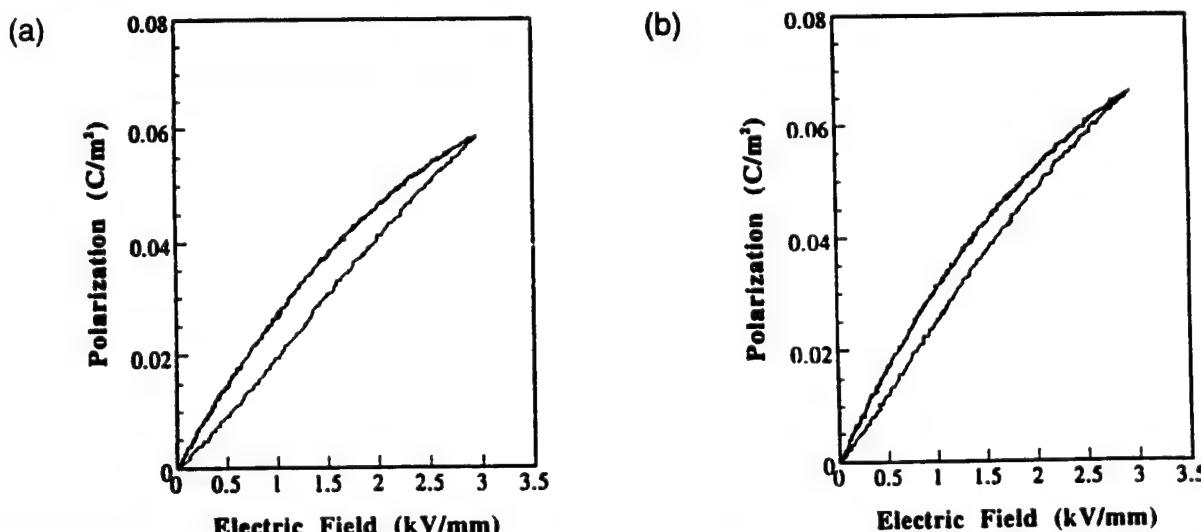


Fig. 6. P - E hysteresis loops at different sample temperatures: (a) 25°C, (b) 98°C (3 kV/mm, 300 Hz).

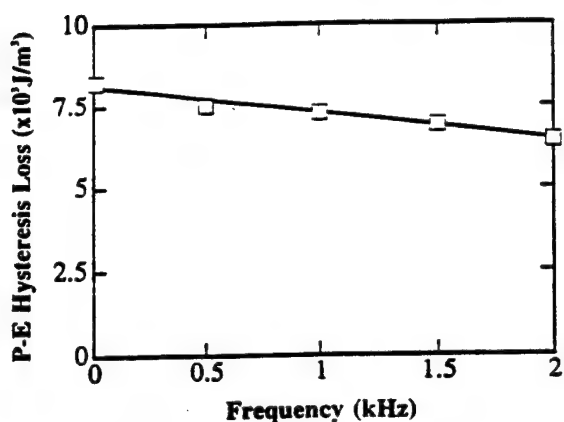


Fig. 8. $P-E$ hysteresis loss as a function of frequency ($T = 25^\circ\text{C}$, $E = 2 \text{ kV/mm}$).

6–30 $\text{W}/(\text{m}^2 \cdot \text{K})$ for free convection in air¹⁷ (our results in Figs. 12 and 13 suggest that \bar{h}_c is close to $20 \text{ W}/(\text{m}^2 \cdot \text{K})$ at free convection state), and it increases when increasing the forced convection (\bar{h}_c is about 10–500 $\text{W}/(\text{m}^2 \cdot \text{K})$ for forced convection in air¹⁸). Therefore, we can take $k(T)$ as a constant relatively insensitive to temperature change. Then, the solution to Eq. (5) for the actuator temperature as a function of time (t) is

$$T - T_0 = \frac{ufv_e}{k(T)A} (1 - e^{-(k(T)A/\rho c)^t}) \quad (7)$$

The time constant in Eq. (4) is

$$\tau = \frac{\rho c}{k(T)A} \quad (8)$$

As $t \rightarrow \infty$, the maximum temperature rise in the actuator becomes

$$\Delta T = \frac{ufv_e}{k(T)A} \quad (9)$$

At $t \rightarrow 0$, where there is no heat dissipation effect, the initial rate of temperature rise is

$$\left(\frac{dT}{dt} \right)_{t=0} = \frac{ufv_e}{\rho c v} = \frac{\Delta T}{\tau} \quad (10)$$

Curve fit to the experimental data with the solution form

$$T = T_0 + \Delta T(1 - e^{-\tau t}) \quad (11)$$

is provided in Fig. 11 as an example. Fitting curves well match the experimental data, which indicates that the analytic result

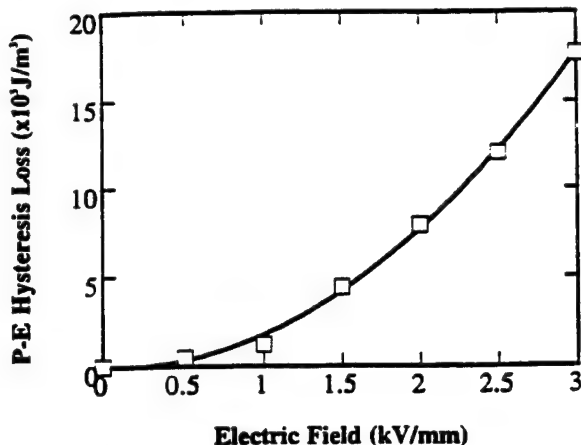


Fig. 10. $P-E$ hysteresis loss as a function of electric fields ($T = 25^\circ\text{C}$, $f = 300 \text{ Hz}$).

adequately describes the heat generation phenomena. Consequently, we can calculate the total loss u of the actuator through Eq. (10). The calculated results are shown in Table II. The experimental data of $P-E$ hysteresis losses are also listed for comparison. It is seen that the $P-E$ hysteresis losses are nearly equal to the total losses. Since the experiments were carried

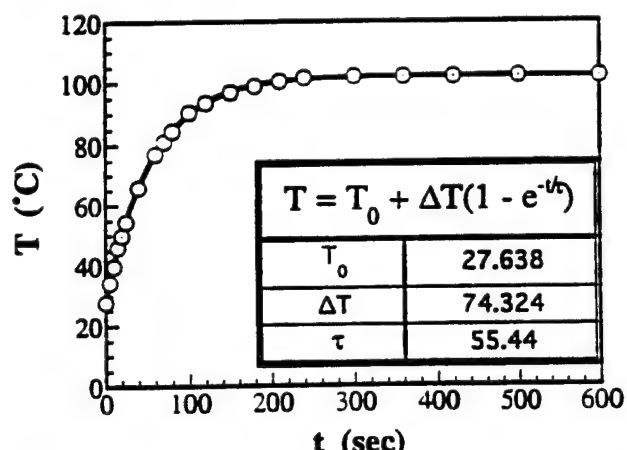


Fig. 11. Curve fit with the equation $T = T_0 + \Delta T(1 - e^{-\tau t})$ (data from the actuator with dimensions of 7 mm \times 7 mm \times 2 mm, driven under 3 kV/mm, 300 Hz).

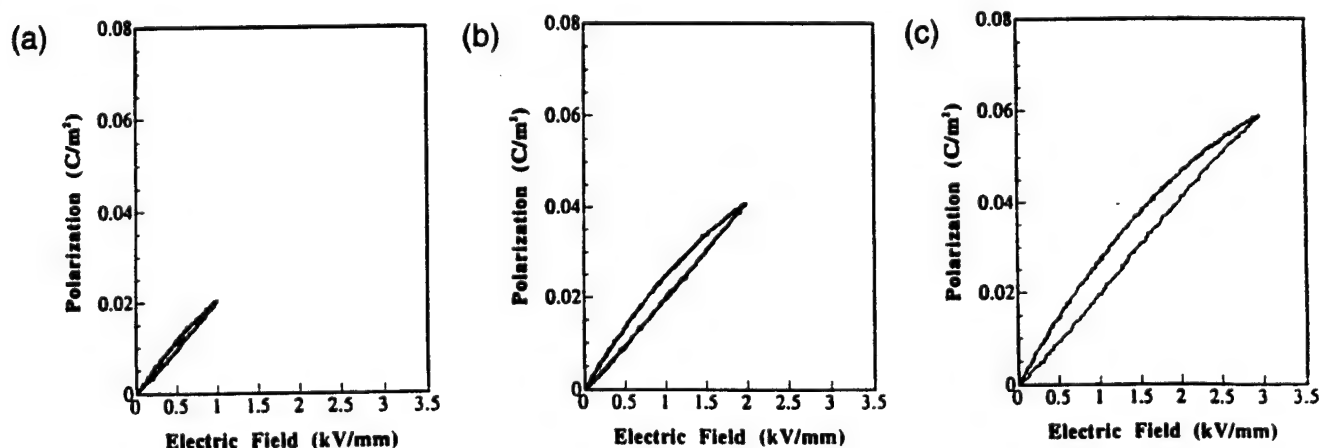


Fig. 9. $P-E$ hysteresis loops of various applied electric fields: (a) 1, (b) 2, (c) 3 kV/mm ($T = 25^\circ\text{C}$, $f = 300 \text{ Hz}$).

Table II. Loss and Overall Heat Transfer Coefficient ($E = 3 \text{ kV/mm}$, $f = 300 \text{ Hz}$)

Actuator	$4.5 \times 3.5 \times 2 \text{ mm}$	$7 \text{ mm} \times 7 \text{ mm} \times 2 \text{ mm}$	$17 \text{ mm} \times 3.5 \text{ mm} \times 1 \text{ mm}$
Total loss ($\times 10^3 \text{ J/m}^3$)			
$u = (\rho c v / f v_e) (dT/dt)_{\rightarrow 0}$	19.2	19.9	19.7
$P-E$ hysteresis loss ($\times 10^3 \text{ J/m}^3$)	18.5	17.8	17.4
$k(T)$ ($\text{W}/(\text{m}^2 \cdot \text{K})$)	38.4	39.2	34.1

out without external stress applying to the samples, it can be concluded that under the stress-free condition, heat generation in piezoelectric actuators is mainly due to ferroelectric hysteresis loss, and mechanical loss is negligibly small.

Regarding the heat generation from piezoelectric vibrators, Hirose *et al.* reported intriguing results.¹⁰ When a piezoelectric vibrator is driven at the resonance point, the main contribution to the total loss is from the mechanical loss under a small vibration velocity level, while the contribution from the dielectric loss increases drastically above a certain critical vibration velocity such as 0.2–0.3 m/s, where the actual heat generation starts to be observed. In our experiment, the driving frequencies are far below the resonances. (For example, the resonance frequency of sample 7 mm × 7 mm × 2 mm is 236 kHz, while the test conditions are below 2 kHz.)

By determining the time constant τ , the overall heat transfer coefficient $k(T)$ can be calculated through Eq. (8). The values of $k(T)$ for various actuators while driving under 3 kV/mm, 300 Hz are provided in Table II. The $k(T)$ as functions of frequency and electric field are shown in Figs. 12 and 13. It is seen from Fig. 12 that $k(T)$ is relatively insensitive to frequency under the low electric field level, while it increases gradually with increasing frequency when the applied electric field level is higher (>1 kV/mm). From Fig. 13, it is seen that $k(T)$ increases with increasing the applied electric field. The increase in $k(T)$ may be caused by the convection increase due to the vibration level (i.e., vibration velocity) change with E and f . If we summarize the frequency dependence of u and $k(T)$, we can see that u is insensitive to frequency, $k(T)$ is also relatively insensitive to f at the low electric field level, but gradually increases with increasing frequency at higher electric field levels (>1 kV/mm). Thus, according to Eq. (9), temperature rise is almost linearly proportional to f under the low electric field level, while at higher electric field levels (>1 kV/mm), the relationship between ΔT and f deviates from the linear trend due to the increase of $k(T)$ at higher f . This analysis coincides with the experimental results shown in Fig. 3. For the electric field dependence, u is proportional to E^2 , while $k(T)$ increases significantly with increasing E . That is why ΔT is nearly proportional to E^2 under low electric field as shown in Fig. 5, while deviating from this square relationship at a higher electric field level.

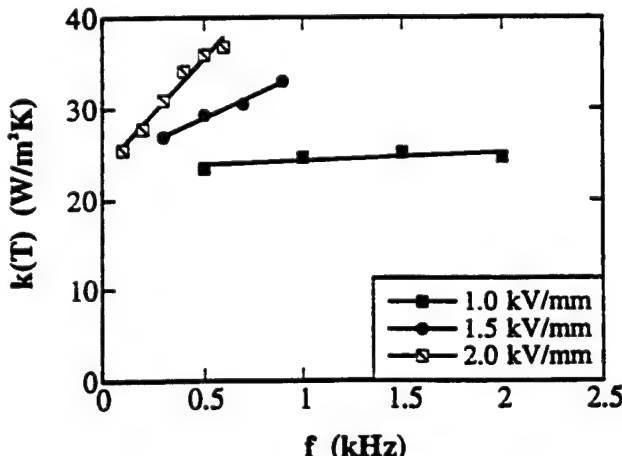


Fig. 12. Overall heat transfer coefficient $k(T)$ as a function of frequency (data from the actuator with dimensions of 7 mm × 7 mm × 2 mm).

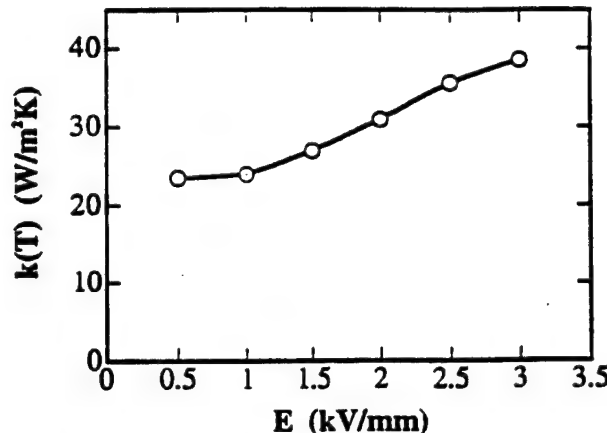


Fig. 13. $k(T)$ as a function of applied electric fields (400 Hz, data from the actuator with dimensions of 7 mm × 7 mm × 2 mm).

Equation (9) can be used to evaluate the temperature rise of piezoelectric actuators at the unclamped state and high field (higher than the threshold field at which domain wall motions occur) applications providing that the equilibrium temperature is lower than the Curie point. By simply measuring the $P-E$ hysteresis loss of the actuator, the temperature rise can be estimated by $ufv_e/k(T)A$, where $k(T)$ can be obtained from Figs. 12 and 13, if the sample has a size similar to the actuator in the figures. If the actuator has a significantly different size from the one in Figs. 12 and 13, the \bar{h}_c at $E = 0$, $f = 0$ can be estimated through the empirical correlation for free convection described in Ref. 20. But notice that \bar{h}_c is frequency and electric field dependent. If the actuator is used under a clamped state (as in most applications), the heat conduction through the sample surface is increased, and the mechanical loss may need to be considered.

V. Conclusion

Heat generation in multilayer piezoelectric actuators was studied. Under the stress free condition, heat generation is mainly due to ferroelectric hysteresis loss, not to mechanical loss. The temperature rise of the actuator can be estimated by the expression $\Delta T = ufv_e/k(T)A$. The proposed analytic method is useful for the design of multilayer and other high-power actuators from the viewpoint of heat generation.

References

- Takahashi, S., T. Yano, I. Fukui, and E. Sato, "Multilayer Piezoelectric Ceramic Actuator with Varying Thickness Layers," *Jpn. J. Appl. Phys.*, **24**, Suppl. 24-3, 206–208 (1985).
- Takahashi, S., "Longitudinal Mode Multilayer Piezoelectric Actuators," *Am. Ceram. Soc. Bull.*, **65** [8] 1156–57 (1986).
- Wersing, W., H. Wahl, and M. Schnöller, "PZT-Based Multilayer Piezoelectric Ceramics with AgPd-Internal Electrodes," *Ferroelectrics*, **87**, 271–94 (1988).
- Takahashi, S., "Recent Developments in Multilayer Piezoelectric Ceramic Actuators and Their Applications," *Ferroelectrics*, **91**, 293–302 (1989).
- Fransen, B. C. H., G. J. Janssen, S. J. J. Oostra, and J. W. C. de Vries, "Integration of Mechanics and Electronics: Low Voltage Ceramic Multilayer Actuators," presented at CARTS-Europe '92, October 5–8, 1992, Brugge, Belgium.
- Uchino, K., "Manufacturing Technology of Multilayered Transducers," pp. 81–93 in *Ceramic Transactions*, Vol. 49, *Manufacture of Ceramic Components*.

Edited by B. Hiremath, A. Bruce, and A. Ghosh. American Ceramic Society, Westerville, OH, 1995.

T. Yano, E. Sato, I. Fukui, and S. Hori. "Piezoelectric Impact Printhead Utilizing Longitudinal Piezoelectric Effect." *Dig. Tech. Pap., 1989 SID Int. Symp.*, 20, 180–83 (1989).

S. H. Chang and H.-C. Wang. "A High Speed Impact Actuator Using Multilayer Piezoelectric Ceramics." *Sens. Actuators A*, 24, 239–44 (1990).

K. Uchino. "Ceramic Actuators: Principles and Applications." *MRS Bull.*, 18 [4] 42–48 (1993).

S. Moriyama, T. Harada, and A. Takanashi. "Precision X-Y Stage with a Piezo-driven Fine-table." *Bull. Jpn. Soc. Precis. Eng.*, 22 [1] 13–17 (1988).

K. Lubitz and H. Hellebrand. "Properties of PZT Multilayer Actuators." *Proc. IEEE Int. Symp. Appl. Ferroelectrics*, 7th, 1990, 509–12 (1990).

A. Ochi, S. Takahashi, and S. Tagami. "Temperature Characteristics for Multilayer Piezoelectric Ceramic Actuator." *Jpn. J. Appl. Phys.*, 24, Suppl. 24-3, 209–12 (1985).

- ¹³J. H. Belding and M. G. McLaren. "Behavior of Modified Lead Zirconate-Lead Titanate Piezoelectric Ceramics under High Electric Fields." *Am. Ceram. Soc. Bull.*, 49 [12] 1025–29 (1970).
- ¹⁴R. A. Gdula. "High-Field Losses of Adulterated Lead Zirconate-Titanate Piezoelectric Ceramics." *J. Am. Ceram. Soc.*, 51 [12] 683–87 (1968).
- ¹⁵B. Lewis. "Energy Loss Processes in Ferroelectric Ceramics." *Proc. Phys. Soc.*, 73, 17–24 (1959).
- ¹⁶H.-J. Hagemann. "Loss Mechanisms and Domain Stabilisation in Doped BaTiO₃." *J. Phys. C: Solid State Phys.*, 11, 3333–44 (1978).
- ¹⁷F. Kreith and M. S. Bohn. *Principles of Heat Transfer*; pp. 17. Harper and Row, New York, 1986.
- ¹⁸A. J. Chapman. *Heat Transfer*, 4th ed.; pp. 13. Macmillan, New York, 1984.
- ¹⁹S. Hirose, S. Takahashi, K. Uchino, M. Aoyagi, and Y. Tomikawa. "Measuring Methods for High-Power Characteristics of Piezoelectric Materials." *Mater. Res. Soc. Symp. Proc.*, 360, 15–20 (1995).
- ²⁰D. R. Pitts and L. E. Sissom. *1000 Solved Problems in Heat Transfer*; pp. 406–407. McGraw-Hill, New York, 1991.

APPENDIX 54

FOURTH EURO CERAMICS - Vol. 5 - pp. 127-132
Electroceramics
Edited by G. Gusmano, E. Traversa
© Gruppo Editoriale Faenza Editrice S.p.A. - Printed in Italy

NEW PIEZOELECTRIC COMPOSITE ACTUATOR DESIGNS FOR DISPLACEMENT AMPLIFICATION

A. Dogan^{*/*}, J. F. Fernández^{*/**}, K. Uchino*, R. E. Newnham*

- * International Center for Actuators and Transducers, Materials Research Laboratory, The Pennsylvania State University, University Park, PA 16802, USA
- ** Supported by: Turkish Science and Technology Council (TUBITAK) and USA NAVY
- ** Current address: Electroceramics Department, Instituto de Cerámica y Vidrio, CSIC, 28500 Arganda del Rey, Madrid, Spain

ABSTRACT:

The moonie actuator is a versatile performer that fills the gap between the multilayer actuator and the bimorph actuator. This paper describes the effect of geometrical change in the endcap on the moonie's actuator characteristics. The effect of cavity dimensions, which are the key parameters for transformation and amplification of radial motion into axial motion, on the characteristics of the moonie actuator were investigated. Actuator properties of the newly designed cymbal actuator were investigated with different ceramic driving element. Characteristics of the different composite ceramic actuator designs were compared based on their displacement, response time and generative forces.

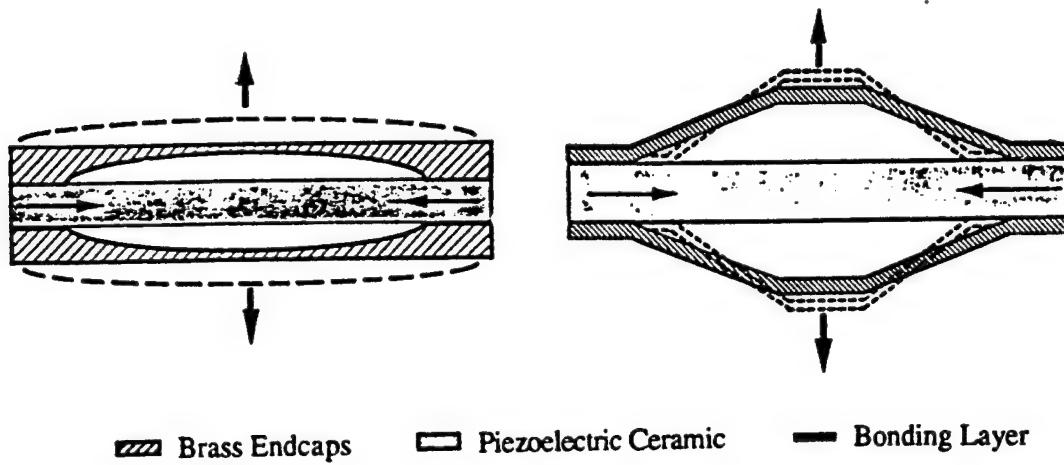
1. INTRODUCTION

Piezoelectric ceramics are widely used as a sensor many years. In recent years, there are lots of attention for the actuator application of the piezoelectric ceramics. Piezoelectric ceramic exhibits Poisson's effect; expansion in longitudinal direction and shrinkage in transverse direction, when an electric field is applied parallel to the polarization direction. There are two actuator designs which use this phenomenon to enhance the displacement for practical applications: multilayer ceramic actuators with internal electrodes and bimorph actuators. The advantages of the multilayer actuator are its generative force and quick response speed. However, small displacement and high capacitance of multilayer actuators make them impractical for certain applications. On the other hand, bimorph actuators show larger displacement. However, low generative forces and small displacement are their disadvantages. There is a need for an actuator with intermediate level displacement and generative force. The moonie and cymbal type of flexensional and roto-flexensional actuators were designed to fill the gap between multilayer and bimorph actuators [1-3]. The ceramic-metal composite moonie and cymbal actuators consist of ceramic driving element, epoxy or metal alloy bonding layer and metal, polymer or glass endcaps. Piezoelectric, electrostrictive, and antiferroelectric-ferroelectric type of ceramic materials can be used as a driving element. The basic configuration of the moonie and cymbal actuators are shown in Figure 1. The metal endcaps serve as mechanical transformer for converting and amplifying the lateral motion of the ceramic into a large axial displacement normal to the endcaps. Both the d_{31} ($=d_{32}$) and d_{33} coefficients of the piezoelectric ceramic contribute to the axial displacement of the composite.

The objective of this study is to evaluate the actuator characteristics of the moonie and cymbal transducers. Cavity beneath the endcaps plays an important role for transformation and amplification of lateral motion into axial motion. The effect of cavity dimensions on the characteristics of the moonie were studied systematically altering the cavity diameter and cavity depth while keeping the endcap thickness constant.

2. EXPERIMENTAL PROCEDURE

The composite actuators were made from electroded PZT-5A (Niobium doped Lead Zirconate Titanate), 0.9PMN-0.1PT (Lead Magnesium Niobate-Lead Titanate) and PNZST ($\text{Pb}_{0.99} \text{Nb}_{0.01}[(\text{Zr}_{0.6}\text{Sn}_{0.4})_{0.94}\text{Ti}_{0.06}\text{O}_{3}]$) (12.7 mm in diameter and 1 mm in thickness) and metal endcaps (12.7 mm in diameter with thickness ranging from 0.3 to 3.0 mm). The endcaps for moonie were machined from brass with composition 30% Zn-70% Cu. A punch die designed was used for the fabrication of the cymbal endcaps. The ceramic disk and the endcaps were bonded together around the circumference with Emerson & Cuming epoxy (Eccobond 45), taking care not to fill the cavity or short circuit the electrodes. The displacement of a composite actuator at 0.01 Hz was measured with a Linear Voltage Differential Transducer (LVDT) having a resolution of approximately 0.05 μm . Fastest response speed of the actuators was calculated from the resonant frequency data which was obtained with a Hewlett-Packard Impedance/Gain-Phase Analyzer HP-4194A.



Dimensions: (all in mm) Endcap diameter; $d_m = 12.7$ mm, PZT diameter; $d_p = 12.7$ mm
 Cavity diameter; $d_c = \text{variable}; 3.0, 5.0, 7.0, 9.0$ / Cavity depth, $h = \text{variable}; 0.3, 0.5, 0.7, 0.9$
 Metal cap thickness; $t_m = 1.0$, PZT thickness; $t_p = 1.0$ Bonding layer thickness; $t_b = 0.020$

Figure 1 The cross sectional view of the moonie (on the left) and cymbal (on the right) actuator. Arrows show the displacement direction

3. EVALUATION OF THE EFFECT OF GEOMETRY ON THE CHARACTERISTICS OF THE MOONIE TRANSDUCER

By altering the geometric parameters, it is possible to change the effective compliance of the composite moonie structure and tailor the desired actuator properties. The effect of the endcap thickness on the performance of the moonie actuator has been studied experimentally in correlation with FEA methods. The results have been reported in earlier publications [3-7]. The displacement shows an inverse relation with endcap thickness. The displacement of the moonie actuator increases with decreasing thickness, because of the increased flexibility of the endcaps. A moonie actuator with 0.3 mm thick brass endcap and with the fixed cavity diameter ratio at

80%, which is the ratio of the inner diameter of the endcap to the outer diameter, exhibits a 22 μm displacement under an applied electric field of 1.0 kV/mm. Generative force of the moonie actuator decreases drastically with decreasing endcap thickness. Although the flexural motion and displacement are largest at the center of the endcaps, the generative force is the lowest at that point. Displacement decreases dramatically when moving from the center to the edge. Conversely, generative force increases when moving from the center to the edge, where it approaches that of PZT ceramic. Therefore, it becomes possible to tailor the desired actuator properties by changing the contact area over the brass endcaps.

Brass endcaps with 3, 5, 7, and 9 mm cavity diameters and 0.3, 0.5, 0.7, and 0.9 mm crescent shaped cavity depths were fabricated by matrix combination while keeping the thickness constant at 1.0 mm, and diameter fixed at 12.7 mm. Figure 2 shows the relation between displacement and cavity diameter. The displacement amplification is exponentially related to the cavity diameter of the endcaps (at constant cavity depth) and linearly related to the cavity depth (at constant cavity diameter). Fastest response time-cavity diameter relations at various constant cavity depths of the moonie actuators is shown in Figure 3. Response time increases rapidly with increasing cavity diameter and decreases slightly with increasing cavity depth.

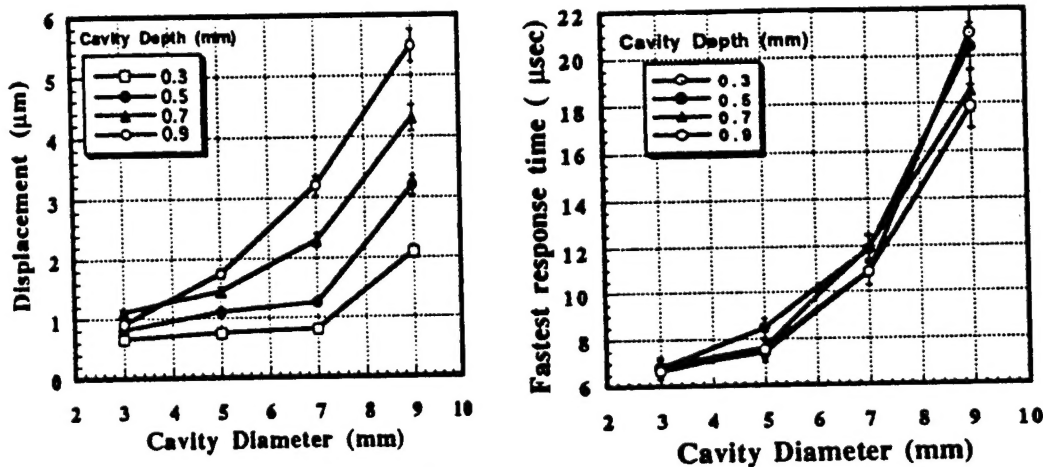


Figure 2. The displacement-cavity diameter relation of the moonie actuator (on the left)
Figure 3. Fastest response time-cavity diameter relation of the moonie actuator (on the right)

The effective coupling factor, k_{eff} , can be derived from the series (resonant) and parallel (antiresonant) resonant frequencies of the transducer [9]. The effective coupling factor for the first resonance mode of moonie actuators with varying cavity depth and cavity diameters were calculated from their admittance spectra. Figure 4 shows the calculated effective coupling factor, k_{eff} , of the moonie actuator as a function of the cavity diameter at various cavity depths. The planar coupling factor of PZT-5A disc with 12.7 mm in diameter and 1.0 mm in thickness is around 0.65. The coupling factor decreases to 0.54 because of the load effect when the PZT-5A ceramic disc is sandwiched between brass endcaps. The moonie actuator with a cavity diameter of 3.0 mm, and a cavity depth of 0.9 mm has the highest effective coupling factor of 0.42. As the cavity diameter increased, the effective coupling factor decreased linearly down to 0.11 for a cavity diameter of 9.0 mm with a cavity depth of 0.3 mm. Effective coupling factor depends heavily on the cavity diameter and shows low sensitivity to the cavity depth.

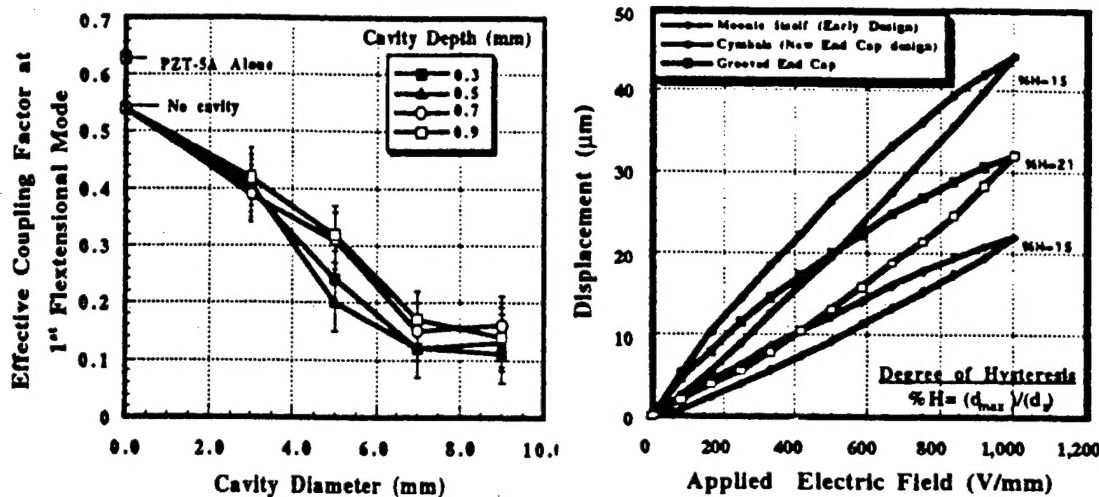


Figure 4 Effect of cavity diameter on the effective coupling factor, k_{eff} , of the moonie transducer at various cavity depths, (on the left).

Figure 5 Displacement hysteresis of different endcap designs, (on the right).

4. CYMBAL ACTUATOR

Finite element analysis in correlation with experimental results showed that there is a high compressive stress on the endcaps just above the bonding layer. Mechanical losses due to this stress concentration reduces the effective force transfer and from the PZT to the endcap. A new actuator design with truncated conical endcaps was developed, named the "Cymbal" [3-4]. The cymbal actuator exhibits higher displacement with larger generative force along with cost effective manufacturing. Displacement hysteresis of the different endcap designs are shown in Figure 5. With the cymbal endcaps displacement values enhanced twice as much as moonie's value. Displacement characteristics of the cymbal actuators with different ceramic materials as the driving unit are shown in Figure 6. Cymbal actuator with PZT-5A exhibits linear displacement. The cymbal actuator with the PMN-PT type ceramic driving element shows larger displacement with lower losses. However, it exhibits non-linear displacement characteristics according with the relaxor characteristics of the PMN-PT ceramic. PNZST is an antiferroelectric-ferroelectric type phase transition material. Unique properties of this material is that the volumetric expansion under applied electric field. With cymbal endcap design this volumetric expansion is converted to the negative axial displacement.

5 SUMMARY

Displacement of the moonie actuator is approximately inversely proportional to endcap thickness, exponentially proportional to the cavity diameter, and linearly proportional to the cavity depth. Response time of the moonie actuator increases with increasing cavity diameter. Moonie shows position dependent behavior with maximum displacement at the center and maximum force at the perimeter. Desired actuator properties can be easily tailored by changing the contact area over the endcaps. The moonie actuator can give displacements of 20 to greater than 100 μm , maximum generative force of 3 N to several N's, and response time of 20 to 100 μsec . By altering some of the dimensions on the moonie design, it is easy to tailor an actuator with desired properties. Cymbal actuator shows twice as big as displacement than moonie for the studied size and much higher generative force due to increased contact surface.

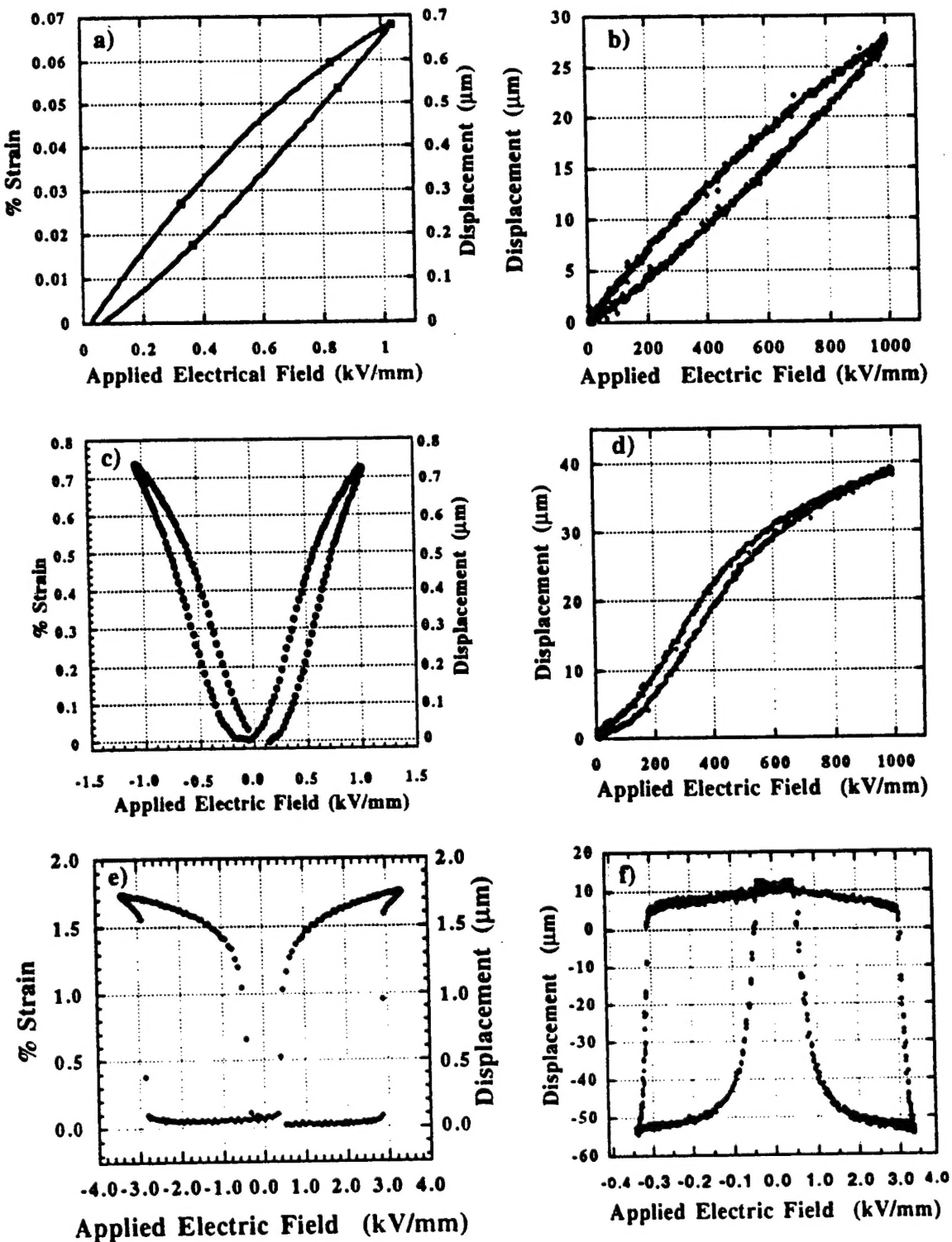


Figure 6. Displacement hysteresis various ceramic discs and cymbal actuators with this ceramics as driving element a) PZT-5A, b) Cymbal with PZT-5A, c) PMN-PT, d) Cymbal with PMN-PT e) PNZST, f) Cymbal with PNZST

Several features of the various solid state actuator designs are listed in Table I. Similar dimensions for each actuator were selected to make a fair comparison. Advantages of the moonie and particularly the cymbal actuators are the easy tailoring the desired actuator properties by altering the cavity size and endcap dimensions with cost effective manufacturing.

Table 1 Comparison of the Solid State Actuator Designs

Features	Multilayer	Bimorph	Rainbow	Cymbal	Moonie
References	[10]	[10]	[11]	[3-4]	[5-8]
Dimensions	5x5x12.7 (LxWxT)	12.7x10x1 (LxWxT)	Φ 12.7 mm T= 0.5 mm	Φ 12.7 mm T= 1.7 mm	Φ 12.7 mm T= 1.7 mm
Driving Voltage (V)	100	100	450	100	100
Displacement (μ m)	10	35	20	40	20
Generative Force (N)	900	0.5-1	1-3	15	3
Fastest Response Time (μ sec)	1- 5	100	100	5-50	5-50
Cost	high	med.	med.	low	low

ACKNOWLEDGMENTS

The authors would like to express their gratitude for the support to the following agencies and organizations: Office of Naval Research Contract no. N00014-92 J 1510, National Science Foundation Grant no. DMR-9223847, Spanish Science Ministry (CICYT MAT94-807 and DGICYT PR94-028), Turkish Science and Technology Council (TUBITAK) and Middle East Technical University, Ankara-TURKEY.

REFERENCES

- [1] R.E.Newnham, Q.C.Xu and S. Yoshikawa, *U.S Patent # 4,999,819 (March 12,1992).*
- [2] Y.Sugawara, K.Onitsuka, S.Yoshikawa, Q.Xu, R.E.Newnham, and K.Uchino, *J.Am.Ceram.Soc., vol. 75, no.4, pp. 996-999, (1992).*
- [3] A. Dogan Ph.D. thesis The Pennsylvania State University (PSU), 1994
- [4] A. Dogan and R.E. Newnham " Flextensional Cymbal Transducer" PSU Invention disclosure No. 94-1395,1994
- [5] A.Dogan, Q.C. Xu, K.Onitsuka, S.Yoshikawa, K.Uchino and R.E.Newnham, *Ferroelectrics, vol. 156, pp. 1-6, (1994)*
- [6] R.E.Newnham, A.Dogan, Q.C. Xu, K.Onitsuka, S.Yoshikawa, K.Uchino IEEE - UFFC , Baltimore 1993
- [7] K.Onitsuka, A.Dogan, J.Tressler, Q.C.Xu, S.Yoshikawa, and R.E.Newnham, *Ferroelectrics, vol. 156, pp. 37-42, (1994)*
- [8] A.Dogan, S.Yoshikawa, K.Uchino and R.E.Newnham, IEEE-UFFC Proceedings Vol II pp 935-939, France 1994
- [9] Mason, W.P., Physical Acoustics Vol 1 Part A, Academic Press, New York, (1964)
- [10] Information was extracted from Tokin Co. product catalog 1993
- [11] Haertling G. *Bull of Am. Ceramic Soc. Vol 73 No 1, pp 93-96, 1994 (1994)*